

p-ISSN 1811-1165
e-ISSN 2413-2179

VOLUME 18, No. 4(38), 2021

EURASIAN
PHYSICAL
TECHNICAL

JOURNAL

E.A. BUKETOV KARAGANDA UNIVERSITY

KARAGANDA, THE REPUBLIC OF KAZAKHSTAN

EURASIAN PHYSICAL TECHNICAL JOURNAL

p - ISSN 1811-1165
e - ISSN 2413-2179

Volume 18, No. 4(38), 2021

1st issue – March, 2004

Journal Founder:

**E.A. BUKETOV
KARAGANDA UNIVERSITY**

**Е.А.БӨКЕТОВ АТЫНДАҒЫ
ҚАРАҒАНДЫ УНИВЕРСИТЕТІ**

**КАРАГАНДИНСКИЙ УНИВЕРСИТЕТ
ИМЕНИ Е.А. БУКЕТОВА**

Contact information:

Editorial board of EPhTJ (Build. 2, room 216)
E.A. Buketov Karaganda University
Universitetskaya Str., 28, Karaganda,
Kazakhstan, 100028
Subscription index: 75240

Tel: +7(7212)77-04-03
Fax: +7(7212)77-03-84
E-mail: ephjt@mail.ru

Signed to print on 21.12.2021.
Format 60x84 1/8. Offset paper.
Volume 14.13 p.sh. Circulation 300 copies.
Agreed price. Order No. 139.

Басуға 21.12.2021 ж. қол қойылды.
Пішімі 60×84 1/8. Офсеттік қағазы.
Көлемі 14.13 ес.-б.т. Таралымы 300 дана.
Бағасы келісім бойынша. Тапсырыс № 139.

Подписано к печати 21.12.2021.
Формат 60 × 84 1/8. Офсетная бумага.
Объем 14.13 печ.л. Тираж 300 экз.
Ценадоговорная. Заказ № 139.

Printed in the Publishing House
of the E.A. Buketov KarU

Е.А. Бөкетов атындағы ҚарУ баспасының
баспаханасында басылып шықты

Отпечатано в Издательстве
КарУ им. акад. Е.А. Букетова

Chief EDITOR

Sakipova S.E., E.A. Buketov Karaganda University, Karaganda, Kazakhstan

EDITORIAL BOARD

Aringazin A.K., L.N. Gumilyov Eurasian National University, Nur-Sultan, Kazakhstan

Dzhumanov S., Institute of Nuclear Physics, Uzbekistan Academy of Sciences, Tashkent, Uzbekistan

Ibrayev N.Kh., Institute of Molecular Nanophotonics, E.A. Buketov Karaganda University, Kazakhstan

Jakovics A., Institute of Numerical Modelling, University of Latvia, Riga, Latvia

Kadyrzhanov K.K., L.N. Gumilyov Eurasian National University, Nur-Sultan, Kazakhstan

Kucherenko M.G., Director of the Laser and Information Biophysics Centre, Orenburg State University, Orenburg, Russia

Kuritnyk I.P., Department of Electronics and Automation, High school in Oswiecim, Poland

Miau J.J., Department of Aeronautics and Astronautics, National Cheng Kung University, Tainan, Taiwan

Narimanova G.N., Tomsk State University of Control Systems and Radioelectronics, Tomsk, Russia

Potapov A.A., V.A. Kotelnikov Institute of Radio Engineering and Electronics of RAS, Moscow, Russia

Pribaturin N.A., Institute of Thermal Physics, SB RAS, Novosibirsk, Russia

Saulebekov A.O., Kazakhstan Branch of Lomonosov Moscow State University, Nur-Sultan, Kazakhstan

Senyut V.T., Joint Institute of Mechanical Engineering of National Academy of Sciences of Belarus, Minsk, Belarus

Shrager E.R., National Research Tomsk State University, Tomsk, Russia

Stoev M., South-West University «Neofit Rilski», Blagoevgrad, Bulgaria

Suprun T., Institute of Engineering Thermophysics of NASU, Kyiv, Ukraine

Trubitsyn A.A., Ryazan State Radio Engineering University, Ryazan, Russia

Zeinidenov A.K., E.A. Buketov Karaganda University, Karaganda, Kazakhstan

Zhanabaev Z.Zh., Al-Farabi Kazakh National State University, Almaty, Kazakhstan

TECHNICAL EDITORS

Kambarova Zh.T., **Akhmerova K.E.**, E.A. Buketov Karaganda University, Karaganda, Kazakhstan

© Karaganda University, 2021

© Қарағанды университеті, 2021

Registration Certificate No.4382-Zh, November 7, 2003.

Re-registration Certificate No.KZ50VPY00027647, October 6, 2020 issued by Information Committee of the Ministry of Information and Public Development of the Republic of Kazakhstan

CONTENTS

PREFACE	3
MATERIALS SCIENCE	
1. Shishulin A.V., Potapov A.A., Shishulina A.V. THE INITIAL COMPOSITION AS AN ADDITIONAL PARAMETER DETERMINING THE MELTING BEHAVIOUR OF NANOPARTICLES (A CASE STUDY ON $\text{Si}_x\text{-Ge}_{1-x}$ ALLOYS)....	5
2. Durgadsimi S.U., Kattimani V.R., Maruti N.S., Kulkarni A.B., Mathad S.N. SYNTHESIS AND STRUCTURAL ANALYSIS OF NICKEL FERRITE SYNTHESIZED BY CO-PRECIPITATION METHOD.....	14
3. Shlimas D., Omarova A., Kozlovskiy A.L., Zdorovets M.V. STUDY OF THE EFFECT OF THE CHANGE IN THE APPLIED POTENTIAL DIFFERENCE ON THE PROPERTIES OF CDSE: Ni THIN FILMS.....	20
4. Yurov V.M., Makhanov K.M. THE HARDNESS OF HIGH-ENTROPY COATINGS OBTAINED BY THE METHOD OF MECHANICAL ALLOYING.....	29
5. Kasimov A.T., Yessenbayeva G.A., Zholmagambetov S.R., Khabidolda O. INVESTIGATION OF LAYERED ORTHOTROPIC STRUCTURES BASED ON ONE MODIFIED REFINED BENDING THEORY.....	37
ENERGY	
6. Razzhivin I. A., Ruban N.Yu., Rudnik V.E. ASSESSMENT OF THE WIND FARM IMPACT ON POWER SYSTEM STABILITY WHILE REDUCING OF TOTAL INERTIA.....	45
7. Shavdinova M.D., Sharipov R.D., Meshherjakova T.Y. ENHANCEMENT OF STEAM-TURBINE CONDENSER STEAM-JET EJECTOR.....	52
8. Tanasheva N.K., Tleubergenova A.Zh., Shaimerdenova K.M., Minkov L.L., Uzbergenova S.Zh. INVESTIGATION OF THE AERODYNAMIC FORCES OF A TRIANGULAR WIND TURBINE BLADE FOR THE LOW WIND SPEEDS.....	59
ENGINEERING	
9. Nizhegorodov A.I., Gavrilin A.N., Moyzes B.B., Ismailov G.M. HYDROSTATIC GENERATOR OF NON-PERIODIC PRESSURE IMPULSES FOR TESTING TECHNICAL PRODUCTS.....	65
10. Kelisbekov A.K., Daniyarov N.A., Akhmetbekova A.M., Orazbayev K.N. CONTROL OF STARTING MODES OF AN APRON CONVEYOR MULTI-MOTOR ELECTRIC DRIVE.....	74
PHYSICS AND ASTRONOMY	
11. Yadav K., Dhobi S.H., Maharajan S., Gupta S.P., Karki B., Nakarmi J.J. ELLIPTICALLY POLARIZED LASER-ASSISTED ELASTIC ELECTRON-HYDROGEN ATOM COLLISION IN COULOMB POTENTIAL.....	82
12. Zhumaev M.R. INVARIANT RELATIVISTIC THEORY OF IDEAL GAS.....	88
SUMMARIES	102
INFORMATION ABOUT AUTHORS	109
GUIDELINES FOR AUTHORS	111

Dear authors and readers!

Dear Colleagues!

It is already becoming a tradition to inform you about the most important achievements of the "Eurasian Physical Technical Journal" as a peer-reviewed scientific publication indexed in the international Scopus database, where the CiteScore 2021 is 0.7 (According to update on December 4, 2021).

On the Scimago Journal & Country Rank (SJR) platform, based on the results of materials published in the "Eurasian Physical Technical Journal" during period 2019 – 2020 **H-index is 2!**

Since January 28, 2021, the "Eurasian Physical Technical Journal" is included in the updated list of journals recommended by the Committee in the following areas: Physics, Energy, Materials Science.

The Open Access "Eurasian Physical Technical Journal" status provides free access to published full-text articles in PDF format, in addition to domestic databases of electronic libraries, also on the US Santa Barbara Library website.

This issue presents original scientific research results on topical problems of physics and technology. It should be noted that, despite the difference in the geography of the authors, the problems being solved are approximately the same. This is all the more valuable, since there is an opportunity to get acquainted with the applied research methods and original results.

The Materials Science section presents the results of modeling phase equilibrium in nanoparticles of the Si-Ge system, which are the main material of modern semiconductor electronics. The thermodynamic interpretation of the simulation results was obtained on the basis of various mechanisms for lowering the free energy of the system. Researchers from India, using a scanning electron microscope, the structural properties of nickel ferrite synthesized by the co-precipitation method studied. Fourier transform infrared spectroscopy of nickel ferrite shows the formation of a cubic structure with two significant absorption bands.

In another article researchers have studied the efficiency of using the effect of nickel doping of thin films based on CdSe using atomic force microscopy, energy dispersive analysis and X-ray diffraction, as well as photocatalytic tests. It has been shown that films in which the NiSe phase predominates are most promising for use as photocatalysts. Authors from Karaganda investigated the hardness of stainless steels, high-entropy coatings, metal glasses based on the analysis of Gibbs energy. Another paper is devoted to the numerical modeling of the stress-strain state of the orthotropic multilayer composite material plates.

The use of renewable energy sources necessitates solving various problems, such as ensuring sustainability when integrating them into electric power systems. The researchers from Tomsk investigated the features of the introduction of wind power plants into the power system, taking into account the influence of their operation on the rate of transient processes, due to a decrease in the total inertia. As another energy-saving solution at the operating thermal power plant, it is proposed to improve the steam-jet ejector of the condenser of steam turbines, which allows, during implementation, to obtain savings in heat consumption for the production of electrical energy. The Engineering section offers various technical solutions. For example, in the Russian authors paper the possibility of using hydrostatic oscillators with nonlinear power elements in the field of mechanical tests for vibration strength and vibration resistance is shown. In the Kazakh authors paper a method for controlling the starting mode of operation of a multi-motor electric drive of a plate conveyor is proposed to ensure its smooth start-up and reduce dynamic loads to increase the service life of the traction belt and to reduce maintenance costs.

The development of laser technologies determines the use of computer technologies to obtain more detailed information about the optical properties. The authors from Nepal show the calculation of the differential cross section using a mathematical model in the presence of a Coulomb potential and an elliptically polarized beam with one-photon absorption. The aim of the Uzbekistan author research is to

develop an original relativistic-invariant theory of an ideal gas. Based on the relativistic invariance of the velocity distribution function, an equation of state for a relativistic ideal gas is obtained, which relates its pressure, average energy density, and temperature.

In accordance with the requirements to international scientific journals, the editorial board members and reviewers are constantly updated and replenished. In this issue we present a new member of the editorial board - candidate of technical sciences, leading specialist of the Institute of Engineering Thermophysics of the National Academy of Science of Ukraine (IET NASU, Kiev), Suprun Tatiana Tarasovna. Her scientific interests associated with fundamental studies of the mechanism and patterns of transport processes in turbulized flows. The T.T. Suprun works are devoted to the experimental study of the regularities of convective heat transfer and hydrodynamics of elements of heat and power equipment, the development of methods for calculating heat transfer on streamlined surfaces under complicated external conditions, typical for the flow path of turbomachines. She has extensive experience as an executor in the implementation of funded projects and scientific programs. Suprun T.T. participated in joint experiments with the Institute of Theoretical and Applied Mechanics of the SB RAS (Novosibirsk), the Institute of Thermomechanics of the Czech Academy of Sciences (Prague), actively worked on a project between the IET NASU and the Institute of Fluid-Flow Machinery of the Polish Academy of Sciences (Gdansk).

It is known that the scientific journal quality is directly determined by the responsible work of editors and reviewers during preparation for publication. For over 10 years, Suprun T.T. provides invaluable assistance in improving the quality of articles in the areas of thermal physics, hydrodynamics and power engineering. We are sure that Suprun T.T. as member of the "Eurasian Physical Technical Journal" editorial board will contribute to the expansion and strengthening of international cooperation in future.

We hope that the proposed scientific works will interest our readers.
I'll be glad to see you among our authors of the next issues materials.

Best regards,
ch. editor of the "Eurasian phys. tech. j." Saule Sakipova
December, 2021

DOI 10.31489/2021No4/5-13

UDC 536.7, 544.012, 544.015.4, 544.3.01, 544.323.2

THE INITIAL COMPOSITION AS AN ADDITIONAL PARAMETER DETERMINING THE MELTING BEHAVIOUR OF NANOPARTICLES (A CASE STUDY ON $\text{Si}_x\text{-Ge}_{1-x}$ ALLOYS)

Shishulin A.V.^{1*}, Potapov A.A.^{2,3}, Shishulina A.V.^{4,5}

¹G.A. Razuvaev institute of Organometallic Chemistry, Russian Academy of sciences, Nizhny Novgorod, Russia,
chichouline_alex@live.ru

²V.A. Kotel'nikov Institute of Radio Engineering and Electronics, Russian Academy of Sciences, Moscow, Russia

³JNU-IREE RAS Joint Laboratory of Information Technology and Fractal Processing of Signals, Jinan University,
Guangzhou, China

⁴R.E. Alekseev Nizhny Novgorod State technical University, Nizhny Novgorod, Russia

⁵N.I. Lobachevsky Nizhny Novgorod State University, Nizhny Novgorod, Russia

Being the basis of modern electronics, silicon-germanium semiconductor alloys are widely used in a great number of fields. In this paper, the phase equilibria in Si-Ge nanoparticles have been simulated using a thermo-dynamical approach. Calculations show that nanoparticles of different diameters and compositions have unique sets of nanoscale liquidus and solidus temperatures which differ significantly from the reference data for the bulk alloy, and the range between nanoscale liquidus and nanoscale solidus temperatures narrows with reducing the particle size. Unlike bulk alloys, the compositions of co-existing liquid and solid phases at different temperatures dramatically differ in nanoparticles with various Si contents while the dependences of equilibrium phase compositions and volume fractions of co-existing phases on particle diameters have turned out to be different at various temperatures and atomic fractions of Si in a nanoparticle. A thermo-dynamical interpretation of the obtained results has also been given based on several mechanisms of lowering the free energy of the system.

Keywords: phase equilibria, nanoparticles, melting, silicon, germanium.

Introduction

Investigation of solid solutions between silicon and germanium at the nanoscale has been of particular increasing interest in recent years. Si-Ge solutions possess a unique set of properties including wide band gap, which can be gradually changed (by varying the germanium content); high mechanical strength; resistance to high temperatures etc [1]. Those properties, some of which can be changed and improved by nanostructuring, make Si-Ge solutions be a very promising material in numerous fields.

Silicon is considered to be the basis of modern electronics, being a relatively inexpensive and abundant semiconductor. Silicon-germanium nanoalloys have been applied to designing metal-oxide-semiconductor field-effect transistors with improved value of carrier mobility, complementary metal-oxide-semiconductor integrated circuits, high speed and high responsivity waveguide photo-detectors and hetero-junction bipolar transistors with dramatically improved performance, including values of cut-off frequency approaching to 300 GHz, and values of gate delay well below 10 ps (the numbers unimaginable in bipolar transistors), add to this, excellent electronic and optical properties allow Si-Ge nanoalloys to be widely utilized in phase change memory (PCM) devices, directly composing some of the PCMs (see [2-5]).

Furthermore, Si-Ge alloys have been widely used for manufacturing thermoelectric generators of different types. Radioisotope Si-Ge thermoelectric generators are installed on various spacecraft (e.g. "Voyager 2") and are working in space for several years almost without deterioration [6]. Thermoelectrical efficiency, which is revealed by a dimensionless figure of merit, ZT , can be greatly enhanced through nanostructural engineering [7, 8]. ZT is directly proportional to the electrical conductivity and inversely proportional to the thermal conductivity; the main approach to the solution of the problem of an increase in ZT is using polycrystalline nanomaterials where the thermal conductivity is decreased due to the formation of multiple grain boundaries which scatter thermal phonons while retaining the values of other parameters, and some other effects (see [8] and Refs. within).

Various types of Si-Ge nanostructures are prepared mainly by melt growth techniques including the zone-melting growth or the vapor-liquid-solid growth technology, however, the key role in fabrication of polycrystalline nanoalloys now belongs to additive manufacturing including direct and selective laser melting [9]. To control and improve those processes, the knowledge of thermodynamic properties at high temperatures (i.e. the phase diagram of Si-Ge solutions) at the nanoscale is critically needed. In the bulk state, pure Si and Ge and their alloys have been fairly well studied [10-12]. In nanosystems, experimental investigations (calorimetry experiments) are extremely challenging and time-consuming to perform, but nano-thermodynamical calculations offer a smart alternative. Despite the fact that some attempts to theoretically predict the phase equilibria in Si-Ge nanoalloys have been made by L.H. Liang *et al.* [13], S. Bajaj *et al.* [14] or by B. Bonham and G. Guisbiers [15] and, there are still a lot of gaps in their description and the considered alloys remain poorly studied at the nanoscale.

In nanomaterials, the description of phase transformations and equilibria is significantly complicated due to some specific effects. The compositions of co-existing phases and phase transition temperatures in nanoscale systems (nanoparticles, nanodroplets etc.) depend on the size of the system [13-23], its shape [16-19, 22] as well as on the thermodynamical properties of all interfaces [23]. In phase diagrams, the mentioned effects can manifest themselves as significant shifts of characteristic points, shifts and deformations of characteristic lines in comparison with phase diagrams for the bulk-state systems. The need to recalculate the phase equilibria at the nanoscale is due to the fact that the displacements of characteristic lines and points for nanoscale systems can exceed hundreds of degrees [13]. These effects have been observed experimentally [24] and can be explained by a great enhancement of the surface-to-volume ratio and surface contribution to the total energy of the system.

In order to calculate the phase equilibria at the nanoscale by thermodynamical methods, it is necessary to minimize the total Gibbs function of the system with allowance for the contribution of all interfaces and to analyze the configuration of its minima (see [16,20,21], for example). Despite the fact that there is a set of papers observing the mentioned effects, the general regularities cannot be obtained from most of them at present due to the substantial differences in the models derived and some critical gaps. For example, as far as the authors are aware, most of the approaches lack the consideration of the dependence of phase diagrams on the composition of the system. The model with the composition effect taken into account (with some simplifying presuppositions) has been introduced by our group and applied to modeling the melting behavior of nanoparticles of a tungsten heavy alloy for special applications [25] as well as the liquid-liquid phase separation in organic and polymeric solutions in small-volume droplets and pores [26]. The calculations have shown that, unlike bulk alloys, where a variation of the chemical composition of the system leads to changes in the volume fraction of co-existing phases (according to the lever rule) but does not affect the mutual solubility of components, in small-volume systems the chemical composition of the system determines not only the volume fractions of the phases, but also their equilibrium composition. Also, the calculations have shown an unusual effect of the significant variation of all phase equilibria characteristics depending on mutual position of co-existing solid and liquid phases in the structure [8, 16, 19, 20, 23] while all the sets of characteristics dramatically differ from each other and from the corresponding values for the bulk state. The shape of the system can also be taken into account using different approaches. For example, in [8, 16, 17, 19], we have suggested a dimensionless coefficient of shape, which is equal to the ratio between the surface areas of the figure under consideration and the sphere of the same volume.

The shape coefficient is a continuous parameter generalizing various versions of isochoric transformations of the system, including smooth deformations. Another way to describe the complex morphology of real particles is using the methods of fractal geometry [8, 16-19]. Formation of highly complicated fractal-shaped structures is generic for many non-equilibrium processes [27], the morphology of such structures is characterized by their fractal dimensions: the examples of structures with various fractal dimensions can be found in [8, 17-19].

In the present paper, we have highly developed the approach from [25] and used it to predict the high temperature phase equilibria for Si-Ge solid *core*-liquid *shell* nanoparticles as well as the tendencies which characterize their deviations from the data for the bulk state. In the bulk state, the considered alloy has a low-temperature symmetric miscibility gap at temperatures below ~ 266.5 K [14]. Above this temperature up to the liquidus, the Si-Ge system exhibits continuous solubility in the solid state with a diamond structure. At high temperatures, Si-Ge alloys have liquidus and solidus curves without a congruent melting point.

1. A mathematical model of solid → liquid phase transitions in nanoscale particles

The system to be modeled has the form of spherical Si-Ge nanoparticles of various diameters and compositions at temperatures above solidus. It is assumed that in phase equilibrium a nanoparticle is consisted of a single spherical solid inclusion (*core*-phase) surrounded by a spherical layer of a melt (*shell*-phase). In a closed binary thermodynamic system, the conservation conditions of matter are given by Eqs. (1):

$$\frac{\pi d^3}{6} = \sum_j V_j, \quad n_1 = xn, \quad n_2 + n_1 = n, \quad n_i = \sum_j n_{ij}, \quad V_j = \sum_i n_{ij} V_i, \quad x_{ij} = \frac{n_{ij}}{\sum_i n_{ij}} \quad (1)$$

where x is the atomic fraction of Si in the whole particle; d is the diameter of the particle under consideration; n is the total number of moles of both components in the particle; V_j is the volume of phase j ; $j=c, s$; the indices c and s refer to the solid *core*- and liquid *shell*- phases, respectively; n_i, n_{ij} and $V_{ij}(T)$ are the number of moles of each component n_i , the number of moles of component i in phase j and the molar volume of component i in phase j (the molar volumes are considered to be temperature-dependent in general case), respectively; $i=1,2$; the indices 1 and 2 refer to Si and Ge, respectively; x_{ij} is the molar of component i in phase j .

Temperature-dependent molar volumes of pure solid Si and Ge (thermal expansion) are expressed as follows: $V_{1c} = 11.989 \cdot \exp(2.280 \cdot 10^{-5} \cdot (T - 293))$, $V_{2c} = 13.648 \cdot \exp(1.725 \cdot 10^{-5} \cdot (T - 293))$ [28]. For melts of pure components: $V_{1s} = 11.100 \text{ cm}^3/\text{mol}$, $V_{2s} = 12.966 \text{ cm}^3/\text{mol}$ [ibid]. The geometric characteristics of the forming phases can be described as follows: $A_c = 4\pi(3V_c/4\pi)^{2/3}$, $A_s = \pi d^2$ where A_c are A_s are the surface areas of the *core*- and *shell*-phases, respectively.

A criterion for whether the system is at equilibrium is a minimum of its Gibbs function with allowance of all interfaces: $g = (n_{1c} + n_{2c})G_c(x_{1c}, T) + (n_{1s} + n_{2s})G_s(x_{1s}, T) + \sigma_s A_s + \sigma_{cs} A_c$, where σ_s, σ_{cs} are the surface energies on the outer (*-shell*) and internal (*core-shell*) boundaries. $G_c(x_{1c}, T)$ and $G_s(x_{1s}, T)$ are the molar Gibbs functions of solid and liquid Si-Ge solutions with compositions x_{ij} at temperature T , respectively.

As the authors of [10] have shown, the Si-Ge system can be described by the model of a regular solid solution:

$$\begin{aligned} G_s(x_{1s}, T) &= RT(x_{1s} \ln x_{1s} + (1 - x_{1s}) \ln(1 - x_{1s})) + \Omega_s(r_s) x_{1s} (1 - x_{1s}), \\ G_c(x_{1c}, T) &= RT(x_{1c} \ln x_{1c} + (1 - x_{1c}) \ln(1 - x_{1c})) + \Omega_c(r_c) x_{1c} (1 - x_{1c}) + \\ &+ x_{1c} \frac{\Delta_m H_1(r_c)}{T_{m1}(r_c)} (T - T_{m1}(r_c)) + (1 - x_{1c}) \frac{\Delta_m H_2(r_c)}{T_{m2}(r_c)} (T - T_{m2}(r_c)) \end{aligned} \quad (2)$$

where R is the ideal gas constant; $\Omega_f(r_f)$ are the regular solid solution parameters for liquid and solid phases, each parameter depends on the characteristic size r_j of the considered phase (on the radius of the solid *core*-phase r_c and the thickness of the liquid layer which forms the *shell*-phase r_s ; both r_c and r_s can be obtained from the given Eqs. after some simple transformations); $\Delta_m H_i(r_c)$ and $T_{mi}(r_c)$ are the size-dependent melting enthalpies and melting points of pure Si and Ge.

Size-dependent regular solution parameters $\Omega_f(r_f)$, melting enthalpies $\Delta_m H_i(r_c)$ and melting points $T_{mi}(r_c)$ as well as melting entropies $\Delta_m S_i(r_c) = \Delta_m H_i(r_c)/T_{mi}(r_c)$ can be calculated within various approaches; in this report, we use simple equations obtained by L.H. Liang *et al.* [13,18]:

$$\Delta_m S_i(r_c) = \Delta_m S_{i\infty} \left(1 - \left(\frac{r_c}{a_i} - 1 \right)^{-1} \right), \quad T_{mi}(r_c) = T_{mi\infty} \exp\left(\frac{-2S_{i\infty}}{3R(r_c/a_i - 1)} \right), \quad \Omega_j(r_j) = \Omega_{j\infty} \left(1 - \frac{2a_i}{r_j} \right) \quad (3)$$

where $S_{i\infty}, T_{mi\infty}$ are the “literature” melting entropies and melting points for pure Si and Ge in the bulk state; $\Omega_{f\infty}$ are the regular solid solution parameters for solid and liquid phases in the bulk state; a_i is the characteristic size of the crystal structure of a pure component; in calculations below, a_i is considered to be

equal to 6 atomic radii [13]. According to a remark made in [13], we use in our calculations the atomic radius of Si which is higher than the one of Ge. For pure Si: $T_{m1\infty} = 1693$ K, $\Delta_m S_{1\infty} = 29.41$ J/(mol·K), $a_1 = 132$ pm; for pure Ge: $T_{m2\infty} = 1210$ K, $\Delta_m S_{1\infty} = 20.57$ J/(mol·K), $a_2 = 122.5$ pm. $\Omega_{c\infty} = 3500$ J/mol, $\Omega_{s\infty} = 6500$ J/mol [25].

Surface energy $\sigma^{LV}(x)$ of Si-Ge liquid solutions as a function of composition x is obtained in [11]. The dependence is close to a linear one and can be approximated by the following relation: $\sigma^{LV}(x) = \sigma_1^{LV}x + \sigma_2^{LV}(1-x)$ where x is the molar fraction of Si, σ_1^{LV} и σ_2^{LV} are the surface energies of pure Si and Ge melts at the considered temperature. A similar equation is used for calculation of surface energies of Si-Ge solid solutions: $\sigma^{SV}(x) = \sigma_1^{SV}x + \sigma_2^{SV}(1-x)$. At crystal – melt interfaces, surface energies can be obtained from the simplified Girifalco-Good equation in the form which has been previously used by the authors of [29]: $\sigma^{SL} = \sigma^{SV} - \sigma^{LV}$.

Temperature dependences of surface energies for pure Si and Ge are calculated from the following linear equations (see Refs. [18, 28]): $\sigma_1^{LV} = 0.865 - 1.3 \cdot 10^{-4}(T - 1637)$, $\sigma_2^{LV} = 0.587 - 1.05 \cdot 10^{-4}(T - 1211.5)$, $\sigma_1^{SV} = 1.081 - 1.3 \cdot 10^{-4}(T - 1637)$, $\sigma_2^{SV} = 0.737 - 1.05 \cdot 10^{-4}(T - 1211.5)$.

In the bulk state, where the surface contribution to the total energy of the system is negligible, the phase equilibria calculated by finding the minima of the Gibbs function (Eqn. 2) (see Figs. 1-3), demonstrate a good agreement with the reference data [10].

2. Results and discussion

In the bulk state of a material, the only, single set of compositions of co-existing liquid and solid phases at a given temperature correspond to all possible compositions of the system (x). The composition of the system determines only the molar fraction of each phase directly according to the lever rule. However, the phase equilibria characteristics of nanoscale particles calculated by minimizing the Gibbs function (and plotted in Figs. 1-5) demonstrate a fundamentally different behavior in comparison with the one of the system in the bulk state. In particular, for each composition of the system (x), there is a unique set of equilibrium compositions of liquid and solid phases (see Figs. 1-3 for nanoparticles containing 25, 50 and 75 at.% Si, respectively). In each figure, the lower horizontal dashed line corresponds to the maximum temperature at which a nanoparticle of the given composition remains entirely solid (“nano-solidus”). The upper horizontal dashed line, in turn, corresponds to the minimum temperature at which a nanoparticle is still entirely liquid (“nano-liquidus”). At temperatures higher than “nano-liquidus” and lower than “nano-solidus”, a minimum of the Gibbs function corresponding to a heterogeneous state does not exist.

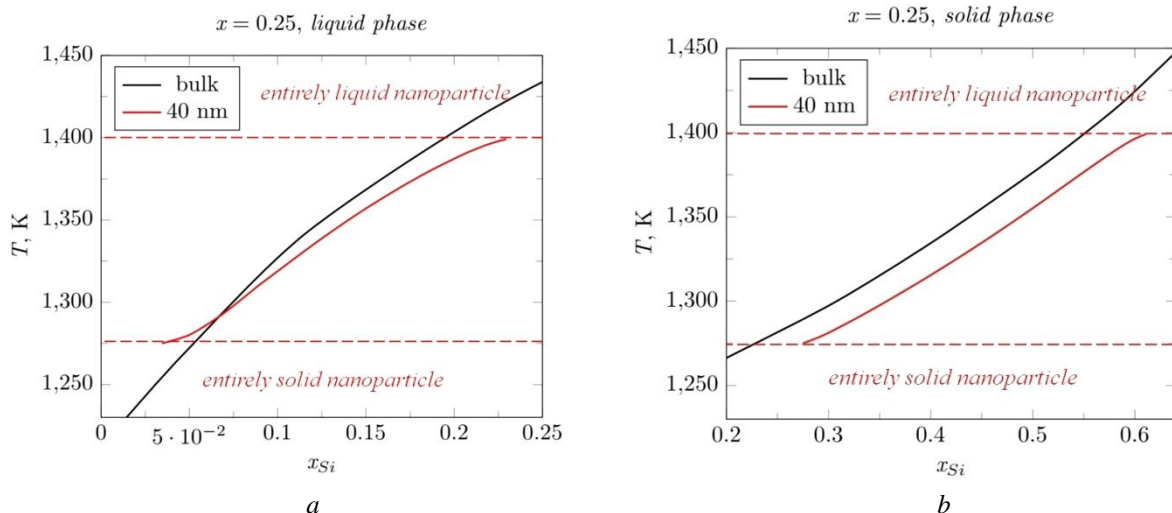


Fig.1. Temperature-dependent atomic fraction of silicon in the liquid (a) and solid (b) phase. The considered nanoparticle contains 25% Si. The red dashed lines indicate the “nano-liquidus” and “nano-solidus” temperature (the upper and lower ones, respectively). At room temperature, the particle diameter is equal to 40 nm. The black solid line represents the bulk behaviour.

At every composition of a nanoparticle and every temperature within the heterogeneous region, the solid phase is richer in Si than the one of the bulk system. The character of deviations of the composition of the liquid phase from the values for the bulk-state material differs depending on the temperature. At high temperatures near the “nano-liquidus”, the atomic fraction of Si in a nanoparticle is higher than in the bulk state while at low temperatures near “nano-solidus”, vice versa, the liquid phase is less rich in Si than such a phase in the bulk-state system. In details, this feature is illustrated in Fig. 4 where the composition of the liquid phase for equiatomic nanoparticles is plotted as a function of nanoparticle diameter at $T=1400$ (left) and $T=1500$ (right).

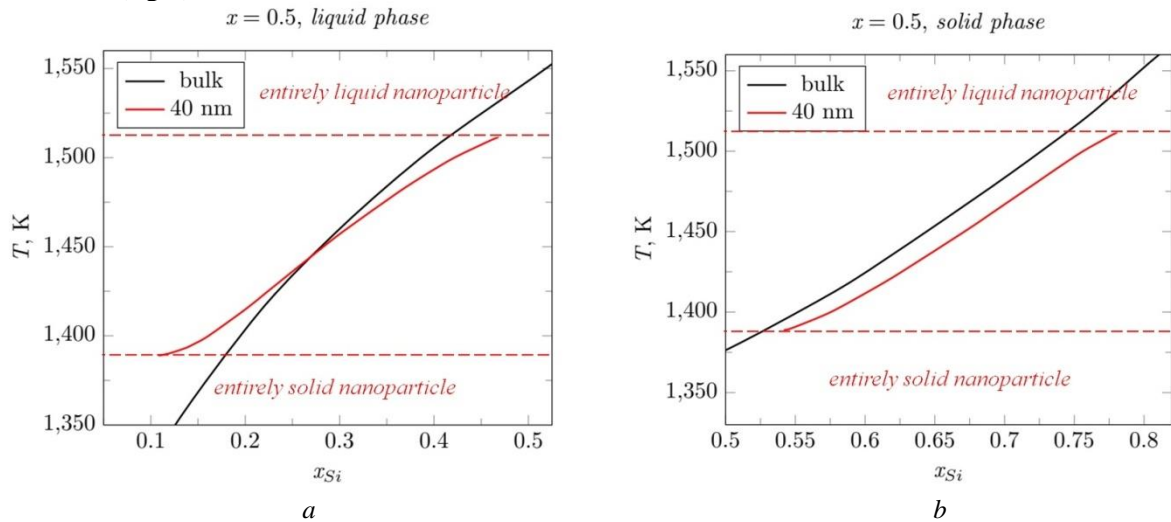


Fig. 2. Temperature-dependent atomic fraction of silicon in the liquid (a) and solid (b) phase. The considered nanoparticle contains 50% Si. The red dashed lines indicate the “nano-liquidus” and “nano-solidus” temperature (the upper and the lower ones, respectively). At room temperature, the particle diameter is equal to 40 nm. The black solid line represents the bulk behaviour.

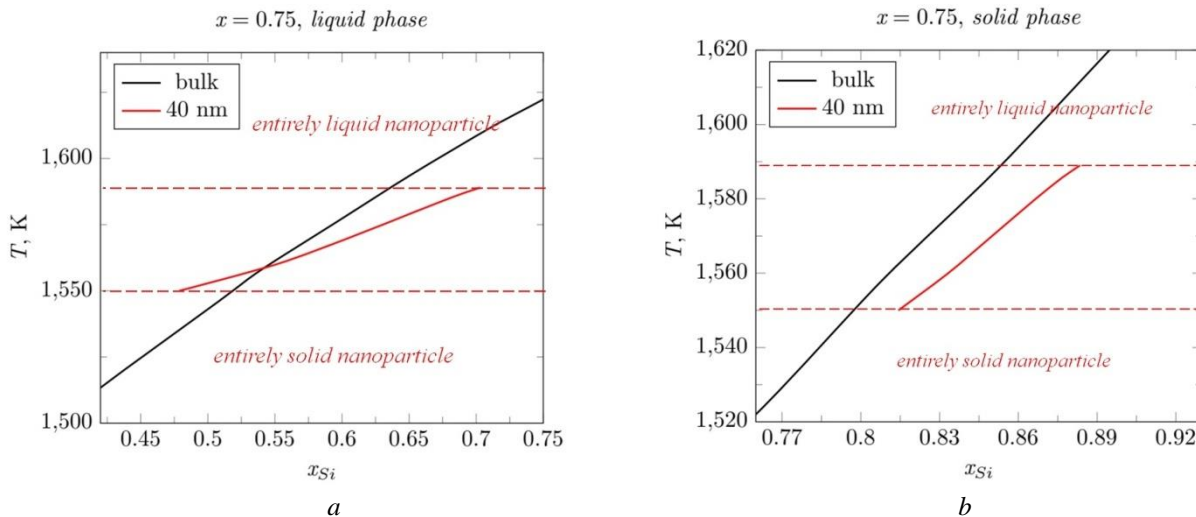


Fig. 3. Temperature-dependent atomic fraction of silicon in the liquid (a) and solid (b) phase. The considered nanoparticle contains 75% Si. The red dashed lines indicate the “nano-liquidus” and “nano-solidus” temperature (the upper and the lower ones, respectively). At room temperature, the particle diameter is equal to 40 nm. The black solid line represents the bulk behaviour.

As shown in Figs. 1-3, a decrease in the size of a particle leads to a decrease in the temperature range in which the system remains in the two-phase state. At every composition, the “nano-liquidus” of a 40-nm-diameter nanoparticle lies much below the corresponding point of the bulk liquidus line (see Fig. 5). The “nano-solidus” for all compositions considered is higher than its macroscopic analogue; the value of a temperature shift is equal to several dozens of degrees (such effect has also appeared in some previous calculations [25] where multiple simplifying presuppositions have been introduced).

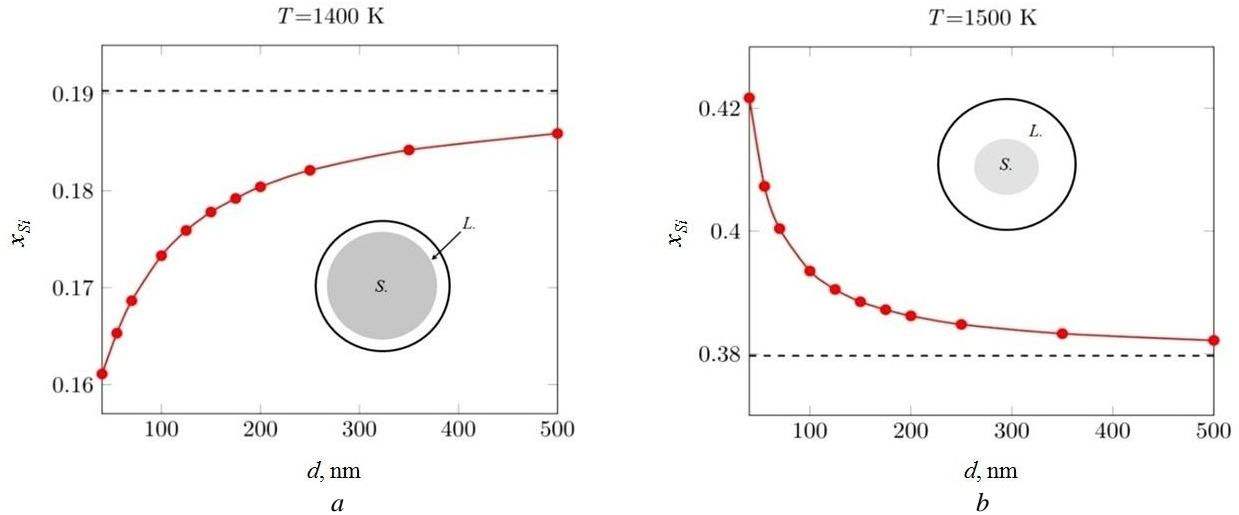


Fig. 4. Size-dependent compositions of the liquid phase (red solid lines) at $T=1400$ K (left) and $T=1500$ K (right) in comparison with the values for the bulk system (black dashed line).

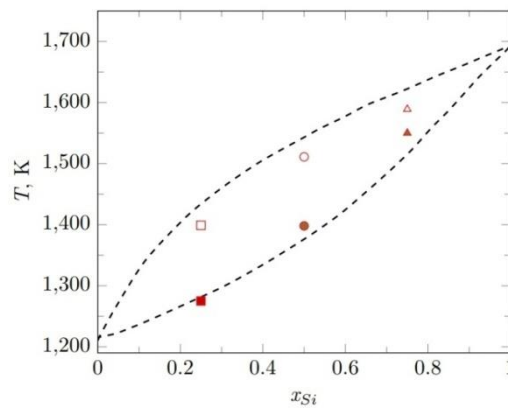


Fig. 5. “Nano-liquidus” and “nano-solidus” temperatures for nanoparticles of various compositions: 25 at.% Si (squares), 50 at.% Si (rounds), 75 at.% Si (triangles). At room temperature, the particle diameter is equal to 40 nm. Empty and filled markers correspond to liquidus and solidus temperatures, respectively. The phase diagram for the bulk-state material is plotted with a black dashed line.

The narrowing of the heterogeneous region for nanoparticle is caused by a great enhancement of the surface contribution to the Gibbs function of the system which makes remaining homogeneous without formation of an inner interface at temperatures near liquidus and solidus values for the bulk-state system thermodynamically more favorable. The changes in compositions of liquid and solid phases within the heterogeneous region can also be explained by the tendency to reduce the contribution of the surface energy which can possibly be realized [17,18,25,26]: (1) as a result of an increase in the total volume fraction of the melt, which is accompanied by a reduction in the inner surface area; (2) as a result of an increase in the content of the component with a higher molar volume (Ge) in the liquid phase, which is also accompanied by a reduction in the inner surface area; (3) as a result of an increase in the content of a lower surface energy component (Ge) in the melt, which leads to a decrease in the surface energy of the outer boundary (surface energies on the inner interface are always much lower than on the outer one [29]).

The performed simulation shows that in nanoparticles containing 50 and 75 at. % Si at low temperatures near “nano-liquidus”, all the three mechanisms are implemented. For example, in a nanoparticle containing 75 at. % Si at $T=1555$ K, a decrease in diameter from 100 nm down to 40 nm is accompanied with an increase of the volume fraction of the liquid phase from ~19 to ~23 vol. % and a slight increase in Ge content in the liquid phase. In an equiatomic nanoparticle of 40 nm in diameter at 1400 K, there is a similar trend: the volume fraction of the melt is about ~18 vol. % in comparison with the value of ~14 vol. % for a 100-nm-diameter nanoparticle, and the atomic fraction of molten Ge in the liquid phase is higher for smaller particle than for larger ones.

At the same time in nanoparticles with 50 and 75 at. % Si at high temperatures near “nano-solidus” and in Ge-rich nanoparticles (25 at. % Si) throughout the temperature region, mechanism 1 prevails (so the phase re-distribution is “volume-controlled”). For example, in a nanoparticle containing 75 at. % Si at $T=1585$ K, while the diameter decreases from 100 nm to 40 nm, the volume fraction of the melt dramatically increases from ~46 to ~62 vol. % and the atomic fraction of Ge in the liquid phase drops from ~36 down to 32 at. %. In the case of an equatomic nanoparticle at $T=1500$ K, the volume fractions of the liquid phase are equal to ~68 and ~76 vol. % for 100-nm-diameter and 40-nm-diameter particles, respectively, while Ge contents in the melt are ~65 and ~58 at. %, respectively. Finally, in a nanoparticle with 25 at. % Si at $T=1277.5$ K, the volume fraction of the liquid *shell*-phase grows from ~9 up to ~15 vol. % with reducing the size from 50 nm to 40 nm. At the same time, it is accompanied by a slight decrease in the atomic fraction of Ge in the liquid phase. At $T=1390$ K, when the particle size reduces from 100 nm to 40 nm, an increase in the volume fraction of the melt and a decrease in Ge content in the liquid phase also show up: from ~82 to ~88 vol. % and from ~81 to ~79 at. %, respectively.

A decrease in particle diameters down to smaller values leads to more significant deviations (than the ones presented in Figs. 1-5) of equilibrium compositions and volumes of co-existing phases from the reference data for the bulk-state material. Note that for particles of a smaller size, surface tensions can become size-dependent, at very small sizes, the basic concepts of thermodynamics could hardly be applied and even the difference between solid and liquids states vanishes [30]. Modeling of such small systems requires using some other approaches (see [31], for example). Note that despite the fact the term “nanoscale effects” is widely used, there is a broad class of systems, especially polymeric ones, with great molecular volumes and masses, in which such effects manifest themselves at characteristic sizes even several thousand times higher [20,26] (and such effects should probably be called “small-amounts-of-matter effects”). In addition to this, high surface-to-volume ratios can be obtained not only in nanoparticle materials but also in mesoporous ones while the morphology of pores also influences the characteristics of phase transitions including the magnetic ones [32].

The spherical geometry of considered particles is also an idealization. A spherical particle of a given volume has the minimal surface area, taking into account more complicated morphologies [8,17-19] leads to an additional increase in the surface contribution to the total Gibbs function and some more significant shifts of characteristic points in the “phase diagram”. As noted above, the shape of considered particle can be considered using one dimensionless parameter such as a coefficient of shape [8,16,17,19] or a fractal dimension [8,16-19] and requires minor changes of the Eqs. above. It is necessary to mention that the configuration of the interface between co-existing phases changes during the initial stages of melting, so the introduced shape parameter needs to be temperature-dependent [18]. In the general case, the specification of phase properties of a nanosystem without detailed and precise information on its size, shape, initial composition and some other properties is almost incorrect. In description of nanoobjects, the well-known concepts such as “phase diagram”, “liquidus”, “solidus” obtain new meanings. The suggested model can easily be applied to the description of the melting behavior in systems of other chemical compositions including three- and polycomponent ones while the appropriate solution model and its coefficients as well as material constants (e.g. surface free energies and their temperature and composition dependence, molar volumes and their temperature dependence etc) are required for simulations. The similar effects in systems with another nature of phase transitions (e.g. nanoparticles of stratifying solid solutions, stratifying liquid solutions in small-volume droplets and pores) can also be described using a model which is quite different in mathematical formulations but shares the same thermodynamical basis (see [17,20,26] for details).

In the case of nanoparticle ensembles containing particles with different morphology characteristics, the average phase composition and functional properties depend on the size and shape distributions in an ensemble. In [33], we have suggested a method for calculating such distributions based on the combined usage of number theory (including the derivations of G.H. Hardy and S. Ramanujan on the theory of partitions), fractal geometry and statistical thermodynamics. For example, the equilibrium size distributions for nanoparticles with fractal dimension D in a free-dispersed system can be expressed as follows:

$$f_D(\phi_p, D, N) \sim \exp\left(-\frac{\sigma A_{sp}(D) + RT \ln f_p}{RT}\right), \quad f_p = \frac{N}{N - \phi_p} \exp\left\{\pi \left(\sqrt{\frac{2}{3}}(N - \phi_p) - \sqrt{\frac{2}{3}}N\right)\right\}. \quad (4)$$

Here, $\phi_p = \omega(d_{eff}/d_{at})^3$ is the number of atoms in a nanoparticle, ω is the lattice packing density, N is the total number of atoms in the system, d_{eff} is the effective diameter of a nanoparticle (the diameter of a sphere of the same volume), $A_{sp}(D)$ is the specific surface area of the ensemble, $d_{at} = 2r_{at}$.

The presented estimates are in perfect accordance with the experimental data (see [33] and Refs. within) and make it possible to model the thermodynamical conditions for the realization of optimal average characteristics of nanoparticles (equilibrium compositions, phase transition temperatures, functional properties etc) as well to predict the degree at which such characteristic are “blurred” in an ensemble.

Conclusion

The performed thermodynamic analysis of phase equilibria in Si-Ge alloy nanoparticles of various compositions leads to the following conclusions:

1) in nanoparticles, the set of phase transition temperatures (liquidus, solidus) and the compositions of co-existing phases at phase equilibrium depend on the nanoparticle size. But in addition to this, at each size and temperature, the Si and Ge contents in solid and liquid phases are dramatically different for different compositions of a nanoparticle. The phase equilibria in a nanosystem can hardly be described by a single phase diagram for all the composition range;

2) the character of the influence of the nanoparticle size on phase compositions differs being temperature-dependent: reducing the particle size can lead either to an increase or to a decrease in Si content in the liquid phase. The explanation of such effects is based on the existence of several mechanisms of lowering the surface energy of the system while the dominant mechanism(s) is (are) different at different compositions and temperatures.

Acknowledgments

The research has been performed in the framework of the state task for IOMC RAS.

The authors cordially thank the anonymous reviewer for the attention to this study and providing valuable remarks.

REFERENCES

- Haddara Y.M., Ashburn P., Bagnall D.M. *Silicon-germanium: properties, growth and applications*. In: S. Kasap, P. Capper (eds.) Springer handbook of electronic and photonic materials, Springer handbooks. Cham, Springer, 2017, pp. 523 – 541. www.doi.org/10.1007/978-3-319-48933-9_22.
- Vivien L., Polzer A., Marris-Morini D., et al. Zero-bias 40Gbit/s germanium waveguide photodetector on silicon. *Optics express*. 2012, Vol. 20, pp. 1096 – 1101. www.doi.org/10.1364/OE.20.001096.
- Alloatti L., Srinivasan S.A., Orcutt J.S., et al. Waveguide-coupled detector in zero-change complementary metal–oxide–semiconductor. *Appl. phys. lett.* 2015, Vol. 107, No. 041104. www.doi.org/10.1063/1.4927393.
- Choi J.H. *High-speed devices and circuits with THz applications*. Boca-Raton, CRC Press, 2017, 261 p.
- Verma A.K., Modak P., Svane A., et al. Atomic structure and electronic properties of the Si_xSb_{100-x} phase-change memory material. *Phys. rev. B.* 2011, Vol. 130, No. 134205. www.doi.org/10.1103/PhysRevB.83.134205.
- Rowe D.M. (ed.) *Thermoelectric handbook macro to nano*. Boca Raton, CRC Press. 2006. 1008 p.
- Dorokhin M.V., Erofeeva I.V., Kuznetsov Yu.M., et al. Investigation of the initial stages of spark-plasma sintering of Si-Ge based thermoelectric materials. *Nanosyst.: phys., chem., math.* 2018, Vol. 9, pp. 622 – 630. www.doi.org/10.17586/2220-8054-2018-9-5-622-630.
- Shishulin A.V., Fedoseev V.B., Shishulina A.V. Phonon thermal conductivity and phase equilibria of fractal Bi-Sb nanoparticles. *Tech. phys.* 2019, Vol. 64, No. 4, pp. 512-517. www.doi.org/10.1134/S1063784219040200.
- Le Dantec M., Abdulstaar M., Leistner M., et al. *Additive manufacturing of semiconductor silicon on silicon using direct laser melting*. In: Industrializing additive manufacturing - proceedings of additive manufacturing in products and applications (AMPA-2017). 2017, pp. 104 – 116. www.doi.org/10.1007/978-3-319-66866-6_10.
- Olesinski R.W., Abbaschian G.J. The Ge-Si (germanium-silicon) system. *Bull. alloy phase diagram*. 1984, Vol. 5, p. 180. www.doi.org/10.1007/BF02868957.
- Ricci E., Amore S., Giuranno D., et al. Surface tension and density of Si-Ge melts. *J. chem. phys.* 2014, Vol. 140, No. 214704. www.doi.org/10.1063/1.4879775.
- Wang Q., Chang J., Wang H.P. Thermodynamical properties and atomic structure of liquid Si-Ge alloys. *Mater. chem. phys.* 2019, Vol. 221, pp. 224 – 231. www.doi.org/10.1016/j.matchemphys.2018.09.043.
- Liang L.H., Liu D., Jiang Q. Size-dependent continuous binary solution phase diagram. *Nanotechnology*. 2003, Vol. 14, pp. 438 – 442. www.doi.org/10.1088/0957-4484/14/4/306.

- 14 Bajaj S., Haverty M.G., Arróyave R., et al. Phase stability in nanoscale material systems: extensions from bulk phase diagrams. *Nanoscale*. 2015, Vol. 7, No. 9868. www.doi.org/10.1039/C5NR01535A.
- 15 Bonham B., Guisbiers G. Thermal stability and optical properties of Si-Ge nanoparticles. *Nanotechnology*. 2019, Vol. 28, No. 245702. www.doi.org/10.1088/1361-6528/aa726b.
- 16 Fedoseev V.B., Potapov A.A., Shishulin A.V., Fedoseeva E.N. Size and shape effect on the phase transitions in a small system with fractal interphase boundaries. *Eurasian phys. tech. j.* 2017, Vol. 14, No.1, pp. 18 – 24.
- 17 Shishulin A.V., Fedoseev V.B. On some peculiarities of stratification of liquid solutions within pores of fractal shape. *J. mol. liq.* 2019, Vol. 278, pp. 363 – 367. <https://doi.org/10.1016/j.molliq.2019.01.050>.
- 18 Shishulin A.V., Fedoseev V.B., Shishulina A.V. Melting behavior of fractal-shaped nanoparticles (the example of Si-Ge system). *Tech. phys.* 2019, Vol. 64, No. 9, pp. 1343 – 1349. <https://doi.org/10.1134/S1063784219090172>.
- 19 Shishulin A.V., Potapov A.A., Fedoseev V.B. *Phase equilibria in fractal core-shell nanoparticles of $Pb_5(VO_4)_3Cl - Pb_5(PO_4)_3Cl$ system: the influence of size and shape*. Advances in artificial systems for medicine and education II. Cham., Springer. 2020, pp. 405 – 413. https://doi.org/10.1007/978-3-030-12082-5_37.
- 20 Shishulin A.V., Fedoseev V.B. Thermal stability and phase composition of stratifying polymer solutions in small-volume droplets. *J. eng. phys. thermophys.* 2020, Vol. 93, No. 4, pp. 802 – 809. www.doi.org/10.1007/s10891-020-02182-9.
- 21 Mendoza-Pérez R., Muhl S. Phase diagrams of refractory bimetallic nanoalloys. *J. nanopart. res.* 2020, Vol. 22, No. 36. www.doi.org/10.1007/s11051-020-05035-x.
- 22 Geoffrion L.-D., Guisbiers G. Chemical ordering in $Bi_{1-x}Sb_x$ nanostructures: alloy, janus or core-shell. *J. phys. chem. C*. 2020, Vol. 124, No. 25, pp. 14061 – 14068. www.doi.org/10.1021/acs.jpcc.0c04356.
- 23 Shishulin A.V., Fedoseev V.B., Shishulina A.V. Environment-dependent phase equilibria in a small-volume system in the case of decomposition of Bi-Sb solid solutions. *Butlerov kommun.* 2017. Vol. 51, No. 7, pp. 31 – 37 [in Russian].
- 24 Straumal B., Baretzky B., Mazilkin A., et al. Increase of Mn solubility with decreasing grain size in ZnO. *J.Eur. ceram. soc.* 2009, Vol. 29, pp. 1963 – 1970. www.doi.org/10.1016/j.jeurceramsoc.2009.01.005.
- 25 Shishulin A.V., Fedoseev V.B. Effect of initial composition on the liquid-solid phase transition in Cr-W alloy nanoparticles. *Inorg. mater.* 2019, Vol. 55, no. 1, pp. 14 – 18. www.doi.org/10.1134/S0020168519010138.
- 26 Shishulin A.V., Fedoseev V.B. Features of the influence of the initial composition of organic stratifying mixtures in microsized pores on the mutual solubility of components. *Tech. phys. lett.* 2020. Vol. 46, No. 9, pp. 938 – 941. www.doi.org/10.1134/S1063785020090291.
- 27 Potapov A.A. On the issues of fractal radio electronics: Processing of multidimensional signals, radiolocation, nanotechnology, radio engineering elements and sensors. *Eurasian phys. tech. j.* 2018, Vol. 15, No. 2, pp. 5 – 15.
- 28 Hourlier D., Perrot P. Au-Si and Au-Ge phase diagrams for nanosystems. *Mater. sci. forum.* 2010, Vol. 653, pp. 77 – 85. www.doi.org/10.4028/www.scientific.net/MSF.653.77.
- 29 Alymov M.I., Shorshorov N.Kh. Effect of size factors on the melting point and surface tension of ultrafine particles. *Metally.* 1999, Vol. 2, pp. 29 – 31 [in Russian].
- 30 Magomedov M.N. On the minimum size of a nanoparticle when the difference between solid and liquid states disappears. *Herald of the Bauman Moscow state technical university.* 2012, Vol. 44, pp. 36 – 49 [in Russian].
- 31 Magnin Y., Zappelli A., Amara H., et al. Size-dependent phase diagrams of nickel-carbon nanoparticles. *Phys. rev. lett.* 2015, Vol. 115, No. 205502. www.doi.org/10.1103/PhysRevLett.115.205502.
- 32 Shishulin A.V., Potapov A.A., Shishulina A.V. On the transition between ferromagnetic and paramagnetic states in mesoporous materials with fractal morphology. *Eurasian phys. tech. j.* 2021, Vol. 18, No.2, pp. 6 – 11.
- 33 Fedoseev V.B., Shishulin A.V. On the size distribution of dispersed fractal particles. *Tech. phys.* 2021, Vol. 66, No. 1, pp. 34 – 40. <https://doi.org/10.1134/S1063784221010072>.

DOI 10.31489/2021No4/14-19

UDC 538.956

SYNTHESIS AND STRUCTURAL ANALYSIS OF NICKEL FERRITE SYNTHESIZED BY CO-PRECIPITATION METHOD

Durgadsimi S.U.¹, Kattimani V.R.², Maruti N.S.³, Kulkarni A.B.^{4*}, Mathad S.N.^{5*}

¹Department of Physics, Basaveshwar Engineering College, Bagalkot, Karnataka, India

²Department of Chemistry, Basaveshwar Engineering College, Bagalkot, Karnataka, India

³Department of Physics, K.R.C.E.S G.G.D Arts B.M.P Commerce and S.V.S Science college, Bailhongal, Karnataka, India

⁴Department of Physics, SKE Society's Govindram Seksaria Science College, Belagavi, Karnataka, India

⁵Department of Engineering Physics, K.L.E Institute of Technology, Hubballi, Karnataka, India,
physicssiddu@gmail.com

The Nickel ferrite has been synthesized by co-precipitation method. X-ray diffraction pattern confirms the formation of cubic spinel structure with lattice constant 8.347Å. Structural properties like X-ray density, average crystalline size, bond length, dislocation density and microstrain have been studied. The scanning electron microscope images show grain of bead structures. The Fourier transform infrared spectroscopy spectrum of nickel ferrite under investigation reveals the formation of a cubic spinel structure showing two significant absorption bands, corresponding to high frequency band ν_1 and low frequency band ν_2 arising from tetrahedral (A) and octahedral (B) interstitial sites respectively.

Keywords: Nickel ferrite, X-ray diffraction pattern, scanning electron microscope, Fourier transform infrared spectroscopy.

Introduction

Ferrites having a general chemical formula of AB_2O_4 with three types of ion distribution inside the structure namely, normal spinel, inverse spinel and mixed spinel [1]. The nickel ferrites are observed to be inverse spinel in nature, where nickel ion mainly occupying the tetrahedral site in the lattice. Structural, magnetic and electrical properties of ferrites are mainly dependent on synthesis conditions, size, metal ions in composition, and distribution of cations at tetrahedral A site and octahedral B sites [2]. The nickel ferrites are having large number of applications due to its good resistivity, good coercivity, good retentivity, optimum saturation magnetization, very high stability [3-4]. The nickel ferrites are found to good material in applications like memory storage devices, magnetic core [5], magnetic shielding [6], microwave devices [7-8], catalytic activity [9], gas sensor [10-12] etc. Nickel ferrites are synthesized using various methods based on the required properties, the methods are namely; auto- combustion method [13], sol-gel method [14], co-precipitation method [15-16], solid-state reaction method [17-18], hydrothermal [19] etc. In this paper, the work is aimed to synthesize $NiFe_2O_4$ nanoparticles by simple, low cost and environment friendly co-precipitation method. The co-precipitation method gives small grain size in the range of nm; the synthesis of particles takes place at room temperature [20]. The particle shape and size can be easily controllable based on the synthesis conditions. Hence Co-precipitation is comparatively having various advantages than other methods. The structural properties of synthesized material are characterized using X-ray diffraction, Scanning Electron Microscope (SEM) and Fourier transform infrared spectroscopy (FTIR).

1. Experimental part

The starting materials $NiCl_2$ and $FeCl_3$ were of analytical grade. The chemicals were taken in stoichiometric proportion; the mixture of chemicals is then dissolved in distilled water. The solution is thoroughly stirred for uniformity. The 3M NaOH is added drop wise for precipitation of solution with constant stirring at 60°C. Oleic acid is added as surfactant to the solution. Obtained brown colour precipitate solution again stirred and then washed with distilled water and ethanol, and then filtered. The precipitate is centrifuged and dried; the dark brown colour product is finely powdered using agate mortar in acetone medium. The end product is annealed at 500°C for 8 hours. The end product is annealed to give better crystallinity and agglomeration. The larger domain structures are helpful in better magnetic properties such

as coercivity and retentivity. The temperature of annealing is chosen keeping all these aspects and as per our previous work [21]. The schematic diagram of synthesis is shown in Fig. 1. Structural characterization of the nickel ferrite powder was carried out on Philips X ray diffractometer (XRD), with Cu K α radiation of wavelength 0.154nm. FTIR spectral analysis of sample was carried out in the wave numbers range between 400 cm⁻¹ to 4000cm⁻¹.

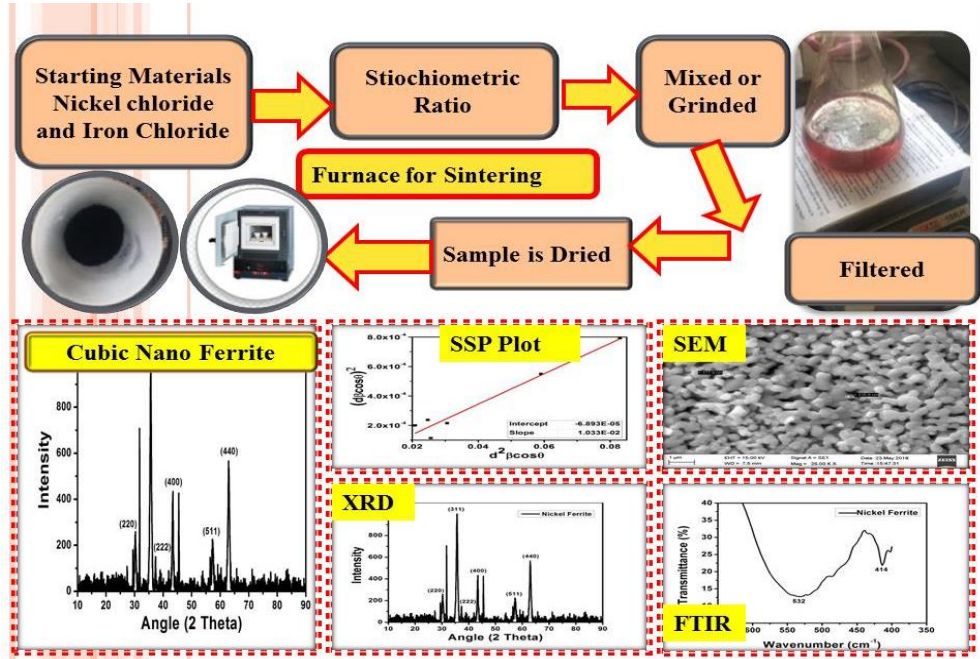


Fig.1. Schematic diagram of synthesis of characterization ferrite samples.

2. Results and discussion

2.1 X-Ray Diffraction Analysis

X-Ray Diffraction Analysis (XRD) pattern of synthesized NiFe₂O₄ is shown in Fig.2. Indexing of the peaks in XRD pattern is done by JCPDS card no.10-0325. Analysis of XRD pattern using Bragg's reflection planes (220),(311),(222),(400),(511)and (440) indicates the formation of cubic spinel structure. Interplanar spacing is calculated using Bragg's equation [17-18]

$$n\lambda = 2d\sin\theta, \quad (1)$$

where 'n' is order of diffraction, λ wavelength of x rays(0.154nm) and 'd' is interplanar spacing. For cubic spinel structure, interplanar spacing in terms of Miller indices is given by the equation

$$d = a/\sqrt{(h^2+k^2+l^2)} \text{ nm} \quad (2)$$

Interplanar spacing 'd' and lattice constant 'a' are calculated with corresponding (hkl) values and are tabulated in table 1.

Table 1. Interplanar spacing and lattice constant.

(hkl)	Angle (2 θ)	d(calculated) (Å)	d(observed) (Å)	Lattice constant(a) (Å)
(220)	30.31	2.950	2.949	8.341
(311)	35.65	2.518	2.518	8.352
(222)	37.36	2.410	2.407	8.338
(400)	43.41	2.087	2.085	8.338
(511)	57.27	1.605	1.609	8.358
(440)	62.92	1.475	1.477	8.355

Lattice constant a = 8.347 (Å)

The calculated and observed values of 'd' are in good agreement for all the peaks. The deviation from the perfect crystallinity results into broadening of the diffraction peaks. In X-ray diffraction the formula which relates the crystallite size to the broadening of a peak in diffraction pattern is Debye-Scherrer's formula which is given by the equation

$$D = 0.9\lambda/(\beta \cos\theta), \quad (3)$$

where D is average crystallite size, λ wavelength of incident X-ray and β angular line width of half maximum intensity (FWHM).

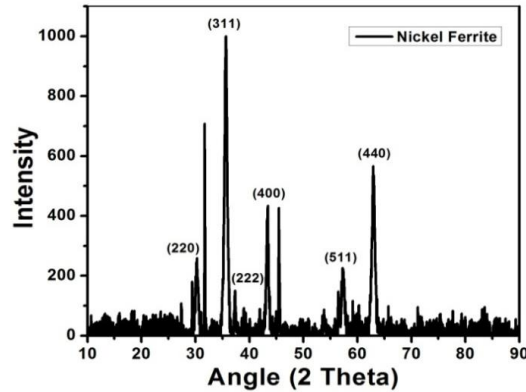


Fig.2.XRD pattern of NiFe₂O₄ nanoparticles

Dislocation density (δ) is defined as ratio of length of the dislocation lines the unit volume of the crystal, which represents the amount of defects in the sample and is calculated using equation (4)

$$\delta = 1/D^2 \quad (4)$$

The microstrain is defined as the deformation of an object divided by its effective length and is represented by ' ϵ '

$$\epsilon = \beta \cos\theta/4 \quad (5)$$

X-ray density (d_x) and lattice constant 'a' are related by the following expression

$$d_x = 8M/N_A a^3, \quad (6)$$

where N_A is Avogadro number, M is the molecular weight of the nano nickel ferrite.

The distance between magnetic ions (hopping length) in tetrahedral A site (L_A) and octahedral B site (L_B) were calculated using the following relations

$$L_A = a\frac{\sqrt{3}}{4} \text{ and } L_B = a\frac{\sqrt{2}}{4}, \quad (7)$$

where 'a' is lattice constant.

The calculated values of crystallite size (D), lattice constant (a), unit cell volume (V), dislocation density (δ), microstrain (ϵ), hopping lengths L_A and L_B and X-ray density (d_x) of NiFe₂O₄ particles are tabulated in Table 2.

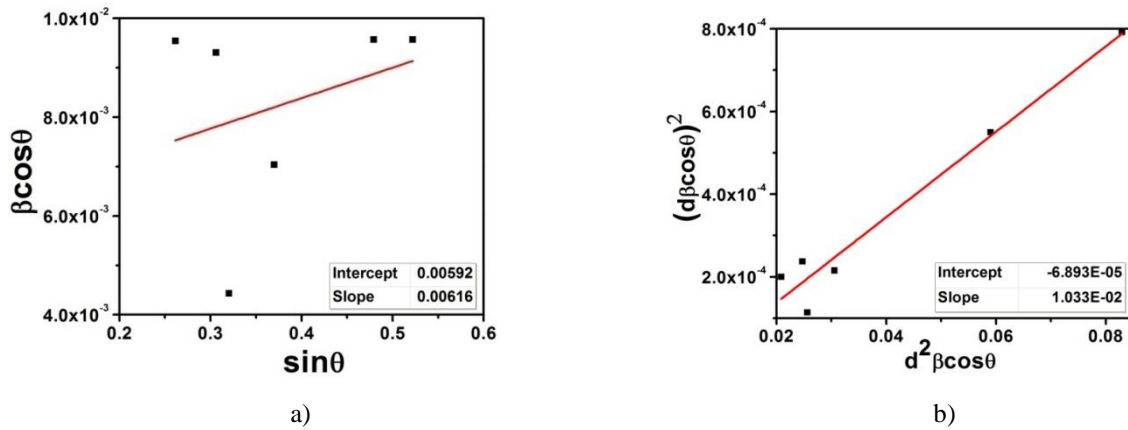
The size-strain broadening are additive components of the total breadth of a Bragg peak [22]. The distinct θ dependencies laid the basis for the separation of size and strain broadening in the analysis of Williamson and hall. The W-H plots are plotted using Eq.8 are plotted in Fig.3a.

$$\beta_{hkl} \cos \theta = \frac{K \cdot \lambda}{D} + 4\epsilon \sin \theta \quad (8)$$

Table 2. Crystallite size, lattice constant, unit cell volume, dislocation density, microstrain (ϵ) hopping lengths (L_A and L_B) and X-ray density.

Crystallite Size (D) (Å)	182	
Lattice constant (a) (Å)	8.347	
Volume (a ³) (Å ³)	581	
Dislocation density (δ)(m ⁻²)	3.72x 10 ¹⁵	
Microstrain (ϵ) (m ²)	2.06 x 10 ⁻³	
Hopping Length (Å)	$L_A = 3.614$	$L_B = 2.951$
X-ray density(d_x) (g/cm ³)	5.353	

Williamson-Hall (WH) and Size Strain Plot (SSP).

**Fig.3.** (a) WH plots and (b) Size strain plots of NiFe₂O₄ ferrite

The evaluation of the SSP parameters are obtained by considering peaks in intermediate range. This gives less weight to data from high angle reflections where the precision is usually less. The SSP plots are shown in Fig.3b which is plotted using Eq.9. [23].

$$(d_{hkl} \beta_{hkl} \cos \theta)^2 = \frac{K \cdot \lambda}{D} (d_{hkl}^2 \beta_{hkl} \cos \theta) + \left(\frac{\epsilon}{2}\right)^2 \quad (9)$$

Table.3 Crystallite size, micro strain and using W-H plots, SSP.

Crystallite size (in Å)		Micro strain ($\epsilon \times 10^{-3}$)	
From W-H graph	From SSP graph	Micro strain $\epsilon = \text{slope}/4$, (WH)	Micro strain $\epsilon = 2 \cdot \text{sqrt}(\text{intercept})$, (SSP)
234	134	1.54	16.60

2.2 Scanning Electron Microscope (SEM) analysis

The SEM image of NiFe₂O₄ nano particles is shown in Fig.4. The particles are observed to be granular in shape and the size of particles lies in the range of 300-400 nm size. The particles show uniformity in size and showing partial agglomeration.

2.3 Fourier Transform Infrared (FTIR) Studies

Fig.5 shows the Fourier Transform Infrared (FTIR) spectrum of NiFe₂O₄.

Waldron [24] observed that both absorption bands of ferrites are due to the familiar tetrahedral octahedral M-O stretching vibration modes. The spectrum of NiFe₂O₄ ferrite under investigation reveals the formation of a cubic spinel structure showing two significant absorption bands, at 532 cm⁻¹ and around 414 cm⁻¹ corresponding to high frequency band ν_1 and low frequency band ν_2 arising from tetrahedral (A) and octahedral (B) interstitial sites respectively [25].

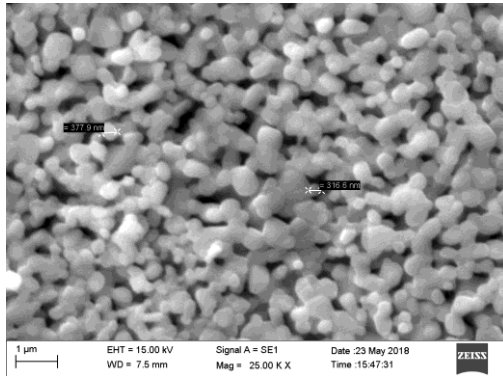


Fig.4. SEM image of NiFe₂O₄ nano particles

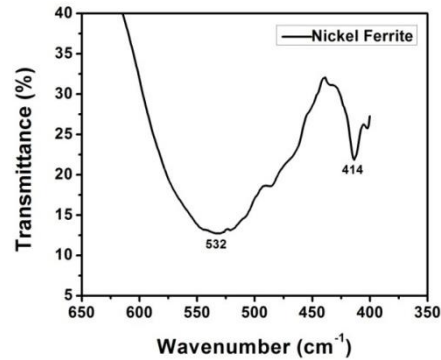


Fig.5. FTIR spectra of NiFe₂O₄

Conclusion

The spinel NiFe₂O₄ ferrite has been synthesized by Co-precipitation method. X-ray diffraction (XRD) pattern confirms the formation of cubic spinel structure with lattice constant 8.347Å. The crystalline size of the sample is observed to be 182Å (Debye-Scherrer method). The SEM images show grain of bead structures with size in the range 300-400 nm. The grains observed to be uniform in size but partially agglomerated. The two bands in FTIR spectra are observed at 532 cm⁻¹ and 414 cm⁻¹ confirming the tetrahedral and octahedral interstitial sites.

REFERENCES

- 1 Soohoo R.F. *Theory and Application of Ferrites*. 1960, 280 p.
- 2 Goldman A. *Modern ferrite technology*, 2006, 438 p.
- 3 Ranganathan, A. Ray Ferrites - what is new? *Pramana*. 2002, Vol. 58(5-6), pp. 995-1002.
- 4 Sugimoto M. The Past, Present, and Future of Ferrites. *J. Am. Cer. Soc.* 2004, Vol. 82(2), pp. 269-280.
- 5 Bahadur D., Giri J., Nayak B.B., et al. Processing, properties and some novel applications of magnetic nanoparticles. *Pramana*. 2005, Vol. 65(4), pp. 663-679.
- 6 Dar M.A., et.al. Surfactant assisted synthesis of Polythiophene/Ni_{0.5}Zn_{0.5}Fe_{2-x}Ce_xO₄ ferrite composites: Study of structural, dielectric and magnetic properties for EMI shielding applications. *Phy.Che.Che.Phy.* 2017, Vol.19, No.16, pp.1-35.
- 7 Bi K., Zhu W., Lei M., Zhou J. Magnetically tunable wideband microwave filter using ferrite-based metamaterials, *Appl. Phys. Lett.*, 2015, Vol. 106, No. 17, pp. 173507.
- 8 Su H., Zhang H., Tang X., Shi Y. Effects of microstructure on permeability and power loss characteristics of the NiZn ferrites, *J. Magn. Magn. Mater.* 2008, Vol. 320, No. 3-4, pp. 483-485.
- 9 Tsuji M., Kato H., Kodama T., Chang S. G., Hasegawa N., Tamaura Y., Methanation of CO₂ on H₂-reduced Ni(II)-or Co(II)-bearing ferrites at 200 C, *J. Mater. Sci.*, 1994, Vol. 29, No. 23, pp. 6227-6230.
- 10 Kamble R. B., Mathe V. L., Nanocrystalline nickel ferrite thick film as an efficient gas sensor at room temperature, *Sens. Actuators B: Chemical*, 2008, Vol. 131, No. 1, pp. 205-209.
- 11 Rezlescu E., et al. Porous nickel ferrite for semiconducting gas sensor *J. Phys.: Conf. Ser.* 2005, Vol. 15, pp. 51-54.
- 12 Darshane S. L., Suryavanshi S. S., Mulla I. S., Nanostructured nickel ferrite: A liquid petroleum gas sensor, *Cer. Int.*, 2009, Vol. 35, pp. 1793-1797.
- 13 Tiwari R., De M., Tewari H. S., Ghoshal S. K., Structural and magnetic properties of tailored NiFe₂O₄ nanostructures synthesized using auto-combustion method, *Results in Physics*, 2020, Vol. 16, pp. 102916.
- 14 Raju G., Murali N., Prasad M.S.N.A., Suresh B., Kishore Babu B., Effect of chromium substitution on the structural and magnetic properties of cobalt ferrite, *Mater. Sci. Energy Tech.*, 2019, Vol. 2, No. 1, pp. 78-82.
- 15 Shivgurunathan P., Gibin S. R., Preparation and Characterization of Nickel nanoparticles via Co-precipitation method with citrate as chelating agent, *J. Mater. Sci.: Mater. Electronics*, 2016, Vol. 27, No. 3, pp. 2601-2607.
- 16 Shashidharagowda H., Mathad S. N., Effect of incorporation of copper on structural properties of spinel nickel manganites by co-precipitation method, *Mater. Sci. Energy Tech.*, 2020, Vol. 3, pp. 201-208.
- 17 Kulkarni A. B., Mathad S. N., Synthesis and Structural Analysis of Co-Zn-Cd Ferrite by Williamson-Hall and Size-Strain Plot Methods, *Int. J. Self-Prop. High-Temp. Synth.*, 2018, Vol. 27, No. 1, pp. 37-43.
- 18 Kulkarni A. B., Mathad S. N., Variation in structural and mechanical properties of Cd-doped Co-Zn ferrites, *Mater. Sci. Energy Tech.*, 2019, Vol. 2, pp. 455-462.
- 19 Jinendra U., et al. Template-free hydrothermal synthesis of hexa ferrite nano-particles and its adsorption capability for different organic dyes: Comparative adsorption studies, isotherms and kinetic studies, *Mater. Sci. Energy Tech.* 2019, Vol. 2, pp. 657-666.
- 20 Kulkarni A. B., et al. Influence of cadmium substitution on structural and mechanical properties of Co-Ni nano ferrite synthesized by co-precipitation method, *Macromol. Symp.*, 2020, Vol. 393, pp. 1900213 (1-7).

-
- 21 Kulkarni A. B., Mathad S. N., Effect of cadmium doping on structural and magnetic studies of Co-Ni ferrites, *Sci. sint.*, 2021, Vol. 53, pp. 1-11.
- 22 Zak K., Abrishami M. E., Majid W. H. A., Yousefi R., Hosseini S. M., X-ray analysis of ZnO nanoparticles by Williamson-Hall and size-strain plot methods, *Ceram. Inter.*, 2011, Vol. 37, pp 393-398.
- 23 Prabhu Y. T., et al. X-Ray Analysis by Williamson-Hall and Size-Strain Plot Methods of ZnO Nanoparticles with Fuel Variation, *World J. Nano Sci. Engg.*, 2014, Vol. 4, pp. 21-28.
- 24 Waldron R. D., Infrared spectra of ferrites, *Phys. Rev.*, 1955, Vol. 99, No. 6, pp. 1727-1765.
- 25 Rendale M. K., Mathad S. N. Puri V., Structural, mechanical and elastic properties of $\text{Ni}_{0.7-x}\text{Co}_x\text{Zn}_{0.3}\text{Fe}_2\text{O}_4$ nano-ferrite thick films, *Microelectronics Int.*, 2017, Vol. 34, No. 2, pp. 57-63.

STUDY OF THE EFFECT OF THE CHANGE IN THE APPLIED POTENTIAL DIFFERENCE ON THE PROPERTIES OF CdSe: Ni THIN FILMS

Shlimas D.^{1,2}, Omarova A.¹, Kozlovskiy A.L.^{1,2*}, Zdorovets M.V.^{1,2,3}

¹L.N. Gumilyov Eurasian National University, Nur-Sultan, Kazakhstan, kozlovskiy.a@inp.kz

²Institute of Nuclear Physics, Almaty, Kazakhstan

³Ural Federal University, Yekaterinburg, Russia

This work is devoted to the study of the efficiency of using the effect of nickel doping of thin films based on CdSe with the possibility of varying the structural and optical properties due to a change in the phase composition of the films. The method of electrochemical reduction of metal ions from aqueous solutions of electrolytes was chosen as a method for obtaining films. The variation of the applied potential difference was used to produce films with different characteristics. To characterize the properties and dynamics of their changes, methods of atomic force microscopy, energy dispersion analysis and X-ray diffraction were chosen. The strength mechanical properties of the films were studied using the indentation method. During experiments conducted dependencies of changes of structural, optical, strength characteristics of synthesized films depending on production conditions are obtained. Photocatalytic tests to determine the rate and efficiency of decomposition of the Rodamine B organic dye showed that films in the composition of which the NiSe phase prevails have the greatest potential for use as photocatalysts.

Keywords: doping, CdSe, photocatalysis, thin films, reaction rate

Introduction

In the modern world, one of the key problems is pollution by products of the chemical and textile industries, which include various organic dyes used to color various materials [1-3]. At the same time, the majority of manufacturing products and waste during disposal retain their resistance to most physical, chemical and mechanical processing methods. One of the most common dyes used in industrial production is Rhodamine B, which allows giving the material a bright saturated color. However, despite the prevalence of this type of dyes, the processes of its utilization and processing are rather complicated, and the efficiency of processing and bringing the decomposition processes to harmless components is low with standard methods of disposal [4,5]. In turn, the accumulation of dye residues in aqueous media can lead to serious negative consequences associated with mutational processes or environmental pollution [6, 7].

To solve this problem, in recent years, methods of photocatalytic reactions with the use of various catalysts based on various semiconducting materials or ferroelectrics have been increasingly used [8-10]. The interest in these classes of materials is due to their optical properties and the band gap, which plays an important role in the processes of photodegradation and splitting of dyes under the influence of UV light. One of the promising materials is thin films based on cadmium-selenium, which have excellent semiconductor and optical characteristics, allowing them to be used as a basis for photoresistors, semiconductors, etc. [11-15]. At the same time, one of the promising areas of research in this field is the modification of thin films by doping them with magnetic elements from the iron subgroup, which make it possible to make significant changes in both the structural and optical properties of the films [16-20]. The main effect on which all changes in the properties of films are based is the replacement of cadmium or selenium with metal ions, followed by the possibility of forming substitutional or interstitial solid solutions. In this case, the formation of such phases leads not only to a change in structural changes, but also has a significant effect on an increase in the structural ordering degree in films and, consequently, a change in the strength properties, as well as an increase in resistance to external influences. It is also worth noting that, in some cases, doping with metals from the iron subgroup allows one to obtain films with grains of the «core-shell» type, which have their own specific features [21, 22].

One of the promising methods for producing thin films is the method of electrochemical reduction of metal ions from aqueous solutions of electrolytes, which makes it possible to obtain films with a controlled thickness, as well as a controlled phase and elemental composition [23-25]. At the same time, this method makes it possible to quite effectively carry out various modifications of films by adding various metal salts to the electrolyte solution, which are reduced on the substrate in the case of creating an applied potential difference. In turn, varying the difference between the applied potentials leads to the possibility of controlling both the thickness of the films and the concentration of recovered metal ions by changing their recovery potentials [26-30]. In this regard, the most urgent research is to assess the possibility of using the method of electrochemical synthesis of thin CdSe films from aqueous solutions of electrolytes with the addition of nickel salts to them to obtain solid solutions of substitution or interstitiality. Based on the above, the purpose of this work is to study the effect of the applied potential difference during the electrochemical reduction of metal ions from aqueous solutions on the change in the phase composition and structural parameters of CdSe films doped with nickel. The resulting films were also used as a basis for photocatalytic decomposition of the organic dye V.

1. Experimental part

The electrolyte solution used for the synthesis of thin films was obtained by dissolving the following salts in an aqueous solution in a given molar ratio: 0.5 M CdSO₄, 0.5 M SeO₂, 0.5 M NiSO₄·7H₂O. Varying the deposition potentials in the range from 1.0 V to 1.5 V was used to obtain films of various phase compositions. Determination of the phase composition and crystal lattice parameters was assessed by analyzing X-ray diffraction patterns obtained with a D8 Advance ECO X-ray diffractometer, Bruker. The X-ray diffraction patterns were recorded in the Bragg-Brentano geometry in the angular range $2\theta=35-75^\circ$, with a step of 0.03, the spectrum acquisition time was 1 sec. To calculate the crystallographic parameters, the DiffracEVA v.4.2 and TOPAS v.4 software codes were used. The phase composition was refined using the method of full-profile analysis of the positions of the diffraction maxima and their comparison with the reference values from the PDF2-2016 database.

The band gap and optical characteristics were determined using the UV-Vis transmission spectrum analysis technique obtained on the Jena Specord-250 BU optical spectrometer.

The determination of the electrophysical characteristics and the dynamics of changes in the I – V curves depending on the conditions for the synthesis of thin films was carried out in the range of -1.0 V to 1.0 V using the four-contact shooting method. The measurements were monitored using an Agilent 34410A multimeter with a Hewlett Packard 66312 A power supply.

The study of the efficiency of doping thin films with nickel on the decomposition rate of the organic catalyst Rhodamine B was evaluated by carrying out a model experiment of the photocatalytic reaction under the action of ultraviolet light. Rhodamine B (30 ml) diluted in distilled water was used as a model solution. A 500 W xenon lamp with a 420 nm light filter was used as an ultraviolet source. The rate of the photocatalytic decomposition reaction was estimated by measuring the absorption curves and determining the optical density by UV-Vis spectroscopy in a given wavelength range of 400-700 nm.

2. Results and discussion

Table 1 shows the results of changes in elemental analysis for the studied films obtained under various synthesis conditions. The determination of elemental analysis was carried out by analyzing the obtained energy-dispersive spectra from different areas of the samples under study and then calculating the average values. Determination of the elements distribution isotropy in the structure was evaluated by obtaining maps of the elements distribution using the mapping method in energy-dispersive analysis. According to the obtained data of the maps of the distribution of elements, it was found that the distribution of elements in the structure is isotropic, without any visible areas with a higher or lower content of elements, which indicates the uniformity of the deposition of elements and the formation of stable structural elements. According to the elemental analysis data, an increase in the potential difference from 1.0 to 1.5 V leads to an increase in the concentration of deposited nickel in the structure of the films from 11.5 at. % up to 26.2 and 34.6 at. % for samples obtained at potential differences of 1.0 V, 1.25 V, and 1.5 V, respectively.

The determination of the phase composition and the change in its dynamics depending on the preparation conditions was carried out on the basis of the analysis of X-ray diffraction patterns obtained in the angular range $2\theta=35-75^\circ$. The general view of the obtained diffraction patterns indicates the

polycrystalline structure of the obtained films with a low degree of structural ordering and a high content of amorphous-like inclusions in the structure of the films.

Table 1. Elemental composition data for the synthesized films

Applied potential difference, V	Cd, at. w. %	Se, at. w. %	Ni, at.w. %
1.0	43.2±1.3	45.3±2.1	11.5±0.9
1.25	37.5±1.6	36.3±1.4	26.2±1.3
1.5	34.2±1.1	31.2±1.6	34.6±1.7

This nature of X-ray diffraction patterns is characteristic of cadmium-selenium-based structures obtained by electrochemical deposition in the range of potential differences of 1.0-1.5 V, characteristic of the production of amorphous films [Fig.1]. According to the obtained X-ray diffraction data, peaks characteristic of two different phases are present on diffraction patterns. According to the data of the Rietveld full-profile analysis method, these reflections are characteristic for the following phases: the hexagonal CdSe phase with the spatial system P63mc (186) and the orthorhombic NiSe phase with the spatial system R3m(160). The distorted shape of these diffraction lines, as well as their large half-widths, indicate that the structure of the films contains rather fine grains, with a strongly distorted and deformed shape.

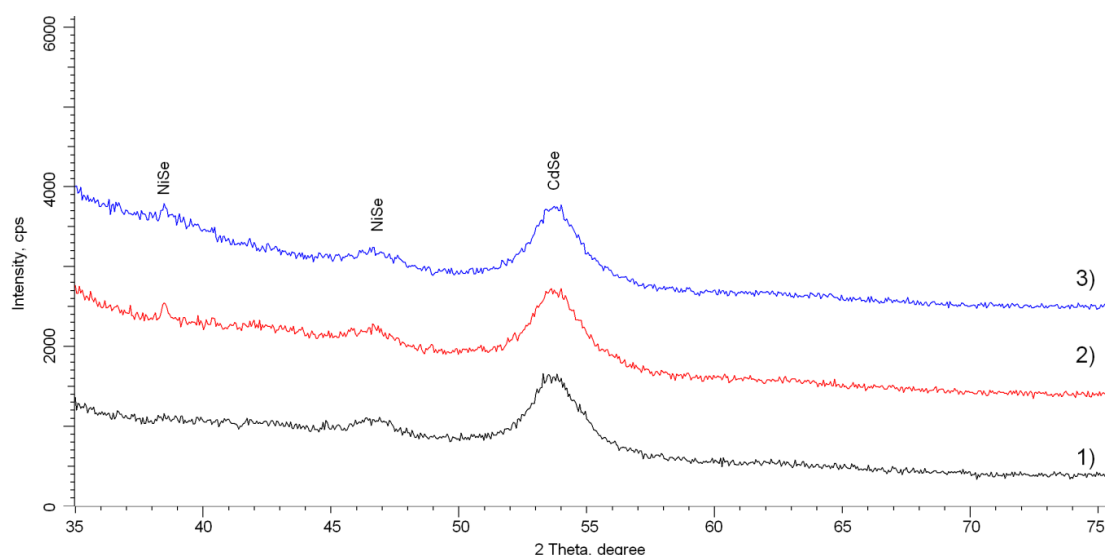


Fig.1. X-ray diffraction patterns of the synthesized films obtained at different potential differences:
1) 1.0 V; 2) 1.25 V; 3) 1.5 V

Estimating the contributions of two phases depending on the applied potential difference, the dependence of the change in the phase composition of the films was plotted, which is shown in Figure 2. In the case of samples obtained at a potential difference of 1.0 V, the NiSe:CdSe phase ratio is approximately 3:1. An increase in the applied potential difference, which leads to an increase in the concentration of nickel in the structure of the films, leads to an increase in the contribution of the NiSe phase, and to a change in the phase ratio. The increase in the contribution of the NiSe phase is due to the fact that with an increase in the applied potential difference, the rate of recovery of nickel ions from aqueous solutions of electrolytes becomes higher, as it approaches the value of the nickel reduction potential, as a result of which cadmium is partially replaced in the structure of the CdSe phase with the subsequent formation of a new NiSe phase. In this case, an increase in the potential difference leads not only to an increase in the contribution of the NiSe phase, but also to an increase in the structural ordering degree, which is expressed in a change in the shape and width of diffraction peaks characteristic of both phases.

Table 2 shows the results of changes in the crystal lattice parameters depending on the synthesis conditions at various potential differences. As can be seen from the data presented, a change in the applied potential difference leads to a decrease in the crystal lattice parameters and its volume, which indicates an increase in the structure ordering during the synthesis, as well as a decrease in the deformation contributions.

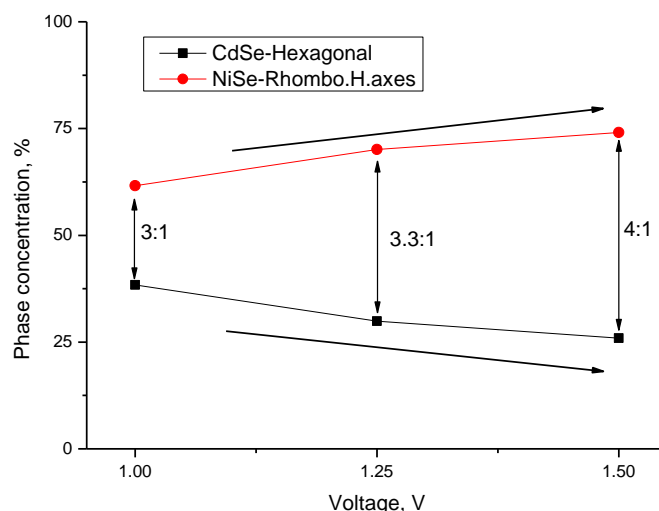


Fig.2. Diagram of changes in the films phase composition depending on the applied potential difference

It should be noted that a change in the phase composition, leading to the displacement of the hexagonal CdSe phase, also leads to an increase in the crystallinity degree by 7.6 % and 12.3 % for the samples obtained at a potential difference of 1.25 V and 1.5 V, respectively. This behavior of changes in the structural ordering degree indicates an improvement in the structure, as well as the formation of a denser lattice and a decrease in porous inclusions, which is also evidenced by a decrease in the volume of the crystal lattice and, consequently, an increase in density.

Table 2. Crystalline parameter data

Applied potential difference, V	Phase	Crystal lattice parameter, Å	Crystallinity degree, %
1.0	CdSe-Hexagonal, P63mc(186)	a=4.23132, c=6.91710, V=107.25 Å ³	67.4
	NiSe – Rhombo.H.axes R3m(160)	a=9.99234, c=3.30785, V=286.03 Å ³	
1.25	CdSe-Hexagonal, P63mc(186)	a=4.21224, c=6.91452, V=106.29 Å ³	75.0
	NiSe – Rhombo.H.axes R3m(160)	a=10.03348, c=3.31598, V=289.01 Å ³	
1.5	CdSe-Hexagonal, P63mc(186)	a=4.19159, c=6.90489, V=105.06 Å ³	79.7
	NiSe – Rhombo.H.axes R3m(160)	a=10.05905, c=3.31953, V=290.88 Å ³	

Figure 3 shows the results of changes in the morphological features of the surface relief of the films synthesized under different conditions. The general view of the changes indicates that an increase in the potential difference leads to a change in both the grain size and their concentration and agglomeration on the surface, which is primarily associated with a change in the grain formation rate, as well as a change in the phase composition and structural ordering degree.

Figure 4 shows the results of changes in the roughness and microhardness of the synthesized films depending on the applied potential difference during deposition. The roughness results were obtained by analyzing the images of the film surface obtained using atomic force microscopy.

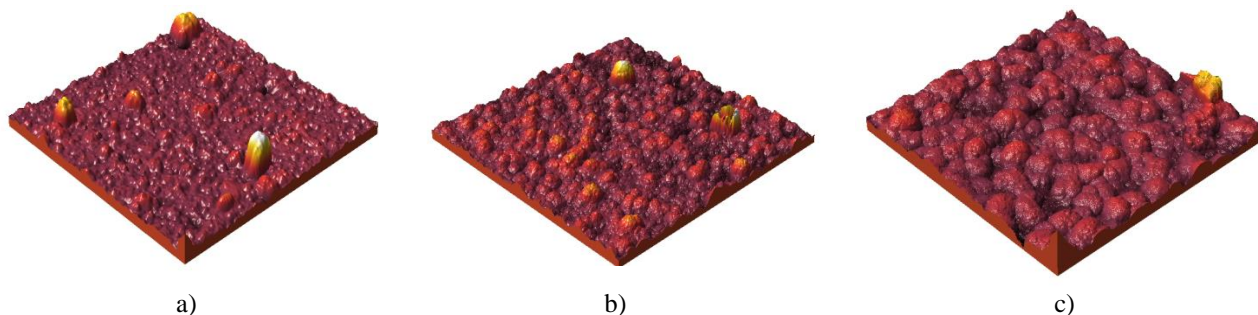


Fig.3. 3D images of morphological features of synthesized films: a) 1.0 V; b) 1.25 V; c) 1.5 V

An increase in the applied potential difference from 1.0 to 1.25 V, as can be seen from the presented data, leads to an insignificant increase in the roughness degree from 11 nm to 26 nm. This increase is due to a change in the size of the grains of which the film consists due to their enlargement. At the same time, an increase in the applied potential difference to 1.5 V leads to an increase in the roughness degree by more than a factor of 5 compared with the analogous value for the samples obtained with an applied potential difference of 1.0 V. At the same time, the analysis of changes in morphological features showed that changes in the synthesis conditions lead not only to enlargement of grains and, consequently, to an increase in the degree of roughness, but also to an increase in the degree of grain size uniformity.

So, at a potential difference of 1.0 V, the grain sizes, according to atomic force microscopy data, are no more than 5-10 nm, while the formation of single grains, the size of which is several tens of nanometers, is observed. An increase in the applied potential difference to 1.25 V leads to an increase in the grain size to 20-30 nm, as well as a decrease in the number of single large grains. At an applied potential difference of 1.5 V, the grain sizes increase to 50-70 nm, while the formation of large single grains in the films structure is practically not observed, which indicates an increase in the homogeneity of the films.

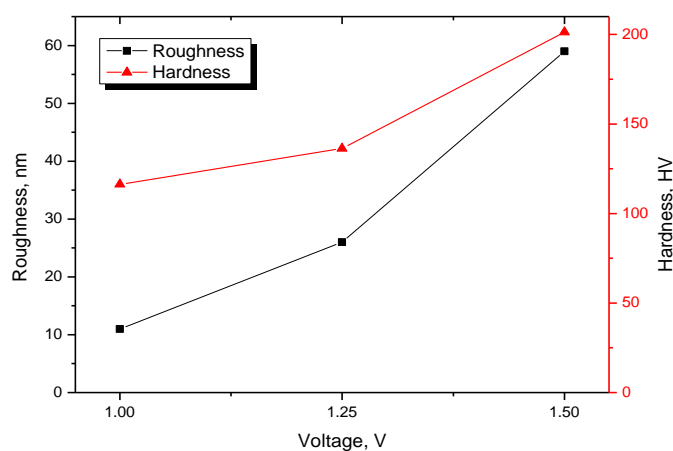


Fig.4. Graph of change of roughness and microhardness of synthesized films depending on the applied potential difference

The results presented of the change in the films microhardness depending on the preparation conditions indicate that a change in both morphological features, due to the coarsening of grains and an increase in the crystallinity degree, leads to an increase in the strength and hardness of the films. This behavior of changes in strength characteristics is due to the porosity decrease processes and the disordering regions content decrease in the films structure. In this case, a change in the potential difference to 1.25 V and 1.5 V leads to an increase in hardness by 17.2 % and 73.1 % in comparison to the samples obtained at a potential difference of 1.0 V. Figure 5 shows the results of the change in the graphs of the I-V characteristics of the studied thin films, filmed in the range from -1.0 to 1.0 V, which are characterized by the presence of two sections of the I-V characteristic, obeying the ohmic nature (-1.0 to 0) V and the quadratic dependence of the I-V characteristic (from 0 to 1.0 V). As is known, the quadratic dependence of the change in the I – V characteristic is most characteristic of semiconductor compounds and is characterized by a limited filling of electron traps, which leads to a sharp increase in conductivity. The analysis of the dependences obtained for

the structures under study showed that an increase in the NiSe phase contribution and the structural ordering degree leads to an increase in the conductivity and a decrease in the resistance. The increase in conductivity is also due to a decrease in the concentration of amorphous inclusions in the structure of the films, as well as to an increase in the grain size, which is accompanied by a decrease in the dislocation density and defect structure.

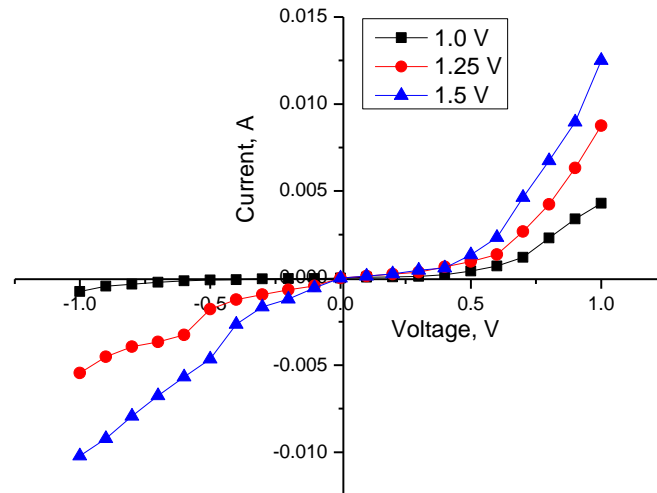


Fig.5. I-V characteristics of synthesized films depending on preparation conditions

Figure 6 shows the results of the change in the fundamental absorption edge shift value in the energy representation, which makes it possible to determine the band gap, as well as its changes depending on the phase composition of the films. The general view of changes in the fundamental absorption edge indicates that a change in the phase composition leads to a shift of the edge to the low-energy region, which indicates a decrease in the band gap. The presented dependences of the change in the band gap and the refractive index, which characterizes the optical density of the material, reflect the inverse dependence of the change in these values from each other. In this case, a change in the phase composition, as well as a decrease in the crystalline porosity, leads to an increase in the refractive index and, consequently, to a decrease in the porosity of the films. In turn, an increase in the NiSe phase contribution leads to a decrease in the band gap and, hence, to a change in the electron density of the films.

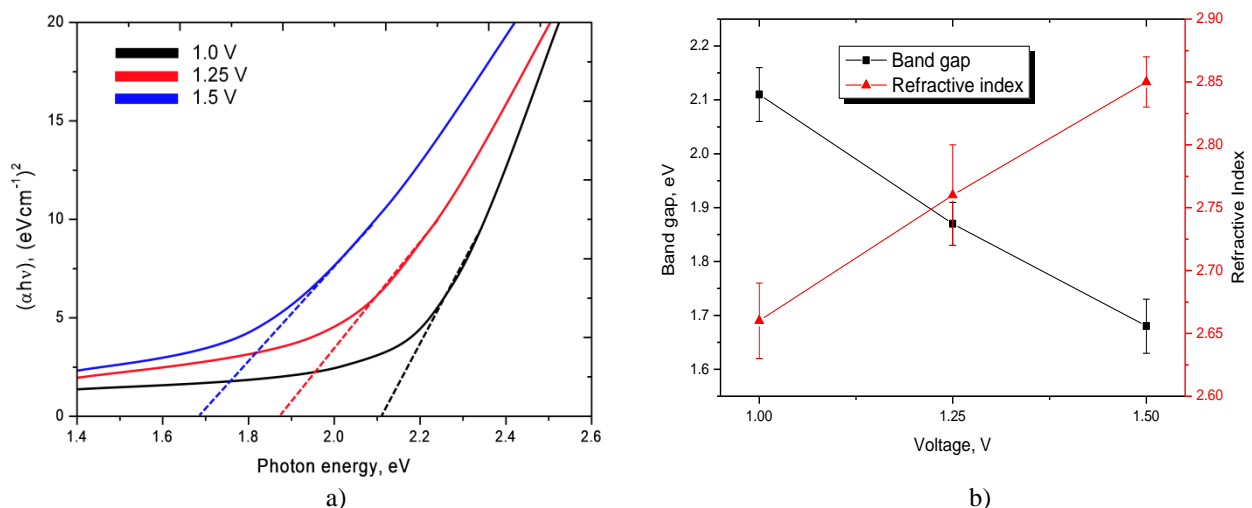


Fig.6. a) Tauc' plots; b) Results of change in the band gap and refractive index

As is known, one of the promising applications of thin films is the photocatalytic decomposition of organic dyes under the action of ultraviolet radiation in the presence of catalysts. In this case, the key factors affecting the efficiency assessment of the use of certain photocatalysts are such indicators as the degradation degree and the decomposition rate of the dye in the presence of a catalyst. Also, an important role is played

by the degree of catalyst resistance to long-term use and performance retention as a result of several cyclic tests. Figure 7 shows the results of changes in the time dependence of the Rhodamine B degradation efficiency during the photocatalytic reaction during interaction with a catalyst in the form of films obtained under different synthesis conditions. The experiment time was limited by the achievement of the maximum decomposition efficiency for one of the selected systems with a catalyst. As can be seen from the data presented in Figure 7, the highest efficiency of the decomposition of Rhodamine B during the photocatalytic reaction is possessed by films obtained at a potential difference of 1.5 V, which amounted to more than 95 % of the decrease in the optical density of Rhodamine B in the time allotted for the experiment. In the case of films obtained at potential differences of 1.0 V and 1.25 V, the efficiency of photocatalytic degradation of Rhodamine B was 57 % and 78 %, respectively.

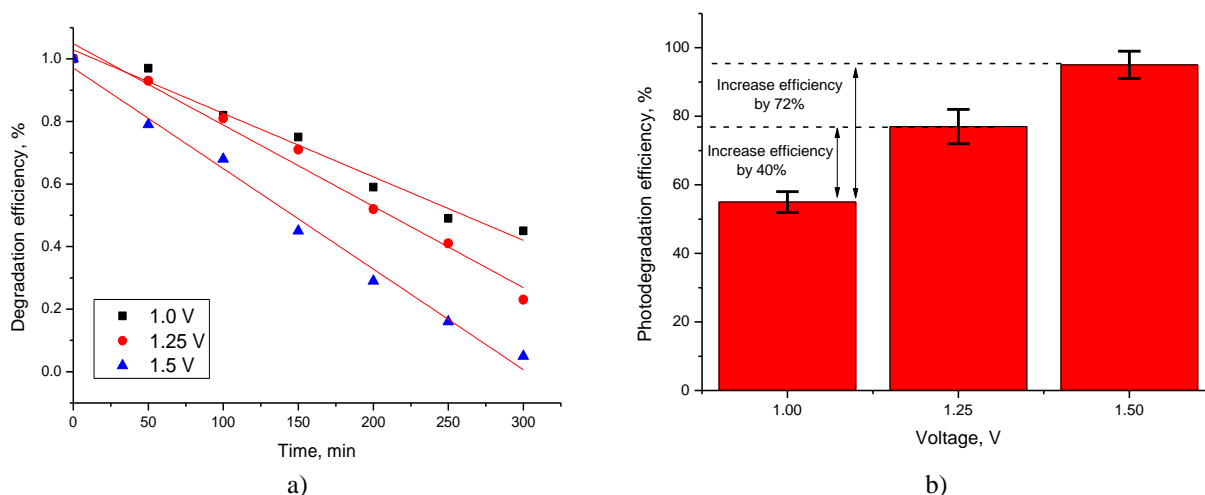


Fig.7. a) Plot of time dependence of Rhodamine B degradation efficiency in case of decomposition reaction; b) Diagram of assessment of decomposition efficiency in the final stage of photocatalytic reaction

Figure 8 shows the results of the assessment of the change in dye concentration ratio before and after the reaction on a logarithmic scale, which allows determination of the reaction rate constant. According to the calculations obtained, it was found that a change in the phase composition of the synthesized films leads to an increase in the decomposition rate by 1.5 and 3 times for samples obtained at potential differences of 1.25 V and 1.5 V.

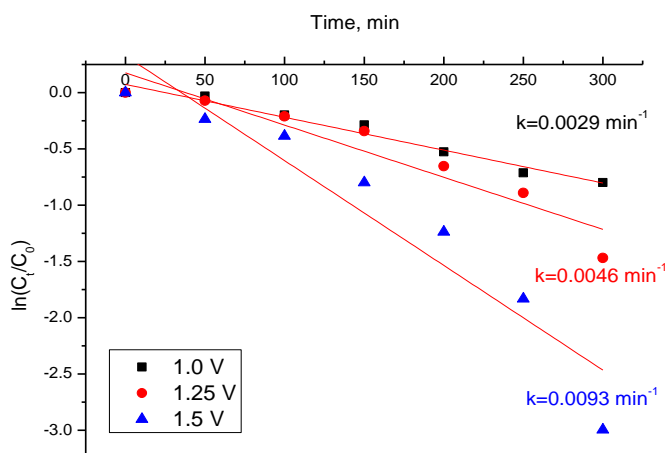
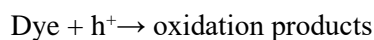
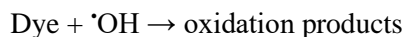
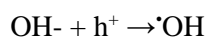
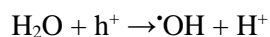


Fig.8. Data on the change in the rate constant of the Rhodamine B decomposition photocatalytic reaction

Such an increase in the degradation rate, as well as an increase in the decomposition efficiency, is caused by a change not only in the phase composition of the films, but also primarily by a change in the band gap, a decrease in which leads to an increase in the yield of electrons and photons under the action of photo-ionization of UV light. The photo-degradation process can be schematically written as follows:



Exposure to UV radiation on the sample leads to the formation of an electron and a photon, which are knocked out of the catalyst surface and, when interacting with water, form a number of $\cdot\text{OH}$ radicals that directly participate in the decomposition of the dye during the initiation of decarboxylation and hydroxylation processes with the formation of harmless components.

Conclusion

During the studies, the dependences of the effect of the applied potential difference on the change in the phase composition, structural features, and the ordering degree in nickel-doped CdSe films were established. It has been determined that an increase in the applied potential difference leads to an increase in the NiSe phase contribution formed during the substitution of cadmium ions by nickel ions during the formation of the crystal structure. It has been determined that an increase in the NiSe phase contribution leads to an increase in the structural ordering degree and hardening of the film structure. During the studies of the optical properties, it was determined that a change in the phase composition leads to a decrease in the band gap, as well as an increase in the optical density of the films. During the evaluation of the applicability of the synthesized films as a basis for photocatalysts, it was found that films with a high NiSe phase content have a high photocatalytic reaction rate as well as a high degree of photocatalytic decomposition of organic dyes.

In conclusion, the selected synthesis conditions, as well as the ratio of the starting salts, make it possible to obtain films with a controlled phase and elemental composition, which are highly promising as a basis for photocatalysts.

Funding

This research was funded by the Science Committee of the Ministry of Education and Science of the Republic of Kazakhstan (No. AP09562582).

REFERENCES

- 1 Liu Hao, et al. Enhanced photocatalytic capability of zinc ferrite nanotube arrays decorated with gold nanoparticles for visible light-driven photodegradation of rhodamine B. *Journal of materials science*. 2016, Vol. 51, No.12, pp. 5872 – 5879.
- 2 Alshammari A., Bagabas A., and Assulami M. Photodegradation of rhodamine B over semiconductor supported gold nanoparticles: the effect of semiconductor support identity. *Arabian Journal of Chemistry*. 2019, Vol. 12, No. 7, pp. 1406 – 1412.
- 3 Sangami G., Dharmaraj N. UV–visible spectroscopic estimation of photo-degradation of rhodamine-B dye using tin (IV) oxide nanoparticles. *Spectrochimica Acta Part A: Molecular and Biomolecular Spectroscopy*. 2012, Vol.97, pp. 847 – 852.
- 4 Parvaz S., Rabbani M., Rahimi M. Fabrication of novel magnetic ZnO hollow spheres/pumice nanocomposites for photodegradation of Rhodamine B under visible light irradiation. *Materials Science and Engineering: B*. 2021, Vol 263 pp. 114863.
- 5 Kozlovskiy A.L., Alina A., Zdorovets M.V. Study of the effect of ion irradiation on increasing the photocatalytic activity of WO₃ microparticles. *Journal of Materials Science: Materials in Electronics*. 2021, Vol. 32, No. 3, pp. 3863 – 3877.
- 6 Kozlovskiy A., et al. The study of the applicability of ionizing radiation to increase the photocatalytic activity of TiO₂ thin films. *Journal of Nanostructure in Chemistry*. 2020, Vol. 10, No. 4, pp. 331 – 346.
- 7 He M. Q., et al. Synthesis of molecularly imprinted polypyrrole/titanium dioxide nanocomposites and its selective photocatalytic degradation of rhodamine B under visible light irradiation. *Express Polymer Letters*. 2014, Vol 8, No. 11, pp 850–861.

8 Larowska D. et al. Graphene oxide functionalized with cationic porphyrins as materials for the photodegradation of rhodamine B. *The Journal of Physical Chemistry C*. 2020, Vol. 124, No. 29, pp. 15769-15780.

9 Jadhav S.A., et al. Magneto-structural and photocatalytic behavior of mixed Ni–Zn nano-spinel ferrites: visible light-enabled active photodegradation of rhodamine B. *Journal of Materials Science: Materials in Electronics*. 2020, Vol. 31, pp. 11352-11365.

10 Fattahimoghaddam H., Mahvelati-Shamsabadi T., Lee B.-K. Efficient photodegradation of rhodamine B and tetracycline over robust and green g-C₃N₄ nanostructures: supramolecular design. *Journal of Hazardous Materials*. 2020, Vol. 403, pp. 123703.

11 Il'chuk, G. A., et al. Peculiarities of the optical and energy properties of thin CdSe films. *Optics and spectroscopy*. 2020, Vol. 128, No. 1 pp. 49-56.

12 Milonakou-Koufoudaki, K., et al. Natural dyes in hybrid chalcogenide multi-layer thin films. *Bulletin of Materials Science*. 2020, Vol. 43, No. 1, pp. 1 - 11.

13 Hamann, Kathryn R., et al. Optically tunable mesoscale CdSe morphologies via inorganic phototropic growth. *Journal of Materials Chemistry C*. 2020, Vol. 8, No. 36, pp. 12412-12417.

14 Chauhan P., et al. Superior electrochemical activity of CdSe thin film by chromium substitutional doping. *Journal of Alloys and Compounds*. 2021, Vol. 862, pp. 158016.

15 Shelke N.T., Karle S.C., Karche B.R.. Photoresponse properties of CdSe thin film photodetector. *Journal of Materials Science: Materials in Electronics*. 2020, Vol. 31, No. 18, pp. 15061-15069.

16 Lohitha B., Thanikaikarasan S., Roji Marjorie S. Growth and characterization of CdS and Fe doped CdS thin films through electrochemical route. *Materials Today: Proceedings*. 2020, Vol. 33, pp. 3068-3071.

17 Patil N.M., et al. Structural, optical and electrical properties of spray-deposited Fe-doped nanocrystalline ZnS_{0.2}Se_{0.8} thin films. *Phase Transitions*. 2021, Vol. 94, No. 6–8, pp. 493–510.

18 Han Chong et al. Carbon Dots Doped with Ni(OH)₂ as Thin-Film Electrodes for Supercapacitors." *ACS Applied Nano Materials*. 2020, Vol. 3, No.12, pp. 12106-12114.

19 Abdulwahab A.M., Asma'a Ahmed A.L.-A., Ahmed A.A.A. Influence of Ni-Co dual doping on structural and optical properties of CdSe thin films prepared by chemical bath deposition method. *Optik*. 2021, Vol. 236, pp. 166659.

20 Tan, Wenyu, et al. Nucleation and growth mechanisms of an electrodeposited Ni–Se–Cu coating on nickel foam. *Journal of Colloid and Interface Science*. 2021, Vol. 600, pp. 492-502.

21 Omarova, A., et al. Study of the influence of synthesis conditions on stoichiometry and the properties of nanostructured CdSe thin films. *Journal of Materials Science: Materials in Electronics*. 2020, Vol. 31, No. 15, pp. 12756-12764.

22 Alasvand A., Kafashan H. Investigation the effect of Pb incorporation on the surface characterizations of electrodeposited CdSe nanostructures. *Journal of Alloys and Compounds*. 2020, Vol. 817, pp. 152711.

23 Ayal, A.K., et al. Sensitization of TiO₂ nanotube arrays photoelectrode via homogeneous distribution of CdSe nanoparticles by electrodeposition techniques. *Journal of Physics and Chemistry of Solids*. 2020, Vol. 153, pp. 110006.

24 Shaikh A.V., et al. Electrodeposition of n-CdSe/p-Cu₂Se heterojunction solar cells. *Engineered Science*. 2020, Vol. 13, pp. 79-86.

25 Saha S., et al. Electrodeposition Fabrication of Chalcogenide Thin Films for Photovoltaic Applications. *Electrochem*. 2020, Vol. 1, No.3, pp. 286-321.

26 Gullu H.H., et al. Temperature effects on optical characteristics of CdSe thin films. *Materials Science in Semiconductor Processing*. 2021, Vol. 123, pp. 105559.

27 Erturk K., et al. Investigation of structural, spectral, optical and nonlinear optical properties of nanocrystal CdS: Electrodeposition and Quantum Mechanical Studies. *Optik*. 2021, Vol. 243, pp. 167469.

28 Thanikaikarasan S., et al. Physical, chemical and optical properties of CdSe and CdSe: Zn thin films obtained through low cost electrochemical route. *Materials Today: Proceedings*. 2020, Vol. 21, pp. 73-77.

29 Zhang Y., et al. Alkaline electrolyte: toward high-quality CdTe films with the assistance of strong complexing agent and organic base. *CrystEngComm*. 2018, Vol. 20, No. 1, pp. 8-11.

30 Zyoud A., et al. Electrochemically and chemically deposited polycrystalline CdSe electrodes with high photoelectrochemical performance by recycling from waste films. *Materials Science in Semiconductor Processing*. 2020, Vol. 107, pp. 104852.

THE HARDNESS OF HIGH-ENTROPY COATINGS OBTAINED BY THE METHOD OF MECHANICAL ALLOYING

Yurov V.M., Makhanov K.M.

E.A. Buketov Karaganda University, Karaganda, Kazakhstan, exciton@list.ru

The article shows that the hardness of most stainless steels is 2-3 times less than high-entropy coatings, which shows the prospect of their use as parts of various industrial structures. Microhardness of metallic glasses, which have a defect-free base, and do not differ from high-entropy coatings. In the article, an equation is obtained that shows that the destruction of the coating is proportional to the surface energy and inversely proportional to the Gibbs energy. For stainless steels, the surface energy is about the same as for high-entropy coatings. The Gibbs energy of high-entropy coatings is 2 times higher than that of stainless steels, which leads to a high hardness of high-entropy coatings, which is observed experimentally.

Keywords: microhardness, high-entropy coating, steel, surface energy, destruction of the coating, nanostructure.

Introduction

This work is a continuation of works [1-3], where the properties of functional and high-entropy coatings are considered. In high-entropy alloys, as a result of the effect of intense mixing, the entropy contribution increases, which stabilizes the formation of a solid solution with a simple structure [4-6]. Based on Boltzmann's hypothesis about the relationship between entropy and system complexity, the configurational change in entropy ΔS_{conf} during the formation of a solid solution of n elements with equiatomic content can be calculated using the following formula:

$$\Delta S_{\text{conf}} = -R \ln(1/n) = R \ln(n), \quad (1)$$

where R is the universal gas constant, n is the number of mixing elements.

At $n = 5$, $\Delta S_{\text{conf}} = 1.61R$ approaches the value of the melting entropy of most intermetallics (about $2R$). However, it was later shown that a high entropy of mixing is not a necessary condition for the formation of a single-phase solid solution, but the very term for the name of such an alloy remains in use.

1. Analysis of publications

First of all, we will mention only those publications that relate to the latest advances in the field of high-entropy coatings. Articles [7-9] provide a review of high-entropy materials with their unique structural characteristics, individual chemical composition and functional properties. They are generating increasing interest in the fields of environmental science and renewable energy technology. Despite all the (potential) advantages inherent in high-entropy materials over conventional alloys, oxides and other compounds, there are some obvious problems associated with their practical use in the energy sector. Rational design of high-entropy materials is very difficult at present. One possibility is an approach using theoretical machine learning methods to design high-entropy materials with the desired properties. From an experimental point of view, a more efficient way would be to select a benchmark of the model and gradually add or replace new elements to change the configuration entropy of the system. Another general strategy is to subdivide components into subcategories according to their roles in the system, and then add or replace the selected item with other similar items in each category.

Article [10] provides a detailed overview of thermal spray coatings. These methods are opposed to the methods of laser cladding and surface alloying for the synthesis of thick high-entropy coatings. The article [11] provides an overview of high-entropy coatings in the aerospace industry. Figure 1 shows the hardness of high-entropy alloys and compounds. based on refractory metals. Modeling showed that materials based on refractory high-entropy alloys, their carbides, borides and nitrides showed a wide spread in the calculated hardness, which ranged from 4.1 GPa to 21.3 GPa. The materials and methods described in the article can

give a positive result for applications in the aerospace industry: sectors that are associated with high loads (frames, chassis, shafts, etc.) and extremely high temperatures (engines, propulsion systems).

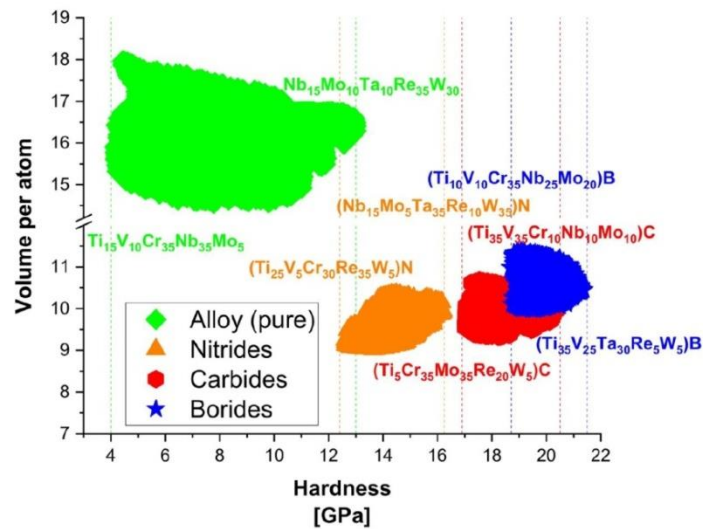


Fig.1. Graphical representation of predicted hardness of high-entropy alloys and compounds based on the refractory metals: dotted lines represent the maximum and minimum hardness [11].

Articles [12-14] provide an overview in the field of high-entropy nitride materials, with particular attention to coatings in which the phases of the solid solution with the formation of simple crystal structures. The latter will include advanced data processing with artificial intelligence and machine learning to aid in the assessment large common datasets from experimental and theoretical work. This change in methodology will be a challenge but will be necessary to fully realize the potential of high-entropy nitride materials. Article [15] is devoted to a review of high-entropy ceramics.

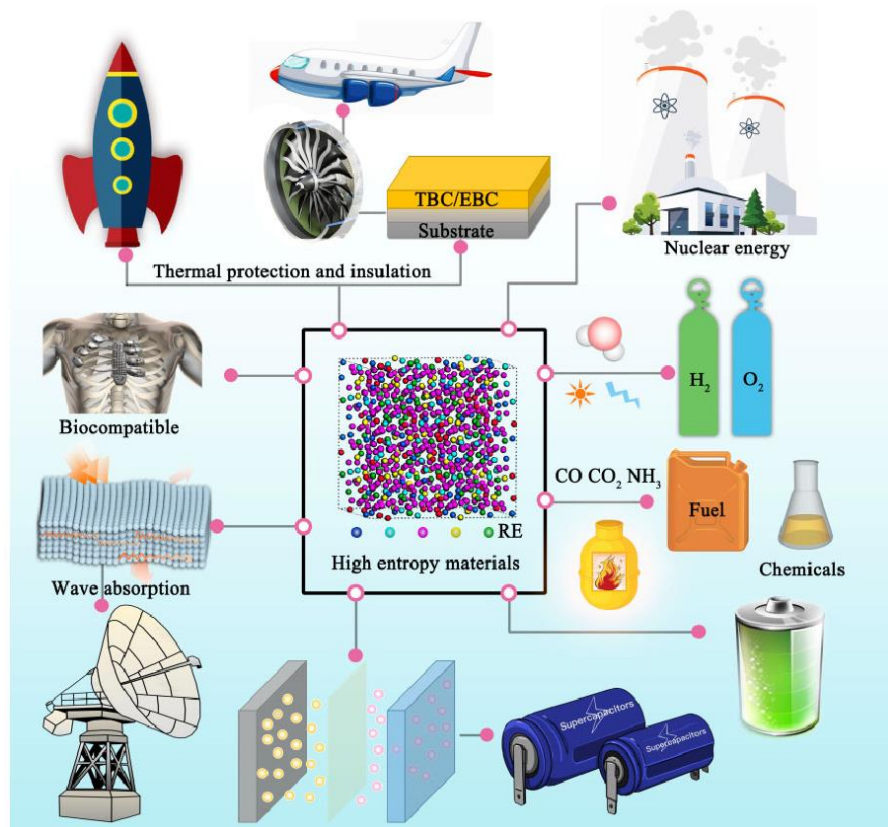


Fig.2. Prospective applications of HECs covering from ultrahigh-temperature structural to energy and catalytic functional applications, [15].

In addition to hardening and low thermal conductivity, which has already been found in high-entropy alloys, new properties such as colossal dielectric constant, superionic conductivity, strong anisotropic coefficient of thermal expansion, strong absorption of electromagnetic waves, etc. have been found in high-entropy ceramics. In response to the rapid development in this nascent field, this article provides a comprehensive overview of design features, theoretical methods for predicting stability and properties, machining routes, new properties, and promising applications of high-entropy ceramics (Figure 2).

The main goal of this work is to experimentally investigate the microhardness of high-entropy coatings and propose a model that will allow, within the framework of the energy theory, to explain the observed effects.

2. Objects and experimental technique

High-entropy (HEC) coatings of the following composition were used as objects of research: TiNiZrCuCr, CrFeNiTiZrCu, TiFeCuAlSn, AlCrNiTiZrCu, PbCrNiTiZrCu, CrNiTiZrAlCu. The coatings were obtained by sputtering magnetron targets of the above compositions on 12X13 steel using an NNV-6.6I1 setup.. These targets were manufactured by us by the method of mechanical alloying [16], in contrast to cast targets obtained by the metallurgy method. Moreover, after annealing in a vacuum chamber, the samples became nanostructured. Fig. 3a shows, as an example, a sample under study with an HEC-coating, in Fig. 3b of their SEM image of the HEC-coating, and in Fig. 3c diagram of the formation of nanostructured HEC-coatings [17]. The roughness of the coating, as an example, measured with the atomic force microscope (AFM) JSPM-5400, is also negligible (Figure 4) [18].

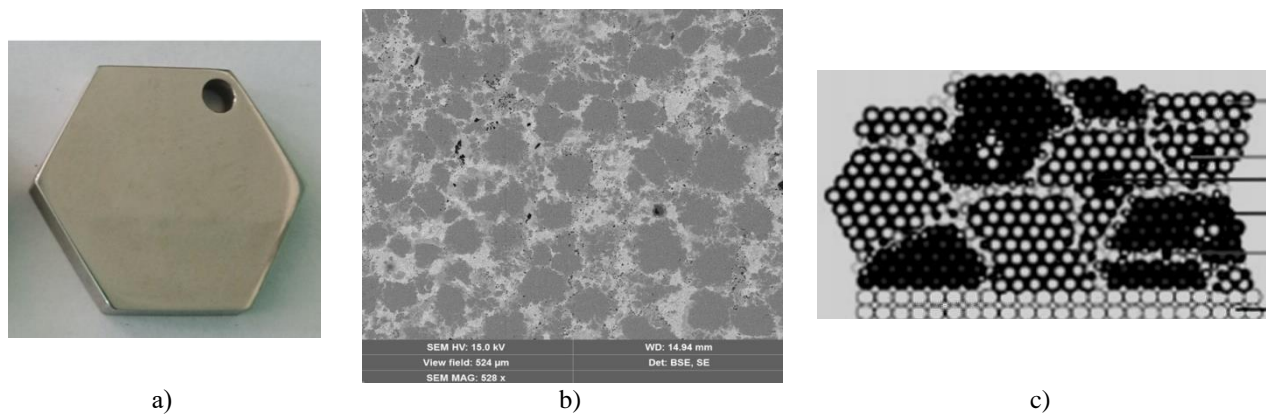


Fig.3. A sprayed sample with an HEC-coating (a), an REM image of an HEC-coating (b), a diagram of the formation of nanostructured coatings of an HEC-coating [17].

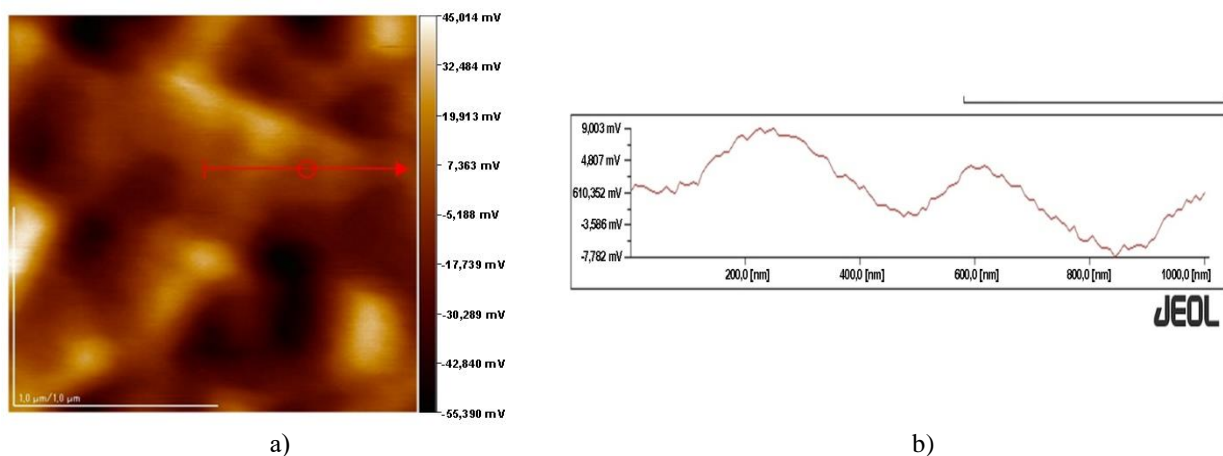


Fig.4. AFM image of TiNiZrCuCr (a) and its roughness (b), [18].

X-ray fluorescence spectroscopy (XPS) (Figure 5), as an example, shows that the investigated coatings form high-entropy coatings in the composition from 5 to 35 at. %. Figure 6 shows the distribution of elements in the coverage, which shows that the elements are evenly distributed.

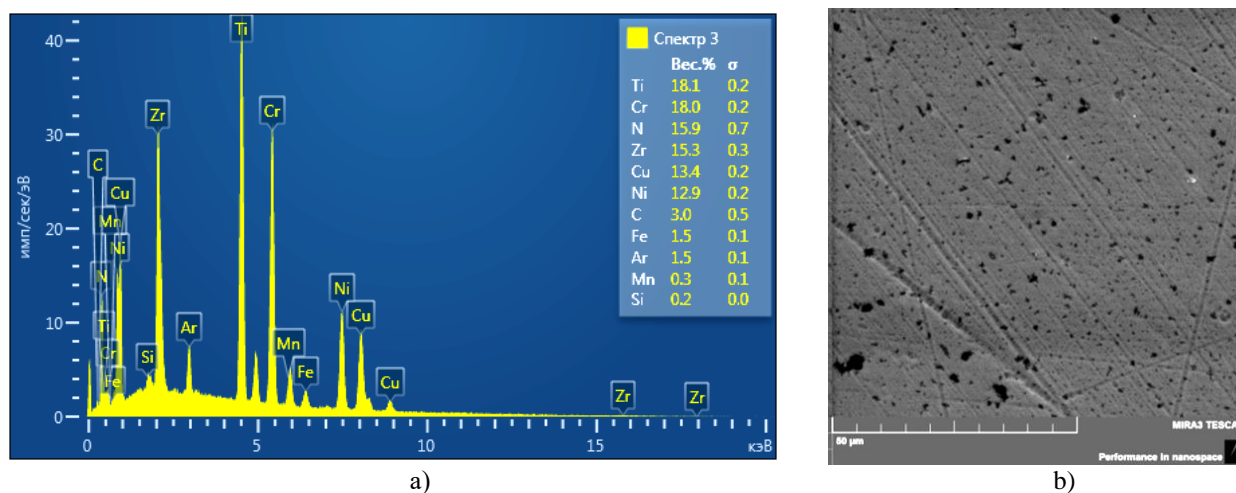


Fig.5. XPS TiNiZrCuCr (a), SEM image of TiNiZrCuCr (b)

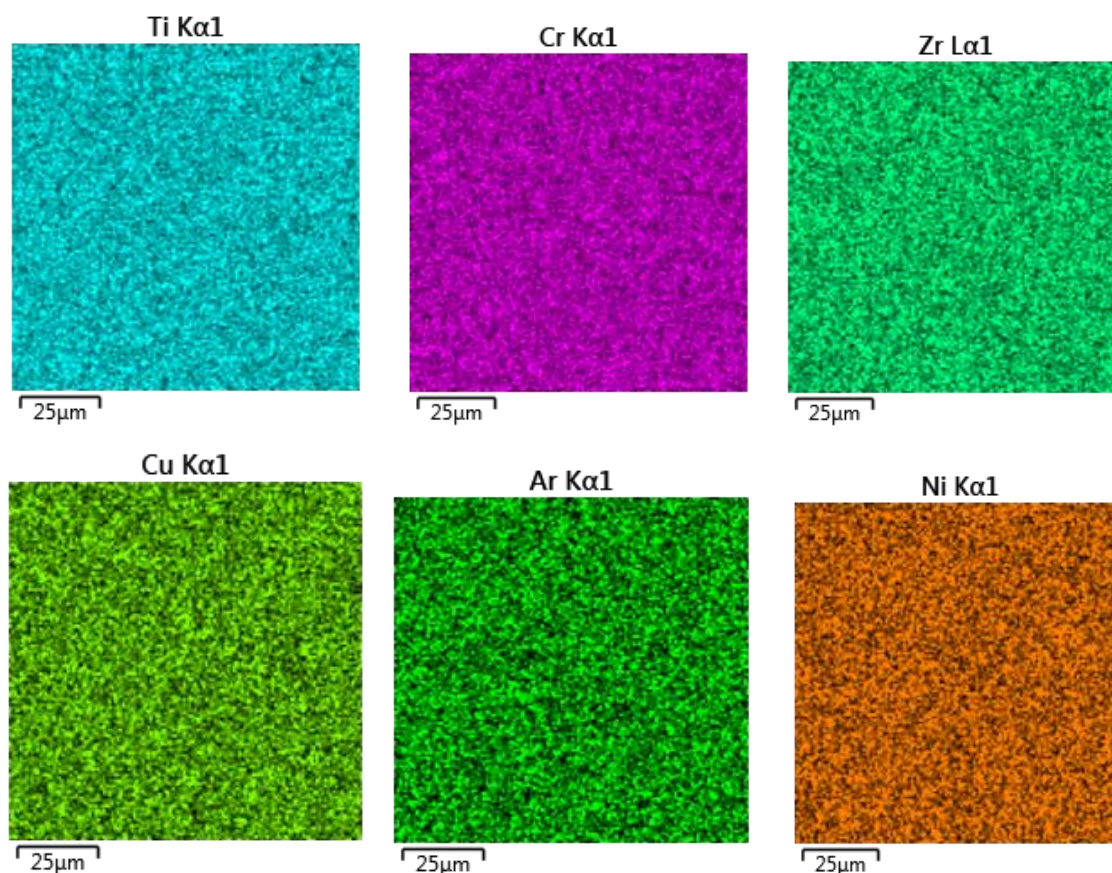


Fig.6. Distribution of TiNiZrCuCr elements deposited on 12X13 steel in argon

Such a distribution occurs in the coating due to a diffusion process that occurs during thermal annealing of the magnetron target in a vacuum chamber for 3-5 hours. We used an HVS-1000A microhardness tester to measure the coatings (Figure 7). This instrument is designed using the latest advances in mechanics, optics, electronics and computer technology to test the hardness of metallic and non-metallic materials, especially small parts or thin hardened layers.

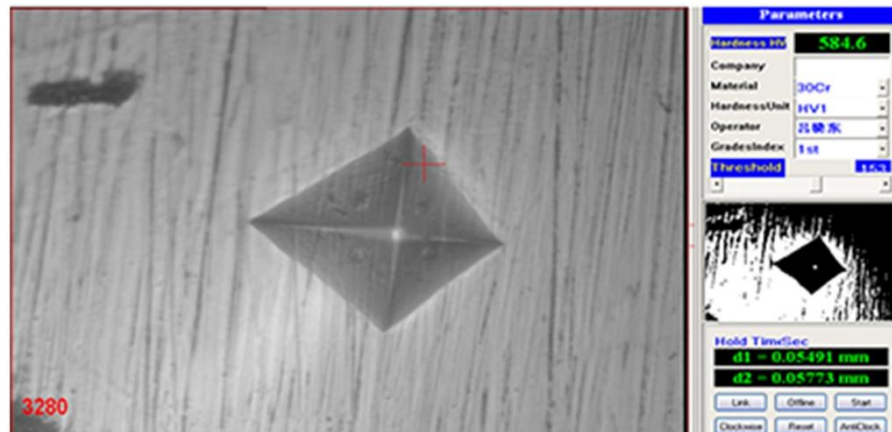


Fig.7. Measurement of coatings on a HVC-1000A microhardness tester

3. Research results and their discussion

Using the above methods, the table of experimental values can be given. Table 1 shows that pentaatomic alloys have higher hardness. Hexaatomic alloys have slightly less hardness.

Table 1. Experimental properties of high-entropy coatings (HEC) and metallic glasses (MG) [19]

HEC	μ , HV	MG	μ , HV
CrTiNiZrCu	890	Fe ₇₈ Mo ₂ B ₂₀	1015
TiFeCuAlSn	700	Fe ₄₀ Ni ₄₀ P ₁₄ B ₆	640
CrFeNiTiZrCu	740	Fe ₇₈ P ₁₃ C ₇	760
AlCrNiTiZrCu	585	Fe ₇₈ Si ₁₀ B ₁₂	890
PbCrNiTiZrCu	560	Ni ₇₅ Si ₈ B ₁₇	860
CrNiTiZrAlCu	530	Co ₇₅ Si ₁₅ B ₁₀	910

Let us compare the hardness of stainless steels [20] with the hardness of high-entropy coatings from Table 2. Table 2 shows that the hardness of most stainless steels is 2-3 times less than high-entropy coatings. This opens up the prospect of using high-entropy coatings on parts of various industrial structures.

Table 2. Hardness of stainless steels [20]

Steel	μ , HV	Steel	μ , HV
12X13	121-187	08X17T	372
40X13	143-229	10X17H13M2T	200
08X18H10	170	12X18H10T	179

For comparison, Table 1 shows the microhardness of metal glasses, which have a defect-free base and do not differ much from high-entropy coatings [19].

What is the reason for this difference?

To determine the resistivity of high-entropy alloys, an experimental setup was assembled and ρ (Ohm m) was measured [21]. It turned out that the specific resistance of the investigated high-entropy alloys lies in the range (5-7) 10^{-8} Ohm m, i.e. slightly different from $\rho_w = 5.5 \cdot 10^{-8}$ Ohm m. According to Ohm's law, the current density in metals is:

$$j = env = 1/\rho \cdot E$$

Whence for the concentration of electrons we have the expression:

$$n = 1/ev\rho \cdot E_F, \quad (2)$$

where the electron charge $e = 1.60217662 \cdot 10^{-19}$ K c; resistivity $\rho = 5 \cdot 10^{-8}$ Ohm m; average electron velocity $v_{Cu} = 74 \cdot 10^{-6}$ m/s; the Fermi energy $E_F = 14 \cdot 10^{-19}$ J. Thus, the concentration of conduction electrons in the alloy near the Fermi level is $n \approx 3 \cdot 10^{18}$.

We will consider the question of the response of a subsystem of n electrons in high-entropy alloys to an external action during friction from the standpoint of nonequilibrium statistical thermodynamics. The electrons in the alloy will be considered as a system of non-interacting particles immersed in a thermostat. The thermostat is a metal alloy minus n "free" electrons. Quantum transitions during friction, caused by the interaction of a system of electrons with a thermostat, will be dissipative (with probability P), in contrast to the interaction during friction (with probability F). Dissipative processes lead to the fact that the secondary field (system response) is always less than the primary one, which causes the formation of heat during friction. We will assume that the electron subsystem exchanges only energy with the thermostat. Then the corresponding ensemble of particles will be canonical. In this case, the expression for the statistical entropy has the form:

$$S = -k \sum_i f_i \ln f_i, \quad (3)$$

where f_i is the distribution function; k is Boltzmann's constant.

Differentiating (3) with respect to time and transforming, we obtain:

$$\frac{dS}{dt} = \frac{k}{2} \sum_{i,j} (\ln f_i - \ln f_j) (P_{ij} f_i - P_{ji} f_j), \quad (4)$$

where P_{ij} is the probability of transition from the initial i (with energy E_i) to the state j excited by friction (with energy E_j). For dissipative processes, the principle of detailed balance has the form:

$$\frac{g_i P_{ij}}{g_j P_{ji}} = e^{\frac{E_j - E_i}{kT}}, \quad (5)$$

where g_i , g_j are statistical weights for the levels E_i and E_j .

Finally, in [22], we obtained the following formula for the destruction efficiency η of a metal coating:

$$\eta = \frac{k^2 \Delta t}{2 \Delta S \cdot \tau} \cdot T \cdot \frac{E_m}{G^0} \cdot \bar{n} = \text{const} \cdot T \cdot \frac{\sigma \cdot S}{\tau \cdot G^0} \cdot \bar{n}, \quad (6)$$

Equation (6) describes the destruction of the coating η proportional to k - the Boltzmann constant, the change in entropy ΔS and the time of motion during friction Δt , the work of friction forces $E_m = A = \sigma S$, the concentration of electrons n near the Fermi level, surface energy σ , contact area S and vice versa is proportional to the relaxation time τ and the Gibbs energy G^0 of the thermostat.

The difference in the destruction of high-entropy coatings from stainless steels is in the analysis of equation (6). It follows from this equation that the destruction of the coating η is proportional to the surface energy σ and inversely proportional to the Gibbs energy G^0 , that is, the condition $\eta \rightarrow \sigma/G^0 \rightarrow \text{min}$ must be satisfied. Since the surface energy σ_{st} for stainless steels is approximately equal to the surface energy of high-entropy coatings σ_n , that is, $\sigma_{st} \approx \sigma_n$. But the Gibbs energy of stainless steels is approximately $1R$ and for high-entropy coatings it is approximately $2R$, that is, $\eta \rightarrow \sigma/G^0 \rightarrow 1/2$. Failure of the coating η can be calculated as the ratio of the hardness of stainless steels to the hardness of high-entropy coatings using the formula $\eta \rightarrow \mu_{st}/\mu_n$. This gives the following result - $\eta \rightarrow 1/2$, which is observed experimentally (Tables 1 and 2). In fig. 8a (according to equation 1) shows an increase in the entropy of mixing with an increase in the number of elements for equimolar alloys.

It can be seen that the entropy of mixing for the phases of the solid solution increases from a small value for conventional alloys to a large value for high-entropy alloys of the composition [4]. Based on the effect of entropy of mixing, it is possible to divide the variety of alloys into three fields, as shown in Fig. 8b. Low entropy alloys are traditional alloys. High-entropy alloys are alloys with at least five basic elements.

Medium entropy alloys are alloys with 2...4 basic elements. The high-entropy effect of activation of the formation of a disordered solid phase occurs essentially in the field of high-entropy alloys and should be present to a lesser extent in medium-entropy alloys. Stabilization of a simple solid solution phase is important for the microstructure and properties that can be obtained in these materials [4-6].

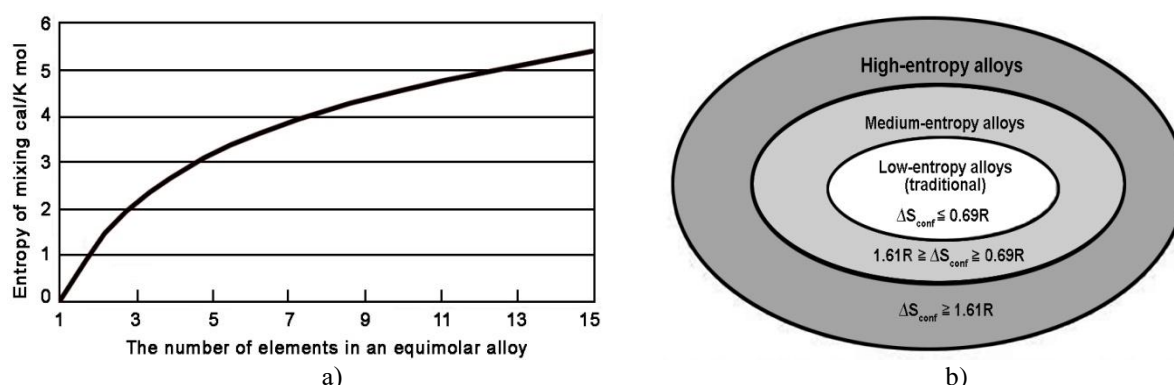


Fig.8. The increase in the entropy of mixing to the number of elements in equimolar alloys in a disordered state (a), the division of the world of alloys by the entropy of mixing (b) [4].

Conclusion

High-entropy coatings TiNiZrCuCr, CrFeNiTiZrCu, TiFeCuAlSn, AlCrNiTiZrCu, PbCrNiTiZrCu, CrNiTiZrAlCu were investigated in this work. Such coatings were obtained on an NNV-6.6II setup by sputtering magnetron targets of the above compositions. These targets were manufactured by mechanical alloying methods, in contrast to cast targets obtained by metallurgy. Moreover, after annealing in a vacuum chamber, the samples became nanostructured.

We have shown experimentally and theoretically that the destruction of high-entropy coatings is proportional to the surface energy σ and inversely proportional to the Gibbs energy G^0 . Failure of the coating η can be calculated as the ratio of the hardness of stainless steels to the hardness of high-entropy coatings using the formula $\eta \rightarrow \mu_{st}/\mu_n$. This gives the following result - $\eta \rightarrow 1/2$, which is observed experimentally.

Acknowledgments

The work was carried out under the program of the Ministry of Education and Science of the Republic of Kazakhstan. Grants No. 0118RK000063 and No. F.0781.

REFERENCES

- 1 Guchenko S.A., Zavatskaya O.N., Yurov V.M., Kasymov S.S., Laurinas V.Ch. Fractal structure of multi-element coating. *Eurasian Physical Technical Journal*. 2018, Vol. 15, No.1 (29), pp. 8-17.
- 2 Eremin E.N., Yurov V.M., Guchenko S.A. Wear resistance and tribological properties of high entropy coatings CrNiTiZrCu. *Eurasian Physical Technical Journal*. 2020, Vol.17, No.1 (33), pp. 13-18.
- 3 Yurov V.M., Guchenko S., Salkeeva A.K., Kusenova A.S. Nitrogening hydraulic cylinder rods. *Eurasian Physical Technical Journal*. 2020, Vol.17, No.1 (33), pp. 25-30.
- 4 Yeh J.-W., Chen S.-K., Lin S.-J., et al. Nanostructured High-Entropy Alloys with Multiple Principle Elements: Novel Alloy Design Concepts and Outcomes. *Advanced Engineering Materials*, 2004, Vol. 6, No. 8, pp. 299-303.
- 5 Yeh J.W., Chen Y.L., Lin S.J. High-entropy alloys – a new era of exploitation. *Materials Science Forum*. 2007, Vol. 560. – P. 1-9.
- 6 Wang Y.P., Li B.Sh., Heng Zh.F. Solid Solution or Intermetallics in a High-Entropy Alloy. *Advanced Engineering Materials*, 2009, Vol. 11, No. 8, pp. 641-644.
- 7 Vyas A., Menghanian J., Natub H. Metallurgical and Mechanical Properties of Laser Cladded AlFeCu CrCoNi-WC10.High Entropy Alloy Coating. *IJE TRANSACTIONS A: Basics*. 2020, Vol. 33, No. 7, pp. 1397-1402
- 8 Yanjiao Ma, Yuan Ma, Qingsong Wang et al. High-entropy energy materials: challenges and new opportunities. *Energy Environ. Sci.*, 2021, Vol. 14, pp. 2883–2905.
- 9 Sharma A. High Entropy Alloy Coatings and Technology. *Coatings*, 2021, Vol. 11, pp. 372-388.
- 10 Meghwal A., Anupam A., Murty B.S., Berndt C.C., Kottada R.S., Ming Ang A.S. Thermal Spray High-Entropy Alloy Coatings: A Review. *Journal of Thermal Spray Technology*, 2020, pp. 1-38.

- 11 Postolnyi B., Buranich V., Smyrnova K. et al. .Multilayer and high-entropy alloy-based protective coatings for solving the issue of critical raw materials in the aerospace industry. *IOP Conf. Series: Materials Science and Engineering*, 2021, 1024, pp. 012009
- 12 Cheng-Yu He, Xiao-Li Qiu, Dong-Mei Yu et al. Greatly enhanced solar absorption via high entropy ceramic AlCrTaTiZrN based solar selective absorber coatings. *Journal of Materiomics*. 2021, Vol. 7, pp. 460-469.
- 13 Lewin E. Multi-component and high-entropy nitride coatings. A promising field in need of a novel approach. *Journal of Applied Physics*, 2020, Vol. 127, pp. 220901.
- 14 Mishra A. Friction Stir Welding/Processing of High Entropy Alloys (HEAs). *Welding Technology Review*, 2021, Vol. 93(1), pp. 27-33.
- 15 Xiang H., Xing Y., Dai F., Wang H. et al. High-entropy ceramics: Present status, challenges, and a look forward. *Journal of Advanced Ceramics*. 2021, Vol. 10(3), pp. 385–441.
- 16 Yurov V.M., Guchenko S.A., Tvardovsky A.N. Two targets for magnetron deposition of high-entropy coatings. *Trends in the development of science and education*, 2020, No. 60(1), pp. 28-34.
- 17 Pogrebnyak A.D., Bagdasaryan A.A. Pink A.V., Dyadyura K.A. Multicomponent nanocomposite coatings with adaptive behavior in surface engineering. *Uspekhi fizicheskikh nauk*. 2017, Vol. 187, No. 6, pp. 629-652.
- 18 Yurov V.M., Guchenko S.A., Makhanov K.M. Atomic force microscopy of high-entropy coatings. *International Journal of Applied and Fundamental Research*. 2020, No. 4, pp. 62-67.
- 19 Cheng Y.Q., Ma E. Atomic-level structure and structure–property relationship in metallic glasses. *Progress in Materials Science*. 2011, Vol. 56, pp. 379–473.
- 20 Povolotskiy D.Ya., Gudim Yu.A. *Stainless steel production*. – Chelyabinsk, 1998. - 236 p.
- 21 Yurov V.M., Guchenko S.A. Electrical conductivity of seven-atom high-entropy alloys. *Interuniversity scientific congress "Higher school: scientific research"*, 2019, Vol. 1, pp. 142-148.
- 22 Yurov V.M., Guchenko S.A., Zavatskaya O.N. Structure and surface tension of composite coatings. *Bulletin of KSU. Physics*, 2012, No. 1 (65), pp. 45-53.

INVESTIGATION OF LAYERED ORTHOTROPIC STRUCTURES BASED ON ONE MODIFIED REFINED BENDING THEORY

Kasimov A.T.¹, Yessenbayeva G.A.², Zholmagambetov S.R.¹, Khabidolda O.²

¹Karaganda Technical University, Karaganda, Kazakhstan

²E.A. Buketov Karaganda University, Karaganda, Kazakhstan, esenbaevagulsima@mail.ru

In the article, constructions made of orthotropic multilayer composite material, in particular, layered orthotropic plates are considered. Numerical modeling and analysis of the stress-strain state for the plates are carried out on the basis of one version for the refined theory of layered plates. The bending problems for plates of medium thickness and thin multilayer plates of symmetric and asymmetric structures are investigated. All studies are conducted taking into account the properties of orthotropy and multilayering for the composite material from which the plates are made. The general algorithm for the numerical calculation of the stress-strain state for layered plates with orthotropic layers is developed on the basis of the finite difference method. This algorithm is implemented on a PC by a software package.

Keywords: orthotropic materials, layered composites, layered (or laminated) orthotropic plate, refined bending theory, transverse shear, deflection, strain, asymmetry, multilayer structure, finite difference method

Introduction

The design of new modern technique and the improvement of technological developments made it necessary to search and create new materials. Composite materials, in particular, multilayer composites, are a new type of such materials with a wide range of operational properties that cannot be achieved using traditional materials. The use of multilayer composite materials in modern apparatuses and devices required taking into account their structural features, physical properties of the materials used, as well as the creation of new methods for calculating the stress-strain state of such structures.

The rapid development of scientific and technological progress requires the creation and implementation of new progressive materials and structures with predetermined properties. Orthotropy is one of these properties. Orthotropic materials are more difficult to analyze than isotropic materials because their properties depend on the direction. In orthotropic materials there are two or three mutually perpendicular axes of symmetry, with respect to which the material properties differ significantly. For example, the properties of wood material along and across the fibers are very different.

Reinforced concrete (with different reinforcement stiffness in mutually orthogonal directions x and y), many polymers (plastics, etc.), wood, metal sheets after rolling or upsetting, composites with two families of threads, layered composites, etc. belong to orthotropic materials. Layered or multilayer composite materials consist of alternating layers of filler and matrix material. This design is often called a package. The design of layered composite structures usually contains separate layers of different materials, connected together and combined into one structure. A layered composite structure has properties that none of its layered components can possess individually.

In multilayer composite structures, the layers are made of such a material and these layers are arranged so as to endow the structure with a number of predetermined positive properties. At the same time, the materials are selected in such a way that, in an optimal combination, they give a qualitatively new type of construction. Or, in other words, in multilayer composite structures, the layers are arranged so that, under operational conditions, the structure better corresponds to its functional purpose. Layered composite structures include layered (or laminated) orthotropic plates.

Layered orthotropic plates are increasingly widely used in various fields of technique, mechanical engineering and construction. The interest in layered plates is primarily due to the fact that they have a set of properties and features that qualitatively distinguish them from traditional structures made of homogeneous materials. The combination of layers in the material makes it possible to obtain a structure that combines high strength and stiffness with relatively low weight and high technical and operational requirements.

In practice, structures made of three-layer material are most widespread. Under operating conditions, such materials are the most rational from the point of view of ensuring a minimum for weight indicators with the required strength and stiffness. But they do not always meet all the requirements for building structures and elements of modern technology. The technical, physical and mechanical properties of structures made of multilayer inhomogeneous materials differ significantly in the thickness of their packages. Therefore, the features study for the operation of structures made of multilayer inhomogeneous materials in the thickness of their package by use refined models is important in the design of new innovative lightweight structures made of multilayer materials. Multilayer plate theories that refine the technical theory should take into account the strain in the transverse direction of the material and the factors associated with it.

The specific features of soft layers of material in multilayer structures, the joint work of the package layers under the influence of external loads and the low resistance of the filler material in the transverse direction give rise to a variety of existing theories [1-12]. Currently, the theory of calculation for multilayer structures is rapidly developing and improving. However, in practice, when solving specific problems, difficulties associated with features of multilayer structures arise.

It should be noted that analytical results for structures made of multilayer composite material were obtained for a limited number of problems. Therefore, approximate numerical methods, the implementation of which opens up great opportunities for researchers, began to be widely used.

The assessment of the stress-strain state for such multilayer systems is a difficult problem, and in practice it is not always possible to obtain their solution in a closed form. In this regard, it becomes necessary to develop an effective numerical calculation, based on a refined theory, which makes it possible to determine and investigate the components of the stress-strain state for the package layers in an automated mode.

1. Initial positions, hypotheses, and the plate model

We consider a rectangular layered plate with sides a_1 and a_2 (fig. 1), with orthotropic layers and a thickness $H = \delta_1 + \delta_2$, consisting of an arbitrary number of orthotropic layers. We consider a plate in an orthogonal coordinate system $x_1, x_2, x_3 = z$. The axes x_1 and x_2 lie on the coordinate plane and their directions coincide with the orthotropy axes of the layers. The coordinate plane is positioned arbitrarily along the height of the plate cross-section. The distance from the coordinate plane to the lower and upper surfaces of the plate is denoted, respectively, by δ_1 and δ_2 .

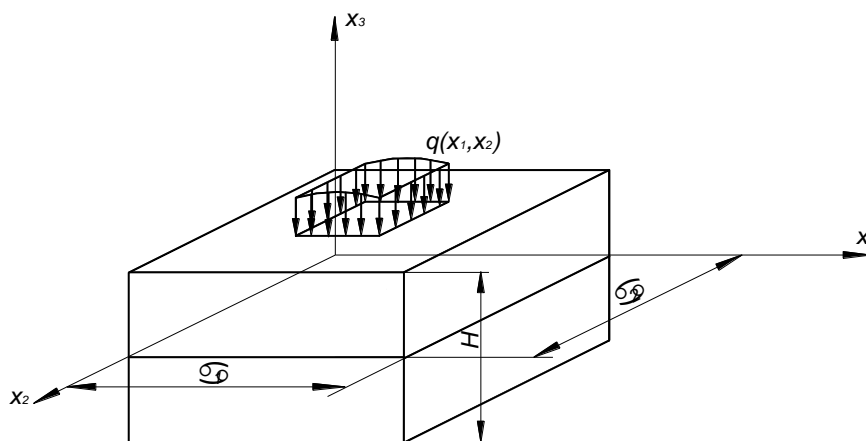


Fig.1. Calculation scheme of the plate

The material layers are numbered from the bottom surface of the plate (fig. 2). The total number of layers in the package is denoted by n , then we take $k = 1, 2, \dots, n$, where k is the number of an arbitrary layer. The layers in which the coordinate surface is located will be denoted by m . All layers of the plate in aggregate in thickness form a package of layers.

In the general case, we assume that the structure of the package is formed by layers of different thickness and stiffness, the physical and mechanical characteristics of which are constant in their thickness. The number and order of the layers are arbitrary.

We assume that at the boundary when passing from layer to layer, the static and kinematic conditions are fulfilled. This corresponds to the operation of their layers without slipping and tearing.

Let a normal load $q(x_1, x_2)$ act on the upper surface of the plate. The normal load $q(x_1, x_2)$ varies according to an arbitrary law. The positive direction of the normal load coincides with the direction of the normal axis $x_3 = z$.

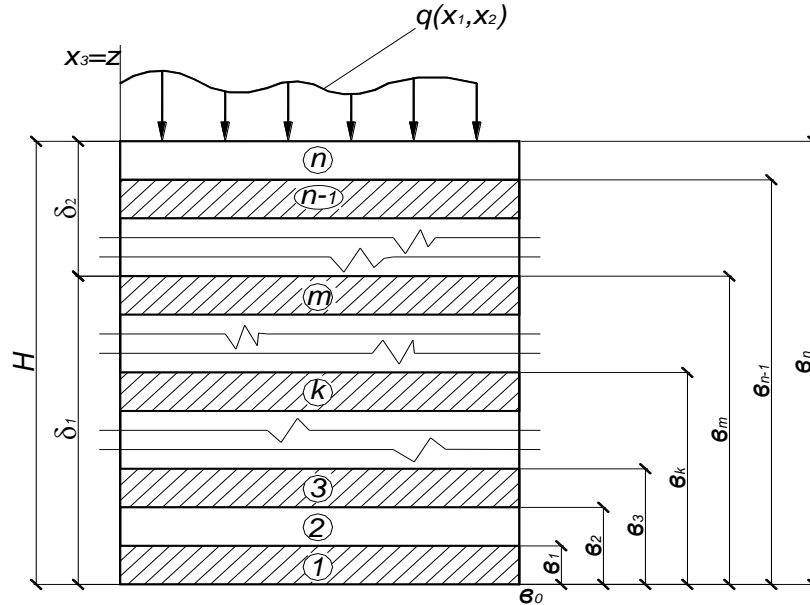


Fig. 2. The cross section of the layered plate

On the plate surface, the boundary conditions take the form

$$\sigma_{33}^n = q(x_1, x_2), \quad \sigma_{i3}^n = 0, \quad \sigma_{i3}^1 = 0, \quad i = 1, 2, 3.$$

As the main assumptions for constructing a new refined model of the stress-strain state for a layered plate of an asymmetric structure with orthotropic layers, we accept the following system of hypotheses

$$\sigma_{i3}^k = G_{i3}^k \psi_{i,3}^k(z) \chi_{,i}; \quad \sigma_{33}^k = - \sum_{i=1}^2 \eta_{3i}^k(z) \chi_{,ii}; \quad u_3^n = W. \quad (1)$$

The given hypotheses are obtained on the basis of the hypotheses proposed by professor A.Sh.Bozhenov [1], by neglecting a number of factors that insignificantly affect the stress-strain state of plates.

Here W и χ are sought functions of the deflection and shear of the coordinate surface, depending on the coordinates x_1 and x_2 . G_{i3}^k is the shear modulus of the material for the k th layer of the plate, remaining components are distribution functions that depend on the transverse coordinate z .

Hypotheses (1) satisfy the conditions for joint operation of layers without separation and displacement, as well as conditions on the plate surfaces and determine the nonlinear law of variation of transverse shear stresses and normal transverse stresses in the plate thickness. It is assumed that normal displacements are equal to deflections.

For the distribution function in expressions (1), we have the following formulas

$$\begin{aligned} \psi_{i,3}^k(z) &= \frac{1}{G_{i3}^k} \left[\eta_{2i}^k(z) - \eta_{1i}^k(z) \delta_i^* \right]; \quad \eta_{1i}^k(z) = \int_{b_{k-1}-\delta_1}^z A_i^k dz + \sum_{j=1}^{k-1} \int_{b_{j-1}-\delta_1}^{b_j-\delta_1} A_i^j dz; \\ \eta_{2i}^k(z) &= \int_{b_{k-1}-\delta_1}^z B_i^k z dz + \sum_{j=1}^{k-1} \int_{b_{j-1}-\delta_1}^{b_j-\delta_1} B_i^j z \cdot dz; \quad \eta_{3i}^k(z) = \int_{b_{k-1}-\delta_1}^z G_{i3}^k \psi_{i,3}^k(z) dz + C_{3i}^k; \end{aligned} \quad (2)$$

where the constants have the form

$$C_{3i}^k = \sum_{j=1}^{k-1} \int_{b_{j-1}-\delta_1}^{b_j-\delta_1} G_{i3}^j \psi_{i,3}^j(z) dz. \quad (3)$$

Here and in what follows, the notation introduced in [1] is adopted. For the components in formulas (2) and (3), we have the following expressions

$$A_i^k = 0,5 \left\{ B_{ii}^k (1 + \nu_{ie}^k) + G_{12}^k \right\}; \quad B_i^k = 0,5 B_{ii}^k (1 + \nu_{ie}^k) + G_{12}^k; \quad B_{ii}^k = E_i^k \nu_0^k;$$

$$\delta_i^* = \eta_{2i}^k / \eta_{li}^k; \quad \nu_0^k = (1 - \nu_{12}^k \nu_{21}^k)^{-1}; \quad B_{i3}^k = (\nu_{3i}^k + \nu_{li}^k \nu_{3l}^k) \nu_0^k.$$

Based on the accepted hypotheses (1), we construct a linear geometric model of a layered plate and establish a relationship between stresses and strains.

2. Development of a bending model for layered orthotropic plates with an asymmetric structure in the thickness

To construct a linear geometric model of a layered orthotropic plate and establish a relationship between stresses and strains, we use some well-known relations for the three-dimensional theory of elasticity.

At the same time, we will take into account that for an arbitrary k th layer of the plate, simplified hypotheses are adopted, they satisfy the conditions for the joint operation of the layers without separation and displacement, as well as the conditions on the surface of the plate, and determine the nonlinear law of variation of transverse shear stresses and normal stresses in the plate thickness. Factors such as a transverse shear in two directions and pressure of layers on each other, as well as orthotropy of layers, will be taken into account by one shear function.

We determine the transverse shear strain from Hooke's law by substituting the hypothesis expression for transverse tangential stresses (1). We find normal transverse strains from the last Cauchy relation taking into account (1).

From the third Cauchy relation, after integrating over z and taking into account formulas (1) and formulas for the transverse shear strain, we obtain an expression for tangential displacements. Normal displacements are considered equal to deflections. The distribution functions are determined from the conditions for the contact of the layers and from the conditions on the coordinate surface.

Tangential strains are determined from the first Cauchy relations, substituting expressions for tangential displacements in them. Taking into account formulas (1) and expressions for tangential strains, the stress are found from the generalized Hooke's law.

Received expressions of displacements and strains allow us to construct a geometric model of multilayer orthotropic plates and determine the components of the stress-strain state at an arbitrary point in the k th layer. Within the framework of the accepted hypotheses, all equations of the elasticity theory are approximately satisfied. Thus, the constructed new model describes the three-dimensional law of the change in the stress-strain state of multilayer plates with an asymmetric structure in thickness. The model is two-dimensional, since all the sought functions are functions of the coordinate surface.

Equations for the bending multilayer orthotropic plates with an asymmetric structure in thickness are obtained from the Lagrange variational principle using the relations received on the basis of the accepted hypotheses. Then, by introducing the force functions, the system of equations and the boundary conditions are transformed into a mixed form. As a result, a system of three equations of the 12th order is obtained; this system describes the bending for a multilayer plate of an asymmetric structure in thickness with orthotropic layers. The system of resolving equations of a layered plate is presented in a transformed form in [1] and in a mixed form this system takes the following form

$$\Delta_F^2 \phi + \Delta_{1S}^2 W - (\Delta_{2S}^2 - \Delta_{13}^2) \chi = 0;$$

$$\Delta_{1S}^2 \phi + (\Delta_{3S}^2 - \Delta_D^2) W + (\Delta_P^2 - \Delta_{23}^2 - \Delta_{4S}^2) \chi = -q;$$

$$\Delta_{2S}^2 \phi + (\Delta_{5S}^2 - \Delta_P^2) W + (\Delta_{P1}^2 - \Delta_{33}^2 - \Delta_{P3}^2) \chi = 0.$$
(4)

The system takes into account a transverse shear, a layer pressure, and normal strains. Three functions of the coordinate surface are unknown; these functions are the function of force, the deflection function, and the shear function. We have the following relations

$$\Delta_f^2 = A_1^* (_)_{,1111} + A_2^* (_)_{,1122} + A_3^* (_)_{,2222};$$

$$\Delta_g = B_1^* (_)_{,11} + B_2^* (_)_{,22}.$$
(5)

Equations (4) contain differential operators of the 4th and 2nd orders, which are determined from (5) with coefficients, respectively, A_j^* ($j=1,2,3$), and B_i^* ($i=1,2$), depending on the stiffness of the layered plate. For different values of f and g , the coefficients of the operators take different values, which are shown in Table 1.

Table 1. Coefficients of differential operators

Value of f	Coefficients			Value of g	Coefficients	
	A_1^*	A_2^*	A_3^*		B_1^*	B_2^*
F	F_1	F_4-2F_2	F_3	P_3	P_{13}	P_{23}
1S	R_1	$R_2+R_3-R_5$	R_4			
2S	I_1	$I_2+I_3-I_5$	I_4			
13	H_1	H_2	H_3			
D	D_{11}	$2(D_{12}+2D_{66})$	D_{22}			
3S	RK_1	RK_2	RK_3			
4S	IK_1	IK_2	IK_3			
23	C_{14}	$C_{14}+C_{24}$	C_{24}			
P	P_{11}	P_{122}	P_{222}			
5S	I_1	$I_2+I_3+I_5$	I_4			
P_1	S_{111}	S_{122}	S_{222}			
33	C_{15}	$C_{15}+C_{25}$	C_{25}			

We note that the solution of the obtained systems of equations is possible when six boundary conditions are satisfied on each contour with respect to the sought functions.

3. Numerical study of the stress-strain state for layered orthotropic plates

The discretization of the system of resolving equations and their corresponding contour conditions [2] is performed by the finite difference method (FDM) in a rectangular grid. In a compact matrix form, a method for the group exclusion of the unknown functions at the contour points for the grid domain of the plate has been developed. Based on the finite difference method, a general algorithm for numerical calculation of the stress-strain state of layered plates with orthotropic layers of arbitrary structure in thickness is developed and implemented on a PC by a software package. This software package contains a head program and several subroutines implemented in the FortRUN language. The flowchart of the head program consists of several blocks, each of which is a standalone module and performs certain functions. A brief explanation is given below for these blocks.

Block 1. Input of the initial parameters. For ease of calculation, all dimensional values are given in dimensionless form.

Block 2. Finding the stiffness characteristics for a layered plate.

Block 3. Drawing up and solving the system of the equilibrium equation for a layered plate.

Block 4. Finding the stress-strain state of a layered plate.

The solution for the obtained systems of equations is possible when six boundary conditions on each contour are satisfied with respect to the sought functions.

If we turn to history, it is easy to recall that fiberglass and carbon fiber were among the first elements of layered composites. However, this type of composite structures, qualitatively transformed and widely used in construction, still needs development and research.

On the basis of the constructed new two-dimensional model according to the proposed numerical method, the study of the bending problem for hinge-supported, symmetric in thickness, square plates with orthotropic layers of carbon fiber in a wide range of variations for h/a is performed. These plates have the following physical, mechanical and geometric characteristics for the corresponding layers of the plates:

- the elastic modulus of the plate layers: $E_1 = 25E_2$, $E_2 = E_3$;
- the shear modulus of the plate layers: $G_{12} = G_{13} = 0.5E_2$, $G_{23} = 0.2E_2$;
- Poisson's ratio of the plate layers: $\nu_{12} = \nu_{23} = \nu_{13} = \nu_{32} = 0.25$, $\nu_{21} = \nu_{31} = 0.01$;
- the plate layer thickness: $h_1 = h_3 = 0.5h$, $h_2 = 0.25h$.

We recall that the elasticity coefficients characterize the physical ability of a material (substance) to deform elastically when a force is applied to it. The elastic modulus or Young's modulus (E) characterizes the physical property of the material, namely, the resistance of the material to tension / compression during elastic deformation. The shear modulus (G) characterizes the ability of a material to resist shear deformation, that is, it determines the ability of a material to resist a change in shape while maintaining its volume. Poisson's ratio (ν) is the ratio of the relative transverse compression to the relative longitudinal tension. This coefficient does not depend on the size of the body, but on the nature of the material from which the structure is made. In Table 2, the presented values of deflections and tensile stresses in the center of the plate are compared with the results of known solutions according to the classical theory and to the methods presented in [3] and [4]. σ_{11} is a tensile stress in the outer fiber of the lower layer, σ_{22} is a tensile stress at the border of the outer and inner layers.

Table 2. Values of deflections and tensile stresses in the plate center

h/a	Classical theory	Exact solution [3]		Solution in trigonometric series [4]		Solution according to the proposed method (FDM)		Calculation error	
	$10^{-7} w, m$	$10^{-7} w, m$	$\frac{\sigma_{11}}{\sigma_{22}}, mPa$	$10^{-7} w, m$	$\frac{\sigma_{11}}{\sigma_{22}}, mPa$	$10^{-7} w, m$	$\frac{\sigma_{11}}{\sigma_{22}}, mPa$	$w, \%$	$\frac{\sigma_{11}}{\sigma_{22}}, \%$
1/20	690.00	820.41	$\frac{217.20}{123.48}$	821.51	$\frac{217.44}{123.48}$	840.56	$\frac{209.08}{118.23}$	2.45	$\frac{3.6}{4.25}$
1/10	43.12	73.70	$\frac{55.90}{40.10}$	73.93	$\frac{56.22}{40.26}$	75.85	$\frac{53.95}{38.46}$	2.9	$\frac{3.4}{4.1}$
1/5	2.70	-	-	9.25	$\frac{16.59}{15.01}$	9.56	$\frac{15.26}{14.85}$	-	-
1/4	1.10	4.96	$\frac{11.52}{10.61}$	5.00	$\frac{11.97}{10.96}$	5.15	$\frac{11.48}{10.19}$	3.8	$\frac{3.47}{3.96}$
1/2	0.07	0.81	$\frac{5.55}{3.34}$	0.80	$\frac{5.57}{3.39}$	0.85	$\frac{5.32}{3.21}$	4.94	$\frac{4.14}{3.29}$

A comparison of the results obtained by the proposed numerical method with the three-dimensional exact solution [3] and the solution [4] in the entire range of the considered parameters h/a shows a sufficiently acceptable accuracy of the numerical method for solving plate bending problems. The calculation results presented in Table 2 also show that the classical theory is not applicable to the problems under consideration.

A comparison for the results of applying the trigonometric series method and the numerical method proposed in the article shows that the results of solving by trigonometric series are more accurate. But here we note two important points.

Firstly, the trigonometric series method is an analytical method. Therefore, this method is more laborious and takes more time than the proposed numerical method implemented on a PC by a software package.

Secondly, the trigonometric series method can be used only for a limited range of plate bending problems, namely, in the presence of hinged support at the plate boundaries. The developed method of numerical calculation for layered orthotropic plates with arbitrary structure in thickness allows us to solve a wider range of problems with varying different boundary conditions, the geometric plate dimensions, the external loads, the thickness of the layers, and their elastic characteristics.

When assessing the reliability of the solutions obtained by the proposed method, the results of an experimental study for the bending of three-layer plates [5] are of great interest. The experiment was carried out on plates, the bearing layers of which were made of duralumin. The elastic modulus equals $E_1 = E_2 = 7 \cdot 10^5$ kg/cm², Poisson's ratio is $\nu_1 = \nu_3 = 0.32$, the layer thickness is equal to 0,081 cm. The filler of the plate was plastic foam, in this case the shear modulus is equal to $G_2 = 890.7$ kg/cm² and the Poisson's ratio is $\nu_2 = 0.4$. The bending of the plate was considered under a uniformly distributed load. So the problems were solved according to the proposed method for a number of plates under the action of a

uniformly distributed load. In the experiment, the maximum deflections were measured. In Table 3, the results obtained are compared with experimental data.

Table 3. Comparison with experimental data for three-layer plates

N	Plate parameters			Load q (kg/cm ²)	Deflections, cm		$\Delta\%$
	a/h	Side length $a=b$ (cm)	Filler thickness (cm)		Experiment [5]	Obtained solution	
1	76.5	112.3	1.306	0.038	0.4267	0.4307	0.93
2	97.4	112.3	0.991	0.0507	0.9119	0.9401	3.09
3	67.36	96.6	1.272	0.0507	0.3124	0.3258	5.56
4	85.49	96.6	0.968	0.0456	0.4801	0.4901	2.08
5	56.14	81.4	1.268	0.0507	0.1829	0.1701	6.9
6	71.4	81.4	0.978	0.0507	0.2845	0.2760	2.98
7	49.44	71.2	1.278	0.0406	0.0889	0.0855	1.9
8	62.02	71.2	0.986	0.0507	0.1651	0.162	1.7
9	38.09	55.8	1.303	0.1268	0.1168	0.1055	9.62
10	48.4	55.8	0.981	0.0761	0.1120	0.0995	11.11

Comparison of the results from Table 3 shows that the differences in deflection values are insignificant and for a large number of plates does not exceed 6%.

Conclusion

In the article a method for numerical calculation of the stress-strain state for structures made of orthotropic, layered composite materials based on one modified refined bending theory is presented. When studying the stress-strain state of a structure, it is necessary to take into account the structure material, the structure texture, boundary conditions, forces and loads acting on the structure, etc. The physical properties of the material from which the structure is made and the material texture are taken into account by the research algorithm. Thus, in hypotheses (1), the conditions for the joint work of layers without separation and displacement are formulated, and the solution of problems is carried out on layers of multilayer structures, taking into account the interaction of layers. The physical properties of the material from which the structure is made are also taken into account by the characteristics of the material, in particular, the elasticity coefficients (E , G , ν , etc.), which are present in the basic relations and equations used.

Comparisons of the results according to the proposed method with known solutions (Table 2) and experimental data (Table 3) indicate the reliability and greater universality of the developed method for the numerical calculation of the stress-strain state for layered orthotropic structures based on one modified refined bending theory.

REFERENCES

- 1 Bozhenov A.Sh. *Theory of multilayer inhomogeneous plates, orthotropic shells and plates*. Abstract of the dissertation of the doctor of technical sciences, Novosibirsk, 1990, 45 p. [in Russian]
- 2 Kasimov A.T. Investigations of the stress-strain state for rectangular multilayer plates by the finite difference method. *Proceedings of the University*, 2002, No. 4, pp. 73 - 75. [in Russian]
- 3 Pagano N.J., Hatfield S.J. Elastic behavior of multilayered bidirectional composites. *American Institute of Aeronautics and Astronautics Journal*, 1972, Vol. 10, No. 7. p. 931 - 933.
- 4 Gorodetsky A.S., Zavoritsky V.I., Lantukh-Lyashchenko A.I., Razkazov A.O. *Automation of calculations of transport facilities*. Moscow, 1989, 232 p. [in Russian]
- 5 Alexandrov A.Ya., Bryukker L.E., Kurshin L.M., Prusakov A.P. *Calculation of three-layer panels*. Leningrad, 1960, 272 p. [in Russian]
- 6 Grigolyuk E.I., Kulikov G.M. Ways of developing the theory of elastic multilayer plates and shells. *Bulletin of TSTU*, 2005, Vol. 11, No. 2A, pp. 439 - 448. [in Russian]
- 7 Annin B.D., Volchko Yu.M. Non-classical models of the theory of plates and shells. *Applied Mechanics and Technical Physics*, 2016, Vol. 57, No. 5, pp. 5 - 14. [in Russian]
- 8 Kasimov A.T. To the application of FDM for the calculation of layered plates taking into account shear strains along its thickness. *Proceedings of the University*, 2018, No. 3, pp. 100 - 103. [in Russian]
- 9 Piskunov V.G., Rasskazov A.O. Development of the theory of layered plates and shells. *Applied Mechanics*, 2002, Vol. 38, No. 2, pp. 22 - 28. [in Russian]

10 Bakulin V. *Methods for optimal design and calculation of composite structures*. Moscow, 2008, Vol.1, 256 p. [in Russian]

11 Popov B.G. *Calculation of multilayer structures by variational matrix methods*. Moscow, MSTU, 1993, 294 p. [in Russian]

12 Alfutov N.A., Zinoviev P.A., Popov B.G. *Calculation of multilayer plates and shells made of composite materials*. Moscow, 1984, 264 p. [in Russian]

Article accepted for publication 11.05.2021

ASSESSMENT OF THE WIND FARM IMPACT ON POWER SYSTEM STABILITY WHILE REDUCING OF TOTAL INERTIA

Razzhivin I.A.*, Ruban N.Yu., Rudnik V.E.

National Research Tomsk State University, Tomsk, Russia, lionrash@tpu.ru

With the development of wind power in the world, the issues of joint operation of wind power plants in power systems become relevant. Modern variable speed wind turbines with are connected to the network through power voltage converters, which, with their significant integration into the power systems, negatively affects the transient stability of such systems, the operation of emergency control devices, etc. The problem is caused by the effect of "decoupling" of the wind turbine generators from the power systems, since the connection of the mechanical moment of the wind turbine with the power system is lost, its frequency characteristics also change, the overall inertia of the system decreases, and as a consequence, these phenomena can lead to rapid fluctuations in frequency and voltage in normal modes, and also an avalanche of frequency and voltage in case of accidents. In addition, a decrease in the total inertia can contribute to the failure of out-of-step protection systems for eliminating the out-of-step mode, due to an increase in the slip frequency. In the article, experimental studies of the implementation of wind power plants in power system to assess the impact of their work on the rate of the transients.

Keywords: wind turbine, inertia, out-of-step mode

Introduction

The world is seeing the dynamics of the penetration of new renewable energy sources (RES), mainly wind power plants (WPP). According to the reports [1-2], the total generated capacity of WPP in the world has more than tripled over the past 10 years and amounts to 651 GW (5.9% of world electricity production). With an increase in the share of RES, their influence on electric power systems (EPS) increases, which creates certain challenges in modes control, maintaining the balance of power, stability and reliability of EPS. Among other things, the problem of reducing the total inertia in EPS is becoming urgent. A decrease in the total inertia is due to the presence of a power voltage converter in the structures of modern renewable energy sources (wind turbines of the 3-rd and 4-th types, solar power plants), there are no rotating mechanisms in solar power plants, and the generators of these wind turbines (WT) essentially become "decoupled" from power system. In addition, the inertia of the system becomes time-varying due to the constant change in the power generated by the RES. In emergency modes in systems with less inertia, the rate of change in frequency and other operating parameters is faster [3-7]. The analysis carried out [6] shows that for the period from 1996 to 2016 the overall value of inertia in Europe decreased by 20%. Systems with less inertia can quickly lose their stability in the event of serious accidents, the out-of-step mode in such systems can be mistaken for a short circuit. Thus, large-scale integration of renewable energy sources reduces the inertial properties of EPS and creates problems with ensuring its stability. In this case, the operating systems of emergency control automation, for example, the out-of-step protection (OSP), can be insensitive to rapidly occurring changes in the EPS.

In accordance with this, the purpose of this article is to evaluate the operation of a WPP consisting of a Type4 WT (with a synchronous generator and excitation from permanent magnets, connected to the EPS through a power voltage converter) for the change in the total inertia of EPS and the rate of the transients.

1 Assessment of the network total inertia

In the electric power engineering, it is customary to evaluate inertia by the value of H – the constant inertia of the unit:

$$H = \frac{E}{S} = \frac{J_{\Sigma}\omega^2}{2S}, \quad (1)$$

where J_{Σ} – total unit inertia, E – kinetic energy, S – rated apparent power of the unit.

The EPS model is implemented in the Hybrid Real-Time Power System Simulator (HRTSim). HRTSim is a hybrid-type multiprocessor software-technical system that combines a set of specialized hybrid processors (SP) of all significant equipment of the simulated EPS [8-9]. The EPS model contains: Slack Bus, 500, 220 and 110 kV transmission lines, transformers, compensating devices, static and dynamic loads (synchronous and induction motors), a turbine generator G2 of a rated capacity of 225 MVA and G3 of a rated capacity of 180 MVA. The WPP is the equivalent of Type4 WT, the SP of which was previously developed and fully verified by the authors [10-11].

For the research, the following conditions and assumptions were adopted:

1. The aerodynamic model is reproduced by the expression generally accepted in world practice [12]:

$$P_M = \frac{1}{2} \rho \pi R^2 V_W^3 C_P(Z, \beta). \quad (5)$$

2. The wind speed change during the simulation according to [13].
3. The mechanical part of the WT is represented by a two-mass model [14].
4. The model for controlling the pitch angle is based on two PI-controllers: the reference signals are the "errors" of the generator power P_G and the turbine speed ω , which are compared with the corresponding settings [14].
5. The torque regulator is represented by a PI-regulator, the function of which allows the wind turbine to work at the point of optimal power (MPPT). The controller is implemented according to [15].
6. The voltage source converter control is implemented according to [16].
7. Protection of Type 4 WT and EPS against overvoltage / current and frequency is not applied, since the article examines the effect on the asynchronous mode.

3. Case study: Assessment of WPP impact on EPS stability

To assess the impact of WPP operation on the stability of the studied EPS, an emergency situation was simulated: a three-phase fault at time $t = 0.2$ sec on the L-2 line with its subsequent disconnection, leading to a break in the connection of the EPS with the Slack bus, violation of stability and the emergence of out-of-step mode. The experiments were carried out while replacing the power of the traditional source G3 with the power generated by the WPP in various ratios, while the total power of the EPS did not change: $P_{WPP} = 20$ MW (11% of the G3 power), $P_{WPP} = 60$ MW (33% of the G3 power), $P_{WPP} = 100$ MW (55% of G3 power) $P_{WPP} = 160$ MW (90% of G3 power). According to (1.2), the change in H_{EPS} of the total inertia of the EPS when replacing traditional generation has the following values:

Table 1. The EPS total inertia value for WPP integration.

WPP power level, MW	H_{EPS} , sec.	ΔH , sec.
0	8.745	-
20	8.341	0.404
60	7.535	1.210
100	6.728	2.017
160	5.478	3.267

In the investigated emergency state, after disconnecting the L-2 line, the G2 and G3 generators are electrically connected through: line L-3, group AT at Substation 2 and lines L-4 and L-5. Suppose that an OSP device is installed on the L-3 line outgoing from Power Plant No2, which measures the angle between the voltages at the ends of the line, i.e. from the Power Plant No2 and at the end of the controlled area (in our case, at the opposite of the line end) on the 220 kV buses of Substation 2. Figure 2 shows waveforms of the mutual angle between the voltages at the ends of the L-3 line.

In the post-emergency state, at the moment of disconnection of the L-2 line ($t = 0.5$ sec), an out-of-step mode is observed, the voltage vectors at the ends of the L-3 line turn relative to each other and the controlled angle δ intersects $\pm 180^\circ$. Turning angle δ in the positive direction corresponds to an increase in frequency and excess power in the part of the EPS connected to the far end of the controlled line. Out-of-step mode also indicates that the electrical swing center is located on the monitored line.

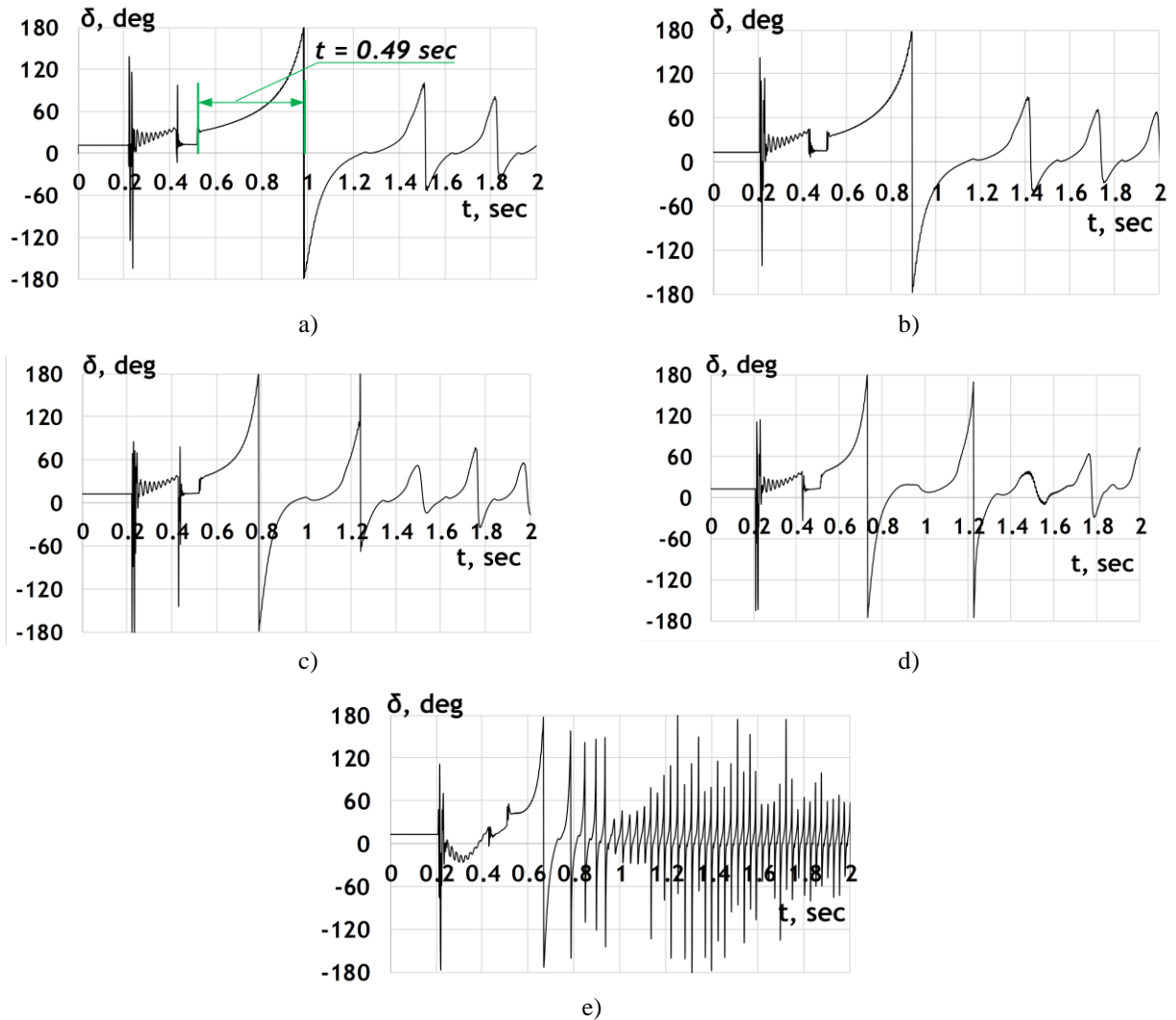


Fig.2. The waveforms of the mutual angle of voltages at the ends of the line L-3
 a) without WPP; b) WPP rated power 20 MW; c) WPP rated power 60 MW; d) WPP rated power 100 MW; e) WPP rated power 162 MW.

In the process of the development of the out-of-step mode, the rate of increase in the angle difference rapidly increases with the increase in the share of WPP power in the EPS, in particular, from the moment the L-2 line is disconnected. A summary is shown in Table 2. With the development of the out-of-step mode in EPS with traditional generation, the change in the angle δ occurs more slowly due to the inertia of electromechanical processes, however, the replacement of traditional generators WPP, which reduce the inertia of the EPS, significantly accelerates the process.

Table 2. The time development of EPS out-of-step mode with WPP integration.

WPP power level, MW	The time of out-of-step mode development, sec.
0	0.49
20	0.39
60	0.29
100	0.23
160	0.19

The Figure 3 shows waveforms of the angle δ (between the EMF) of the generators G2, G3 and the Slack Bus and the relative angle δ_{23} , which characterizes the operation of G2 and G3 in post-emergency state, when they remain isolated from the Slack Bus.

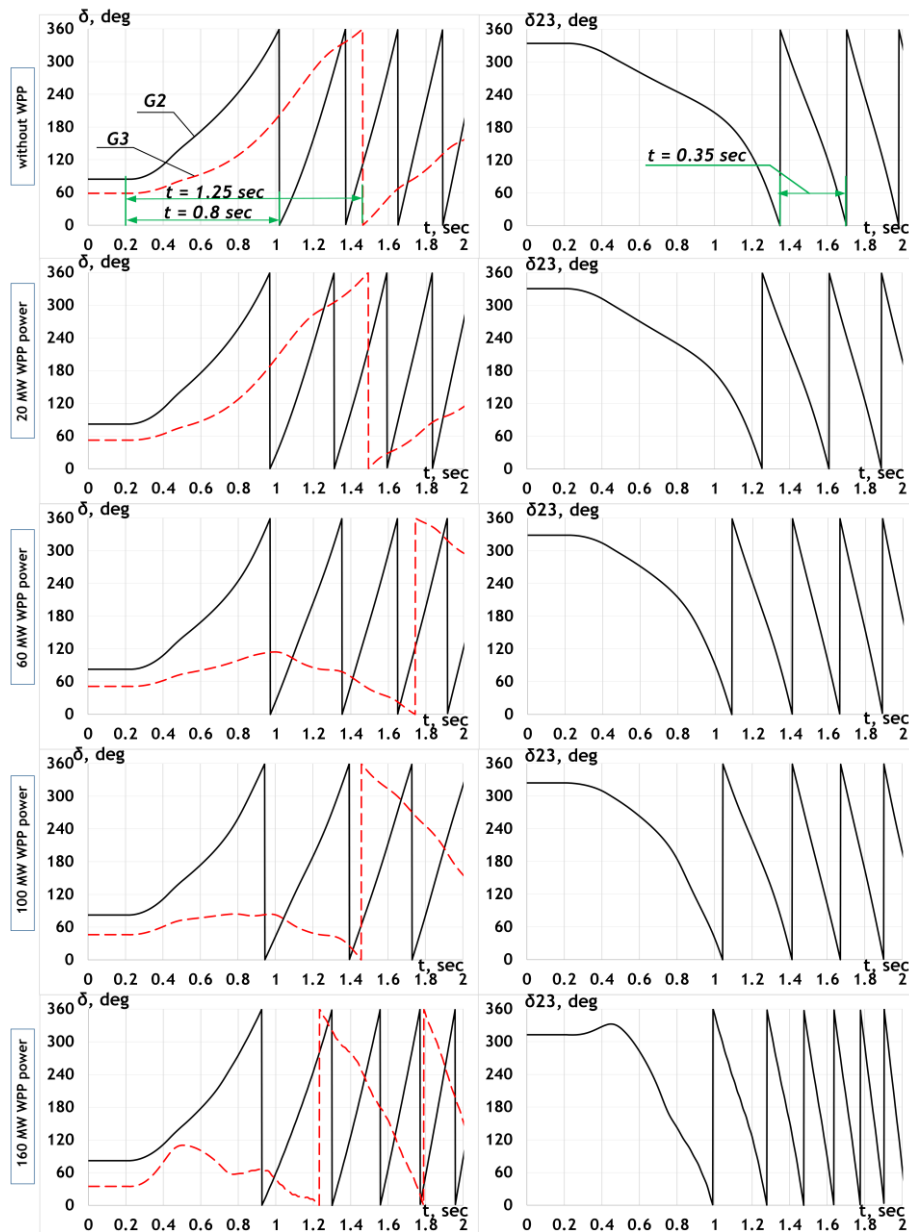


Fig.3. The waveforms of the G2 and G3 δ angle between slack bus and waveform of δ_{23} angle between to each other

At a WPP power of 0 and 20 MW, respectively, rotation of the angle δ G3 is observed once, i.e. then G3 returns to stable operation. In general, a similar situation is observed when, for example, a change in the angle δ G3 in a post-emergency state in EPS with a predominant traditional generation occurs more slowly due to inertia, however, when the power G3 is replaced by the power of WPP, the processes accelerate. In particular, the violation of the synchronous operation of G3 during the integration of the WPP occurs faster, and the relative angle δ_{23} also changes faster, which is noticeable from the cycles of asynchronous swings in the EPS. The summary data on the time for which the stable operation of G3 is disrupted and the time of the first cycle of out-of-step mode between G2 and G3 in the post-emergency state are given in Table 3.

Acceleration of processes can lead to improper operation of both the OSP device itself and OSP protection from redundant triggers when the angle δ of the protected object is changed, which is not related to the development of out-of-step mode, since the main sign of the difference between the out-of-step mode development process and emergency and switching processes is an increase in the operating parameter at the

current measurement interval by no more than two times in relation to its change at the previous measurement intervals. Experiments show that the acceleration of processes, in particular the development of the out-of-step mode and the change in the mutual angle between the voltages at the ends of the L-3 line, occur quickly enough, which can cause the emergency automation to malfunction.

Table 3. Disturbance of G3 stability and the time of the first cycle of out-of-step mode

WPP power level, MW	Break through time stable operation G2, sec.	Break through time stable operation G3, sec.	Time of the first cycle of out-of-step mode, sec.
0	0.80	1.25	0.35
20	0.78	1.32	0.35
60	0.78	1.52	0.31
100	0.78	1.29	0.36
160	5.478	3.267	0.28

Conclusions

Experiments carried out in the article showed that with the integration of WPP, the total inertia in the EPS decreases. Due to the decrease in the total inertia, changes in the out-of-step mode parameters also occur. In particular, with an increase in the power of the WPP, the development time of the out-of-step mode and the time during which traditional generators fall out of synchronism decreases, which confirms the fact that the WPP affects the total inertia in the EPS and the rate of transient processes. In addition, with a sufficiently high share of WPP power in the EPS, equal to 90% (160 MW), strong fluctuations are observed.

The impact of WPP integration on the change in the total inertia requires the deep analysis. The directions of the further research will be devoted to the study of the influence of the WPP on transient processes and the reduction of the total inertia at various locations of the WPP in the EPS. Studies are also planned aimed at varying the models of WPP and infinite bus models for transient processes in EPS in various operating modes.

Acknowledgements

The work was supported by Ministry of Science and Higher Education of Russian Federation, according to the research project No. MK-3249.2021.4.

REFERENCES

- 1 Renewables 2020 Global Status Report. Available at: <https://www.ren21.net/reports/global-status-report/>
- 2 GWEC. *Global Wind Statistics 2019*. Global Wind Energy Council, Brussels, Belgium, Tech. Rep. (2020). Available: <https://gwec.net/global-wind-report-2019/>
- 3 Tielens P., Hertem D. V. The relevance of inertia in power systems. *Renewable Sustain. Energy Rev.* 2016, Vol. 55, pp. 999–1009, doi:10.1016/j.rser.2015.11.016.
- 4 Erlich I., Wilch M. Primary frequency control by wind turbines. *Proceedings of the "2010 IEEE power and energy society general meeting"*, Minneapolis, USA. 2010, pp. 1–8.
- 5 Gautam D., Goel L., Ayyanar R., Vittal V., Harbour T. Control strategy to mitigate the impact of reduced inertia due to doubly fed induction generators on large power systems. *IEEE Transactions on Power Systems.* 2011, Vol. 26, No. 1, pp. 214–224, doi: 10.1109/TPWRS.2010.2051690.
- 6 Fernandez-Guillamon A. et al. Power systems with high renewable energy sources: A review of inertia and frequency control strategies over time. *Renewable and Sustainable Energy Reviews*, 2019, Vol. 115, pp. 109369. doi: 10.1016/j.rser.2019.109369
- 7 Gonzalez-Longatt, F. Impact of emulated inertia from wind power on under-frequency protection schemes of future power systems. *Journal of Modern Power Systems and Clean Energy*, 2016, pp. 1 – 8. doi:10.1007/s40565-015-0143-x.
- 8 Razzhivin, I., Askarov, A., Rudnik, V. and Suvorov, A. A Hybrid Simulation of Converter-Interfaced Generation as the Part of a Large-Scale Power System Model, *International Journal of Engineering and Technology Innovation*, 2021, 11(4), pp. 278–293. doi: 10.46604/ijeti.2021.7276.

-
- 9 Suvorov A., Gusev A., Ruban N., et al. Potential Application of HRTSim for Comprehensive Simulation of Large-Scale Power Systems with Distributed Generation. *International Journal of Emerging Electric Power Systems*. 2019, Vol. 20, No. 5, pp. 20190075.
 - 10 Ufa R., Andreev M., Ruban N., et al. The hybrid model of VSC HVDC. *Electrical Engineering*. 2019, Vol.101, No. 1, pp. 11 – 18. doi: 10.1007/s00202-018-00752-y.
 - 11 Andreev M., Ruban N., Suvorov A., et al. A Hybrid Model of Type-4 Wind Turbine – Concept and Implementation for Power System Simulation. *Proceedings of the “2020 IEEE PES Innovative Smart Grid Technologies Europe (ISGT-Europe)”*. 2020, pp.799 – 803. doi: 10.1109/ISGT-Europe47291.2020.9248860
 - 12 Price W.W., Sanchez-Gasca J.J. Simplified Wind Turbine Generator Aerodynamic Models for Transient Stability Studies. *Proceedings of the “IEEE PES Power Systems Conference and Exposition”*. 2006, pp. 986-992. doi: 10.1109/PSCE.2006.296446.
 - 13 Obukhov S.G., Plotnikov I.A., Masolov V.G. Dynamic wind speed model for solving wind power problems *Eurasian phys. tech. j.* 2020, Vol.17, No.33, pp.77 – 84.
 - 14 Clark, N. W. Miller, and J. J. Sanchez-Gasca, Modeling of GE wind turbine-generators for grid studies *GE energy*, vol. 4, pp. 0885–8950,2010
 - 15 Wu B., Lang Y., Zargari N., Kouro S. *Power Conversion and Control of Wind Energy Systems*. 2011, 480 p.
 - 16 Yaramasu V., Dekka A., Duran M.J., Kouro S., Wu B. PMSG-based wind energy conversion systems: Survey on power converters and controls. *IET Electr. Power Appl.* 2017, Vol. 11, pp. 956–968. doi:10.1049/iet-epa.2016.0799.

ENHANCEMENT OF STEAM-TURBINE CONDENSER STEAM-JET EJECTOR

Shavdinova M.D.*, Sharipov R.Zh., Meshherjakova T.Y.

Kazakh-German University in Almaty, Almaty, Kazakhstan, shavdinova@dku.kz

A three-stage steam-jet ejector EPO-3-200 with a working steam flow rate of 850 t / h is installed at the Combined Heat and Power Plant-2 of the city of Almaty on heating turbines. In this paper, the replacement of the existing three-stage steam-jet ejector with a two-stage steam-jet ejector is proposed and substantiated. As a result of the replacement, they obtained a saving of heat (steam) for their own needs for the production of electrical energy. It has been established that at a pressure in the turbine condenser significantly lower than 100 kPa, it is advisable to install a new two-stage ejector EPO-2-80 instead of EPO-3-200. Using the existing calculation methods, the geometric characteristics of the new ejector were obtained. The working steam flow rate of the new two-stage ejector is 579 t / h. In addition, the use of two stages makes it possible to simplify the design and make it more reliable, and also makes it possible to increase the pressure in the cooler of the 1st stage of the ejector. This is especially important for cogeneration turbines, which may have a high temperature of the main condensate, which adversely affects the performance of a conventional three-stage ejector.

Keywords: steam-jet ejector, raising of efficiency, three-stage ejector, two-stage ejector, cooler, mathematical model, steam turbine.

Introduction

Steam jet ejectors are designed to remove air from condenser and vacuum system; they are among the most important technical components of condensing systems [1]. We know steam jet multistage ejectors of various manufacturers (Leningrad Metal Plant (LMP), Ural Turbine Works (UTW), Kharkiv Turbine Plant (KhTP), Kaluga Turbine Works (KTW)), such as EP-3-700, EP-3-3, EP-3-25/75 and others consisting of three stages each of which contains a nozzle, a receiving chamber, a diffuser and a cooler [2].

We know a steam jet ejector with external coolers – an equivalent of EPO-3-135 developed by the UTW, with "external tube bundle" coolers [3]. This ejector solves the main problem of multistage steam jet ejectors associated with inter-stage vapor-air mixture (VAM) leakages. Based on the analysis of experimental characteristics of multi-stage steam-jet ejectors of steam turbines, a set of questions was framed to refine the physical model of gas dynamics in the flow path of steam-jet device and the calculation method for ejectors, as well as the performance features of intermediate coolers. It has been established that the cooler efficiency depends on the steam pressure which is determined by the operation of steam jet ejector on the steam jet stage following after the cooler, the temperature and the cooling water flow rate. The steam contained in the air-vapor mixture entering the cooler is generally overheated relative to the saturation temperature of the mixture steam. This is to be taken into account when calculating the cooler. Long-term operation changes the roughness of walls in the ejector mixing chamber. The effect of such change in the wall roughness on the ejector characteristic is similar to that of the back pressure of steam jet stage. Up to a certain value of roughness, the injection factor of ejector stage operating out-of-limit remains practically unchanged. When critical roughness is reached, the ejector switches to pre-limiting operating mode [4].

The developed and approved design solutions were presented [4] that allow to enhance the ejector performance. Coolers are designed in separate bodies, so the vapor-air mixture cannot move from high-pressure zones to low-pressure zones and the maintainability of the units increases. The U-type pipes compensate for the expansion effect of intercooler pipes and increase the heat exchange area.

In [5-8], the axial position of ejector nozzle was analyzed. The studies mentioned were carried out for various substances used as working and entrained flows, but not for water and water steam. In [9] the ejector structural design was analyzed. In many cases, ejectors are designed quite empirically, and the main flow sections are the only elements of ejector geometry that require design force. Some other elements, such as the length of mixing zone or the secondary flow inlet angle, are left to a designer's discretion. A design was proposed that takes into account the effect of a rim between conical and cylindrical parts. The authors of the

paper [10] have made the model of steam jet ejector, and then carried out CFD analysis for its geometry. The inlet status data was verified by evaluating the performance of jet ejector to find the entrainment factor which was then compared to the experimental data.

Adriano Milazzo and Federico Mazzelli have developed CFD (ANSYS Fluent) model of ejector using the user defined functions. The scheme is based on a single liquid approach and solves the transfer equations for a uniform mixture combined with the conservation equations for a number of droplets and volume ratio of liquid. The model is checked for compliance with a test version of the steam nozzle, and then compared to experimental data of the steam ejector with a significant volume of resulting liquid phase. The simulation showed a good ratio, both in terms of mass flow rates and pressure profile data [11]. In [12], a CFD model of ejector was also developed and an experimental test was carried out in a wide range of operating conditions for various configurations of the ejector. The study results show that the length of pseudo-shock has a dominant influence on the entrainment characteristics and geometry optimization. A significant difference in the length of the pseudo-shock for gas and gas-liquid ejectors was noted. This is due to the fact that the similarity of viscosity differs markedly in the range of 0.01–1.0, depending on the used primary and secondary fluids. Therefore, the optimal ‘mixing tube length/diameter’ ratio is approximately 1:2 for conventional gas-liquid ejectors and 5:7 for gas ejectors. The article [13] presents a mathematical model describing the flow inside a real ejector. Comparison of calculations with measurements is more than acceptable, and this method seems to be suitable for similar devices with converging nozzle. An ejector with different diameters of neck and diffuser can be used to create a new ejector with an increased airflow.

The authors of [14] propose a procedure for optimizing the ejector without taking into account the region of mixed supersonic flow, and constructs the design curves taking into account the constant ratios of general temperature, molecular weight and specific heat. In some applications involving high temperature gases, such as gas turbine facilities, an annular supersonic ejector is more appropriate where annular injection of the motive gas at the periphery of the flow passage is desired to avoid the exposure of the motive gas flow nozzle to the high temperature combustion product gases. The design and optimization procedure for an annular supersonic ejector was developed based on a simplified one-dimensional mixing of a constant model area and checked using CFD Fluent software.

In [15] the ejector is designed using CRMC method. CRMC ejector provides higher entrainment factor with the same critical condenser pressure. On the other hand, with the same entrainment ratio, CRMC ejector can operate at a higher critical condenser pressure. This confirms that the CRMC method improved the performance of the ejector. A new highly efficient ejector with external coolers EPO-3-80 was calculated, designed, manufactured and installed at TPP. Experimental studies of the developed ejector were conducted. Industrial testing was carried out for 1.5 years. Currently, EPO-3-80 ejector is successfully operating as part of a turbine unit with K200-130 turbine of LMP RF. The author has carried out a comparative analysis of the characteristics of serial ejectors and a new ejector. It follows from the analysis that the performance (length of operating characteristic) of new EPO-3-80 ejector is higher than that of serial ejectors. The suction pressure of the new ejector at low air flow rates is also minimal as compared to serial ejectors [4].

In [16], the ejector performance map is developed. The proposed ejector performance map can be used in numerical analysis of the ejector system to study the architectures of new cycles based on the ejector experimental data, thus increasing the accuracy of the system model. This can also help the system design engineers in making decisions on choosing the ejector system after careful analysis of system performance.

EPO-3-120 ejector is the closest to the new model in terms of its technical essence, its design corresponds to the utility model patent [17]. The known steam jet ejector is three-stage and includes nozzles, receiving chambers, mixing chambers, diffusers, reducing pipes and coolers located in each stage in a successive order along the path of motive steam. The nozzles are designed with a possibility of axial movement relative to the diffuser. The reducing pipes are located below diffusers. The ejector coolers are vertical and external, with U-shaped tubes. The coolers are triangular to each other, with equal body diameters. This engineering solution aims at increasing the reliability and efficiency of steam-jet ejectors for suction of non-condensable gases from the inner space of condensers of steam-turbine cogeneration plants (SCP) by reducing the total compression ratio of vapor-air mixture and the consumption of motive steam. The technical result achieved by the new model of ejector is decreased heat consumption for own needs of steam-turbine cogeneration plant (SCP).

The object under consideration is the cogeneration turbine T-100 / 120-130-3 of the Combined Heat and Power Plant-2 of the city of Almaty. The barometric pressure at the station is approximately 100 kPa. The

turbine is equipped with a three-stage steam-jet ejector EPO 3-200. It is necessary to replace the three-stage ejector with a two-stage one.

Thus, we obtain a simple and reliable design of a steam jet ejector for suction of non-condensable gases from steam turbine condensers of heating plants operating at barometric pressure below normal values ($B \approx 100$ kPa). Allowing to reduce the total compression ratio of the steam-air mixture and the consumption of working steam, as well as to reduce the heat consumption for the auxiliary needs of a steam turbine cogeneration plant (STU), due to the use of two steam jet stages and the installation of intermediate baffles with sealing elements in the first stage cooler, which ensures high efficiency cogeneration turbine plant.

2. Materials and methods

Calculations were made for the first stages of existing three-stage steam-jet ejector EPO-3-200 and the new two-stage steam-jet ejector EPO-2-80 (Table 1). The initial data for calculation: motive steam pressure $p_0 = 490$ kPa, motive steam temperature $T_0 = 157$ °C, condenser pressure $p_k = 7$ kPa obtained from the calculation according to the developed mathematical model of condenser [18], inlet circulating water temperature $t_{1w} = 22.5$ °C, geometrical characteristics of ejector. The calculation was carried out using the method described in [19], [20]. The Table 2 shows the geometric characteristics of the new ejector.

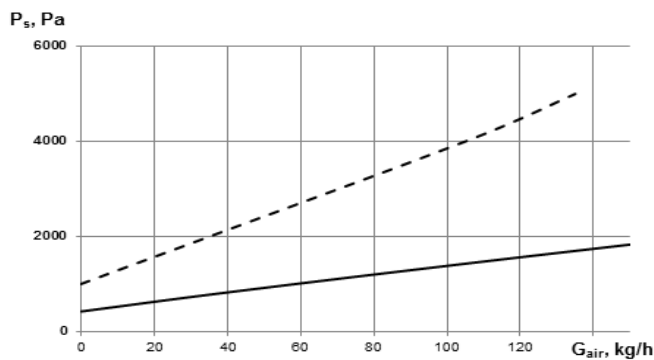
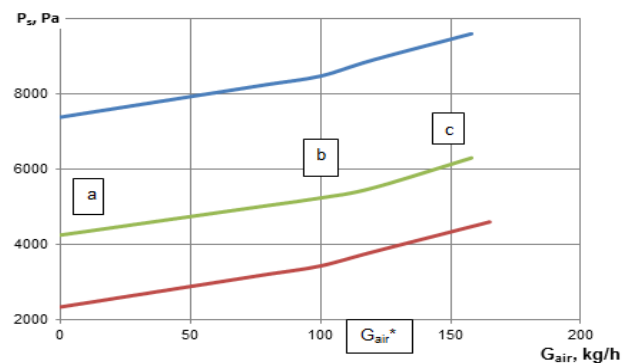
Table 1. Calculation of the 1-st stages of steam-jet ejectors EPO-3-200 and EPO-2-80

Item No.	Parameter	Designation	Unit	Value	
				EPO-3-200	EPO-2-80
1	Pressure in receiving chamber $P_s = p_k \cdot 0.92$ [20]	P_s	Pa	6440	6440
2	Pressure of mixture $p_d = P_s \cdot \varepsilon$	p_d	Pa	141680	225760
3	Compression ratio	ε	-	22	4.0
4	Ejector volumetric efficiency $V_n = G_{air} \cdot (t_s + 273.15) \frac{R_{air}}{(p_s - p_{va}) \cdot 1000}$ [20]	V_n	m ³ /h	8569	6406
5	Motive steam consumption $G_s = G_w + G_{vam}$	G_s	kg/h	519	400
6	Steam consumption in VAM $G_{vam} = \frac{p_{vam} V_n}{R_s (t_s + 273.15)}$ [20]	G_{vam}	kg/h	261	241
7	Injection factor $u = \left(\mu \frac{F_3}{F_{cr}} - \frac{1}{q_{va}} \right) \frac{k_{air}}{k_s} \frac{\Pi_{air^*}}{\Pi_{s^*}} \frac{a_s}{a_n} \frac{p_{air}}{p_s}$ [20]	u	-	0.8	0.80
8	Heat exchanger outlet mixture temperature $t_{mix} = (t_s(p_k)) \cdot 0.7 + t_{1w} \cdot 0.3$ [20]	t_{mix}	°C	46	46
9	The amount of steam condensed by the heat exchanger	$G_{s,HE}$	kg/h	189	208

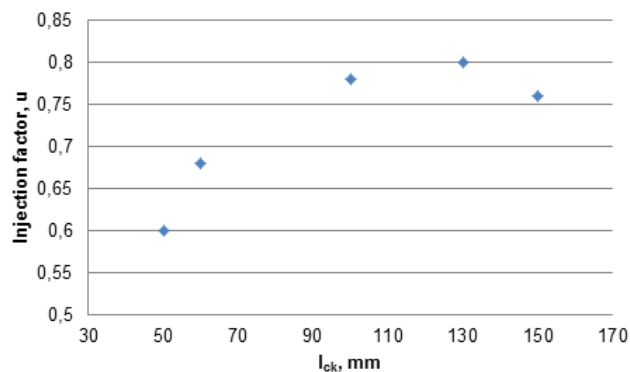
Figure 1 shows that the curve of the new ejector is lower. The new ejector will help maintain a deeper vacuum on the turbine. Figure 2 shows the curve of the 1st stage of ejector sucking off the vapor-air mixture, depending on the temperature of mixture t_{mix} . The curve of the ejector sucking dry air or vapor-air mixture at a certain temperature has two different sections. The first section (ab), to a certain section G_B^* , is called a working section, this is comparatively flat. The second section (bc), $G_B > G_B^*$, is called a shifting section, this is much steeper. Air flow rate G_B^* is called a maximum operating capacity. The maximum operating capacity is different in dry air and vapor-air mixture of a certain temperature. For example, for section ab $G_B^* = 100$ t/h. Resulting from calculations, the curves $P_{sp} = f(G_{air})$ of the 1st ejector stage are plotted for "dry" air (Fig.1) and for ejector sucking off the vapor-air mixture (Fig.2). Also, the calculation results can establish the dependence of the injection factor u on the distance from nozzle exit section to mixing chamber inlet section l_{ck} (Fig.3). Figure 3 shows that the optimal injection factor for the first ejector stage will be $u = 0.8$.

Table 2. Geometrical dimensions of the new ejector EPO-2-80

Item No.	Parameter	Designation	Unit	Value	
				1 stage	2 stage
1	Nozzle throat diameter $d_{cr} = \sqrt{\frac{4G_s a_s}{3600 k_s \cdot \Pi_s \cdot p_s \cdot 10^6 \cdot 3.14}} [20]$	d_{cr}	mm	13.9	9.3
2	Nozzle exit diameter $d_c = \sqrt{\frac{d_{cr}}{q_{va}}} [20]$	d_c	mm	39.2	16.4
4	Diameter of the mixing chamber cylindrical section $d_{cyl} = d_{cr} \left(\frac{F_3}{F_{cr}}\right)^{0.5} [20]$	d_{cyl}	mm	109.1	29.1
5	Length of exit, conical section of nozzle $L_c = \frac{d_2 - d_3}{2tg(6^\circ)} [20]$	L_c	mm	120	34
6	Distance from nozzle exit section to mixing chamber inlet section $L_{ck} = \frac{55.79d_3}{12.64 + d_3/(d_{cr} \cdot 2)} - L_{con} - L_c [20]$	L_{ck}	mm	131	40
7	Length of the mixing chamber cylindrical section $L_{cyl} = 5d_3$	L_{cyl}	mm	546	146
8	Length of diffuser $L_d = \frac{d_4 - d_3}{2tg(4^\circ)} [20]$	L_d	mm	186	75

**Fig.1.** Curve of the 1-st ejector stage for "dry" air:
— new ejector, - - - existing ejector**Fig.2.** Curve of the 1st ejector stage EPO-2-80 for ejector sucking off the vapor-air mixture

— t_{mix}=30C — t_{mix}=40C — t_{mix}=20C

**Fig.3.** The dependence of the injection factor on the distance from nozzle exit section to mixing chamber inlet section for ejector EPO-2-80

3. Results and discussion

Analysis of the operation data on operating modes of turbine T-100/120-130 at Almaty Thermal Power Plant-2 for 2020 showed that the steam pressure in the turbine condenser was higher than 7 kPa for much of the year. At the same time, barometric pressure is 92...93 kPa. For such process parameters, the main ejector was developed which differs from the rated (serial) ejector of T-100/120-130 turbine (EP-3-2 or EPO-3-200) in a number of characteristics. The new ejector is two-stage, the motive steam consumption per ejector is 579 kg/h, in contrast to the serial one with steam consumption of 850 kg/h.

The proposed EPO-2-80 steam jet ejector is a series-connected nozzle located in the direction of movement of the working steam in the corresponding casings of the steam jet stages, communicated with the receiving chamber, which is connected to the mixing chamber, a diffuser located below and communicated with the mixing chamber, a transition pipe, which on the one hand it is connected to the diffuser, and on the other hand it is connected to the shell-and-tube cooler. The cooler is made remote in a vertically located housing, inside of which U-shaped heat exchange tubes are located, characterized in that it contains two steam jet stages, the bodies of which are located vertically. The cooler of the first steam-jet stage and the cooler of the second steam-jet stage are connected in series through the cooling water. Condensate is supplied to the water chamber of the first stage cooler, and the condensate is removed from the water chamber of the second steam jet cooler. The calculations resulted in a two-stage steam-jet ejector EPO-2-80 (Fig. 4).

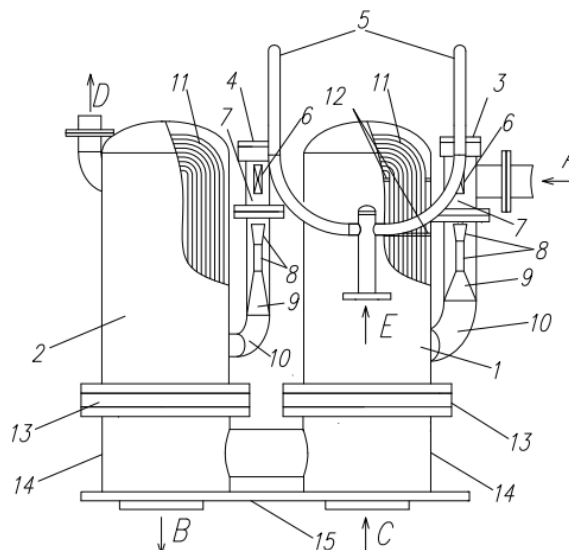


Fig.4. Steam-jet ejector EPO-2-80:

A - steam-air mixture supply, B - cooling water outlet, C - cooling water supply, D - air exhaust, E - working steam supply, 1 - first stage cooler, 2 - second stage cooler, 3 - first steam jet, 4 - second steam jet, 5 - steam line, 6 - working nozzle, 7 - receiving chamber, 8 - mixing chamber, 9 - diffuser, 10 - reducer, 11 - U-shaped tubes, 12 - intermediate partitions, 13 - tube sheet, 14 - water chamber, 15 - support frame

The new steam-jet ejector is distinguished by its intermediate baffles made in an annular shape; sealing elements are made as sealing collars; sealing elements are made of fluoro plastic; sealing elements are fixed along the outer diameter over total circumference of the annular intermediate baffle; the sealing elements are bolted to the intermediate baffles and fitted with a metal base.

The technical and economic effect of the new ejector was assessed in comparison with the serial one. This effect consists in saving heat (steam) of own needs for electrical energy production. According to the operation data of Almaty Thermal Power Plant-2, motive steam is supplied to the main ejectors of T-100/110-130 turbine from the general station steam collector at 1.3 MPa. Steam is supplied to this collector from the production extraction of turbine PT-80/100-130/13 or ROU 130/13. The new main ejector will reduce the steam consumption by 271 kg/h as compared to the serial ejector.

When the steam from extraction of PT-80/100-130/13 turbine is supplied to the collector, the new ejector consumes less steam heat by 168 kW (0.144 Gcal/h). Then PT-80/100-130/13 turbine can generate 43.2 kW of extra power by saving steam for the main ejector of T-100/120-130 turbine. Thus, thanks to the new ejector, we saved 84 tons of oil equivalent (t.f.e).

If live steam enters the general station collector, then the savings from the new ejector can be calculated based on the characteristic of PT-80/100-130/13 turbine in condensing mode. Savings from the new ejector will be 70.6 kW. The new ejector will save 137 tons of oil equivalent (t.o.e). The effect obtained does not take into account the increase in turbine power due to a very likely decrease in condenser steam pressure (deepening of vacuum) with a new ejector installed which has a higher volumetric efficiency as compared to serial ejectors. Vacuum deepens at partial steam flows in the condenser and increased air inflows in the vacuum system in excess of the standard values. The presented analysis was performed without taking into account the cost of ejector replacement. To assess the effectiveness of the project for modernization of T-100/120-130 turbine at Almaty Thermal Power Plant-2, a feasibility study is necessary.

The new two-stage steam-jet ejector is designed for exhaust air compression ratio $\varepsilon = 3.5 \dots 4.0$. Comparison of the new model with the prototype reveals the following distinctive features:

- two steam-jet stages;
- vertically arranged bodies of two steam-jet stages;
- the cooler of the first steam-jet stage and the cooler of the second steam-jet stage are connected in series through cooling water.

Distinctive features of the proposed utility model allow to conclude that it meets the "novelty" criterion. The new steam jet ejector is made of materials known in the industry, structural units and parts, which are connected into a single structure by assembly operations and are in a structural unity. All this ensures the achievement of a technical result. This allows conclude the proposed model meets the criterion of "industrial applicability".

Conclusion

To save steam for own needs, it was proposed to replace the existing three-stage steam-jet ejector at Almaty Thermal Power Plant-2 with a two-stage ejector. Calculations were carried out for the 1st stage of the existing three-stage ejector EPO-3-200 and two-stage ejector EPO-280. Geometric characteristics of the new ejector were obtained. The curve of the 1-st ejector stage for "dry" air was plotted. The curve of the new ejector is lower; this ejector will probably maintain a deeper vacuum on the turbine. The curve is plotted for the 1st stage of ejector sucking off the vapor-air mixture, depending on the temperature of mixture t_{mix} .

The dependence of the injection factor on the distance from nozzle exit section to mixing chamber inlet section was plotted. The optimal injection factor for the first ejector stage will be $u = 0.8$. The advantage of the new model is that, with the same productivity for exhaust dry air, the analogue and the existing ejector consume 1.5 times more motive steam than the declared design.

In the proposed design of the new ejector, the steam pressure in the first-stage cooler is higher than in the existing and existing ejectors, which makes it possible to reliably operate the ejector at condensate temperatures 10 ... 15 ° C higher than the existing and existing ejectors.

A utility model patent for a two-stage steam jet ejector was obtained. The technical and economic effect of the new ejector was assessed in comparison with the existing one. The new main ejector will reduce the steam consumption by 271 kg/h as compared to the serial ejector. When the steam from extraction of PT-80/100-130/13 turbine is supplied to the collector, the new ejector consumes less steam heat by 168 kW. In this case, the new ejector will save 84 tons of oil equivalent (toe).

If live steam enters the general station collector, then the savings from the new ejector can be calculated based on the characteristic of PT-80/100-130/13 turbine in condensing mode. In this case, the new ejector will save 137 tons of oil equivalent (toe). To assess the effectiveness of the project for modernization of T-100/120-130 turbine at Almaty Thermal Power Plant-2, a feasibility study is necessary.

REFERENCES

- 1 Ryabchikov A.Yu., Aronson K. É., Brodov Yu. M., et al. Increasing the reliability of steam-jet ejectors in power plant turbines. *Power Technology and Engineering*. 2017, Vol. 50, No. 5. DOI: 10.1007/s10749-017-0748-5
- 2 Belevich, A.I. RD 34.30.302-87: *Methodical Guidelines on adjustment and operation of steam-jet ejectors of turbine condensing plants at TPP and NPP*. M. Ministry of Energy of the USSR, 1990, 34 p. [in Russian]
- 3 Barinberg, G. D. *Steam turbines and turbine plants of the Ural Turbine Works*. Yekaterinburg, 2007, 460 p.
- 4 Aronson K. É., Ryabchikov A.Yu., Kuptsov V.K., et al. Ejectors of power plants turbine units efficiency and reliability increasing. *IOP Conf. Series 891: Journal of Physics*. 2017, pp. 104 – 110. DOI:10.1088/1742-6596/891/1/012249

- 5 Fan, J., Eves, J., Thompso, H.M., et al. Computational fluid dynamic analysis and design optimization of jet pumps. *Computers & Fluids*. 2011, Vol. 46, pp. 212–217
- 6 Ruangtrakoon N., Aphornratana S., Sriveerakul T. Experimental studies of a steam jet refrigeration cycle: Effect of the primary nozzle geometries to system performance. *Experimental Thermal and Fluid Science*. 2011, Vol. 35, pp. 676–683. DOI:10.1016/j.expthermflusci.2011.01.001
- 7 Szabolcs V., Oliveira A.C., Ma X., et al. Experimental and numerical analysis of a variable area ratio steam ejector. *International Journal of Refrigeration*. 2011, Vol. 34, No 7, pp. 255 – 262. DOI:10.1016/j.ijrefrig.2010.12.020
- 8 Narmine H.A., Karameldin A., Shamloul M.M., et al. Modelling and simulation of steam jet ejectors. *Desalination*. 1999, Vol. 123, pp. 1-8.
- 9 Grazzini G., Milazzo A., Mazzelli F. Ejector Design. *Ejectors for Efficient Refrigeration*. 2018, pp.71-115 DOI:10.1007/978-3-319-75244-0_3
- 10 Singhal A., Chitkara T., Ameenuddin M. CFD Analysis and Performance Evaluation of the Steam Jet Ejector. *National Convention of Aerospace Engineers*. University of Petroleum & Energy Studies. Dehradun, India. 2013, p. 3.
- 11 Mazzelli F., Giacomelli F., Milazzo A. CFD modeling of condensing steam ejectors: Comparison with an experimental test-case. *International Journal of Thermal Sciences*. 2018, Vol. 127, pp. 7 – 18. DOI: 10.1016/j.ijthermalsci.2018.01.012
- 12 Li C., Li Y., Wang L. Configuration dependence and optimization of the entrainment performance for gasegas and gaseliquid ejectors. *Applied Thermal Engineering*. 2012, Vol. 48, pp. 237-248.
- 13 Jakub A. *Mathematical model of ejector and experimental verification*. Setkani kateder mechaniky tekutin a termomechaniky, Mikulov, 2012, pp. 26. – 28. [in Czech]
- 14 Sathiyamoorthy K., Iyengar V.S., Pulumathi M. Annular Supersonic Ejector Design and Optimization. *ASME 2012 Gas Turbine India Conference*. 2012, pp. 212-219. DOI:10.1115/GTINDIA2012-9547
- 15 Kittrattanaa B., Aphornratanaa S., Thongtipb T. Comparison of traditional and CRMC ejector performance used in a steamejector refrigeration. *Energy Procedia*. 2017, Vol. 138, pp. 476 – 481.
- 16 Haider M., Elbel S. Development of Ejector Performance Map for Predicting Fixed-geometry Two-phase Ejector Performance for Wide Range of Operating Conditions. *International Journal of Refrigeration*. 2021, pp. 456-483. DOI:10.1016/j.ijrefrig.2021.03.022
- 17 Brodov, Yu. M., Kuptsov, V. K., Ryabchikov, A. Yu., et al. *Patent for steam-jet three-stage ejector*. RU170935. 2016119824. Publ. 2016.05.23, 9 p. [in Russian]
- 18 Shavdinova M., Aronson K., Borissova N. Development of condenser mathematical model for research and development of ways to improve its efficiency. *Journal of Applied Engineering Science*. 2020, Vol. 18, pp. 578 – 585 DOI: 10.5937/jaes0-27517
- 19 Aronson, K. E., Ryabchikov, A. Yu., et al. *Steam-gas turbine units: ejectors of condensing units: study guide for higher education institutions*. Moscow, 2018, 75 p. [in Russian]
- 20 Sokolov, Ye.Ya. *Jet devices*. Moscow, Ergoatomizdat, 1989, 115 p. [in Russian]

INVESTIGATION OF THE AERODYNAMIC FORCES OF A TRIANGULAR WIND TURBINE BLADE FOR THE LOW WIND SPEEDS

Tanasheva N.K.¹, Tleubergenova A.Zh.¹, Shaimerdenova K.M.¹,
Minkov L.L.², Uzbergenova S.Zh.³

¹ E.A. Buketov Karaganda University, Karaganda, Kazakhstan, shymkent.a7@mail.ru

² National Research Tomsk State University, Tomsk, Russia

³ Kokshetau University named after Sh. Ualikhanov, Kokshetau, Kazakhstan

This article investigates the aerodynamic characteristics and finds the critical angle of attack of a triangular sail blade of a wind turbine for low wind speeds. For this purpose, a triangular sail blade of various parameters has been developed. The prototype is made of metal frame rods, the material of the triangular sail blade consists of a light and durable material (silk), one end of which is fixed to the top of the frame with a strong thread and support rods and bearing with an inner diameter of 8 mm. A sail blade differs from other blades in that the sails are made with the ability to change the angle of attack using a movable thread. To determine the critical angle of attack, the aerodynamic forces of the sail blade were investigated at different angles of attack 0°; 15°; 30°; 45°; 60°; 75°; 90°. From the data analysis, it was found that the critical angle of attack is 15°, at which the value of the lift is maximum. Furthermore, at the critical angle of attack, the dependences of the lift and drag force on the air flow velocity were established, the value of which varied from 4 to 12 m/s.

Keywords: sail, wind power plant, flow speed, aerodynamic force, wind tunnel T-1-M, angle of attack.

Introduction

The wind has been used to generate electricity since the 10s-20s of the twentieth century. Although, wind energy began to develop since the 90s of the previous century by the 21st century the development acquired a significant impetus and has now accelerated.

Today, wind turbines are one of the most affordable forms of energy production without the use of fossil fuels. Wind occurs due to uneven heating of the atmosphere surrounding the planet Earth, unevenness of the earth's surface, and air movement relative to the earth's surface, mainly in the horizontal direction. Therefore, the wind is found in all areas of the Earth. The wind generators' first prototype was windmills, which convert wind energy into mechanical energy. With the invention of electric machines, it was possible to convert wind energy into electrical energy.

Wind generators do not require additional costs after their installation if not taking into account the failure of power equipment and breakdowns in the mechanical links of the wind generator. Concerning the environmental aspect of wind energy, the annual installation of a 500 megawatt (MW) wind farm capable of generating 1.5 million MW of energy per hour will prevent emissions of 1.5 million tons of greenhouse gases, 12 thousand tons of sulfur oxide, 7.8 thousand tons of nitrogen oxide, 12.6 thousand tons of ash and 420 thousand tons of solid waste.

The average annual wind speed in 10% of the territory of Kazakhstan will be 6 m/s and higher, which will contribute to the better development of wind energy in the future. Wind energy potential in Kazakhstan is about 1,820 billion kWh per year [1].

The climate in Kazakhstan is favorable for the construction of wind farms due to wind corridors with a wind speed of more than 5 m/s, which is necessary for the operation of wind turbines [2].

The main important part of the wind turbine is a blade. The blades of a wind generator are a complex and basic element of the device, which determines its technical parameters, the possibility of installation in one place or another, and its geometric dimensions [3].

The wind affects the blades of the generator and this force, or in other words thrust, acts in the direction of the air flow. In turn, a lifting force acts perpendicular to the thrust force, which is exactly what works in wind generators with a horizontal axis of rotation.

In [4], the drag force values were determined as a function of various parameters. A distinctive feature is that the sail blades have small geometric dimensions.

A known invention [5] aims to increase the windage of the blades and increase the efficiency of using wind energy.

There is also an invention [6], a method and device of Volkov's system to produce energy by the "Parachute capture" method. The method of generating electricity consists in the fact that the rotation of the wind generator blades is carried out due to the wind captured with the help of the concentrator-diffuser system installed on the rotary axis with the ability to rotate in the wind, forming a Laval nozzle in the longitudinal section, in the narrow part of which the wind wheel is installed, and provide creating a lift in the concentrator-diffuser.

The article [7] sets out the foundations of a sailing wind turbine theory. The calculation of a sail-type turbine is presented. The resistance of a blade in the form of a rectangular plate at slight bevel angles $0^\circ \leq \alpha \leq 20^\circ$ of a four-blade turbine is determined.

In article [8], the performance coefficients of the sail model and the optimal sail angle are determined based on the results of tests in a wind tunnel.

The authors of [9] provided a detailed overview of the various features of leeward sail flow, including the effect of separation bubbles and vortices at the leading edge.

The authors of this work have developed a sail-type blade of a triangular shape. The developed sail blade presented in this work was tested at speed in the range of 4-12 m/s.

The purpose of this study is to use wind turbine blades with a dynamically changing shape of surfaces, made in the form of a flexible triangular sail with a movable end, as power elements.

1. Research methodology

One of the most important aspects of understanding when learning how a sail works is understanding the acting forces.

The main aerodynamic forces that act on the sail blade during air flow are the lift and drag forces. As shown in Figure 1, these are the perpendicular forces that play a decisive role in the propeller's rotation.

The drag force F_d is the force parallel to the sail, which is essentially the force that changes the direction of the wind and pushes the propeller sideways.

The lift force F_l is the force perpendicular to the sail that provides energy forwards to the sail. Since the lift is directed forward, the wind wheel uses this force to rotate. This is precisely the energy our sailing wind turbine needs to rotate, so it is essential to figure out how to eliminate any other force or circumstance that prevents it.

The resulting force R is the total component of the aerodynamic forces affecting the sail blade when flowing around with an air stream.

Angle α is the angle of attack, that is, the angle between the jets of the undisturbed incoming flow and the chord (the straight line connecting the extreme points of the sail or fin section).

In order for a lifting force to appear on the sail blade, it should have a given profile and be located to the incoming air stream at a certain angle of attack.

Experiments show that at a certain angle of attack, the boundary layer is separated from the leeward surface of the sail, and with a further increase, an extensive vortex cavity is formed. This is accompanied by a drop in rarefaction and its redistribution along the sail chord; as a result, the lifting force of the sail drops sharply, and the drag increases.

The angle of attack that provides the maximum coefficient of the lift is called the critical angle of attack. This is also called the "stall angle of attack". Below the critical angle of attack, the lift coefficient decreases as the angle of attack decreases. Conversely, above the critical angle of attack, when the angle of attack increases, air begins to flow less smoothly along the upper surface of the profile and begins to separate from the upper surface. With an increase in the attack angle on most profiles, the point of separation of the flow from the upper surface moves from the trailing edge to the leading edge. At a critical angle of attack, the flow on the upper surface is more split and the airfoil or wing provides maximum lift. With a further increase in the angle of attack, the upper surface flow becomes more divided, and the lift coefficient further decreases.

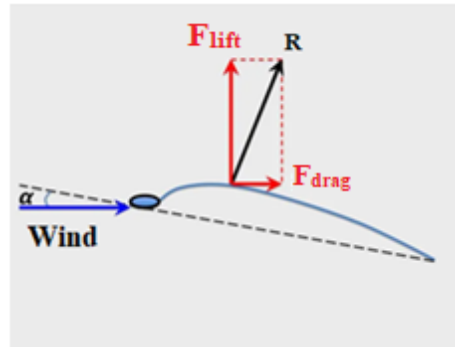


Fig. 1. Location of aerodynamic forces when air flow around the sail blade

Figure 2 shows the mechanism for influencing the air flow on the sail blade, depending on the angle of attack.

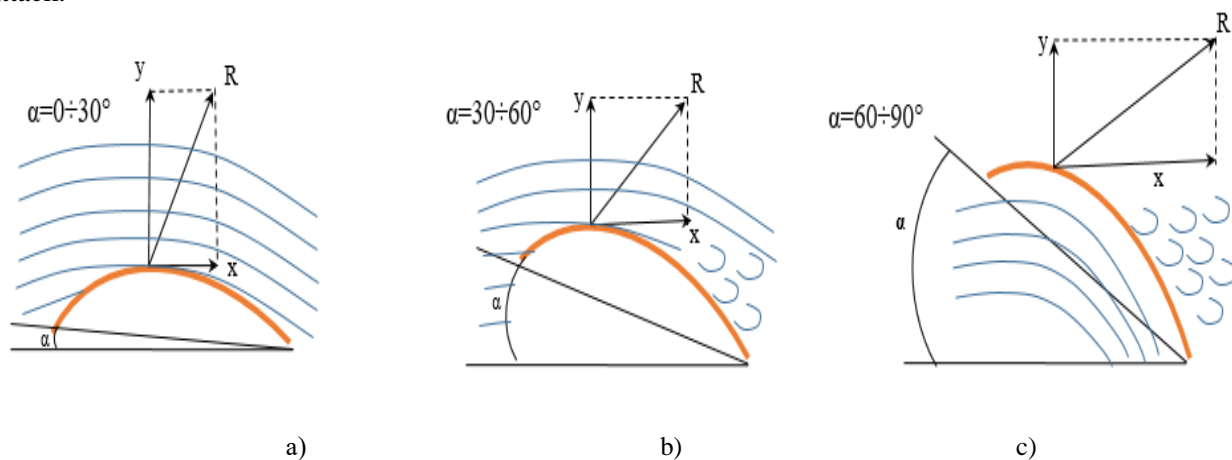


Fig. 2. The location of the sail blade relative to the angle of attack:
a) $\alpha = 0 \div 30^\circ$; b) $\alpha = 30 \div 60^\circ$; c) $\alpha = 60 \div 90^\circ$.

As could be seen from the figure, with an increase in the angle of attack from $0^\circ - 30^\circ$, the lift increases sharply, while the drag remains practically at the initial level. In the range of angles of attack of $30^\circ - 60^\circ$, the lift ceases to increase, but the drag force begins to grow strongly, and the resulting total force increases. Finally, at $60^\circ - 90^\circ$, the lift gradually disappears, and the drag increases slightly, reaching a maximum. However, the entire force tends to decrease due to the disappearance of the lifting force.

For the study of aerodynamic forces, a prototype blade with a dynamically changing shape (a sail) was created. The prototype is made of metal frame rods, the material of the triangular sail blade consists of a light and durable material (silk), one end of which is fixed to the top of the frame with a strong thread and support rods and bearing with an inner diameter of 8 mm. Fixed to the rack with support rods.

Several prototypes of elastic, lightweight, and durable blades were tested to create an actual wind turbine design with sailing blades. The material is polyester with a high density, also has a large roughness of the streamlined surfaces. The elasticity and lightness of the raincoat fabric material provide surface flexibility that lends itself well to fluctuations in the air flow, which reduces its resistance. An estimated comparison of the resistance of a solid triangular plate of a similar area showed significantly greater resistance than that of a movable, self-regulating triangular sail shape.

A sail blade differs from other blades in that the sails are made with the ability to change the angle of attack. Figure 3 shows a prototype of a dynamically variable blade shape.

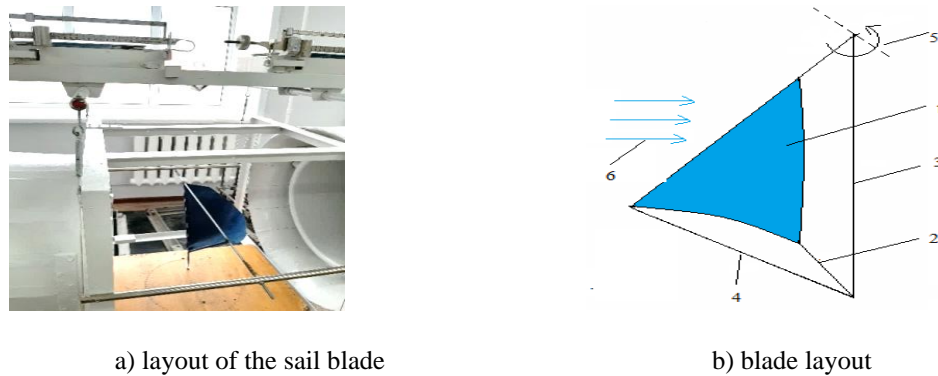


Fig. 3. Laboratory layout of a sail blade with dynamically variable form:
1 - wind turbine blade with a dynamically variable surface shape, 2,3,4 - frame, 5 - adjustable flexible attachment of the movable end of the blade, made of solid thread, 6 - wind direction

A number of studies have been carried out to determine the aerodynamic characteristics of a prototype sailing blade with a dynamically variable shape. All experimental tests to determine aerodynamic characteristics were carried out in a T - I - M wind tunnel.

In the experiments, the laboratory sample of the blade was air flowed at different speeds. Figure 3 shows the location of the model of the blade sample in the test section of the T-1-M wind tunnel (laboratory of aerodynamic measurements). The flow velocity varied from 3 m/s to 12 m/s.

In the experiments carried out, a three-component aerodynamic balance of the mechanical type was used, Figure 1.

The main units found in all designs of aerodynamic scales are: 1) a supporting device that connects the model installed in the flow to the scales; 2) a system of decomposition of the forces and moments perceived by the model into their components; 3) weighing elements for reading measured values; 4) a device for changing the angles of attack and sliding of the model.

The accuracy of determining the aerodynamic coefficients significantly depends on the suspension's design. Therefore, for greater accuracy of measurements made on balance, the design of the supporting devices must meet two conditions:

- 1) the aerodynamic forces acting on them (primarily the frontal resistance force) should be small compared to the forces acting on the tested model;
- 2) it should distort the incident flow around the model less.

2. Research results

To determine the critical angle of attack, measurements were made of the lift and drag force of the reduced size sail blade on the wind speed.

Figure 4 shows a graph of the drag force dependences and the lift force on the angles of attack of the sail blade at 12 m/s.

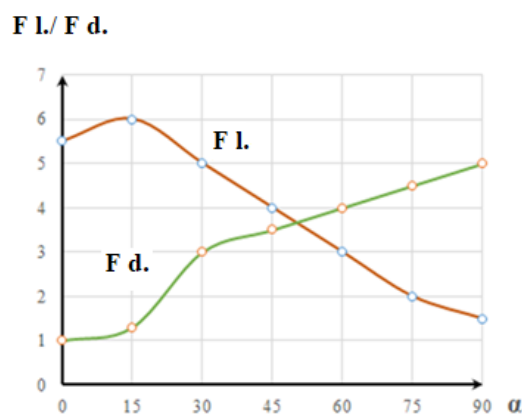


Fig. 4. Dependence of the aerodynamic forces of the sail blade on the angle of attack at 12 m/s.

As could be seen from the figure, with an increase in the angle of attack, the sail blade flows around smoothly, the vacuum on the leeward side of the blade increases, and the zone of increased pressure extends from the point of complete deceleration to the entire lower surface of the sail. As a result, the lifting force rises to 6 N.

With an increase in the lifting force, the drag also increases, determined by the frictional force in the boundary layer and the pressure force generated by the pressure difference in front of the sail and behind it. The stream flowing around the sail deflects downward. The greater the angle of attack, the greater the flow deviation. With an increase in the angle of attack to 90° , the boundary layer grows and turbulizes, and the flow begins to stall from the surface of the sail blade. The lift starts to decrease and then drops sharply due to the intense stalling of the flow at an attack angle from 15° to 90° .

At an angle of attack of 15° , the sail blade has a maximum lifting force; therefore, this angle of attack is critical for the sail blade. As the critical angle of attack approaches, the increase in drag accelerates due to the incipient flow stall.

Figures 5 and 6 show the aerodynamic forces at the critical angle of attack of the sail blade.

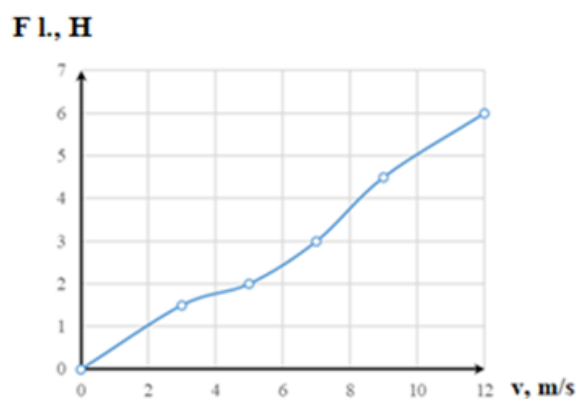


Fig. 5. Graph of the dependence of lift on air velocity

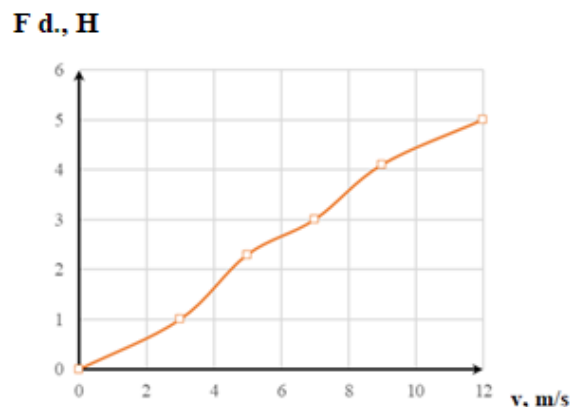


Fig. 6. Graph of the dependence of the drag force on the air flow rate

The obtained dependences show the proportional dependence of the lift force and the drag force of the blades on the flow velocity. The maximum lifting force at an angle of attack of 15° is 6 N., and the maximum drag force is about 5 N.

Conclusion

Based on experimental studies of the aerodynamic forces of a triangular blade of a wind turbine for low wind speeds, the following optimal results were obtained:

- it has been established that the critical angle of attack for a triangular sail blade is $0 \div 15^\circ$, at which the maximum value of the lifting force and the minimum value of the drag force is observed. With a further

increase in the angle of attack, the lift ceases to increase, but the drag force begins to grow strongly. This phenomenon is explained by the turbulization of the boundary layer.

- the dependences of the aerodynamic forces of the sail blade on the air flow speed at a critical angle of attack of 15° were obtained.

- it is determined that the maximum value of the lifting force at an angle of attack of 15° is 6 N., as well as the maximum value of the drag force is about 5 N.

REFERENCES

- 1 Sakipova S.E., Tanasheva N.K. Modeling aerodynamics of the wind turbine with rotating cylinders. *Eurasian Physical Technical Journal*. 2019, Vol. 16, No 1(31), pp. 88-93.
- 2 Kussaiynov K., Sakipova S.E., Kambarova Zh.T., Tanasheva N.K., et al. *Wind turbine for low wind speeds*. Patent of the Republic of Kazakhstan. No. 30829 F03D 1/00. Published December 25, 2015.[Bul.12, 3 p.] [in Russian]
- 3 Sakipova S.E., Tanasheva N.K., Minkov L.L. Modeling aerodynamics of a wind turbine with cylindrical blades in a turbulent air flow. *Eurasian Physical Technical Journal*. 2020, Vol. 17, No 1(33), pp. 106-112.
- 4 Kambarova Zh.T., Alibekova A.R., Turgunov M.M., Kussaiynov E.K., Ranova G.A. Study of the lab resistance of a triangular blade of a wind turbine for low wind speeds. *Tomsk University Bulletin. Series of mathematics and mechanics*. 2014, No. 3 (29), pp. 75-81.
- 5 Dyadchenko N.P. Wind power plant. Patent for invention. Patent number: RU 2625080 C1 Patent office: Russia. Year of publication: 2017; Application number: 2016138908; Date of registration: 03.10.2016; Date of publication: 11.07.2017.
- 6 Volkov A.E. Method and device of the Volkov system for energy production by the "Parachute capture" method. Patent for invention. Patent number: RU 2348831 C2. Year of publication: 2009.
- 7 Ershina A.K., Kaptagay G.A. The theory of sailing wind turbines. *International Journal of Applied and Fundamental Research*. 2011, No. 6, pp. 128-131. <https://applied-research.ru/ru/article/view?id=1328>
- 8 Jianhai He, Yihuai Hu, JuanJuan Tang, Shuye Xue. Research on sail aerodynamics performance and sail-assisted ship stability. *Journal of Wind Engineering and Industrial Aerodynamics*. 2015, Vol.146, pp. 81-89.
- 9 Jean-Baptiste R. G. Soupez; Abel Arredondo-Galeana; Ignazio Maria Viola. Recent Advances in Numerical and Experimental Downwind Sail Aerodynamics. *J Sailing Technol.* 4 (01): pp. 45–65. Paper Number: SNAME-JST-2019-03 <https://doi.org/10.5957/jst.2019.4.1.45>

HYDROSTATIC GENERATOR OF NON-PERIODIC PRESSURE IMPULSES FOR TESTING TECHNICAL PRODUCTS

Nizhegorodov A.I.¹, Gavrilin A.N.², Moyzes B.B.^{2*}, Ismailov G.M.³

¹Irkutsk National Research Technical University, nastromo_irkutsk@mail.ru

²National Research Tomsk Polytechnic University, Tomsk, Russia, mbb@tpu.ru

³Tomsk State Pedagogical University, Tomsk, Russia, gmismailov@rambler.ru

The article reviews the possibility of using the hydrostatic generators of oscillators with nonlinear power elements (elastic shells) as part of the structures of various test benches in the field of mechanical tests for vibration strength and vibration resistance, as well as when testing with external and internal pressure. The hydrostatic generator of non-periodic pressure impulses for engineering products testing is a new patented technical solution in the field of testing machines. The ratios of the angular velocities of the shafts, which provides the movement of the operating fluid into the actuator of the test bench in the form of a non-periodic function and with impulses varying in amplitude in a random manner were obtained. It makes a continuous and non-repetitive sequence of pressure impulses and corresponds to the operation of the tested objects in real conditions. The random nature of the amplitudes settings is provided by signals controlled from electric generators through controlled hydraulic valves. The development of a hydrostatic generator with a power element in the form of an elastic shell is represented by a hydromechanical diagram of a generator of non-periodic pressure impulses with corresponding kinematic and dynamic dependencies. In addition, there were developed three hydro-mechanical systems with the use of a new hydrostatic generator for engineering products testing both for mechanical random vibration and for testing the external and internal pressure of engineering objects that operate in such conditions. The result of the research is the expansion of the range of systems and methods for the test processes implementation under random non-periodic force effects on various engineering objects.

Keywords: hydrostatic generator, non-periodic pressure impulses, technical products, testing.

Introduction

The vibration damage on mechanisms, hydraulic and pneumatic devices, electronic and radio relay devices, on-board computers and other mechanical and electrical devices is due to the resonance phenomena. The dynamic loads arising in this case lead to functions disorder and mechanical breakdowns of structural elements of such devices: wire breakage, leakage, short circuits, electrical contacts breakdown, breakdown of various frames, racks, brackets, etc. [1-3]. About 70% of failures of such and similar products in mechanical engineering are the results of vibration [3-10]. The use of hydrostatic generator of oscillators with nonlinear power elements (elastic shells) in the structure of testing and a number of technological machines makes it possible to implement a variety of controlled processes. Such dynamic systems are used, for example, in technological processes of vibration transportation and vibration segregation of bulk materials [1], in the systems for dynamic damping of harmful vibrations [2]. They are very promising in the field of engineering products testing for vibration strength and vibration resistance [11-13].

At present, many technical instruments and devices are being developed for various underwater technical objects, which require testing of a large number of instruments and apparatus at high external pressure with variable pulses [14-19]. This is a new application of the developed hydro-mechanical systems for mechanical effect testing, as well as external and internal variable pressure impulses [20, 21].

The purpose of the research is to synthesize a hydrostatic generator with a power element in the form of an elastic shell to create non-periodic pressure impulses for different type's machines testing.

1. Hydrostatic generator of non-periodic pressure impulses

To create non-periodic pressure pulses, there are power section and a control system in the hydrostatic generator (Fig. 1). The basis of the power section is an elastic shell 1 (high pressure hydraulic hose), clamped between the plates of the plungers 2 and screw pairs 3, and fixed in the generator housing. On one side (top), a connection fitting is inserted into it, by which the generator is connected to the hydraulic line of the

operating mechanism, and on the other (below) – a high-pressure valve 4 with a conical shut-off element, which, if necessary, provides a hermetic shut-off of the hydraulic line of the regulated pump 5. When the valve 4 is open, a given volume of operating fluid is pumped through the shell per unit time. The pump valve 5 provides adjustment of the pressure in the shell and the hydraulic system of the actuator.

Eccentrics 6 with equal eccentricities are located between the pairs of plungers. Rolling bearings 7 are placed on the surfaces of the eccentrics. With the "neutral" position of the eccentrics (see the left and right pairs of plungers), there is a minimum clearance between the ends of the plungers and the bearings, which excludes simultaneous contact of the eccentric with two plungers at once.

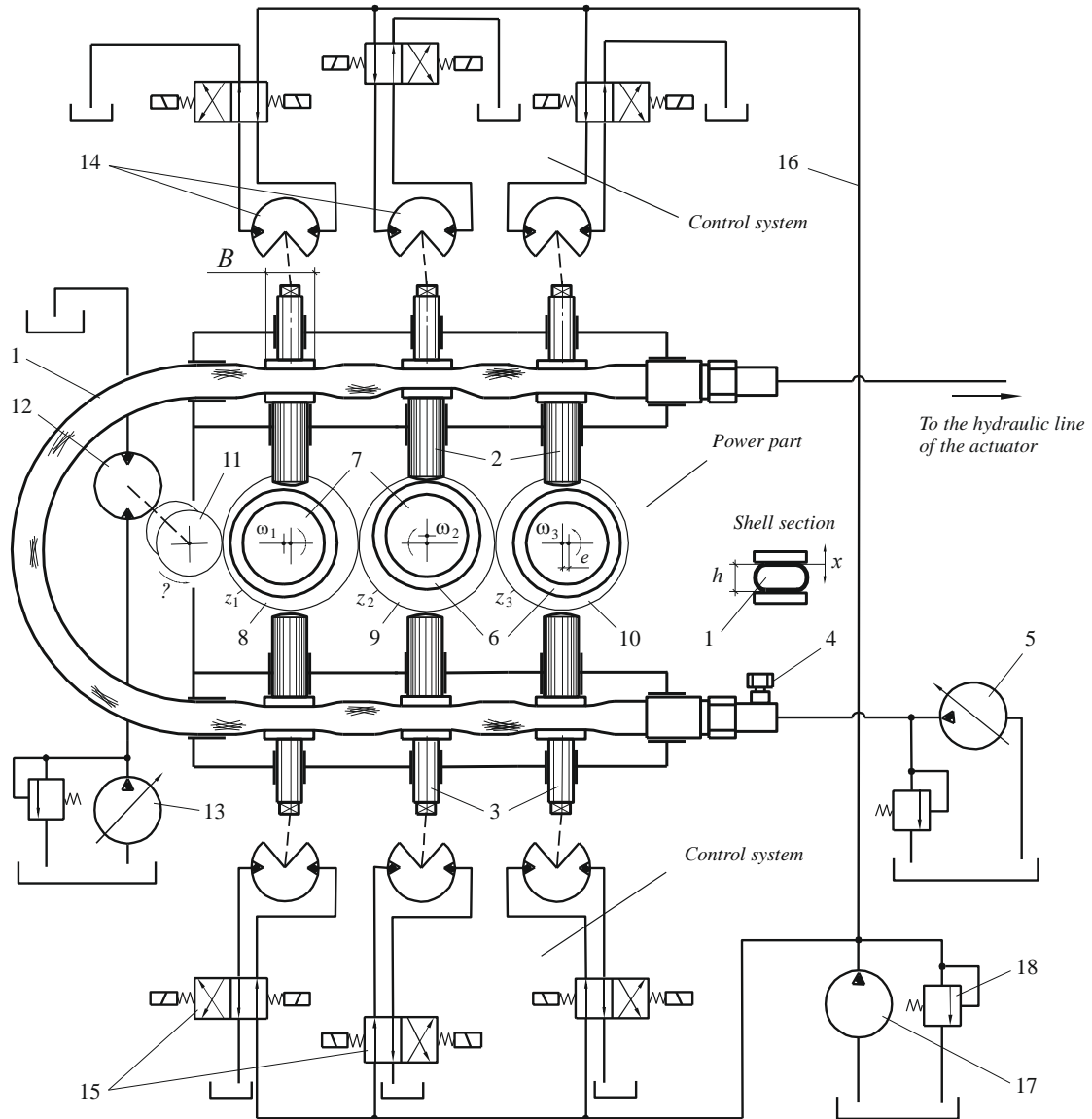


Fig.1. Hydromechanical diagram of the hydrostatic generator.

Gears 8, 9 and 10 are fixed on the eccentric shafts, which are in engaged with each other, while the ratio of the numbers of teeth of the gears 8 and 9, as well as the ratio of the numbers of teeth 9 and 10, are infinite non-periodic fractions, for example:

$$\frac{z_1}{z_2} = \frac{47}{49} \approx 0.9592 \quad (1)$$

$$\frac{z_2}{z_3} = \frac{49}{51} \approx 0.9608 \quad (2)$$

Obviously, the angular speeds of the gears will also be related

$$\frac{\omega_1}{\omega_2} = \frac{47}{49} \approx 0.9592 \quad (3)$$

$$\frac{\omega_2}{\omega_3} = \frac{49}{51} \approx 0.9608 \quad (4)$$

This is a key feature of the generator, since from the moment of its first start-up, such a relative position of the eccentrics, as shown in Fig. 1, will no longer be repeated, however, like any other of their relative position.

The drive of the eccentric gears is carried out through the drive gear 11, rotating at an angular speed ω , connected to the gear 8 and the shaft of the hydraulic motor 12. The drive gear has a flywheel on its shaft, which eliminates the pulsation of the angular velocity of rotation. The hydraulic motor 12 through the gear system provides the reciprocating movement of the plungers and the operation of the generator. The hydraulic motor is driven by a variable pump 13 equipped with a safety valve. Hydraulic systems of the generator both in the power section and in the control system are shown in a simplified manner.

The shell in each pair of plunger-screw has a preliminary compression h . Preliminary compression can be changed by turning the screws 3 in the range $h_{\max} \dots h_{\min}$ using rotary hydraulic cylinders 14. The rotary hydraulic cylinders 14 are controlled by on-off valves 15. On-off valves 15 are controlled by generators of random signals (not shown in Fig. 1). The maximum duration of the signals t income at the valve coils is due to by the time required for a complete rotation of the shaft of any of the hydraulic cylinders 14. But it can decrease randomly, like the very alternation of these signals. The operating fluid is supplied to the hydraulic line 16 from the unregulated pump 17 in such way that it is enough for the simultaneous operation of all rotary hydraulic cylinders for a time t . But such a coincidence when simultaneously all generators of random signals produce a signal with a maximum duration of t is extremely unlikely. At any arbitrary period of time, the pump flow is excessive. Therefore, it is equipped with an overflow valve 18, which transfers excess operating fluid to the tank.

Due to the abovementioned minimum clearance between the ends of the plungers and the bearings of the eccentrics, the operating stroke of each plunger (up and down) and the displacement of the liquid from the shell correspond to the rotation of the eccentric by $165 \dots 170^\circ$. Thus, if the preliminary compression of the shell h on any of the plungers does not change and has a maximum value of h_{\max} , then the minimum volume of the operating fluid w_{\min} displaced by it will be repeated with each revolution of the corresponding eccentric (Fig. 2). In this case, a pause takes place along the abscissa axis $\omega_1 t$ (upper plunger). The operating stroke of the opposite (lower) plunger is performed antiphase and there is also a pause in this movement.

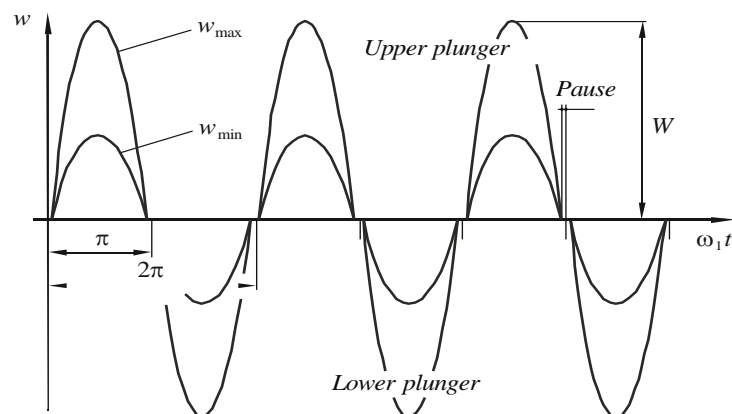


Fig. 2. Intervals between the volume impulses at different degrees of compression of the elastic shell

Thus, one period is equal to the time of one revolution of the eccentric and is a sum of four pauses t_p and the time t_d for displacing the volume w , which corresponds to one pressure impulse:

$$T = t_p + t_d,$$

but it can vary over a wide range by changing the feed of the variable pump 13, and the angular speed of rotation of the driving generator gears 11 (Fig. 1). Let us consider another key element of the hydrostatic generator. It is the ability to regulate the volume of the operating fluid displaced from the shell w by changing the upfront pressure build up h .

Let us introduce the concept of the kinematic characteristic of the elastic shell, which is the main power part of the generator of non-periodic impulses. The full volume of pump 5 (Fig.) 1 is passed through the elastic shell. The elastic shell together with the plungers, provide a non-periodic supply of volumes of operating fluid and make it possible to control their value. The kinematic characteristic is the dependence of the displaced volume w on the relative radial deformation of the shell x (see the shell section Fig. 1) without taking into account the effect of pressure.

The indicated dependence is quadratic, so omitting the intermediate formulas, we write:

$$w = a_1 x + a_2 x^2, \quad (5)$$

where a_1 and a_2 are the coefficients of the kinematic characteristics that determine the range of regulation of the amplitude W of the displaced volume (Fig. 2):

$$a_1 = \pi \cdot \left[\frac{B}{2}(d-h) + \frac{1}{4}(d-h)^2 \right], \quad (6)$$

$$a_2 = 0.25\pi \cdot (B+d-h), \quad (7)$$

where B is the length of the compressed section of the shell, d is its outer diameter, which does not change with the increasing of internal pressure, h is the preliminary compression set by screws 3 (Fig. 1).

The limits of variation of the parameter h have design constraints:

$$h_{max} = d - e, \quad (8)$$

$$h_{min} = d - 0.5d_0 + e, \quad (9)$$

where d_0 is the inner diameter of the shell.

Thus, the larger the standard size of the shell (high pressure hose), the wider the range of regulation of the amplitude W of the displaced volume. In addition, when pressure increases, the inner diameter increases as well, and this expands the h regulation range.

Moreover, only in the «neutral» (initial) state their phase positions will be equal:

$$\varphi_1 = \varphi_3 = \varphi_2 = 0,$$

and with the beginning of rotation, the phase relations will change and during a very long time interval t the ratio of the current values:

$$\frac{\varphi_1(t)}{\varphi_2(t)} = \frac{\omega_1}{\omega_2} \approx 0.9592; \quad \frac{\varphi_2(t)}{\varphi_3(t)} = \frac{\omega_2}{\omega_3} \approx 0.9608$$

remain infinite non-periodic fractions.

Obviously, time between pressure and volume impulses generated by the plungers are never exactly the same because the ratios of the angular velocities of the eccentrics are expressed in infinite periodic decimal fractions. Therefore, the total volume of liquid displaced by all plungers is a non-periodic (random) sequence of impulses. The estimated graph of the total liquid volume random time changes are shown in Figure 3. The graph shows the possible behavior of the operational liquid displaced by the plungers at one period.

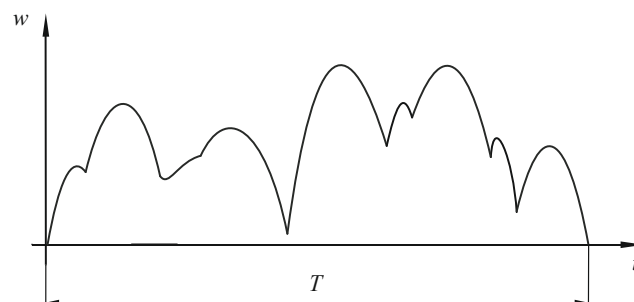


Fig. 3. Graph shows the frequency at which the volume of liquid displaced from the elastic shell of the generator of non-periodic pressure impulses

The period corresponds to the full revolution of the eccentric which rotates with the angular velocity ω_1 . In the next period, the impulse sequence will be different. Harmonic analysis of such sequences gives a continuous spectrum of harmonics, which is constantly changing in the ratio of amplitudes and frequencies over time [20].

2. The use of generator in testing machines.

A large number of failures in mechanical engineering products are caused by vibration that occurs during the operation of their own power plants, from transport vibration and other reasons. At the same time, heavy dynamic loads can lead to functional disorder of hydromechanical, pneumatic, electrohydraulic and similar devices (vibro stability loss) as well as to mechanical breakage of structural elements of such devices (vibration strength loss). Before these products will be sent into mass production, they must be tested under extreme conditions [22-28].

There are several methods to test for vibration:

- the method of gradual increase of excitation frequency;
- the method of amplitude-modulated oscillations, etc.

The best effect is given by the tests carried out in a random vibration mode [19, 20], since any technical object and its elements vibrate at a spectrum of natural frequencies resonating to the continuous spectrum of the harmonics of the exciting impulses.

Figure 4 shows a simplified hydraulic diagram of a bench for technical products testing for vibro stability and vibration strength with a hydrostatic generator of non-periodic pressure impulses 1. A hydraulic motor 2 and an adjustable pump 3 rotate its eccentrics.

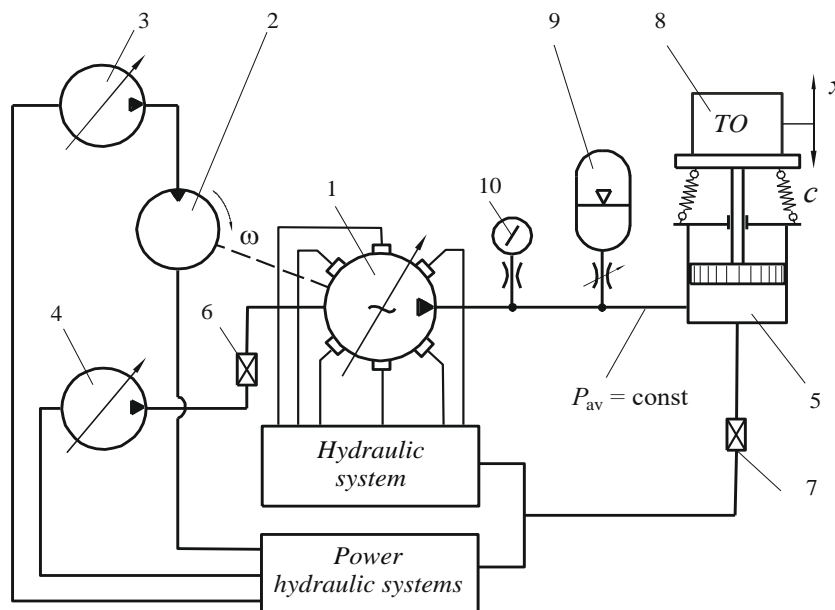


Fig.4. Hydraulic diagram of the bench for testing the technical objects

Pump 4 is designed to fill the generator, hydraulic lines connected with it and the actuator – hydraulic cylinder 5. When a set initial pressure is reached, the pump is turned off, and the hydraulic lines are closed with sealed valves 6 and 7. After starting the generator, the pressure impulses enter the piston holes and cause random oscillations of the hydraulic cylinder table. The test object 8 (TO) is fixed on the hydraulic cylinder table. The hydraulic and pneumatic accumulator 9 maintains an average pressure, compensating for leaks of the operating fluid in the rod end of the hydraulic cylinder, and the pressure gauge 10 serves to control the average pressure P_{av} .

To eliminate the influence of the impedance of the actuator moving part, its natural frequency should be beyond the frequency range covered, and the stiffness of the oscillatory system, determined mainly by the volumes of fluid contained in the both hydraulic cylinder holes:

$$c = c_{sp} + 2F_2^2 \frac{E}{W_0},$$

should be maximum (c_{sp} is the total stiffness of the springs, F is the area of the piston, E is the elastic modulus of the fluid, W_0 is the volume of fluid in the holes of the hydraulic cylinder and adjacent lines).

The volume of the piston holes of the hydraulic cylinder and the volumes of the hydraulic lines should be minimized in design, and the natural frequency of oscillations of the hydraulic cylinder table f_0 , taking into account the added mass of the test object, should exceed the upper limit of the frequency range f_{max} by at least an order of magnitude:

$$f_0 = \frac{1}{2\pi} \sqrt{\left(\frac{1}{(m + m_{TO})}\right) \cdot \left(c_{sp} + \frac{2F_2^2 E}{W_0}\right)} > 10f_{max}, \quad (10)$$

where m is the mass of the moving parts of the hydraulic cylinder, m_{ou} is the mass of the test object.

Not only mechanical vibration can lead to failures of elements of hydraulic systems of machines and equipment, but also pressure pulsation that occurs when external loads are abruptly removed from the operating equipment of machines, when occurs hydraulic shocks of various origins, with the occurrence of resonant vibrations in hydraulic devices, etc. Hydraulic jump and non-periodic sequences of pressure impulses as mechanical factors can lead to dynamic loads. They can cause not only failure of normal functioning (vibrostability loss) and even mechanical failure of such elements (vibration strength loss).

A special bench based on a hydrostatic generator of non-periodic pressure impulse which is shown in Fig.5, can be used for testing hydraulic devices, hydraulic panels, hydraulic units, as well as high-pressure hoses when loaded with pulsating pressure.

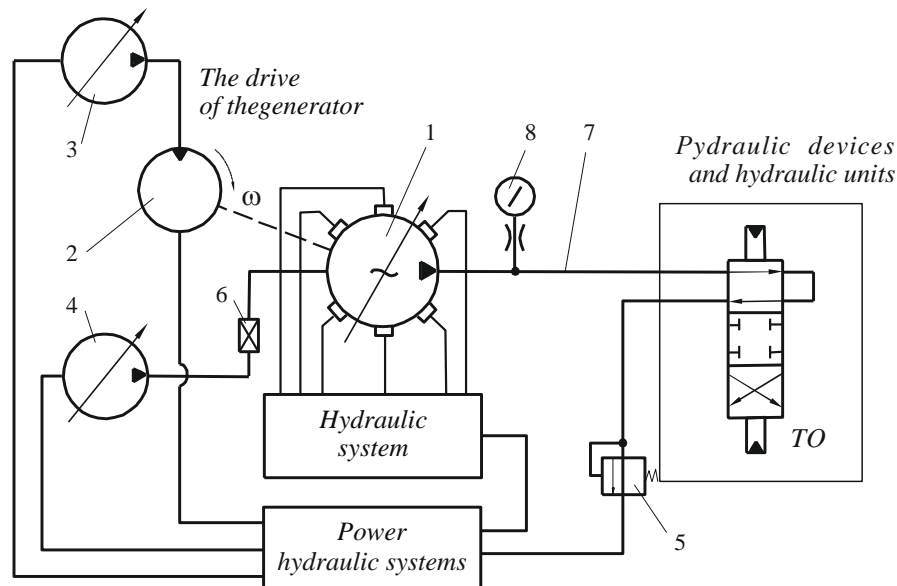


Fig.5. Hydraulic diagram of the bench for testing of the technical products by internal pressure.

Analogically to the described above test bench, the present one also operates with one main power unit that is also the hydrostatic generator 1. The generator is connected to rotary hydraulic cylinders and electrohydraulic valves are included in the hydraulic control system. The hydraulic motor 2, which is connected to the pump 3, rotates the generator eccentrics. There is a pump 4 that fills the generator, hydraulic lines and the connected test object, but it also creates a flow of operating fluid under the operating pressure of the test object created by the back-up valve 5. When valve 6 is opened, the flow of high pressure operating fluid is passed through line 7 to the technical product under test. The flow of operating fluid subjects it to a continuous sequence of non-periodic impulses. The impulses are formed during the operation of the generator. Pressure gauge 8 controls the pressure level.

During the tests, the constant operation must be provided for the hydraulic distributor, valve, hydraulic lock, or a set of elements of the hydraulic panel or valve body as an integral unit and the same ways as in normal conditions. In recent years, different equipment for submersible operation is developed and, in particular, unmanned submersible vehicles that perform many different tasks. It requires a large number of instruments and equipment – optical, lighting, speed and pressure sensors and many others, which must undergo a set of pressure tests [3, 29].

There is a bench shown in Figure 6. That bench is design to put pressure on submersible equipment on the conditions of constant sequence of non-periodic impulses. It allows to carry out dynamic tests of the mentioned submersible devices and equipment for hermiticity, strength and stability of operating parameters under conditions of chaotically changing dynamic pressure of the environment.

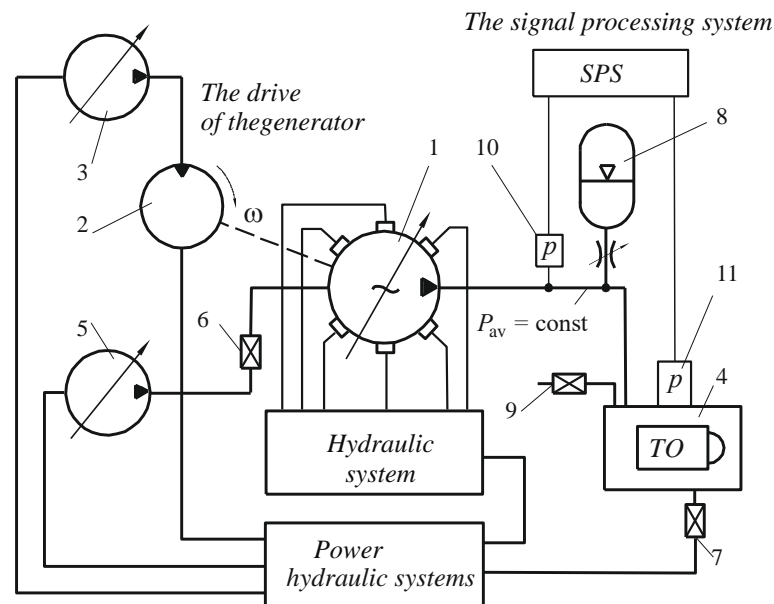


Fig.6. Hydraulic diagram of the test bench for testing technical devices by external pressure

When the eccentrics of the hydrostatic generator 1 is rotated by the hydraulic motor 2 and the pump 3, then a continuous sequence of non-periodic pressure impulses is created in the test chamber 4, where the TO test object is located, against the background of constant pressure created by the pump 5. Pump 5 pre-fills chamber 4, creating the required static pressure in it and turns off. Valves 6 and 7 provide seal the chamber, and the hydraulic and pneumatic accumulator 8 maintains a constantly maintains pressure at average value in the chamber, compensating for pressure leaks. Valve 9 is to release air when filling the test chamber. The signal processing system contains pressure sensors 10 and 11. Since the angular velocities of the eccentrics are related as infinite periodic decimal fractions (3 and 4), the phase angles of the eccentrics of the generator, figure 1 will never be equal.

The sequences of impulses generated by the plungers are added so that the total fluid volume which is compressed in the test chamber 4, figure 6 will change in the same way as shown in figure 3. If we consider the fluid elasticity modulus k (N/m^2) to be free of pressure, then a gas free fluid [30] equation will look as follow

$$k = w_0 \frac{\Delta p}{w_\Sigma}, \quad (11)$$

where w_0 is the initial fluid volume in the test chamber at the initial average pressure P_{av} , Δp is the change in dynamic pressure relative to the initial one caused by the total fluid volume w_Σ entering the test chamber.

It follows from the formula (11) that in order to achieve maximum pressure impulses, the initial volume w_0 , as well as the volume of all hydraulic lines approaching the test chamber, should be minimal. According to the signal waveform alteration passing from the sensor 10 to the measuring and processing system of vibration signal with a constant signal waveform from the pressure sensor 11 it is possible to diagnose the test object. Also it is possible to diagnose them by using spectral analysis data.

Conclusions

In the result of our work we have created a new patented technical solution in the field of testing machines - a hydrostatic generator of non-periodic pressure impulses. While creating the hydrostatic generator of non-periodic pressure impulses, we also developed an alternative concept of hydrostatic generators to generate non-periodic pressure impulses and mechanical effects in the form of random

vibration on various test objects, such as hydraulic and pneumatic devices, electronic and radio relay devices, on-board computers and other technical devices.

During the tests we have obtained the ratios of the angular velocities of the shafts, which provide the movement of the operating fluid into the actuator of the test bench in the form of a non-periodic function which impulses varying in amplitude in a random manner. It produces a continuous and non-repetitive sequence of pressure impulses and corresponds to the operation of the tested objects in real conditions. The random nature of the amplitudes settings is provided by the signals controlled from electric generators through controlled hydraulic valves. The random nature of the amplitudes settings is provided by signals controlled from electric generators through controlled hydraulic valves.

In addition, there were obtained the kinematic and dynamic dependencies for the developed hydro-mechanical systems using a new hydrostatic generator. The new hydrostatic generator is designed to test engineering objects for both mechanical random vibration and external and internal pressure tests of those objects that operate in such conditions. In our research and tests resulted the expansion of the range of systems and methods for the implementation of test processes under random non-periodic force effects on various engineering objects.

REFERENCES

- 1 Chelomej V.N. *Vibrations in technology: a handbook in 6 volumes. Vol. 4. Vibration processes and machines*. Moscow, Mashinostroenie, 1981, 509 p. [in Russian]
- 2 Gavrilin A.N., Moyzes B.B., Zharkevich O. Constructive and processing methods of reducing vibration level of the metal-working machinery elements. *Journal of Vibroengineering*. 2015, Vol. 17, No. 7, pp. 3496–3504.
- 3 Klyuev V.V. *Test equipment: reference book*. Moscow, Mashinostroenie, 1982, 560 p. [in Russian]
- 4 Surzhikov A.P., Frangulyan T.S., Ghyngazov S.A. A thermoanalysis of phase transformations and linear shrinkage kinetics of ceramics made from ultrafine plasmochemical $ZrO_2(Y)-Al_2O_3$ powders. *Journal of Thermal Analysis and Calorimetry*. 2014, Vol. 115, No. 2, pp. 1439-1445. doi:10.1007/s10973-013-3455-y.
- 5 Surzhikov A.P., Pritulov A.M., Lysenko E.N., Sokolovskii A.N., Vlasov V.A., Vasendina E.A. Influence of solid-phase ferritization method on phase composition of lithium-zinc ferrites with various concentration of zinc. *Journal of Thermal Analysis and Calorimetry*. 2012, Vol. 109, No. 1, pp. 63-67. doi:10.1007/s10973-011-1366-3.
- 6 Adam S.A., Abdul Jalil N.A., Rezali K.A. Md., Ngb Y.G., Sound and Vibration Research Group. The effect of posture and vibration magnitude on the vertical vibration transmissibility of tractor suspension system. *International Journal of Industrial Ergonomics SO*. 2020, Article No. 103014. doi: <https://doi.org/10.1016/3.ergon.2020.103014>.
- 7 Adams M. *Rotating Machinery Vibration: From Analysis to Troubleshooting*. Boca Raton, 2009, 476 p.
- 8 Halit E. *Acceleration, Vibration, and Shock Measurement*. Abingdon, CRC Press LLC, 1999, 33 p.
- 9 Goinaraghi F., Kuo B. *Automatic Control Systems*. New York City, McGraw-Hill Education, 2017, 1160 p.
- 10 Steinwolf A. Random Vibration Testing beyond PSD Limitations. *Sound & vibration*, 2006, Vol. 40, pp. 12-21.
- 11 Nizhegorodov A.I., Gavrilin A.N., Moyzes B.B. Hydraulic power of vibration test stand with vibration generator based on switching device. *Key Engineering Materials*. 2015, Vol. 685, pp. 320-325.
- 12 Ahirrao N.S., Bhosle S.P., Nehete D.V. Dynamics and Vibration Measurements in Engines. *Procedia Manufacturing*, 2018, Vol. 20, pp. 434-439. doi: 10.1016/j.promfg.2018.02.063.
- 13 Czichos H. *Handbook of Technical Diagnostics. Fundamentals and Application to Structures and Systems*. Berlin, Springer Verlag Berlin Heidelberg, 565 p.
- 14 Ahirrao, N.S., Bhosle, S.P., Nehete, D.V. Dynamics and Vibration Measurements in Engines. *Procedia Manufacturing*. 2018, Vol. 20, pp. 434-439. doi: 10.1016/j.promfg.2018.02.063.
- 15 Forental, V.I., Forental, M.V., Nazarov, F.M. Investigation of dynamic characteristics of the hydraulic drive with proportional control. *Procedia Engineering*. 2015, Vol. 129, pp. 695-701. doi: 10.1016/j.proeng.2015.12.093.
- 16 Li L., Huang H., Zhao F., Liu Z. Operation scheduling of multi-hydraulic press system for energy consumption reduction. *Journal of Cleaner Production*. 2017, Vol. 165, pp. 1407-1419. doi: 10.1016/j.jclepro.2017.07.158.
- 17 Seimert, M., Gühmann, C. Vibration based diagnostic of cracks in hybrid ball bearings. *Measurement: Journal of the Intern.Measurement Confederation*. 2017, Vol. 108, pp. 201-206. doi: 10.1016/j.measurement.2017.03.001
- 18 Harris, C., Piersol, A. *Harris' Shock and Vibration Handbook*. (New York: McGraw-Hill Professional).
- 19 Guoqing Jiang, Yu Wang, Fengming Li, Xingjian Jing. An integrated nonlinear passive vibration control system and its vibration reduction properties. *Journal of Sound and Vibration*. 2021, Vol. 509, Article 116231.
- 20 Tyablikov Yu.E., Karamyshkin V.V., Frolov K.V. Features of the interaction of an oscillatory system of a given structure with an energy source. *Elastic and hydroelastic vibrations of machine elements and structures*. 1979, pp. 15-21. [in Russian]

-
- 21 Krasilnikov A.V. *Assembly and testing of units and systems of robotic marine technical equipment*. Saint-Petersburg, Saint-Petersburg institute of precision mechanics and Optics, 2013, 152 p. [in Russian]
- 22 Wang J., Qin H., Chen Y. Energy performance evaluation of an innovative hydrostatic motor. *Renewable Energy*. 2013, Vol. 57, pp. 197-505. doi:10.1016/j.renene.2013.01.059.
- 23 Schulte H., Gerland P. Observer-based estimation of pressure signals in hydrostatic transmissions. *IFAC Proceedings*. 2010, Vol. 43, No. 7, pp. 425-430. doi:10.3182/20100712-3-DE-2013.00053.
- 24 Delmas H., Ngoc Tuan Le, Barthe L., Julcour-Lebigue C. Optimization of hydrostatic pressure at varied sonication conditions - power density, intensity, very low frequency - for isothermal ultrasonic sludge treatment. *Ultrasonics Sonochemistry*, 2015, Vol. 25, pp. 51-59. doi:10.1016/j.ultsonch.2014.08.011.
- 25 Shamshirband S., Dalibor Petkovic D., Amini A. et al. Support vector regression methodology for wind turbine reaction torque prediction with power-split hydrostatic continuous variable transmission. *Energy*, 2017, Vol. 67, pp. 623-630. doi:10.1016/j.energy.2014.01.111.
- 26 Nizhegorodov, A.I., Gavrilin, A.N., Moyzes, B.B., Cherkasov, A.I., Zharkevich, O.M., Zhetessova, G.S., Savelyeva, N.A. Radial-piston pump for drive of test machines. *IOP Conference Series: Materials Science and Engineering*. 2018, Vol. 289, No. 1, art. no. 012014. doi: 10.1088/1757-899X/289/1/012014.
- 27 Gavrilin, A.N., Chuprin, E.A., Moyzes, B.B., Halabuzar, E.A. Land-based sources of seismic signals. *Proceedings of 2014 International Conference on Mechanical Engineering, Automation and Control Systems, MEACS 2014*, 2014, art. no. 6986947. doi: 10.1109/MEACS.2014.6986947.
- 28 Youhong Sun, Yuanling Shi, Qingyan Wang, A Ei, Zongwei Yao. Study on speed characteristics of hydraulic top drive under fluctuating load. *Journal of Petroleum Science and Engineering*. 2018, Vol. 167, pp. 277-286.
- 29 Pavlov A.I., Polyanin I.A., Kozlov K.E. Improving the Reliability of Hydraulic Drives Components. *Procedia Engineering*, 2017, Vol. 206, pp. 1629-1635. doi:10.1016/j.proeng.2017.10.689.
- 30 Prokofiev V.N. *Mechanical engineering hydraulic drive*. Moscow, Mashinostroenie, 1978, 495 p. [in Russian]

CONTROL OF STARTING MODES OF AN APRON CONVEYOR MULTI-MOTOR ELECTRIC DRIVE

Kelisbekov A.K.^{1*}, Daniyarov N.A.², Akhmetbekova A.M.¹, Orazbayev K.N.³

¹O.A. Baikonurov Zhezkazgan University, Zhezkazgan, Kazakhstan, akelisbekov@mail.ru

²Kazakhmys Corporation” LLP, Karaganda, Kazakhstan

³I. Razzakov Kyrgyz State Technical University, Bishkek, Kyrgyzstan

The practice of operating an apron conveyor at mining enterprises has shown that, due to their design features, they can be successfully applied in various industries for transporting a wide range of goods. Starting a multi-drive chain conveyor of large length is a rather difficult task, since this process can be accompanied by excessive relaxation of the traction body. Especially unfavorable are the conditions for starting an apron conveyor, the belt of which has sagging sections, as a result of which the rigidity of the working body, which is a function of its tension and load on it, is relatively small. In this regard, ensuring a smooth start of a multi-motor chain conveyor is an important practical task and is undoubtedly relevant for managing and maintaining a workable dynamic state of the main an apron conveyor structure operated in difficult mining and geological conditions. A method of controlling the starting mode of a multi-motor electric drive operation of an apron conveyor to ensure its smooth start and to reduce dynamic loads, to increase the service life of the traction belt and to reduce maintenance costs was developed.

Keywords: an apron conveyor, multi-motor electric drive, start-up mode control, smooth start-up.

Introduction

The operation of a conveyor is known to be characterized by a certain sequence of technological processes: start-up, motor, steady-state, emergency and braking modes. At the same time, ensuring a smooth start-up of a multi-motor apron conveyor is of great practical importance and is undoubtedly relevant for the control and maintenance of an efficient static and dynamic state of the main an apron conveyor structure operated in complicated mining and geological conditions [1-4]. When operating long main apron conveyors, there are used multi-motor designs. With a reloading-free scheme of transporting the rock mass, due to the presence of a large number of intermediate drives in apron conveyor, it is necessary to solve the problems of controlling the starting modes of multi-motor electric drives operation and automatic distribution of the total load between its drives [5-7].

Purpose of work is development of a method to controlling the starting modes of the multi-motor electric drive of an apron conveyor operation by means of a frequency-controlled electric drive.

1 Analyzing the problems and features of the starting mode of multi-drive an apron conveyor operation

The studied experience of operating multi-drive chain conveyors shows that a high efficiency of their use is possible provided that conveyors are equipped with systems and tools of automatic distribution of the conveyor total load between its drives, regulating the speed of the conveyor belt, eliminating the equalizing forces in the traction circuit of the conveyor, and a number of other factors.

It is known that starting a long multi-drive an apron conveyor is a rather difficult task, since this process can be accompanied by excessive relaxation of the traction element. The conditions for starting an apron conveyor, which belt has sagging sections are especially unfavorable, and the working body rigidity that depends on its tension and the load on it, is relatively small. It is also known that in chain conveyors there are kinematic gaps between the individual links of the mechanism and slacks in the traction chains, etc. The presence of slacks, gaps, as well as the elastic properties of the traction-bearing body causes significant mechanical stresses in the parts of the conveyor when starting electric drives. These overloads often reach high values with which one or another part of the conveyor fails [8]. The processes taking place in this case

are very complex and oscillatory in nature. It should be noted that decreasing dynamic overloads in the drive elements and the traction-bearing body of the chain conveyor during start-up can be achieved in practice by reducing the reduced kinematic clearance of the mechanism and the initial starting torque of the electric drive. The initial value of the reduced kinematic clearance is determined by the manufacturing technology of the conveyor elements and increases with the service life due to wear. In this regard, the most effective way to reduce mechanical stresses is to lower artificially the initial motor torque to values that are lower than the resistance torque. This engine torque is called preliminary. When switched on with a preliminary torque, only the kinematic clearance and slack in the conveyor traction chain are taken up.

It is known that for unregulated asynchronous electric drives of mining machines including conveyors, starting modes are the most difficult. They are characterized by large starting currents that are many times higher than the nominal values and fluctuations in the starting torque [9 - 11]. This is, on the one hand, the cause of overheating the windings of the electric motor and decreasing its resource, and on the other hand, it leads to overloads in the gearboxes and in the chain traction unit. Large inrush currents also have a negative effect on electrical networks leading to unacceptable voltage drops [12 - 14]. In connection with the above-said, in this work there are considered the existing technical solutions for starting multi-motor chain conveyors, their features are analyzed and their advantages and disadvantages are identified.

2 Development a of controlling the multi-motorelectric drive of the apron conveyor starting method

For multi-drive conveyors, the solution to the start-up problem is very complicated, since in the presence of intermediate drives, control of the initial tension of the traction element is possible only when a tensioner is placed at each drive, which is constructively feasible but difficult.

There is a known method of tensioning the traction body of a multi-drive conveyor that is characterized by fixing the traction body at the tensioning station, turning on the drive of the tensioning station and sequential tensioning the sections of the traction body between the drives of the traction body by braking the initial part of each section and, then, moving the end part of this section with the following fixing. It differs in that in order to increase reliability of the traction body due to its optimal tension, the tension of the sections of the traction body between the drives is carried out by simultaneous turning on all the drives of the traction body and subsequent sequential braking the drives of the traction body, starting from the first drive of the traction body along the way of its movements [15].

It should be noted that the proposed method considers only preliminary tension of the traction element using an electric drive and a hydraulic tensioning station before starting the conveyor, without acceleration and reaching the nominal rotation speed of the conveyor electric drive. The performance of the take-up station when operating at low ambient temperatures deteriorates, which in general reduces reliability of the conveyor drive. There is also known a method of smooth starting a multi-motor electric drive of an apron conveyor that is based on measuring the load currents and isolating their active components, as well as in controlling the drives during the start-up process. At this in the process of starting the multi-motor electric drive of an apron conveyor, at the initial start-up moment, the minimum rotation frequency of the conveyor electric drives is set, and with intense increasing the active component of the master drive load current, the reference for the rotation speed of the master and slave drives is increased to the nominal value [16].

This article describes a method of smooth starting a two-drive apron conveyor without braking the tail driven electric drive, which does not fully ensure the working branch tension of the traction-bearing body of an apron conveyor. Based on the analysis and identification of the above solution shortcomings, there has been proposed a technical solution that can be used to control an interconnected four-motor electric drive when starting an apron conveyor. The task of the proposed method is to provide control of the interconnected multi-motor electric drive of an apron conveyor in starting modes, taking into account elastic properties of the traction-bearing body, and the technical result is to increase reliability of an apron conveyor operation by reducing the dynamic loads on the traction-bearing body in starting modes and increasing its resource.

The essence of the technical solution consists in the method of controlling a multi-motor electric drive of an apron conveyor in starting modes that is interconnected through an elastic traction element based on measuring load currents and isolating their active components. It differs in that, in the process of starting an interconnected multi-motor electric drive of an apron conveyor, the working branch of the traction element is pretensioned in each section by a corresponding electric drive, for which at the initial moment of start-up the last, fourth slave conveyor drive is slowed down. Then, in the following sequence, there is started the third

intermediate electric drive, the second intermediate electric drive and then the first master electric drive. They, in their respective sections at the minimum speed movements extend the working branch of the traction-carrying body. When the branch tension in all the sections reaches the design value, as evidenced by increasing the consumed load current of the first, second and third electric drives, the corresponding electric motors synchronously, with the same acceleration, increase the rotation speed of all the drives to the nominal value [17]. On the basis of this proposed method of controlling the starting mode of operation, a mathematical description has been developed that describes the dynamics of this technological mode of operation.

3 Mathematical description of a four-drive an apron conveyor in the starting mode of operation

The multi-drive apron conveyor is started at the creeping speed until the moment of acceleration. The proposed scheme for starting a four-drive apron conveyor is shown in Figure 1. The fourth slave electric drive is in the decelerated state.

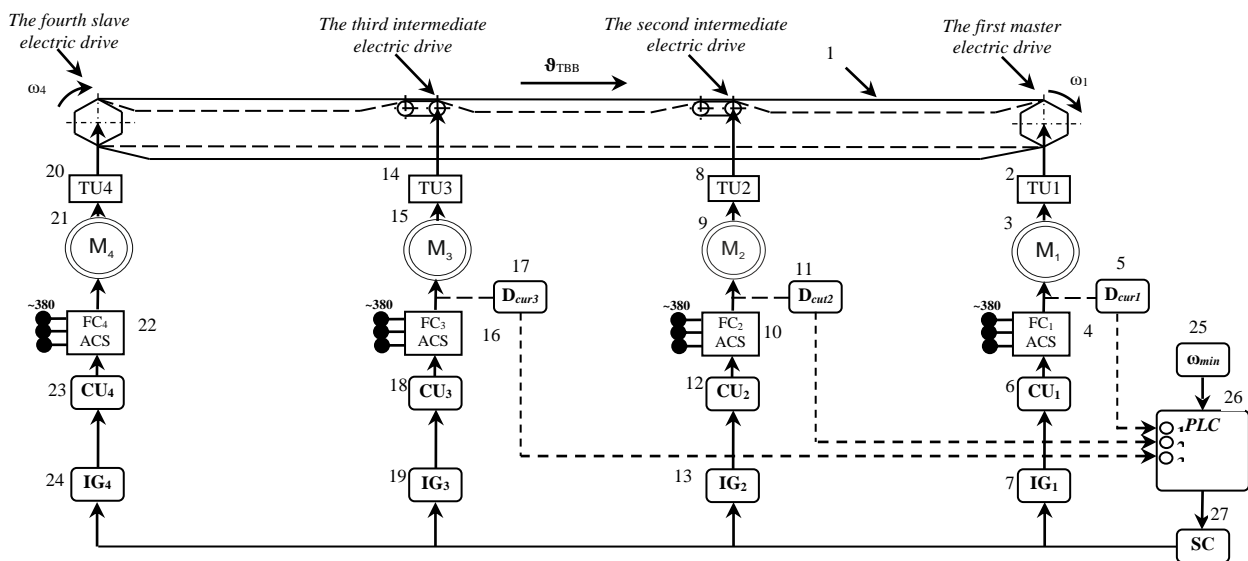


Fig.1. Block diagram of a frequency-controlled multi-motor electric drive with a smooth start system for an apron conveyor

The first master, the second slave intermediate and the third slave intermediate electric drives smoothly pull out the slack of the traction chain until the upper branch of the traction carrier is fully drawn, which will be evidenced by the actuation of all the three current sensors.

The mathematical description of the initial moment of starting a multi-drive (four-drive) an apron conveyor is represented by the following equations:

$$J_1 \frac{d\omega_1}{dt} = M_{AM1} - M_{c1} \quad (1)$$

$$J_2 \frac{d\omega_2}{dt} = M_{AM2} - M_{c2} \quad (2)$$

$$J_3 \frac{d\omega_3}{dt} = M_{AM3} - M_{c3} \quad (3)$$

where

J_1 is the moment of inertia of the first electric drive;

J_2 is the moment of inertia of the second electric drive;

J_3 is the moment of inertia of the third electric drive;

ω_1, ω_2 are the angular speeds of rotation of the first and second electric drives, respectively;

ω_3 is the angular speed of rotation of the third electric drive rotor;

M_{AM1} is the electromagnetic moment of the first master electric motor;

M_{c1} is the static moment reduced to the first motor shaft;

M_{AM2} is the electromagnetic moment of the second slave motor;

M_{c2} is the static moment reduced to the second motor shaft;

M_{AM3} is the electromagnetic moment to the third slave motor;

M_{c3} is the static moment reduced to the third motor shaft.

At the initial moment of starting the 1st, the 2nd, and 3rd asynchronous electric motors, the working body (chain) is drawn out, so, there is no elasticity at the moment. In this regard, the fourth electric drive is restrained, so, $\omega_4 = 0$. After full drawing the working branch of the traction-bearing body from the controller PLC through the corresponding control units, a signal is sent to accelerate all the four electric drives to the rated rotation speed. This moment of acceleration of electric drives is represented by the following system of equations:

$$J_1 \frac{d\omega_1}{dt} = M_{AM1} - M_{c1} - M_l - c_1 \int (\omega_1 - \omega_2) dt + c_1 \int (\omega_4 - \omega_1) dt, \quad (4)$$

$$J_2 \frac{d\omega_2}{dt} = M_{AM2} - M_{c2} - M_l + c_2 \int (\omega_2 - \omega_1) dt + c_2 \int (\omega_2 - \omega_3) dt, \quad (5)$$

$$J_3 \frac{d\omega_3}{dt} = M_{AM3} - M_{c3} - M_l + c_3 \int (\omega_3 - \omega_2) dt + c_3 \int (\omega_3 - \omega_4) dt, \quad (6)$$

$$J_4 \frac{d\omega_4}{dt} = M_{AM4} - M_{c4} + c_4 \int (\omega_4 - \omega_1) dt + c_4 \int (\omega_4 - \omega_3) dt \quad (7)$$

where

c_1, c_2 are the rigidity factors of the 1st and the 2nd electric drives, respectively;

c_3, c_4 are the rigidity factors of the 3rd and the 4th electric drives, respectively;

J_4 is the moment of inertia of the 4th electric drive;

ω_4 is the angular speed of rotation of the 4th electric drive rotor;

M_{AM4} is the electromagnetic moment of the 4th slave motor;

M_{c4} is the static moment reduce to the 4th drive shaft;

M_l is the moment of resistance from the load.

The proposed block diagram of a frequency-controlled multi-motor electric drive with a smooth starting system for apron conveyor can be implemented as follows and includes standard units. The traction-bearing body of an apron conveyor 1 is a load-bearing belt made of steel plates attached to the chain traction body, while the first transfer unit (TU1) 2, the second transfer unit (TU2) 8, the third transfer unit (TU3) 14, the fourth transfer unit (TU4) 20 are made in the form of standard helical gearboxes.

The first electric motor 3 of the first master electric drive, the second electric motor 9 of the second intermediate electric drive, the third electric motor 15 of the third intermediate electric drive and the fourth electric motor 21 of the fourth slave electric drive are asynchronous electric motors with a squirrel-cage rotor. The first current sensor 5, the second current sensor 11 and the third current sensor 17 are standard sensors that measure electric current consumed by the electric motor. The first frequency converter (FC₁+ACS) 4, the second frequency converter (FC₂+ACS) 10, the third frequency converter (FC₂+ACS) 16 and the fourth frequency converter (FC₄+ACS) 22 are standard converters that convert alternating voltage of the mains voltage into varying frequency of power supply of electric motors 3, 9, 15, 21, respectively. The first control unit (CU₁) 6, the second control unit (CU₂) 12, the third control unit (CU₃) 18, the fourth control unit (CU₄) 23 are standard control units for frequency converters. The first intensity generator (IG₁) 7, the second intensity generator (IG₂) 13, the third intensity generator (IG₃) 19 and the fourth intensity generator (IG₄) 24 are made in the form of standard intensity generators providing a smooth change in the output signal to the values corresponding to the set speed values. The block of setting the minimum speed 25 is performed in the form of a controlled voltage divider. The speed controller 27 is made in the form of a standard element that sets the speed, in this case, it accepts the task for the minimum speed at the initial moment of starting, and at full drawing of the working branch for accelerating the rotation of all the electric drives to the rated speed value. The PLC controller 26 is a programmable logic controller used to automate technological processes, energy, transport and other control systems.

4 Results and discussion

Based on the results of the research, an algorithm was developed for starting a four-motor electric drive of the conveyor, which can be carried out in the following order (Figure 2).

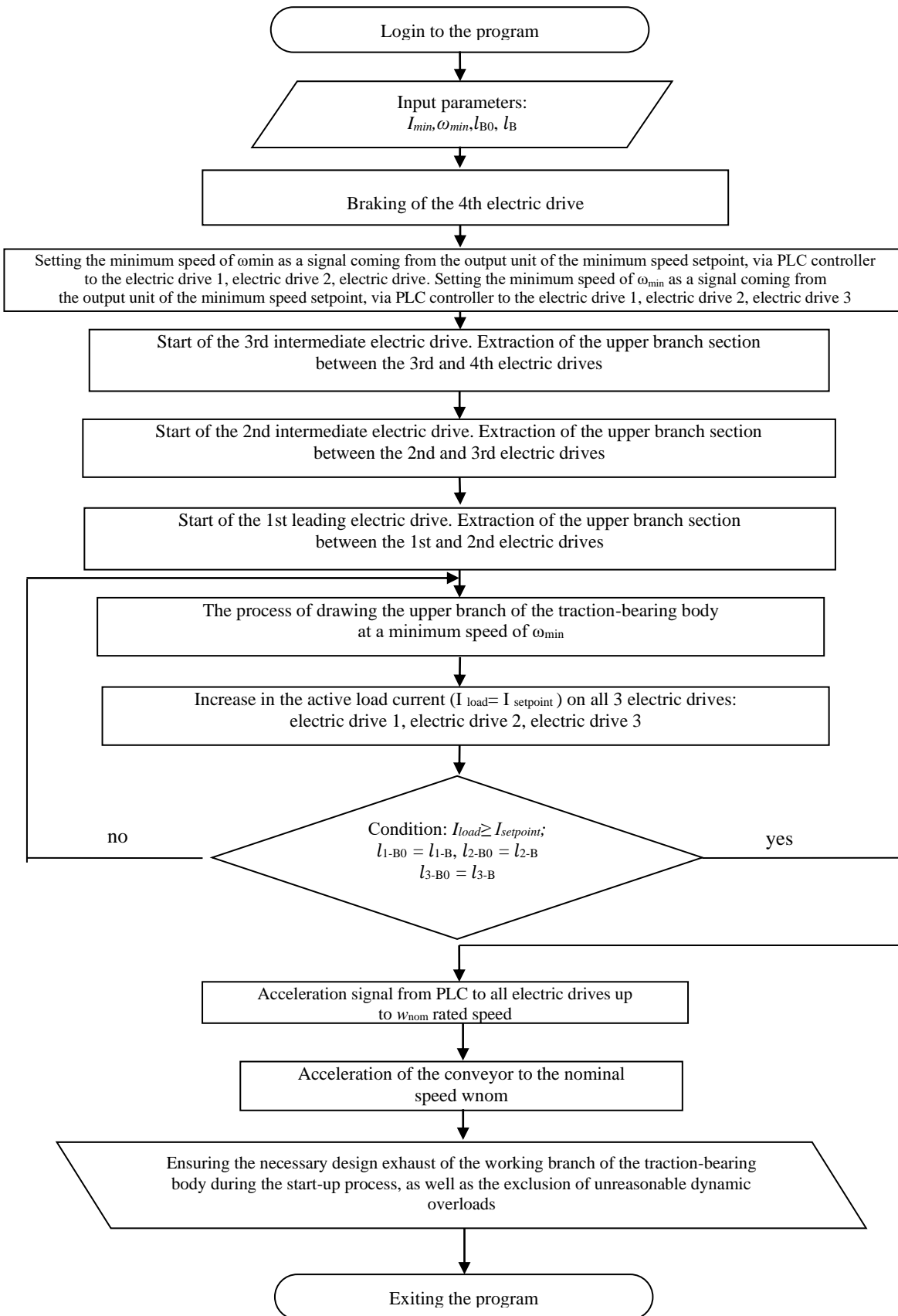


Fig.2. Block diagram of the algorithm for controlling the start of a four-motor electric drive of an apron conveyor.

At the initial moment before starting the multi-motor electric drive of apron conveyor, the fourth slave electric drive of the conveyor is fixed by braking. Then, in the following sequence, the following are started: the third intermediate electric drive, the second intermediate electric drive, the first leading electric drive and, at the minimum speed of movement, the upper working branch of the traction-bearing body 1 is extracted, while each electric drive is the corresponding sections between the fourth and third, third and second, second and first drives. The minimum rotation speed is set by a signal coming from the output of the minimum speed set point unit 25, via the PLC controller 26, the speed setter 27. The output signal of the speed setter 27 enters the inputs, respectively, of the first intensity setter 7, the second intensity setter 13, the third intensity setter 19 and provides a smooth change in speeds by setting the input of the first control unit 6, the second control unit 12, the third control unit 18 signal corresponding to the minimum frequency of the output voltage of the first frequency converter 4, the second frequency converter 10 and the third frequency converter 16. Accordingly, the driving electric motor 3, the second intermediate electric motor 9, the third intermediate electric motor 15 through the first transfer device 2, the second transfer device 8 and the third transfer device 14 begin to pull the working branch of the traction-bearing body 1.

The signal of full extraction of the working branch of the traction-bearing body 1 will be an increase in the active current consumed by the load of electric motors 3, 9, 15. Further, from the first current sensor 5, the second current sensor 11, the third current sensor 17, the signals are sent to the PLC controller 26 simultaneously or in different order depending on the amount of sagging of the working branch sections until the conveyor is started. In this case, the condition for full extraction of the working branch of the traction-bearing body 1 is the receipt of signals from all current sensors 5, 11, 17 (about an increase in the active component of the load current of the first, second and third electric motors 3,9,15) to the PLC controller 26. After that, the algorithm (recorded in the PLC controller 26) is triggered to generate an acceleration signal with the same value up to the nominal rotation speed of the interconnected multi-motor electric drive. This signal from the PLC controller 26 output goes to the speed setter 27, and then through the corresponding setters (7, 13, 19, 24), control units (6, 12, 18, 23), frequency converters (4, 10, 16, 22), asynchronous electric motors (3, 9, 15, 21), transfer devices (2, 8, 14, 20) and through the corresponding sprockets, the traction-bearing body of apron conveyor is accelerated to the nominal value.

Verification of the operation of the developed algorithm for starting a four-motor electric drive of the conveyor was previously implemented in the computer environment of the FRCONFIGURATOR2 program at the benches of the Mitsubishi Electric with a frequency converter of the FR-A800 series of the Automation of Production Processes Department of Karaganda Technical University. The frequency of the electric motor was controlled through external control devices: toggle switches STR, RH, RM, RL by switching which the starting signal was supplied. The graphs of changing the values of the output electrical characteristics of conveyor electric motors (frequency, current and voltage) obtained by the results of bench tests in on-line mode through the function "Function - Trend monitor" are shown in Figure 3.

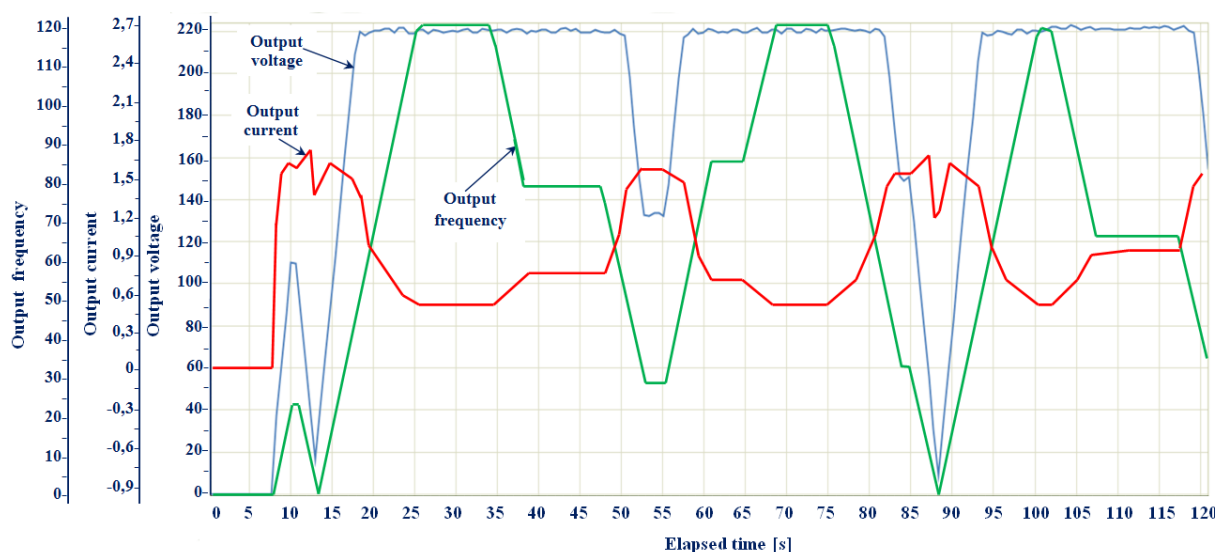


Fig.3. Dynamics of changing the characteristics of electric motors of a four-drive apron conveyor in the starting mode of operation

The analysis of the obtained graphs shows that at the initial moment of starting the conveyor, up to about 13 seconds from start-up, the main electrical characteristics of the drive (current, voltage, frequency) change the same way. Then, as the motor armature speed increases, the output voltage value increases, and the amount of consumed current changes inversely proportional to the voltage and frequency. As already noted, in the developed block diagram of the algorithm for controlling the start of a four-motor electric drive of an apron conveyor, the signals of smooth pulling of the working branch of the traction-bearing body will be periods of the stepwise increasing of the active load current of the first, second and third electric motors, as shown by the dynamics of changes in the characteristics of electric motors obtained in laboratory conditions when starting a multi-drive conveyor.

Conclusion

Thus, based on the results of comprehensive studies, the authors propose a method of controlling the starting mode of operation of an interconnected frequency-controlled four-motor electric conveyor drive based on measuring load currents and isolating their active components, which, in comparison with the existing analogues, makes it possible to achieve the necessary calculated extraction of the working branch of the traction-bearing belt during the conveyor start, which, in the authors' opinion will eliminate unreasonable static and dynamic overloads in the traction body.

The field observations of the starting modes of the KM PP 2-10-60 apron feeder operation with a Mitsubishi Electric E-700 frequency converter used to supply coal to the concentrator in the conditions of the Molodezhnaya coal mine of the Kazakhmys Coal LLP, in accordance with the conclusions of production specialists, confirmed the identity of the data obtained in laboratory conditions by computer modeling in the FRCONFIGURATOR2 environment. Accordingly, the estimated increasing of the economic efficiency from the operation of a multi-drive apron conveyor, taking into account the smooth start of its traction-bearing body, is determined by the following:

- increasing the service life of the conveyor by 1.2-1.3 times due to decreasing the dynamic and static loads on the working body of the conveyor and increasing its fatigue life;
- reducing the costs for maintenance and overhaul of the working body of the conveyor by 27-28%.

As it was noted, the developed method makes it possible to implement the necessary mode of starting the conveyor without additional equipping it with a tensioner.

Acknowledgments

The authors are appreciated and express deep gratitude to doctor of technical sciences, professor Breido I.V., who died suddenly in July 2021, for consultations and valuable advice in preparing this article.

REFERENCES

- 1 Saginov A.S., Daniyarov A.N., Akashev Z.T. *Fundamentals of design and calculation of career apron conveyors*. Alma-Ata: Nauka, 1987, 328 p. [in Russian]
- 2 Verma M., et al. Medium Voltage Adjustable Speed Drives: Power Factor and Motor Control-A Beautiful Combination. *Conference Proceedings - IEEE-IAS/PCA Cement Industry Technical Conference*, 2019, pp. 14–16.
- 3 Pajchrowski T. Comparison of control structures for direct drive with PMSM motor with variable inertia and load torque. *Przegląd Elektrotechniczny*. 2018, 94(5), pp. 133–138.
- 4 Wojcik A., Pajchrowski T. Application of iterative learning control for ripple torque compensation in PMSM drive. *Archives of Electrical Engineering* [this link is disabled](#), 2019, 68(2), pp. 309–324.
- 5 Štatkić, S., Jeftenić, I.B., Bebić, M.Z., et al. Reliability assessment of the single motor drive of the belt conveyor on Drmno open-pit mine. *International Journal of Electrical Power and Energy Systems*. 2019, 113, pp. 393-402.
- 6 Windmann S., Niggemann O., Stichweh H. Computation of energy efficient driving speeds in conveying systems. *At-Automatisierungstechnik*, 2018, 66 (4), pp. 308-319.
- 7 Świder J., Herbuś K., Szewerda K. Control of Selected Operational Parameters of the Scraper Conveyor to Improve Its Working Conditions. *Advances in Intelligent Systems and Computing*. 2019, No. 934, pp. 395-405.
- 8 Semykina I.Y., Tarnetskaya A.V. Control of energy efficient belt conveyor gearless drum-motor. *EAI Endorsed Transactions on Energy Web*. 2019, 19(22), pp 144–146.
- 9 Pajchrowski T., Wójcik A. Analysis of influence of linear regulators' structure on level of speed unevenness of PMSM direct drive. *PMSM. Przegląd Elektrotechniczny*. 2020, No. 96(7), pp. 59–67.

10 Kashirskikh V., et al. On the Issue of Increasing Reliability of Electric Mining Machinery. *E3S Web of the International Innovative Mining Symposium, IIMS*. 2020, Vol. 174, Article No. 03024, 11p. doi:10.1051/e3sconf/202017403024.

11 Semykina I.Y., Tarnetskaya A.V. Control of energy efficient belt conveyor gearless drum-motor. *EAI Endorsed Transactions on Energy Web*. 2019, Vol. 19, Issue 22, 6p. doi:10.4108/eai.13-7-2018.156435.

12 Eshchin E.K. Model of asynchronous motor in power supply system. *Russian Electrical Engineering*. 2002, Vol. 73, Issue 1, pp. 53-58.

13 Eshchin E.K. Reduction to risk of operation of systems of electro supply of coal mining equipment. *Ugol'*. 2005, Issue 9, pp. 39 – 42. [in Russian]

14 Eshchin E.K. Scraper face conveyors dynamic load control. *Journal of Mining Institute*. 2019, Vol. 239, pp. 570-575.

15 Daniyarov A.N., Akashev Z.T., Rozhkov A.V., Kuchin V.N. *A method of tensioning a traction element of a multi-drive conveyor*. Patent of USSR, No. 1312025, Publ. 05.23.1987, Bul. 19, 5 p. [in Russian]

16 Breido I.V., Kelisbekov A.K. *Method for smooth start-up of a multi-motor electric drive of an apron conveyor*. Utility model patent of the Republic of Kazakhstan.No. 3982, Publ. 05.03.2019, 4 p. [in Russian]

17 Breido I.V., Daniyarov N.A., Kelisbekov A.K. *Method of controlling the start of a multi-motor electric drive of an apron conveyor*.Utility model patent of the Republic of Kazakhstan. No. 5122. Publ.07.03.2020, 5 p. [in Russian]

DOI 10.31489/2021No4/82-87

UDC: 535-46; 537.563.3; 621.397.331.265; 544.147.2

ELLIPTICALLY POLARIZED LASER-ASSISTED ELASTIC ELECTRON-HYDROGEN ATOM COLLISION IN COULOMB POTENTIAL

Yadav K.¹, Dhobi S.H.^{2,3*}, Maharajan S.¹, Gupta S.P.¹, Karki B.⁴, Nakarmi J.J.^{1,2}¹ Department of Physics, Patan Multiple Campus, Tribhuvan University, Lalitpur-44700, Nepal,² Innovative Ghar Nepal, Lalitpur-44700, Nepal, saddam@ran.edu.np³ Robotics Academy of Nepal, Lalitpur-44700, Nepal⁴ Department of Physics, Tri-Chandra Multiple Campus, Tribhuvan University, Kathmandu-44600, Nepal

The advancement of laser technology is causing the research field of optics to become more active, and with the help of advancement of technology, more detailed information can be obtained. The primary goal of this work is to calculate differential cross section by using a mathematical model in presence of coulomb potential and elliptically polarized beam with single photon absorption. The developed model shows the differential cross section increases with wavelength and decreases with electron energy with elliptically polarized beam. The differential cross section become maximum at 1.56 radian polarized angle and minimum at -1.56 radian polarized angle. The observation is based on 1.5eV laser photon energy, laser field intensity 10^{14}Wcm^{-2} , polarized angle 1.56 radian angle, and electron energy 0 to 600eV. Using the born first approximation and the Volkov wave function, the developed equation is obtained. The numerically obtained differential cross section in this work is approximately 10^{-19}m^2 to 10^{-20}m^2 , which is less than the differential cross section obtained by Flegel et al. (2013), which is approximately 10^{-17}m^2 .

Keywords: elliptical polarization, differential cross-section, Born first approximation, Volkov wave function.

Introduction

These days, the study of electron-atom collisions in the presence of a laser beam has gotten a lot of interest. This is due to various application in disciplines of science (such as plasma heating or driven fusion) as well as in nuclear collision field. Observation of multiphoton events has become possible due to the development of powerful and adjustable lasers with relatively low light field intensities. When compared to the problems associated with field-free electron-atom scattering, the theoretical analysis of electron-atom collisions in the presence of a laser field becomes extremely complex. The study of collision in laser field introduces certain new parameters, such as laser frequency, intensity, polarization, and influence collision interactions. In interaction laser field (Photons) act as a "third body" in the universe. The existence of photons acts as a "third body" in the collision, "dressing" the atomic states [1]. For simplicity, to study the differential cross section in presence of laser field, the energy of the target atom is neglected because it does not change states during phenomena of collision but the potential is not neglected because potential replicate the electron-atom collision interaction. The simple reaction with laser-assisted elastic electron-atom scattering is given by equation (1) as,

$$e_{q_i} + A_i \rightarrow e_{q_f} + l\hbar\omega + A_i, \quad (1)$$

where A is target atom remains in its ground state during the collision while the electron exchanges l quanta with photon field ($l < 0$ for absorption and $l > 0$ for emission) to change momenta from q_i to $q_f = q_i + \hbar\omega$. The scattering equation represented in equation (1) also known as a free-free transition. The Kroll-Watson theorem [2] is one of the oldest and most reliable theoretical results in multiphoton physics. This theorem also described scattering of an electron by a potential in the presence of a low frequency linearly polarized laser field. The majority of theoretical studies of electron scattering by atoms in an intense radiation field are based on perturbation theory [3]. Kroll and Wastonon's also contribute to perturbation theory using the soft photon approximation and numbers of researchers have recently working on laser-assisted scattering more detail [4, 5].

Instead of number of difficult to observe laser-assisted electron impact atomic excitation in the presence of a strong field some of researcher is active to develop a simple model to understand the laser-assisted collision [7, 8]. The electron-target system in laser-assisted collisions, known as simultaneous electron-photon excitation (SEPE), can absorb or emit one or more photons from the laser field, causing the atom to be excited. In laser-assisted elastic and inelastic [9, 10] electron-atom collisions, the exchange of one or more photons between the electron-atom system and the laser field has been observed in several experiments. In the presence of a field, the collision can be treated in such a way that electron-field coupling is the dominant process. Mason and Newell in 1982 reported experimental evidence of atoms being excited by both electrons and photons at the same time. The majority of the experimental studies have been conducted with noble gases [11], with Abdelkader et al. [12] conducting a recent one with Nd: YAG laser. He-target and low-field laser field were tested in two states: (i) SEPE, electron energy below the excitation threshold of the metastable $2S^3$ state collide with ground state $1S^1$ and achieve excitation because laser supplies energy; and (ii) SEPE, electron energy above the excitation threshold of the metastable $2S^3$ state collide with ground state $11S$ and achieve excitation because laser supplies energy. (ii) SEPE has also been observed from higher excited states [13]. Shinha et al. [4] investigated the free-free transition for an electron-hydrogen atom system in the ground state in the presence of an external homogeneous, monochromatic, and linearly polarized laser field at very low incident energies. The incident electron is thought to be non-perturbatively dressed by the laser field by selecting Volkov solutions in both the initial and final channels. For single-photon absorption or emission in the soft photon limit, the laser intensity is much lower than the atomic field intensity, and the laser-assisted differential and total elastic cross-sections are calculated.

The hydrogen atom is one of the most basic atoms to work with and can be used to collect interesting aspects of the problem. The free-free process can be studied theoretically on several levels. The goal of this paper is to investigate the impact of various collision and laser parameters on the collision process in an elliptically polarized laser-assisted elastic electron-hydrogen atom collision. The authors attempt to develop a detailed calculation of differential cross section for laser-assisted electron-hydrogen collisions in this paper. The Volkov wave [14] is used to treat the interaction between the field and the projectile as non-perturbation. The authors focused on the elliptical polarization laser field for polarized potential. To begin, consider a collision event in which an incoming electron with momentum k_i interacts with a hydrogen atom that is initially in the state I in the presence of a single-mode laser beam and moves to the excited state j through the exchange of l photons between the electron and the laser field.

1 Theory and Method of calculation

1.1 Volkov- wave function

Consider an elastic collision at the ground state between a fast (non-relativistic) electron of mass (m) and charge ($-e$) with hydrogen as the target atom. The collision takes place in the presence of a laser field, which is assumed to be a monochromatic, single-mode, and homogeneous electromagnetic field. Therefore, the vector potential of a field propagating along the Z-axis in the Coulomb gauge is obtained as,

$$A(t) = A_0 \left\{ \hat{x} \cos(\omega t) + \hat{y} \sin(\omega t) \tan\left(\frac{\eta}{2}\right) \right\}, \quad (2)$$

where $A_0 = \frac{cE_0}{\omega}$, E_0 is the electric field and ω is frequency, η is measured the degrees of ellipticity of the field. η determine the nature of laser field as, for linear polarization ($\eta = 0$), for circular polarization ($\eta = \frac{\pi}{2}$) and for elliptical polarization ($-\frac{\pi}{2} \leq \eta \leq \frac{\pi}{2}$). The wave function of the projectile embedded in the field is given by the non-relativistic Volkov wave function

$$\chi^V(\vec{r}, t) = (2\pi)^{-3/2} \exp\left(i\vec{k} \cdot \vec{r} - \frac{i}{\hbar} \int_{-\infty}^t \left(\frac{p^2}{2m} + \frac{e}{mc} \vec{A} \cdot \vec{p}\right) dt\right) \quad (3)$$

On solving integration of equation (3),

$$\chi^V(\vec{r}, t) = (2\pi)^{-3/2} \exp\left(i\vec{k} \cdot \vec{r} - \frac{iE_k t}{\hbar} - \frac{ie}{m\omega c} \vec{A}_0(t) \left[(\hat{x} \cdot \vec{k}) \sin\omega t - (\hat{y} \cdot \vec{k}) \tan\left(\frac{\eta}{2}\right) \cos\omega t \right]\right) \quad (4)$$

Assuming, $\hat{x} \cdot \vec{k} = R \cos\gamma_k$, $(\hat{y} \cdot \vec{k}) \tan\left(\frac{\eta}{2}\right) = R \sin\gamma_k$ as $R = \frac{ie}{m\omega c} \vec{A}_0(t)$ then equation (4) becomes

$$\chi^V(\vec{r}, t) = (2\pi)^{-3/2} \exp\left(i\vec{k} \cdot \vec{r} - \frac{iE_k t}{\hbar} - R \sin(\omega t - \gamma_k)\right) \quad (5)$$

Equation (5) is the required form of the Volkov wave function with $R = \alpha_0 D_0 k$, $D_0 = \left[\cos^2 \theta + \sin^2 \theta \tan^2 \frac{\eta}{2} \right]^{1/2}$, $\tan \gamma_k = \frac{\vec{k} \cdot \hat{y}}{\vec{k} \cdot \hat{x}} \tan \left(\frac{\eta}{2} \right)$ and $\alpha_0 = \frac{eE_0}{m\omega^2}$.

1.2 Calculation of S-matrix element

The general S-matrix theory is used to study multi-photon ionization and also define T-matrix in terms of S-matrix matrix elements, i.e. transition amplitude is the S-matrix matrix elements. Kroll and Watson in 1973 developed the S-matrix formulation for a low-frequency response. This formulation was developed in the search for a non-perturbative approach hand suitable not only for free-free scattering but also for ionization, recombination, and excitation. Unlike other methods, this method does not suffer from energy loss or gain. As a result, in the case of multi-photon ionization, this method is more applicable for calculating total transition rate and differential cross-section, because total transition rate divided by incident flux gives the differential cross-section, which is proportional to the square of the transition matrix. The S-matrix element is given by

$$S = \frac{-i}{\hbar} \langle \chi_{\vec{k}_f}^* V \chi_{\vec{k}_i} \rangle \quad (6)$$

Equation (6) related transition amplitude from the momentum state \vec{k}_i to \vec{k}_f as

$$S_{k_f k_i} = \frac{-i}{\hbar} \iint_{-\infty}^t \chi_{\vec{k}_f}^* V \chi_{\vec{k}_i} d^3 r dt \quad (7)$$

Where \vec{k}_i the initial is wave vector of the particle and \vec{k}_f is the final wave vector of the scattered particle. Substituting the value of for $\chi_{\vec{k}_i}$ and $\chi_{\vec{k}_f}$ from (5) in (7) and on solving,

$$S_{k_f k_i} = \frac{-i}{\hbar} \frac{1}{(2\pi)^3} \iint_{-\infty}^t \exp[-i(\vec{k}_f - \vec{k}_i) \cdot \vec{r}] \exp \left[\frac{(E_{k_f} - E_{k_i})t}{\hbar} \right] V(\vec{r}) \exp[i(\vec{k}_f - \vec{k}_i) \alpha_0 A_0 \sin(\omega t - \gamma_k)] d^3 r dt \quad (8)$$

Let us assume $\Delta = \vec{k}_f - \vec{k}_i$ be the momentum transfer then equation (8) become

$$S_{k_f k_i} = \frac{-i}{\hbar} \hat{V}(\Delta) \int_{-\infty}^t e^{i(\Delta \alpha_0 A_0) \sin(\omega t - \gamma_k)} e^{i(E_{k_f} - E_{k_i}) \frac{t}{\hbar}} dt \quad (9)$$

where, $\hat{V}(\Delta) = \frac{1}{(2\pi)^3} \int e^{-i\Delta \cdot \vec{r}} V(\vec{r}) d^3 r$ and $V(\vec{r})$ is independent of time (t) and authors considering space integration. So that $\hat{V}(\Delta)$ can be taken outside the time integration. On using the generating function of the Bessel Polynomial is [15],

$$e^{ix \sin \phi} = \sum_{-\infty}^{\infty} J_n(x) e^{ni\phi} \quad (11)$$

where, $x = \Delta \cdot \alpha_0 D_0$ and $\phi = \omega t$ equation (11) becomes

$$e^{i\Delta \alpha_0 A_0 \sin \omega t} = \sum_{l=-\infty}^{\infty} J_l(\Delta \cdot D_0 \alpha_0) e^{il\omega t} \quad (12)$$

On substituting the value from equation (12) in equation (9) the S-matrix element becomes

$$S_{k_f k_i} = \frac{-i}{\hbar} \int_{-\infty}^t T_{k_f k_i}^l e^{i(E_{k_f} - E_{k_i} + l\hbar\omega) \frac{t}{\hbar}} dt \quad (13)$$

here $T_{k_f k_i}^l = \hat{V}(\Delta) \sum_l J_l(\Delta \cdot D_0 \alpha_0) e^{il\gamma_{k_i}}$ is the transition matrix from the momentum state k_i to k_f , and time-independent. Therefore equation (13) becomes

$$S_{k_f k_i} = \frac{-i}{\hbar} T_{k_f k_i}^l \int_{-\infty}^t e^{i(E_{k_f} - E_{k_i} + l\hbar\omega) \frac{t}{\hbar}} dt \quad (14)$$

1.3 Calculation of transition matrix and differential cross section

The relation for the differential cross section of an electron with the transfer of l photon is

$$\frac{d\sigma}{d\Omega} = \frac{m^2}{(2\pi)^2 \hbar^4} \frac{k_f}{k_i} |T_{k_f k_i}^l|^2 \quad (15)$$

On substituting the value of $T_{k_f k_i}^l$ and $\hat{V}(\Delta)$ from above in (15) we get a differential cross section for $l = 0$ (no photon transfer during scattering) as,

$$\frac{d\sigma}{d\Omega} = \frac{m^2}{(2\pi)^2 \hbar^4} \sum_l J_l^2(\Delta, D_0 \alpha_0) |\hat{V}(\Delta)|^2 \quad (16)$$

Moreover, equation (16) can be represented as

$$\left(\frac{d\sigma}{d\Omega}\right)^{\text{free-free}} = \left(\frac{d\sigma}{d\Omega}\right)^{\text{field-free}} \sum_l J_l^2(\Delta, D_0 \alpha_0) \quad (17)$$

Using sum rule $\sum_l J_l^2(\Delta, D_0 \alpha_0) = 1$ equation (17) becomes,

$$\left(\frac{d\sigma}{d\Omega}\right)^{\text{free-free}} = \left(\frac{d\sigma}{d\Omega}\right)^{\text{field-free}} \quad (18)$$

Thus, in this limit free-free differential cross section is equal to the differential cross section in the absence of the laser field. As we have

$$|T_{k_f k_i}^l|^2 = \sum_l J_l^2(\Delta, D_0 \alpha_0) |\hat{V}(\Delta)|^2 \quad (19)$$

For spherically symmetric potential, $V(\vec{r}) = V(r)$ therefore we have,

$$\hat{V}(\Delta) = -\frac{1}{2\pi^2} \int_0^\infty \frac{\sin(\Delta r)}{\Delta} V(r) dr \quad (20)$$

If we choose $V(r)$ as coulomb potential,

$$V(r) = -\frac{ZZ'e^2}{r} \quad (21)$$

The Fourier transform of the coulomb potential of equation (21) is given by

$$\hat{V}(\Delta) = \frac{e^2}{2\pi^2 \Delta^2} \quad (22)$$

On substituting the value of equation (22) in equation (19),

$$|\hat{V}(\Delta)|^2 = \left| \frac{e^2}{2\pi^2 \Delta^2} \right|^2 = \frac{e^4}{4\pi^4 \Delta^4} \quad (23)$$

The higher-order terms can be neglected for small momentum transfer. To calculate $\sum_l J_l(\Delta, D_0 \alpha_0)$ all we have to do is to replace x by Δ, D_0, α_0 in the expression of Bessel function under $l = 1$ that corresponds to stimulated Bremsstrahlung (one photon emission) at low frequency [16],

$$J_1(\Delta, D_0 \alpha_0) = \frac{\Delta D_0 \alpha_0}{2} \quad (24)$$

Also at low frequency

$$|T_{k_f k_i}^l|^2 = \sum_l J_l^2(\Delta, D_0 \alpha_0) |\hat{V}(\Delta)|^2 = \frac{\Delta^2 D_0^2 \alpha_0^2}{4} \left(\frac{e^4}{4\pi^4 \Delta^4} \right) \quad (25)$$

On substituting the value of equation (25) in equation (19),

$$\frac{d\sigma}{d\Omega} = \frac{m^2 D_0^2 \alpha_0^2 e^4 k_f}{64\pi^6 \hbar^4} \frac{1}{k_i \Delta^2} \quad (26)$$

Substituting for $\Delta^2 = k_i^2 \left[\left(1 - \frac{\hbar\omega}{E_{k_i}}\right) - 2 \left(1 - \frac{\hbar\omega}{E_{k_i}}\right)^{\frac{1}{2}} \cos\theta + 1 \right]$ in equation (26) and solving the case of inverse Bremsstrahlung ($l = -1$),

$$\frac{d\sigma}{d\Omega} = C \left(\cos^2\theta + \sin^2\theta \tan^2 \frac{\eta}{2} \right)^{\frac{1}{2}} \frac{I \lambda^4}{E_{k_i}} \left(1 + \frac{\hbar\omega}{E_{k_i}} \right)^{\frac{1}{2}} \left[\left(1 + \frac{\hbar\omega}{E_{k_i}} \right) - 2 \left(1 + \frac{\hbar\omega}{E_{k_i}} \right)^{\frac{1}{2}} \cos\theta + 1 \right]^{-1} \quad (27)$$

Here, C is $\frac{m^2 \alpha_0^2 e^4}{64\pi^6 \hbar^4} = \frac{1}{256\pi^9}$ in a.u., D_0 is $(\cos^2\theta + \sin^2\theta (\tan \frac{\eta}{2})^2)^{1/2}$, m is mass of the electron, k_i is initial momentum vector of the electron, E_{k_i} is the initial kinetic energy of the incident electron, $\hbar\omega$ is photon energy of the laser, l is no. of the photon transfer during the interaction, θ is scattering angle, Δ is momentum transfer, α_0 is $\frac{eE_0}{m\omega^2}$, E_0 is the amplitude of the electric field of the laser, E_0 is $\frac{8\pi I}{c} \eta$ is elliptically polarized angle and I is the intensity of the laser.

3 Results and Discussion

The authors investigate the elastic scattering of an electron-atom interaction with photon absorption in the presence of an elliptically polarized laser field in this paper. Equation (27), the new resultant equation, is used to investigate the differential cross section. The differential cross section is determined by, the wavelength of the assisting laser beams field, and the electron's kinetic energy. Figure 1 depicts the differential cross section with the electron beams energy. The representation is based on visible energy photon=1.5eV, high intensity laser field 10^{14}Wcm^{-2} (frequency = 10^{14}Hz) Sprangle and Hafizi [17], $\theta = 0.209$ radian, $\eta = 1.56$ radian angle and energy of electron 0 to 600eV. The SI unit for differential cross section is m^2 . Because the intensity of a laser is directly proportional to its differential cross section, and the differential cross section studied in this work is for visible photons at high intensities, As a result, for high intensity laser radiation, we consider the existence of the laser that Sprangle and Hafizi used in their work.

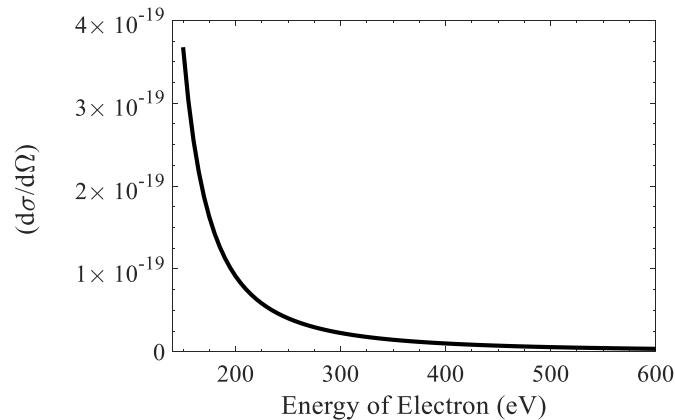


Fig.1. Variation of $d\sigma/d\Omega$ with K.E. of the incident electron at $\eta = 1.56$ radian and $\theta = 2.09$ radian

At 25eV, the differential cross section is high, and the differential cross section is not observed below 25eV. This is due to the fact that the interaction of low-energy electrons with atoms does not require atom (probability of interaction-free and bounded electron is zero). The differential cross section decreases as the energy of the electron increases because the interaction between the incidence electron and the atom increases (probability of interaction of free and bounded electron is high). When the incidence electron's energy is greater than 500eV, the differential cross section is minimum and constant (probability of interaction-free and bounded electron very low). Figure 2 shows the variation of a differential cross section with an elliptical polarization angle of $\theta = 2.09$ radian and energy of 10eV. The differential cross section assistant by the elliptically polarized angle is minimum at -1.56 radian and maximum at +1.5 radian. The differential cross section between -1.5 radian and +1.56 radian angle is nearly constant and decreases sharply at -1.56 radian and +1.56 radian. This sharp increase and decrease are due to the elliptical polarized potential and the non-uniform interaction between free and bounded electrons (probability of interaction is either high or low).

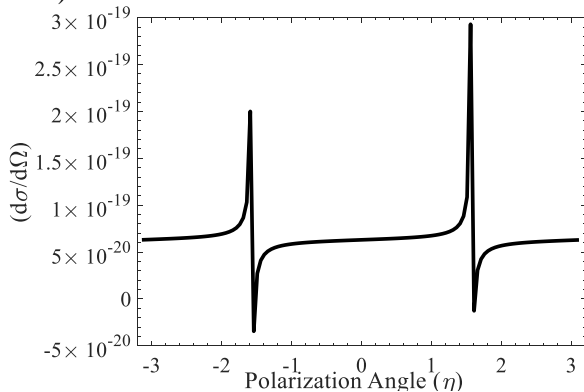


Fig.2. Variation of $\frac{d\sigma}{d\Omega}$ with polarizing angle (η).

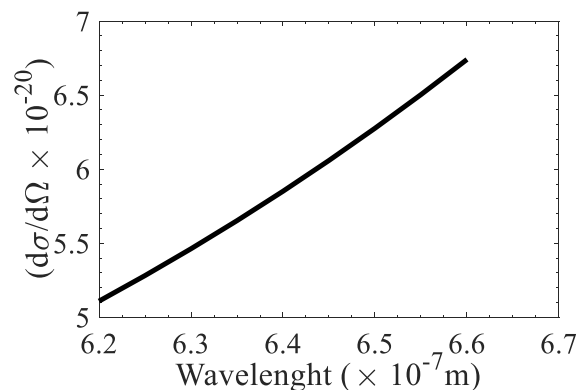


Fig.3. Variation of $\frac{d\sigma}{d\Omega}$ with assisting laser photon wavelength

As shown in Figure 3, the differential cross section increases with the wavelength of the laser photon at $\eta = +1.56$ radian, electron energy 10eV. Because the energy of the laser photon assisting the electron decreases as the wavelength increases, the differential cross section increases. The reduction in photon energy benefits electrons by reducing the interaction of free electrons with bound electrons. Because the free electron was diverted away from the reference target, the differential cross section increased. The larger the differential cross section value, the less accurate the information about the target. The ellipticity of the laser field affects the angular distribution of scattered electrons in the simplest geometry. This is due to the fact that it destroys the axial symmetry of the angular distribution that exists for $\eta = 0$ to the direction of the polarization vector.

Conclusion

The developed equation (27) depicts the differential cross section for an elliptically polarized potential with single-photon absorption. The differential cross section is determined by the polarization angle, electron energy, laser intensity, and photon energy. The observed differential cross section is large at 25eV (electron energy), but not below 25eV. The differential cross section is minimum and constant at high energies greater than 500eV. The differential cross section increases as the wavelength of the laser photon assisting the electron increases. Furthermore, the ellipticity of the laser field influences the angular distribution of scattered electrons by destroying axial symmetry. The nature differential cross section is based on existence numerical data from Sprangle and Hafizi 2014 research work.

Acknowledgement

Authors would like to thanks all the faculties' members of Department of physics, Patan Multiple Campus, Tribhuvan University. Similarly authors extended their thanks to all members of Innovative Ghar Nepal and Robotic Academy of Nepal for providing suitable environment and motivation during this work.

REFERENCES

- 1 Mason N.J. Laser-assisted electron-atom collisions. *Rep. Prog. Phys.* 1993, Vol. 56, pp.1275-1346.
- 2 Kroll N.M., Watson K.M. Charged-particle scattering in the presence of a strong electromagnetic wave. *Phys. Rev. A.* 1973, Vol. 8, Is.2, pp.804-809.
- 3 Yadav K., Nakarmi J.J. Free-free scattering theory of the elastic scattering of an electron. *Int. J. Phys.* 2015, Vol.3, pp.32-39.
- 4 Sinha C., et al. Laser-assisted free-free transition in electron-atom collisions. *Phys. Rev. A.* 2011, Vol. 83, Iss.6, pp.1-3.
- 5 Mittleman M.H. *Introduction to the theory of laser-atom interactions*. Springer Science and Business Media, Switzerland, 2013, 198 p.
- 6 Flegel A.V., et al., Control of atomic dynamics in laser-assisted electron-atom scattering through the driving-laser ellipticity. *Phys. Rev. A.* 2013, Vol. 87, Is.3, pp.1-5.
- 7 Mason N.J., Newell W.R. Simultaneous electron-photon excitation of the helium 2^3S state. *J. Phys., B.* 1987, Vol.20, Is.10, pp.323-325.
- 8 Wallbank B., et al. Simultaneous off-shell excitation of He 2^3S by an electron and one or more photons. *Z. Phys. D At. Mol. Clusters.* 1988, Vol.10, Is.4, pp.467-472.
- 9 Makhoute A., et al. Electron-impact elastic scattering of helium in the presence of a laser field: non perturbative approach. *J. Phys. B: At., Mol. Opt. Phys.* 2016, Vol.49, Is.7, pp.1-30.
- 10 Agueny H. et al. Laser-assisted inelastic scattering of electrons by helium atoms. *Phys. Rev. A.* 2015, Vol. 92, Is.1, pp.1-5.
- 11 Makhoute A., Agueny H., Chqondi S. Floquet theory in electron-helium scattering in Nd: YAG laser field. *Opt. Photonics J.* 2013, Vol. 3, pp.18-27.
- 12 Wallbank B., et al. Simultaneous electron-photon excitation of He 2^3S : an experimental investigation of the effects of laser intensity and polarisation. *J. Phys. B: At., Mol. Opt. Phys.* 1990, Vol.23, Is.17, pp.2997-3000.
- 13 Volkov D.M. The solution for wave equations for a spin-charged particle moving in a classical field. *Z. Phys.* 1935, Vol.94, pp.250-260.
- 14 Watson G.N. *A treatise on the theory of Bessel functions*. Cambridge University Press. (1995).
- 15 Yadav K. Theoretical study of multi-photons ionization of hydrogen atom by nonperbative method with intense laser pulse, PhD Thesis, Tribhuvan University, Nepal 2016.
- 16 Flegel A.V. et al. Analytic description of elastic electron-atom scattering in an elliptically polarized laser field. *Phys.Rev. A, 2013, Vol.87, Is.1, pp.2-6.*
- 17 Sprangle P., Hafizi B. High-power, high-intensity laser propagation and interactions. *Phys. Plasmas.* 2014, Vol. 21, pp.1-2.

DOI 10.31489/2021No4/88-101

UDC 530.1

INVARIANT RELATIVISTIC THEORY OF IDEAL GAS

Zhumaev M.R.

Bukhara Engineering Technological Institute, Uzbekistan, Bukhara, mrjumaev2011@mail.ru

The purpose of this study is to develop an original theory of a relativistic ideal gas and to prove the validity of the postulate of the special theory of relativity for the characteristic (i.e., arithmetic mean, root-mean-square) velocities of particles of a relativistic ideal gas even in the massless limit. In this work, the following original methods are used for the first time in the theory of a relativistic ideal gas: the method of nonlinear transformation to prove of the distribution function to find the distribution function of the velocities of particles of a relativistic ideal gas; the equation of state of a relativistic ideal gas was first obtained by averaging the relativistic - invariant components of the energy - momentum tensor of a system of noninteracting particles, i.e. ideal gas by the distribution function of the velocities of their particles. The uniqueness and definiteness of the distribution function of the velocities of the particles of a relativistic ideal gas are proved on the basis of the well-known relativistic invariance of the distribution function. For the first time, expressions were obtained for the arithmetic mean and mean square velocities of particles of a relativistic ideal gas. For the first time, a fundamental conclusion is made about the validity of the postulates of the special theory of relativity for the characteristic velocities of particles of a relativistic ideal gas. An equation of state for a relativistic ideal gas is obtained, which relates its pressure, average energy density and temperature.

Keywords: distribution function, relativistic ideal gas, arithmetic mean and mean square velocity, equation of state, massless limit.

Introduction

In the last twenty years, especially on the eve of the celebration of the centenary of the creation of the special theory of relativity by the great A. Einstein, interest in the problems of relativistic statistical physics has sharply increased (see, eg, [1,2] and the literature cited in these works). Naturally, this is due to the need to solve a number of problems in plasma physics [3], relativistic kinetic theory [4,5], super - nonequilibrium relativistic thermodynamics in subatomic physics [6]. It should be noted that such questions arose immediately after the construction of the special theory of relativity. Planck and other classics of physics noted that the Maxwellian distribution of velocities contradicts the fundamental postulate of relativity - according to which the speed of particles is limited by the speed of light in emptiness - the limiting speed in nature [7]. The history of generalization of the Maxwellian velocity distribution for the relativistic case lasts more than a hundred years [2,5,7-11]. As the analysis of the literature on this topic shows, the first work in this direction was published by F. Juttner [12]. Despite the fact that the Juttner velocity distribution was the correct relativistic generalization of the Maxwellian velocity distribution (which we will prove below), there is still a serious debate about its correctness and the search for various "modifications" of the Juttner velocity distribution continues. Even in the work of recent years [2, 7], continue to obtain, in the language of their authors, curiously surprising results in this regard. Therefore, we have to admit (although this seems unlikely) that the problem formulated at the beginning of the twentieth century remains unsolved. Those no work has proved the validity of the fundamental postulate of the special theory of relativity for the velocities of particles of a relativistic ideal gas. It is clear that for this it is necessary to find the distribution function of the particle velocity of a relativistic ideal gas and, on its basis, to determine the expressions for the characteristic velocities of the particles of a relativistic ideal gas. And then, by passing to the limit, prove that even in the massless limit, these speeds do not exceed the limiting speed in nature.

Another important issue of relativistic statistical physics, as is known, is the derivation of the equation of state for a relativistic ideal gas [7-11] - which establishes a relationship between the pressure, average energy density and temperature of a relativistic ideal gas. In the existing literature, the equation of state for a relativistic ideal gas is obtained thermodynamically [1,4,5,7-12], namely, on the basis of a relativistic generalization of the expression for the free energy or the Gibbs partition function (through which all thermodynamic quantities describing the states of an ideal gas [13, 14]). In our work, we present a new derivation of the equation of state for a relativistic ideal gas by an original method, namely, on the basis of

averaging the temporal and spatial components of the energy tensor - momentum of a system of noninteracting relativistic (structureless) particles over the velocity distribution function of particles of a relativistic ideal gas. In the context of the problem under consideration, this method seems to us more expedient - a direct method and corresponds to the spirit of Maxwell's own works [15]. Consequently, the proposed theory is a relativistic generalization of the Maxwellian theory of an ideal gas and goes over to the latter in the nonrelativistic limit.

In accordance with the above, the article is organized as follows. In the first section, the distribution function of the particle velocity of a relativistic ideal gas is found using the method of transformation. In the second section, formulas for the mean and root-mean-square velocity of particles of a relativistic ideal gas are obtained. The form of the distribution function of the particle velocity of a relativistic ideal gas in the ultra - relativistic limit is also found here in the case of massless particles (massless particles). The third section is devoted to a new derivation of the equation of state for a relativistic ideal gas - by averaging macroscopic quantities over the distribution function of the particle velocity of a relativistic ideal gas. In the conclusion, the main conclusions of the proposed theory are presented, as well as their possible applications in high energy physics and relativistic cosmology.

1. The distribution function of the particle velocity of a relativistic ideal gas

We will begin the presentation of the proposed theory of a relativistic ideal gas by finding the distribution function of the particle velocity of this gas, since it plays a key role in any statistical system [13-15] and, in particular, in the theory of an ideal gas of relativistic particles [1-12]. Figuratively speaking, the distribution function is the cornerstone of kinetic theory.

Note that the desired velocity distribution function can be found in various ways: as a stationary equilibrium solution of the relativistic kinetic Boltzmann equation [2,4,5]; based on the principle of maximum entropy [8-11]. Without discussing here the methods used (they are discussed in more detail in the above literature) and without diminishing the value of these works, we propose the simplest way to determine the velocity distribution function - using the method of transforming the distribution function (see, for example, [18]).

According to this method, on the basis of the known distribution function of the moment of the particles of a relativistic ideal gas $f(\vec{P}) = f(P_x, P_y, P_z)$, we must determine the distribution function of the velocity of particles of a relativistic ideal gas $\varphi(\vec{v}) = \varphi(v_x, v_y, v_z)$. Here: P_x, P_y, P_z and v_x, v_y, v_z are the components of moments and velocities of particles along the corresponding axes x, y, z . Then, based on the method of transformation, we easily obtain the following relation. Using the transition from the moment of particles to their velocities, we obtain:

$$\int f(P_x, P_y, P_z) dP_x dP_y dP_z = \int \varphi(v_x, v_y, v_z) D |dv_x dv_y dv_z|. \quad (1)$$

Here D is the transformation determinant defined by the following expression

$$D = \begin{vmatrix} \frac{\partial P_x}{\partial v_x} & \frac{\partial P_x}{\partial v_y} & \frac{\partial P_x}{\partial v_z} \\ \frac{\partial P_y}{\partial v_x} & \frac{\partial P_y}{\partial v_y} & \frac{\partial P_y}{\partial v_z} \\ \frac{\partial P_z}{\partial v_x} & \frac{\partial P_z}{\partial v_y} & \frac{\partial P_z}{\partial v_z} \end{vmatrix}. \quad (2)$$

Note that the determinant of the transformation $D \equiv \frac{\partial(P_x, P_y, P_z)}{\partial(v_x, v_y, v_z)}$ will be unique and the same for any type of $Df(\vec{P})$ (the form of which we specify below).

Here: P_x, P_y, P_z is defined according to the special theory of relativity by the following expressions:

$$\vec{P} = P_x \vec{i} + P_y \vec{j} + P_z \vec{k} = \frac{m\vec{v}}{\sqrt{1 - \frac{v^2}{c^2}}}, \quad \vec{v} = v_x \vec{i} + v_y \vec{j} + v_z \vec{k}. \quad (3)$$

Now, taking into account the expression D_1, D_2 and D_3 (9), we obtain that $D_1 - D_2 + D_3 = \gamma^2$. The determinant of the transformation D from pulses P_x, P_y, P_z to velocities v_x, v_y, v_z is finally determined by the following expression [2, 24, 25]:

$$D = m^3 \gamma^5 = m^3 \left(1 - \frac{v^2}{c^2}\right)^{-\frac{5}{2}}. \tag{4}$$

Note that the found determinant of the transformation D from momenta to velocity remains valid for an arbitrary distribution function of momenta of particles of a relativistic ideal gas. In particular, for quantum relativistic ideal gases, the particles of which obey, as is well known to the statistics of Fermi-Dirac and Bose-Einstein [19].

Before proceeding to the definition of the distribution function of the velocities of the particles of a relativistic ideal gas, I would like to bring the following transformation of the elementary volume from the space of momenta to the space of velocities (which follows from (1):

$$dP_x dP_y dP_z = D dv_x dv_y dv_z \tag{5}$$

Hence, in particular, it follows that

$$P^2 dP = D v^2 dv \tag{6}$$

which is easy to verify, given that

$$P = \frac{mv}{\sqrt{1 - \frac{v^2}{c^2}}}, \quad \frac{dP}{dv} = \frac{m}{\left(1 - \frac{v^2}{c^2}\right)^{\frac{3}{2}}}. \tag{7}$$

Now let us determine the distribution function of the velocity of particles of a relativistic ideal gas using the Boltzmann distribution for the momenta of particles of a relativistic ideal gas [18]:

$$f(\vec{p}) = f(P_x, P_y, P_z) = B \exp\left[-\frac{\sqrt{E_0^2 + p^2 c^2}}{kT}\right]. \tag{8}$$

where $E_0 = mc^2$ is the rest energy of a gas particle, kT is thermal energy, B is a constant, which is determined, as always, by the normalization condition for the distribution function, will be found below.

Further, taking into account that the momentum of a relativistic particle \vec{P} is related to its velocity \vec{v} in a nonlinear manner, according to expression (3)

$$E = \sqrt{E_0^2 + p^2 c^2} = mc^2 \left(1 - \frac{v^2}{c^2}\right)^{-\frac{1}{2}}, \tag{9}$$

based on the DF of the moments (8) $f(\vec{P})$ (14), we find the distribution function of the velocity vector of the particles of the relativistic ideal gas

$$\varphi(v_x, v_y, v_z) = B \exp\left[-b \left(1 - \frac{v^2}{c^2}\right)^{-\frac{1}{2}}\right], \quad b = \frac{mc^2}{kT} \tag{10}$$

Therefore, the probability that the speed lies in the interval $(\vec{v}, \vec{v} + d\vec{v})$ or that, the same - the components of the velocity in the interval $(v_x, v_x + dv_x)$, $(v_y, v_y + dv_y)$ and $(v_z, v_z + dv_z)$ is determined according to (10) as follows

$$dW = \varphi(v_x, v_y, v_z) dv_x dv_y dv_z. \tag{11}$$

Finally, in the conclusion of the section, we find the distribution function of the modulus of particle velocities based on the formula for transforming the distribution function from $f(\vec{p})$ to $f(\vec{v})$ (1) and formula (6), taking into account expressions (3) and (10):

$$\int f(\vec{p})d\vec{p} = \int \varphi(\vec{v})d\vec{v} = B \cdot 4\pi \int_0^c m^3 \left(1 - \frac{v^2}{c^2}\right)^{\frac{5}{2}} \cdot v^2 \exp\left[-b\left(1 - \frac{v^2}{c^2}\right)^{\frac{1}{2}}\right] dv \equiv \int_0^c F(v)dv. \quad (12)$$

Thus, the distribution function of the velocity modulus of particles of a relativistic ideal gas is determined by the following expression

$$F(v) = 4\pi m^3 v^2 \left(1 - \frac{v^2}{c^2}\right)^{\frac{5}{2}} \exp\left[-b\left(1 - \frac{v^2}{c^2}\right)^{\frac{1}{2}}\right] \cdot B. \quad (13)$$

Further, introducing the normalized particle velocity $u = \frac{v}{c}$, we can find on the basis of (13) the reduced distribution function of the modulus of the normalized particle velocity $F(u)$

$$\int_0^c F(v)dv = B \cdot 4\pi (mc)^3 \int_0^1 F(u)du. \quad (14)$$

Here

$$F(u) = u^2 (1 - u^2)^{\frac{5}{2}} \exp\left[-b(1 - u^2)^{\frac{1}{2}}\right]. \quad (15)$$

Now we find the constant B using the normalization condition for the distribution function of the velocity moduli of particles of a relativistic ideal gas $F(v)$

$$\int_0^c F(v)dv = B \cdot 4\pi (mc)^3 \int_0^1 F(u)du = 1. \quad (16)$$

Therefore, the constant B according to (14) - (16) is determined by the expression

$$B = \frac{1}{4\pi (mc)^3} \cdot \frac{b}{k_2(b)}.$$

Thus, the reduced distribution function of the moduli of the normalized velocities of particles of a relativistic ideal gas can be written in the following compact form:

$$\Phi(u) = \frac{bF(u)}{k_2(b)} \equiv \frac{b}{k_2(b)} u^2 (1 - u^2)^{\frac{5}{2}} \exp\left[-b(1 - u^2)^{\frac{1}{2}}\right]. \quad (17)$$

The distribution function of the velocity modulus of particles of an ideal gas found by us can be used to calculate the cross section for collisions of particles in a relativistic ideal gas [20] and the cross section for reactions of ultrarelativistic particles in subatomic physics [6]. It may be of interest in studies of the relativistic ionization of atoms by high-energy gas particles, as well as in the field of relativistic laser spectroscopy.

At the end of the section, we present a proof of the invariance of the particle velocity distribution functions of a relativistic ideal gas. The proof given here of the derivation of the velocity distribution function of particles of a relativistic ideal gas MB is final. This follows from the fact that the relativistic Boltzman distribution function for moments is relativistic invariant. Indeed, taking into account that the four-dimensional momentum of gas particles is

$$P^i = mv^i = m \left(\frac{c}{\sqrt{1 - \frac{v^2}{c^2}}}, \frac{v}{\sqrt{1 - \frac{v^2}{c^2}}} \right)$$

and the four-dimensional velocity of the rest coordinate system ($V = 0$) is

$$V^i = (c, 0)$$

we get that

$$P^i v = \frac{mc^2}{\sqrt{1 - \frac{v^2}{c^2}}} = \sqrt{(mc^2)^2 + P^2 c^2}$$

Since the scalar product of any four-dimensional vectors is invariant, any equilibrium distribution possesses this property.

Obviously, the total probability

$$\int f(P_1, P_2, P_3) dP_1 dP_2 dP_3 = 1$$

does not depend on the transformation of the distribution function, which was used to find the relativistic velocity distribution function.

Let us assume that the momentum distribution function of particles of a relativistic ideal gas (8) is invariant if the relation is invariant

$$\frac{i_0}{T_0} = \frac{i}{T}$$

Here $i_0 = i = p_\mu v^\mu$ — according to the above, it is an invariant-as a scalar product of the vectors p_μ and v^μ and, as is known, does not change under Lorentz transformations.

Hence, we get that the condition $T_0=T$ must be fulfilled, i.e. the temperature of the RIC is the same in all Inertial System Frame (ISF). Thus, the main drawback of the existing non-invariant RIG theories is eliminated, according to which, during Lorentz transformations, both the DF and the macroscopic characteristics of the RIG change – which contradicts the invariance of the laws of nature in all ISF.

Summarizing the above, we will come to the fundamental conclusion that during the transition from one ISF to another, the statistical properties of the RIG do not change: neither the velocity distribution function nor the equation of state of the RIG do not change under Lorentz transformations, i.e. they are invariant in all ISF. Naturally, this also holds true for quantum rigs.

2. Characteristic velocities of particles of a relativistic ideal gas

Based on the distribution function of the velocity module of particles of a relativistic ideal gas found in the previous section, it is possible to find any macroscopic characteristic of this gas depending on the velocity based on the formula for calculating the mean

$$\langle G \rangle = \int_0^c G(v)F(v)dv \tag{18}$$

The quantity included in this expression, as is known, gives the probability of finding the particle velocity modulus in the velocity interval $[v, v + dv]$

$$dW = F(v)dv. \tag{19}$$

Then, using the explicit form of the relativistic velocity distribution $F(v)$ (19) and the definition of the function $\Phi(u)$ (17), we obtain the following expression to find the above mentioned probability

$$dW = B \cdot 4\pi m^3 v^2 \left(1 - \frac{v^2}{c^2}\right)^{-\frac{5}{2}} \exp\left[-b\left(1 - \frac{v^2}{c^2}\right)^{-\frac{1}{2}}\right] dv = \Phi(u)du. \tag{20}$$

Here $\Phi(u)$ is the reduced distribution function of the modulus of the normalized particle velocities determined according to (17), by the formula

$$\Phi(u) = \frac{dW}{du} = \frac{b}{k_2} u^2 (1 - u^2)^{-\frac{5}{2}} \exp\left[-b(1 - u^2)^{-\frac{1}{2}}\right]. \tag{21}$$

However, according to the Maxwell distribution, which is obtained from the relativistic distribution (13) in the limit $kT \ll mc^2$ and $v \ll c$, i.e. in the nonrelativistic approximation, the probability that the modulus of the particle's velocity belongs in the velocity range $[v, v + dv]$ is determined by the expression [15]

$$dW = F_M(v)dv = \frac{4}{\sqrt{\pi}} \cdot u^2 \exp(-u^2) du = \Phi_M(u)du. \tag{22}$$

Here u is the particle velocity normalized to the most probable velocity $v_{mp} = \sqrt{\frac{2kT}{m}}$ i.e. $u = \frac{v}{v_{mp}}$. Comparing the relativistic distribution function $\Phi(u)$ with the Maxwellian distribution function $\Phi_M(u)$, we come to the conclusion that, unlike the latter, the first distribution cannot be represented in a single universal form for all gases. The reason for this difference, as can be seen from the comparison of the two distributions, is the presence of the parameter b in the relativistic distribution, which is equal to the ratio of the rest energy of gas particles to the thermal energy kT . In particular, as we will prove below, it is this circumstance that leads to the fact that for a relativistic ideal gas the law of uniform distribution of the average kinetic energy over the degrees of freedom does not hold. Attention was drawn to this, for example, in Pauli's book [21].

The unusualness of the relativistic distribution function (or what, the same thing, the relativistic distribution) $\Phi(u)$ makes us be more attentive to this attractive person (it is clear that such people are extremely rare, if not completely!). Of course, we are primarily interested in, as in the case of the Maxwellian distribution, the characteristic velocities of the relativistic distribution, namely: the most probable, mean and root-mean-square velocities of particles of a relativistic ideal gas.

The most probable particle velocity corresponds to the maximum of the relativistic velocity distribution function $F(v)$ or the relativistic distribution function $\Phi(u)$. It is determined by the extremum condition $\frac{dF(v)}{dv} = 0$, which is equivalent to condition $\frac{d\Phi(u)}{du} = 0$. Calculating this derivative and making a number of simplifications, we obtain the following equation

$$\left[2 + \frac{u^2}{1-u^2} \left(5 - \frac{b}{\sqrt{1-u^2}} \right) \right] \Phi(u) = 0. \quad (23)$$

Further, taking into account that for the values of the parameter b other than zero: $\Phi(u) = 0$ at $u = 0$ and $u = 1$, we come to the conclusion that these values of the velocities correspond to the zeros of the relativistic distribution.

In addition to these roots, equation (23) also has intermediate roots, as follows from it, determined by the solution of the following equation

$$bu^2 = (2 + 3u^2)\sqrt{1-u^2}. \quad (24)$$

We further restrict ourselves to analyzing its solutions only for very large and very small values of the parameter b ¹.

As follows from equation (24), for any finite values of b , its roots belong to the interval of normalized velocities $0 < u < 1$.

For $u \ll 1$, which corresponds to nonrelativistic particles, from (24) we obtain that if $b \gg 1$ or $kT \ll mc^2$, it has the following approximate solution

$$u_{mp} = \frac{v_{mp}}{c} = \sqrt{\frac{2}{b}} = \sqrt{\frac{2kT}{mc^2}}. \quad (25)$$

Therefore, as expected, in this nonrelativistic limit we obtain a result following from the Maxwellian distribution of $F_M(v)$ or $\Phi_M(u)$ - which is valid in this case.

Now we find a solution to equation (24) close to the limiting one, i.e. $u = 1 - \varepsilon$ ($0 < \varepsilon \ll 1$). Then it follows from this equation that

$$u \approx 1 - \frac{b^2}{50}. \quad (26)$$

This solution corresponds to very small values of the parameter $b \ll 1$, which means an ultrarelativistic limit. Further, taking into account the asymptotic behavior of the modified second-order Bessel function $\kappa_2(b) \approx \frac{2}{b^2}$, according to (21), we come to the conclusion that the maximum of DF $\Phi(u)$ is described by the following expression

¹We will not give general solutions to this equation because of its cumbersomeness.

$$\Phi_{Max} \approx \frac{2}{b^2}. \tag{27}$$

Therefore, in contrast to the Maxwell distribution $\Phi_M(u)$ (22), which has a maximum at $u_{mp} = 1$ at any value of b , the relativistic distribution $\Phi(u)$ (21) has a maximum value depending on the parameter b . In particular, at $b \ll 1$, according to (27), the maximum of this distribution grows, i.e. the relative number of particles grows with velocities close to the limiting $u \approx 1$. However, as is known, the maximum of the Maxwellian distribution $F_M(v)$ decreases with increasing temperature, i.e. tends to zero at very high temperatures. This is the main difference between the relativistic distribution $F(v)$ and the Maxwellian distribution $F_M(v)$!

We now turn to determining the average velocity of particles of a relativistic ideal gas. According to the formula for calculating the means (18), we obtain that

$$\langle v \rangle = \int_0^c v F(v) dv = c \int_0^1 u \Phi(u) du = c \langle u \rangle. \tag{28}$$

Using expression (28), we obtain the following formula for the average velocity of particles of a relativistic ideal gas [2, 24, 25]:

$$\langle u \rangle = \frac{2e^{-b}}{k_2(b)} \left(\frac{1+b}{b^2} \right). \tag{29}$$

In a similar way, we determine the mean square of the velocity again using the formula for calculating the means (18), according to which

$$\langle v^2 \rangle = \int_0^c v^2 F(v) dv = c^2 \int_0^1 u^2 \Phi(u) du = c^2 \langle u^2 \rangle. \tag{30}$$

Using (21) and (30), we obtain the following formula for the mean square of the normalized velocity of particles of a relativistic ideal gas [2, 24, 25]

$$\langle u^2 \rangle = 1 - \frac{k_1(b) - k_i(b)}{k_2(b)} b. \tag{31}$$

The found expressions for the mean modulus and the mean square of the modulus of the normalized particle velocity (38), (39) allow us to determine another most important characteristic of the relativistic distribution (27) - the root-mean-square fluctuation of the velocity of gas particles:

$$Dv = \langle v^2 \rangle - \langle v \rangle^2 = c^2 [\langle u^2 \rangle - \langle u \rangle^2] = c^2 Du, \tag{32}$$

which describes the characteristic spread of the velocities of particles of a relativistic ideal gas.

Now let us analyze the behavior of the found characteristic velocities for a very large value of the parameter b , i.e. $b \gg 1$. In this case, as already noted, the thermal energy kT is much less than the rest energy of the particles mc^2 . Further, taking into account the asymptotics of $k_1(b)$ and $k_i(b)$ [22]:

$$k_1(b) \approx \sqrt{\frac{\pi}{2b}} e^{-b} \left(1 + \frac{3}{8b} - \frac{15}{2} \cdot \frac{1}{(8b)^2} + \dots \right), \tag{33}$$

$$k_i(b) \approx \sqrt{\frac{\pi}{2b}} e^{-b} \left(1 - \frac{5}{8b} + \frac{129}{128} \cdot \frac{1}{b^2} + \dots \right), \tag{34}$$

in the considered limit, we obtain

$$[k_1(b) - k_i(b)]b \approx \sqrt{\frac{\pi}{2b}} e^{-b} \left(1 - \frac{9}{8b} \right). \tag{35}$$

Now recalling the asymptotics of the modified second-order Bessel function $k_2(b)$

$$k_2(b) \approx \sqrt{\frac{\pi}{2b}} e^{-b} \left(1 + \frac{15}{8b} + \dots \right), \tag{36}$$

on the basis of expressions (30), (35), (36) we obtain the following formula for the mean square of the velocity of ideal gas particles

$$\langle v^2 \rangle \approx c^2 \cdot \frac{3}{b} \left(1 - \frac{45}{(8b)^2} \right) \approx \frac{3\kappa T}{m}. \quad (37)$$

This is a result following from the Maxwellian distribution for the mean square of the particle velocity in the nonrelativistic limit.

In the same limit, in accordance with expressions (28), (29), and (36), we obtain

$$\langle v \rangle \approx c \cdot 2 \sqrt{\frac{2}{\pi}} \cdot \frac{1}{\sqrt{b}} \approx \sqrt{\frac{8}{\pi}} \cdot \frac{\kappa T}{m}. \quad (38)$$

This is the formula for the average velocity of the Maxwellian distribution. Thus, within the framework of the applicability of the Maxwellian distribution, the root-mean-square fluctuation of the velocities of particles of an ideal gas according to (32), (37), and (38) is determined by the following expression

$$Dv = c^2 Du \approx c^2 \left(3 - \frac{8}{\pi} \right) \frac{1}{b} \approx \left(3 - \frac{8}{\pi} \right) \frac{\kappa T}{m}. \quad (39)$$

Finally, consider the case of ultrarelativistic (or massless) particles, which corresponds to very small values of the parameter b , i.e. $b \ll 1$ (or $b \rightarrow 0$). Then, taking into account the asymptotics of the functions $k_1(b)$, $k_2(b)$ and $k_i(b)$ in this limit [22]

$$k_1(b) \approx \frac{1}{b}, \quad k_2(b) \approx \frac{2}{b^2}, \quad k_i(b) \approx \frac{\pi}{2}, \quad (40)$$

we obtain from (29) and (31) the following results

$$\langle u \rangle = 1 - b^2, \quad \langle u^2 \rangle \approx 1 - \frac{1}{2} b^2. \quad (41)$$

The latest results mean that as $m \rightarrow 0$, these characteristic speeds tend to the speed of light c .

Consequently, in the ultrarelativistic limit, the root-mean-square fluctuation of the velocities of particles of an ideal gas is determined by the following formula

$$Dv = c^2 Du \approx c^2 \frac{3}{2} b^2 \approx \frac{3}{2} c^2 \left(\frac{mc^2}{\kappa T} \right)^2. \quad (42)$$

Thus, in this section, on the basis of the relativistic distribution of velocities (19), it is proved that the characteristic velocities of gas particles: the most probable, mean and root-mean-square velocities do not exceed the speed of light. In particular, taking into account the unattainability of absolute zero temperature, proved by Nernst, we come to the conclusion that only massless particles at any temperature have speeds equal to the speed of light. In addition, it is possible to show the boundedness of the root-mean-square fluctuations of particle velocities for any value of the parameter b . Concluding the section, we note that these qualitative considerations in obtaining solution (24) can be easily obtained by finding the values of b corresponding to the most probable velocities $u_{mp} = \frac{v_{mp}}{c}$ which are determined as follows:

$$b = \left(3 + \frac{2}{u^2} \right) \sqrt{1 - u^2}.$$

From here, for $u \ll 1$ and $u \approx 1 - \varepsilon$ ($0 < \varepsilon \ll 1$), we obtain approximate solutions (25) and (26) of equation (24).

Based on the above analyzes, we come to the conclusion that in the massless limit all characteristic particle velocities tend to the speed of light. In other words, the distribution function of the velocity modulus of particles of an ultra relativistic ideal gas becomes delta-shaped $F_0(\vartheta) = \delta(\vartheta - c)$, and their directions are completely random and equally probable, i.e. distributed isotropically. Indeed, the relativistic distribution function of the normalized velocity $\Phi(u)$ at $b \ll 1$ takes the following form

$$\Phi(u) \approx \frac{b^3}{2} \cdot u^2 (1 - u^2)^{-\frac{5}{2}} \exp \left[-b(1 - u^2)^{-\frac{1}{2}} \right].$$

Further, setting $u^2 = 1 - \varepsilon^2$ ($\varepsilon \rightarrow 0$), we obtain

$$\Phi(u) \approx \frac{b^3}{2\varepsilon^5} \exp\left(-\frac{b}{\varepsilon}\right).$$

Hence it is clear that if $b = \sqrt{\varepsilon}$, then at $\varepsilon \rightarrow 0$ the function $\Phi(u)$ tends exponentially to zero. If $b = \varepsilon^{\frac{3}{2}}$, then at $b \rightarrow 0$ $\Phi(u)$ becomes infinite. Therefore, in this case, the reduced distribution function will be delta-shaped, i.e.

$$\Phi(u) = \delta(1 - u) \text{ (fig. 1).}$$

Thus, based on the analysis of the expressions for the characteristic velocities of the particles of a relativistic ideal gas, we come to the fundamental conclusion that the most probable average and root-mean-square velocity does not exceed the speed of light - the limiting velocity in nature. This proves the validity of the postulates of the special theory of relativity in relativistic statistical physics.

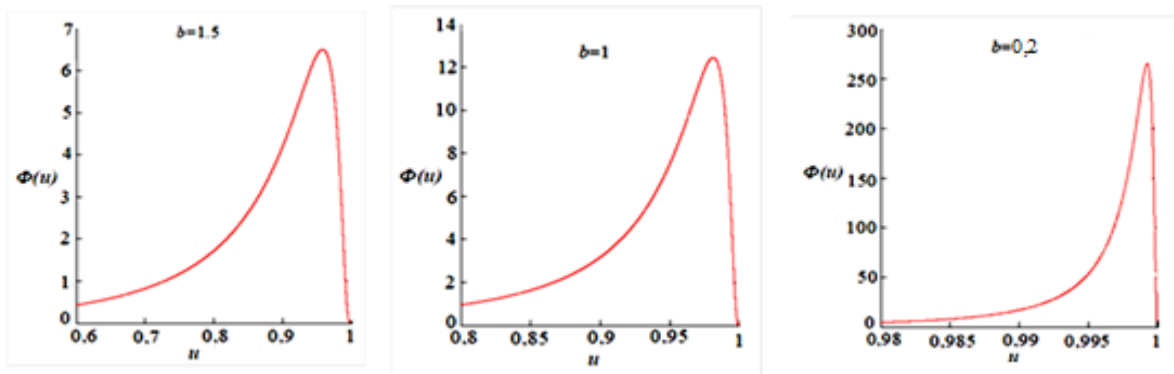


Fig.1. The distribution function of the moduli of the normalized velocities of the particles of a relativistic ideal gas ($b = 1.5; 1; 0.2$)

As an example, we find the root-mean-square velocity of the particles of a relativistic ideal gas at the value of the parameter, when the thermal energy is equal to one third of the rest energy of the gas particle.

Using formula (31) and taking into account the values of the special functions appearing in it, we obtain

$$g_{kg} \equiv \sqrt{\langle g^2 \rangle} \approx 0.515 c.$$

However, according to Maxwell's formula for the mean square velocity (37) $g_{kg} = c$. This result has no physical meaning, since, according to the special theory of relativity, no particle with a nonzero mass can have a speed equal to the speed of light. The latter conclusion also follows from the relativistic distribution function of the particle velocity modulus found by us: if $m \neq 0$, then at $g \rightarrow c$ the function $F(g) \rightarrow 0$.

3. Equation of state for a relativistic ideal gas

As is known, the properties of any ideal gas are determined by its equation of state, which connects three thermodynamic quantities: pressure, average energy density and temperature [13, 23]. Therefore, our goal in this section is to determine the equation of state for a relativistic ideal gas. Before proceeding with the direct solution of this problem, we give a short proof of expressions for the average energy density and pressure of a relativistic ideal gas. To do this, we use the following well-known expression for the energy-momentum tensor of a system of noninteracting particles [23]:

$$T^{ik} = nmc \left\langle \frac{dx^i}{dt} \cdot \frac{dx^k}{dS} \right\rangle, \quad dS = c \sqrt{1 - \frac{v^2}{c^2}} dt. \tag{43}$$

where n is the number of particles per unit volume, and the angle brackets denote averaging over the velocity distribution function of gas particles.

Further, taking into account the definitions of the four-dimensional radius vector of the particle x^i

$$x^i = (x^0, x^1, x^2, x^3) = (ct, x, y, z) = (ct, r^{\rightarrow}), \tag{44}$$

we find the following expressions necessary to find T^{ik} :

$$\frac{dx^i}{dt} = (c, v^{\rightarrow}) = (c, v_x, v_y, v_z), \tag{45}$$

$$\frac{dx^k}{dS} = \left(\frac{1}{\sqrt{1 - \frac{v^2}{c^2}}}, \frac{v^{\rightarrow}}{c\sqrt{1 - \frac{v^2}{c^2}}} \right), \quad (46)$$

where v^{\rightarrow} is the usual three-dimensional particle velocity. Therefore, using expressions (43) - (46), one can determine any component of the energy-momentum tensor T^{ik} of a system of noninteracting particles, for example,

$$T^{00} = nmc^2 \left\langle \frac{1}{\sqrt{1 - \frac{v^2}{c^2}}} \right\rangle, \quad T^{\alpha\alpha} = nm \left\langle \frac{v_\alpha^2}{\sqrt{1 - \frac{v^2}{c^2}}} \right\rangle, \quad (47)$$

where $\alpha = x, y, z$.

Hence it follows that the time component of the energy-momentum tensor T^{00} is equal to the average energy density ρ of the relativistic ideal gas, determined by the expression

$$\rho = nmc^2 \left\langle \frac{1}{\sqrt{1 - \frac{v^2}{c^2}}} \right\rangle. \quad (48)$$

Now, using the spatial components of the energy-momentum tensor, we obtain that

$$T^{xx} + T^{yy} + T^{zz} = nmc^2 \left\langle \frac{v^2}{c^2 \sqrt{1 - \frac{v^2}{c^2}}} \right\rangle. \quad (47^*)$$

However, for any isotropic distribution of particle velocities (otherwise it cannot be due to the equality of all directions in space)

$$T^{xx} = T^{yy} = T^{zz} = P, \quad (49)$$

Thus, from (47*) and (49) we obtain the following expression for the pressure of a relativistic ideal gas:

$$P = \frac{nmc^2}{3} \left\langle \frac{v^2}{c^2 \sqrt{1 - \frac{v^2}{c^2}}} \right\rangle. \quad (50)$$

We emphasize that we did not cite here the expressions for the mixed components of the energy-momentum tensor T^{ik} when i and k are not equal, simply because they are all equal to zero. Now using the identity

$$\frac{1}{\sqrt{1 - u^2}} = \sqrt{1 - u^2} + \frac{u^2}{\sqrt{1 - u^2}}, \quad u = \frac{v}{c}, \quad (51)$$

and taking into account expressions (48) and (50), we obtain the following important equality, which establishes a relationship between the pressure P and the average energy density ρ of a relativistic ideal gas

$$\rho - 3P = nmc^2 \left\langle \sqrt{1 - \frac{v^2}{c^2}} \right\rangle. \quad (52)$$

Thus, as follows from the expressions for the average energy density ρ (48) and pressure P (50), as well as the equation of state (52) connecting them, they are all determined by statistical averaging based on the relativistic distribution of the velocities of their particles $F(v)$ (13). This is the originality of the method used by us for the first time for finding the indicated macroscopic quantities of a relativistic ideal gas.

Let's start solving this problem by determining the average energy density of a relativistic ideal gas based on expressions (48) and (13):

$$\rho = nmc^2 \int_0^c \frac{1}{\sqrt{1-\frac{v^2}{c^2}}} F(v) dv = nmc^2 \int_0^1 \frac{1}{\sqrt{1-u^2}} \Phi(u) du. \tag{53}$$

Now, applying the substitution $u = thx(0 < x < \infty)$ and taking into account expression $\Phi(u)$ (21), we obtain

$$\rho = nmc^2 \frac{b}{k_2(b)} \left(\int_0^\infty sh^2 x e^{-bchx} dx + \int_0^\infty sh^4 x e^{-bchx} dx \right) \tag{54}$$

The integrals included in (54) are respectively equal [22]

$$I_1 = \frac{k_1(b)}{b}, \quad I_2 = 3 \frac{k_2(b)}{b^2}, \tag{55}$$

where $k_1(b)$ and $k_2(b)$ are the modified Bessel functions of the first and second order.

Thus, for the average energy density ρ of a relativistic ideal gas, we obtain the following beautiful expression

$$\rho = nmc^2 \left[\frac{k_1(b)}{k_2(b)} + \frac{3}{b} \right], \quad b = \frac{mc^2}{\kappa T}. \tag{56}$$

Next, we calculate the right-hand side of equality (52)

$$nmc^2 \left\langle \sqrt{1-\frac{v^2}{c^2}} \right\rangle = nmc^2 \frac{b}{k_2(b)} \int_0^\infty sh^2 x e^{-bchx} dx. \tag{57}$$

Now, taking into account the first integral in expression (55), from this we obtain

$$nmc^2 \left\langle \sqrt{1-\frac{v^2}{c^2}} \right\rangle = nmc^2 \frac{k_1(b)}{k_2(b)}. \tag{58}$$

Substituting the found mean in the right-hand side of equality (52), we find the following expression for the pressure of the Maxwell-Boltzmann relativistic ideal gas

$$P = nkT. \tag{59}$$

Of course, this result can also be obtained by direct averaging of the expression for pressure (50). However, now, unlike the nonrelativistic ideal gas theory, the pressure of a relativistic ideal gas will not be directly proportional to the average kinetic energy of gas particles $\langle E_k \rangle$, since, according to (56)

$$\langle E_k \rangle = mc^2 \left[\frac{k_1(b)}{k_2(b)} + \frac{3}{b} - 1 \right],$$

is a nonlinear function of the thermal energy kT and the rest energy of the gas particle mc^2 . In particular

$$\frac{\langle E_k \rangle}{kT} = b \cdot \left[\frac{k_1(b)}{k_2(b)} + \frac{3}{b} - 1 \right]$$

Using this formula, by measuring $\langle E_k \rangle$ and T , you can determine the rest energy of gas particles mc^2 in a non-trivial way. Thus, the equation of state of a relativistic ideal gas connecting its pressure, average energy density and temperature is determined by the following expression

$$\rho - 3P = nmc^2 \frac{k_1(b)}{k_2(b)}, \quad b = \frac{mc^2}{\kappa T}. \tag{60}$$

We emphasize that the above results can be obtained by other statistical methods, which were mentioned at the beginning of the first section.

Let us now investigate the asymptotic behavior of the pressure and average energy density of a relativistic ideal gas at the limiting values of the parameter b . If the thermal energy kT is negligible compared to the rest energy of the gas particles mc^2 , then the parameter $b \gg 1$. Further, taking into account the asymptotics of the functions $k_1(b)$ and $k_2(b)$ (36), we have

$$\frac{k_1(b)}{k_2(b)} \approx 1 - \frac{3}{2b} - \frac{45}{64b^2}. \quad (61)$$

Then it follows from (56) that in this limit the mean energy density is determined by the following formula

$$\rho \approx nmc^2 + \frac{3}{2}nkT. \quad (62)$$

However, M. Consequently, only for a nonrelativistic ideal gas, the law on the uniform distribution of the average kinetic energy over the degrees of freedom is valid, i.e.

$$\langle E_k \rangle = \frac{3}{2} \kappa T. \quad (63)$$

In the opposite limit $b \ll 1$ (which means not only $T \rightarrow \infty$, but also $m \rightarrow 0!$), The modified Bessel functions of the first and second order have the asymptotics indicated in expression (40).

Then from (56) we obtain the following formula for the average energy density of an ultrarelativistic ideal gas (or a relativistic gas of massless particles)

$$\rho \approx 3nkT \left[1 + \frac{1}{6} \left(\frac{mc^2}{\kappa T} \right)^2 \right]. \quad (64)$$

In this limit, from (60) follows the so-called limiting equation of state

$$P \approx \frac{\rho}{3}, \quad (65)$$

which corresponds to the highest possible pressure at a given average energy density ρ .

Based on the above analyzes of the equation of state (60) relating pressure, average energy density and temperature of a relativistic ideal gas, we can write the following approximate equations of state:

$$P \approx 0, \quad P \approx \frac{\rho}{3}, \quad (66)$$

usually used in the equations of motion of matter (matter and radiation) in cosmological theories [23]. Here, the first equation of state corresponds to a nonrelativistic gas with an ultralow temperature ($T \rightarrow 0$), the second - to an ultrarelativistic gas with a very high temperature ($T \rightarrow 0$) or equilibrium radiation. These approximate equations of state used are virtually independent of temperature. Therefore, based on the analysis of the equation of motion of matter, where the equations of state are used, which does not take into account the dependence of pressure and average energy density on temperature, it is impossible, in principle, to determine the change in the temperature of the Universe during its evolution. An additional argument in favor of this conclusion is the fact that the very establishment of the equilibrium Boltzmann distribution and the resulting relativistic distribution of the velocities of gas particles is possible only in statistical equilibrium, with a constant temperature in time. In conclusion, we emphasize that the pressure and average energy density of a relativistic ideal gas take only non-negative values according to their physical meaning. This conclusion remains valid for quantum relativistic ideal gases, since the expressions for the pressure (50) and average energy density (48) of a relativistic ideal gas, as well as the equation of state (52) connecting them, remain valid in the case of quantum statistics. Only averaging follows, it is carried out over the distribution function of the momenta of quantum relativistic ideal gases [24-26]. Thus, no substance can have negative pressure and negative average energy density. This excludes the possibility of the existence of the supposed "dark" matter with such hypothetical properties.

Conclusion

Let us summarize the consequences of the proposed theory of a relativistic ideal gas, compare them with previously known results, and also discuss issues of their further development. The presentation will be carried out in accordance with the sequence of the issues considered in the article.

1. The distribution function of the particle velocity of a relativistic ideal gas, obtained by us by transforming the distribution function, which is described by expression (13), agrees with the result of Juttner's work [12], obtained by him on the basis of a relativistic generalization of the Gibbs statistic. The "modified" Juttner distribution of velocities obtained in [7] is incorrect, since, according to the authors themselves, it contains a factor - the reciprocal of the energy of a relativistic particle. This leads to the

erroneous conclusion that in the ultra - relativistic limit the "Modified" Juttner distribution of velocities tends to zero. This contradicts the result (27) and does not correspond to reality (see also a number of curious results given in [7]).

2. The formulas describing the mean and root-mean-square velocity of particles of a relativistic ideal gas were not obtained by either Juttner or his "modifiers". Consequently, for the first time in our work, it was proved on their basis that the characteristic velocities of particles of a relativistic ideal gas are limited - the limiting velocity in nature. This confirms the validity of the fundamental postulate of the special theory of relativity in relativistic statistical physics.

3. The equation of state of a relativistic ideal gas, relating the pressure, average energy density and temperature of a relativistic ideal gas described by expressions (56), (59) and (60), agrees with the results obtained by Juttner [12], as well as other researchers [4, 5, 8-11,16,17]. But unlike these works, in which thermodynamic methods were used to obtain the equation of state (based on free energy, the principle of maximum entropy, etc.), here it was obtained by a new method, namely, by averaging macroscopic quantities for a system of relativistic non-interacting particles, i.e., e. for a relativistic ideal gas from the distribution function of the velocity of their particles. As far as we know, no one has previously used such a method for obtaining the equation of state for a relativistic ideal gas. It is of great interest to generalize the theory of a relativistic ideal gas developed above for reference frames moving with constant acceleration [16], as well as for relativistic plasma of colliding beams [3].

4. Analysis of limit case

A. Substantially Nonrelativistic Ideal Gas $b = \frac{mc^2}{kT} \gg 1$.

In this limit, it should be taken into account that

$$E \approx mc^2 + \frac{p^2}{2m}, k_2(b) = \sqrt{\frac{\pi}{2b}} e^{-b} \left(1 + \frac{15}{8b}\right).$$

Then we get

$$f \approx \frac{1}{4\pi} \sqrt{\frac{2}{\pi}} \cdot \frac{1}{(mkT)^{\frac{3}{2}}} \exp\left(-\frac{p^2}{2mkT}\right).$$

B. Ultra-relativistic limit.

$b = \frac{mc^2}{kT} \ll 1$ (or $b \rightarrow 0$). Then, taking into account the asymptotics of the function in this limit $k_2(b)$, we obtain $k_2(b) \approx \frac{2}{b^2}$. In addition it should be taken into account that

$$E \approx pc.$$

Therefore, we have

$$f(p) \approx \frac{1}{8\pi} \cdot \left(\frac{c}{kT}\right)^3 \cdot \exp\left(-\frac{pc}{kT}\right)$$

Hence it follows that if $T \rightarrow 0$, $f(p) \rightarrow \delta(p)$.

C. Of the effective cross section of colliding particles

$$\frac{\sigma}{\sigma_{max}} = \langle \sqrt{(\vec{u}_1 - \vec{u}_2)^2 - [\vec{u}_1, \vec{u}_2]^2} \rangle$$

Here $u_{1,2} = \frac{u_{1,2}}{c}$. $u_{1,2}$ — normalized velocities colliding particles of RIG.

Further, the case is considered when, for example, $u_2=0$. Then, the previous formula is greatly simplified.

$$\frac{\sigma}{\sigma_{max}} = \langle u \rangle$$

Consequently, for parameter values significantly less than one, i.e. for the UR particles, for example, at $b=10^{-4}$ (which was possible in experiments on particle collisions at CERN, as well as in experiments in Controlled Nuclear Fusion in France), we obtain according to the formula for the average velocity

Maxwellian distribution $\langle u \rangle \approx 2 \sqrt{\frac{2}{\pi}} \cdot 10^2$.

This result obviously has no physical meaning, since it means that the speed of particles exceeds the speed of light 100 times. But at the same time, according to the formula for the average RIG speed, in this limit we get

$$\langle u \rangle = 1 - b^2 = 1 - 10^{-4}$$

Consequently, according to the latest results, the effective cross-section of colliding particles of a relativistic ideal gas cannot exceed the effective cross-section of a stationary particle. I.e., starting from a certain threshold energy, the effective cross-section practically does not depend on the average kinetic energy of colliding particles, which is confirmed by experiments conducted at CERN. As an application of the theory of a relativistic ideal gas, one can point out its possible application for calculating the cross section for collisions of ultra - relativistic heavy ions in a high energy collider [27], as well as for the relativistic kinetic description of the production of fermions and bosons in cosmology.

Completing the work, we cannot but pay attention to, perhaps - not very pleasant and annoying, strange circumstance that has developed in the history of the theory of a relativistic ideal gas: for more than a century after Juttner's work [12], they were engaged in an essentially meaningless business - they tried "Modify" ... the correct Juttner velocity distribution! Here, as they say, there is nothing to be done - this is the nature of things. But the truth, although it is bitter, is always fair ...

REFERENCES

- 1 Cubero D., et al. Thermal equilibrium and statistical thermometers in special relativity. *Phys. Rev. Lett.* 2007, Vol. 99, 170601-4.
- 2 Fanchi J.R. Comparative analysis of Juttner's calculation of the energy of a relativistic ideal gas and implications for accelerator physics and cosmology. *Entropy.* 2017, Vol. 19, pp. 374 – 399.
- 3 Chason-Acosta G., et al. Manifestly covariant Juttner's distribution and equipartition theorem. *Phys. Rev., E*, 2010, Vol. 81, pp. 1 – 9.
- 4 Debbasch F. Equilibrium distribution function of a relativistic dilute perfect gas. *Phys. A.* 2008, Vol. 387, pp.2443-2454.
- 5 Schieve W.C. Covariant relativistic statistical mechanics of many particles. *Found. Phys.* 2005, Vol. 35, pp.1359-1381.
- 6 Dunkel J., et al. Relative entropy, Haar measures and relativistic canonical velocity distributions. *New Journ. of Phys.* 2007, Vol.9, pp. 144 – 158.
- 7 Kowalski K., et al. *Lorentz covariant statistical mechanics and thermodynamics of the relativistic ideal gas and preferred frame.* 2007, arxiv07.12.2725 v.2 [hep-th] 18 Dec.
- 8 Gonzalez-Narvaez R.E., et al. Mixing of relativistic ideal gases with relative relativistic velocities. *Annals of Phys.* 2016, 2017 / 01 Vol. 376. pp1-21.
- 9 Jumaev M.R. Nonlinear fluctuation mechanism for matter creation and reminds of the universe. *Sci. Rep. of Bukhara Univ.* 2005, No. 1, pp. 66 – 76.
- 10 Jumaev M.R. Theory of relativistic ideal gas for quasi and ordinary particles. *Proc. of the NATO Adv. Res. Workshop on nonlinear dynamics and fundamental interactions*, Kluwer Acad. Publ., Amsterdam. 2006, pp. 155-165.
- 11 Jumaev M.R. *The quantum relativistic ideal gas and of the relict radiation.* Lambert Acad. Publ., Germany, 2016, 214 p. [in Russian]
- 12 Jumaev M.R., et al. Distribution function velocities of the particles relativistic ideal gas. *Sci. reports Bukhara Univ.* 2020, No. 1, pp. 14-18. [in Russian]
- 13 Von F. Juttner. Das Maxwellllesche Gefetz in der relative theorie. *Ann. d. Phys.* 1911, Vol. 34, pp. 856-882.
- 14 Jumaev M.R., et al. Fluctuational and parametric phenomena in condensed and nanoscopic systems. *Abstract Doctor thesis (DSc).*, Tashkent, 2021, 72 p.
- 15 Landau. L.D., Lifshitz E.M. *Theory of field.* Moscow, Nauka. 1988, 512 p. [in Russian]
- 16 Eichler J. Theory of relativistic ion-atom collisions. *Phys. Rev.* 1990, Vol.193, pp. 165 – 277.
- 17 Kaniadakis G. Towards a relativistic statistical theory. *Phys. A.* 2006, No. 365, pp. 17 – 23.
- 18 Landau. L.D., Lifshitz E.M. *Statistical physics.* Pergamon press, 1970, 497p. [in Russian]
- 19 Van Kampen N. G. *Stochastic processes in physics and chemistry.* North-Holland, Amsterdam. 2003, 479p.
- 20 De Groot S.R., et al. *Relativistic kinetic theory.* North-Holland, Amsterdam. 1980, 355 p.
- 21 Chuang Liu. Einstein and relativistic thermodynamics in 1952: a historical and critical study of a strange episode in the history of modern physics. *Br. J. Hist. Sci.* 1992, No. 25, pp. 185 – 195.
- 22 Hakim R. *Introduction to relativistic statistical mechanics, classical and quantum.* World Scient. 2011, 295p.
- 23 Earias C., et al. What is the temperature of a moving body? *Scient. Rep.* 2017, No. 7, pp. 17657 – 17600.
- 24 Huang Y.S. *Relativistic quantum statistical mechanics in the framework of NRT.* 2019. Available at: www.researchgate.net/publication/332037148.
- 25 Nakamura T.K. Relativistic equilibrium distribution by relative entropy maximization. *Europhys. Lett.* 2008, No. 88, pp. 40009-15.
- 26 Gradstein I.S., Ryzhik I.M. *Tables of integrals, series and products.* Acad. Press. 1965, 326 p.
- 27 Nakamura T.K. Three views of a secret in relativistic thermodynamics. *Progr. Theor. Phys.* 2012, No. 128, pp.463 – 468.

SUMMARIES	ТҮСІНІКТЕМЕЛЕП	АННОТАЦИИ
<p>Шишулин А.В., Потапов А.А., Шишулина А.В. БАСТАПҚЫ ҚҰРАМЫ НАНОБӨЛШЕКТЕРДІҢ БАЛҚУ ТӘРТІБІН АНЫҚТАЙТЫН ҚОСЫМША ПАРАМЕТР РЕТІНДЕ ($Si_x - Ge_{1-x}$ X ЖҮЙЕСІ МЫСАЛЫНДА) Заманауи жартылай өткізгіш электрониканың негізгі материалдарының бірі болып табылатын Si-Ge жүйесінің қорытпалары әр түрлі технологиялық қолданыстарға ие. Берілген жұмыста Si-Ge нанобөлшектеріндегі фазалық тепе-теңдік термодинамикалық тәсіл аясында модельденді. Есептеулер көрсеткендей, әр түрлі диаметрлі және құрамды нанобөлшектерге «нано-ликвидус» және «нано-солидус» температураларының әр түрлі жиынтығына сәйкес келеді, олар өз кезекте макроскопиялық өлшемді құрылымдар үшін тиісті мәндерден ерекшеленеді, ал «нано-ликвидус» және «нано-солидус» арасындағы температуралық аралық бөлшектің өлшемінің азаюымен кемиді. Макроөлшемді құрылымдардан айырмашылығы әр түрлі Si құрамына ие нанобөлшектердегі берілген температурадағы қатар өмір сүретін сұйық және қатты фазалардың құрамы айтарлықтай ерекшеленеді, сонымен бірге қатар өмір сүретін фазалардың құрамы мен көлемдік үлесінің нанобөлшектің диаметріне тәуелділіктер сипаты бөлшектердің температурасы мен Si үлестермен анықталады. Жүйенің еркін энергиясын төмендеуінің әр түрлі механизмдері негізінде алынған нәтижелердің термодинамикалық түсіндірмесі ұсынылған.</p> <p>Шишулин А.В., Потапов А.А., Шишулина А.В. НАЧАЛЬНЫЙ СОСТАВ КАК ДОПОЛНИТЕЛЬНЫЙ ПАРАМЕТР, ОПРЕДЕЛЯЮЩИЙ ПОВЕДЕНИЕ ПЛАВЛЕНИЯ НАНОЧАСТИЦ (НА ПРИМЕРЕ СИСТЕМЫ $Si_x - Ge_{1-x}$) Являясь одним из основных материалов современной полупроводниковой электроники, сплавы системы Si-Ge имеют широкий спектр разнообразных технологических приложений. В настоящей работе фазовые равновесия в наночастицах Si-Ge смоделированы в рамках термодинамического подхода. Расчеты показывают, что наночастицам различного диаметра и состава соответствуют различные наборы температур «нано-ликвидуса» и «нано-солидуса», отличающиеся от соответствующих значений для структур макроскопического размера, в то время как температурный интервал между «нано-ликвидусом» и «нано-солидусом» сокращается с уменьшением размера частицы. В отличие от макроразмерных структур, составы сосуществующих жидких и твердых фаз при заданной температуре в наночастицах с различным содержанием Si существенно различаются, а характер зависимостей составов и объемной доли сосуществующих фаз от диаметра наночастицы определяется температурой и долей Si в частице. Представлена термодинамическая интерпретация полученных результатов на основе различных механизмов понижения свободной энергии системы.</p>		
<p>Durgadsi S.U., Kattimani V.R., Maruti N.S., Kulkarni A.B., Mathad S.N. БІРГЕ ТҮНДЫРУ ӘДІСІМЕН СИНТЕЗДЕЛГЕН НИКЕЛЬ ФЕРРИТІН СИНТЕЗДЕУ ЖӘНЕ ҚҰРЫЛЫМДЫҚ ТАЛДАУ Зерттелетін никель ферриті бірге тұндыру әдісімен синтезделген. Рентгенограмма 8,347 Å тор тұрақтысымен шпинельдің кубтық құрылымының пайда болуын дәлелдеді. Рентгендік тығыздығы, кристалдардың орташа өлшемі, байланыс ұзындығы, дислокация тығыздығы және микродеформация сияқты құрылымдық қасиеттер зерттелген. Сканерлеуші электрондық микроскоптың көмегімен алынған суреттер түйіршікті құрылымдардың түйіршіктілігін көрсеткен. Зерттелінетін никель ферритінің Фурье түрлендірумен инфрақызыл спектроскопия спектрі сәйкесінше тетраэдрлік (А) және октаэдрлік (В) енгізу позицияларынан туындайтын екі маңызды жұтылу жолақтарымен шпинельдің кубтық құрылымының түзілуін көрсетті.</p> <p>Durgadsi S.U., Kattimani V.R., Maruti N.S., Kulkarni A.B., Mathad S.N. СИНТЕЗ И СТРУКТУРНЫЙ АНАЛИЗ ФЕРРИТА НИКЕЛЯ, СИНТЕЗИРОВАННОГО МЕТОДОМ СОСОАЖДЕНИЯ Исследуемый феррит никеля синтезирован методом соосаждения. Рентгенограмма подтверждает образование кубической структуры шпинели с постоянной решетки 8,347 Å. Были изучены такие структурные свойства, как рентгеновская плотность, средний размер кристаллов, длина связи, плотность дислокаций и микродеформации. Изображения, полученные с помощью сканирующего электронного микроскопа, показывают зернистость гранулированных структур. Спектр инфракрасной спектроскопии с преобразованием Фурье исследуемого феррита никеля показывает образование кубической структуры шпинели с двумя значительными полосами поглощения, соответствующими высокочастотной полосе ν_1 и низкочастотной полосе ν_2, возникающей из тетраэдрических (А) и октаэдрических (В) позиций внедрения соответственно.</p>		

Шлимас Д., Омарова А., Козловский А.Л., Здоровец М.В.

CDSE:NI ЖҰҚА ҚАБЫРШАҚТАРДЫҢ ҚАСИЕТТЕРІНЕ ҚОЛДАНБАЛЫ ПОТЕНЦИАЛДАР АЙЫРМАШЫЛЫҒЫ ӨЗГЕРУЛЕРІНІҢ ӨСЕРІН ЗЕРТТЕУ

Бұл жұмыс қабыршақтардың фазалық құрамының өзгеруіне байланысты құрылымдық және оптикалық қасиеттерін өзгерту мүмкіндігімен CdSe негізіндегі жұқа қабыршақтарды никельмен допирлеуді қолдану тиімділігінің әсерін зерттеуге арналған. Қабыршақтарды алу әдісі ретінде электролиттердің сулы ерітінділерінен металл иондарын электрхимиялық тотықсыздандыру әдісі таңдалған. Әр түрлі сипаттамаларға ие қабыршақтарды алу үшін әр түрлі потенциалдар айырмасы пайдаланылды. Қасиеттер мен олардың өзгеру динамикасын сипаттау үшін атомды-күштік микроскопиясы, энергия дисперсиялық талдау және рентгендік дифракция әдістері таңдалды. Қабыршақтардың беріктік механикалық қасиеттері индентирлеу әдісімен зерттелген. Жүргізілген тәжірибелер барысында алу шарттарына байланысты синтезделген қабыршақтардың құрылымдық, оптикалық және беріктік сипаттамаларының өзгеру тәуелділіктері алынды. Родамин В органикалық бояғышының ыдырау жылдамдығы мен тиімділігін анықтауға фотокаталитикалық сынақтар фотокатализатор ретінде қолданыс үшін құрамында NiSe фазасы басым болатын қабыршақтар ең перспективті екенін көрсетті.

Шлимас Д., Омарова А., Козловский А.Л., Здоровец М.В.

ИССЛЕДОВАНИЕ ВЛИЯНИЯ ИЗМЕНЕНИЯ РАЗНОСТИ ПРИКЛАДЫВАЕМЫХ ПОТЕНЦИАЛОВ НА СВОЙСТВА ТОНКИХ ПЛЕНОК CDSE:NI

Данная работа посвящена исследованию эффективности применения эффекта допирования никелем тонких пленок на основе CdSe с возможностью вариации структурных и оптических свойств, обусловленной изменением фазового состава пленок. В качестве метода получения пленок был выбран метод электрохимического восстановления ионов металлов из водных растворов электролитов. Варьирование разности прикладываемых потенциалов было использовано для получения пленок с различными характеристиками. Для характеристики свойств и динамики их изменений были выбраны методы атомно-силовой микроскопии, энергодисперсионного анализа и рентгеновской дифракции. Прочностные механические свойства пленок были исследованы с применением метода индентирования. В ходе проведенных экспериментов получены зависимости изменения структурных, оптических, прочностных характеристик синтезированных пленок в зависимости от условий получения. Фотокаталитические испытания на определение скорости и эффективности разложения органического красителя Родамина В показали, что пленки в составе которых преобладает фаза NiSe обладают наибольшей перспективностью применения в качестве фотокатализаторов.

Юров В.М., Маханов К.М.

МЕХАНИКАЛЫҚ ҚОСПАЛАУ ӘДІСІМЕН АЛЫНҒАН ЖОҒАРЫ ЭНТРОПИЯЛЫҚ ЖАБЫНДЫЛАРДЫҢ ҚАТТЫЛЫҒЫ

Мақалада тот баспайтын болаттардың көпшілігінің қаттылығы жоғары энтропиялық жабындыларға қарағанда 2-3 есе кем екендігі көрсетілген, бұл өз кезекте оларды әр түрлі өнеркәсіптік құрылымдардың бөліктері ретінде пайдалану перспективасын көрсетеді. Ақаусыз негізі бар металл шынылардың микроқаттылығы жоғары энтропиялы жабындылардан ерекшеленбейді. Мақалада жабындының бұзылуы беттік энергияға пропорционал және Гиббс энергиясына кері пропорционал екенін дәлелдейтін теңдеу алынған. Тот баспайтын болаттар үшін беттік энергия жоғары энтропиялы жабындылармен бірдей. Жоғары энтропиялы жабындылардың Гиббс энергиясы тот баспайтын болаттарға қарағанда 2 есе жоғары, бұл тәжірибеде байқалғандай жоғары энтропиялы жабындылардың жоғары қаттылығын көрсетеді.

Юров В.М., Маханов К.М.

ТВЕРДОСТЬ ВЫСОКОЭНТРОПИЙНЫХ ПОКРЫТИЙ, ПОЛУЧЕННЫХ МЕТОДОМ МЕХАНИЧЕСКОГО ЛЕГИРОВАНИЯ

В статье показано - твердость большинства нержавеющей сталей в 2-3 раза меньше высокоэнтропийных покрытий, что показывает перспективу их применения в качестве деталей различных промышленных конструкций. Микротвердость металлических стекол, которые имеют бездефектную основу, не отличаются от высокоэнтропийных покрытий. В статье получено уравнение, которое показывает, что разрушение покрытия пропорционально поверхностной энергии и обратно пропорционально энергии Гиббса. У нержавеющей сталей поверхностная энергия примерно одинакова высокоэнтропийным покрытиям. Энергия Гиббса высокоэнтропийных покрытий в 2 раза больше, чем у нержавеющей сталей, что и приводит к высокой твердости высокоэнтропийных покрытий, что и наблюдается экспериментально.

Касимов А.Т., Есенбаева Г.А., Жолмагамбетов С.Р., Хабидолда О.

КӨПҚАБАТТЫ ОРТОТРОПТЫ ҚҰРЫЛЫМДАРДЫ ТҮРЛЕНГЕН БІР НАҚТЫЛАНҒАН ИІЛУ ТЕОРИЯСЫ НЕГІЗІНДЕ ЗЕРТТЕУ

Мақалада ортотропты көпқабатты композиттік материалдан жасалған құрылымдар, атап айтқанда, қабатты ортотропты пластиналар қарастырылады. Пластиналардың кернеулі-деформациялық күйін сандық модельдеу мен талдау қабатты пластиналардың нақтыланған теориясының бір нұсқасы негізінде жүзеге асырылды. Симметриялық және асимметриялық құрылымды орташа қалыңдықты және жұқа көпқабатты пластиналардың иілу есептері зерттелген. Бүкіл зерттеулер пластиналар құрылатын композиттік материалдың ортотропиялық және көп қабаттылық қасиеттерін ескеруімен жүргізілген. Соңғы айырма әдісінің негізінде ортотропты қабаттарына ие қабатты пластиналардың кернеулі-деформациялық күйін сандық есептеудің жалпы алгоритмі әзірленді. Бұл алгоритм компьютерлік бағдарламалар пакет көмегімен жүзеге асырылған.

Касимов А.Т., Есенбаева Г.А., Жолмагамбетов С.Р., Хабидолда О.

ИССЛЕДОВАНИЕ СЛОИСТЫХ ОРТОТРОПНЫХ КОНСТРУКЦИЙ НА ОСНОВЕ ОДНОЙ МОДИФИЦИРОВАННОЙ УТОЧНЕННОЙ ТЕОРИИ ИЗГИБА

В статье рассматриваются конструкции из ортотропного многослойного композиционного материала, в частности, слоистые ортотропные пластины. Численное моделирование и анализ напряженно-деформированного состояния пластин проведены на основе одного варианта уточненной теории слоистых пластин. Исследованы задачи изгиба пластин средней толщины и тонких многослойных пластин симметричной и несимметричной структуры. Все исследования проведены с учетом свойства ортотропности и многослойности композиционного материала, из которого созданы пластины. На основе метода конечных разностей разработан общий алгоритм численного расчета напряженно-деформированного состояния слоистых пластин с ортотропными слоями. Данный алгоритм реализован на компьютерном пакете программ.

Разживин И.А., Рубан Н.Ю., Рудник И.Е.

ЖЕЛІНІҢ ЖАЛПЫ ИНЕРЦИЯСЫНЫҢ ТӨМЕНДЕУІ КЕЗІНДЕ ЖЕЛ ЭЛЕКТР СТАНЦИЯЛАРЫНЫҢ ЭНЕРГИЯ ЖҮЙЕСІНІҢ ТҮРАҚТЫЛЫҒЫНА ӘСЕРІН БАҒАЛАУ

Әлемде жел энергетикасының дамуымен электр энергиялық жүйелерде жел энергиялы қондырғылардың бірлескен жұмысы өзекті мәселеге айналуда. Ауыспалы айналу жылдамдығына ие заманауи жел энергиялы қондырғылар желіге кернеудің күштік түрлендіргіштері арқылы қосылады, бұл өз кезекте олардың электр энергетикасы жүйелеріне айтарлықтай интеграциялауы кезінде мұндай жүйелердің тұрақтылығына, апаттарға қарсы автоматика құрылғыларының жұмысына теріс әсер етеді. Мәселе жел энергиялы қондырғыларының генераторларының электр энергиялық жүйесімен «айрығы» әсерінен туындайды, себебі жел энергиялы қондырғының механикалық моментінің энергия жүйесінің қалған бөлігімен байланысы жоғалады, оның жиілік сипаттамалары өзгеріп, жүйенің жалпы инерциялығы төмендейді, нәтижесінде бұл құбылыстар қалыпты режимдердегі жиілік пен кернеудің ауытқуларына, сондай-ақ апаттар туындаған кезде жиілік пен кернеудің көшкініне әкелуі мүмкін. Сонымен қатар, жалпы инерцияның төмендеуі асинхронды жүрістің сырғу жиілігінің артуына байланысты асинхрондық режимді жою автоматикасының құрылғыларының жұмыс істемеуіне ықпал етуі мүмкін. Мақалада жалпы инерцияның төмендеуі себебінен олардың жұмысының ауыспалы процестердің өту жылдамдығына әсерін бағалау үшін жел энергиялы қондырғыларды энергия жүйесіне енгізудің эксперименттік зерттеулері жүргізілген.

Разживин И.А., Рубан Н.Ю., Рудник И.Е.

ОЦЕНКА ВЛИЯНИЯ ВЕТРОЭЛЕКТРОСТАНЦИЙ НА УСТОЙЧИВОСТЬ ЭНЕРГОСИСТЕМЫ ПРИ СНИЖЕНИИ ОБЩЕЙ ИНЕРЦИИ СЕТИ.

С развитием ветроэнергетики в мире становятся актуальными вопросы совместной работы ветроэнергетических установок в электроэнергетических системах. Современные ветроэнергетические установки с переменной скоростью вращения присоединяются к сети через силовые преобразователи напряжения, что при значительной их интеграции в электроэнергетические системы негативно сказывается на устойчивости таких систем, работе устройств противоаварийной автоматики. Проблема вызвана эффектом «развязки» генераторов ветроэнергетических установок с электроэнергетической системой, поскольку утрачивается связь механического момента ветроэнергетической установки с остальной энергосистемой, изменяются и ее частотные характеристики, снижается общая инерционность системы и как следствие данные явления могут приводить к колебаниям частоты и напряжения в нормальных режимах, а также лавине частоты и напряжения при возникновении аварий. Кроме того, снижение общей инерции может способствовать несрабатыванию устройств автоматики ликвидации асинхронного режима, ввиду увеличения частоты скольжения асинхронного хода. В статье проведены экспериментальные исследования внедрения ветроэнергетических установок в энергосистему для оценки влияния их работы на скорость протекания переходных процессов, ввиду снижения общей инерции.

Шавдинова М.Д., Шарипов Р.Ж., Меццьякова Т.Ю.

БУ ТУРБИНАСЫ КОНДЕНСАТОРЫНЫҢ БУ АҒЫНЫНЫҢ ЭЖЕКТОРЫН ЖЕТІЛДІРУ

Алматы электр ТЭЦ-2 станциясында жылыту турбиналарында ЭПО-3-200 үш сатылы бу ағынды эжекторы орнатылған, оның жұмыс буының шығыны 850 т/сағ. Бұл жұмыс қолданыстағы үш сатылы бу ағынды эжекторын екі сатылы бу ағынды эжекторымен ауыстыруы ұсынылып, негізделген. Ауыстыру нәтижесінде электр энергиясын өндіру үшін өз қажеттіліктері үшін жылудың (будың) үнемдеуіне қол жеткізілді. Турбина конденсаторындағы қысым 100 кПа-дан айтарлықтай төмен болған кезде ЭПО-3-200 орнына жаңа екі сатылы ЭПО-2-80 эжекторын орнату орынды екені анықталды. Қолданыстағы есептеу әдістерін қолдана отырып, жаңа эжектордың геометриялық сипаттамалары алынды. Жаңа екі сатылы эжектордың жұмыс буының шығыны 579 т/сағ. Сонымен қатар, екі кезеңді пайдалану конструкцияны қарапайымдылауға және оны сенімдірек етуге мүмкіндік берді, сонымен қатар эжектордың 1-ші сатысының салқындатқышында қысымды арттыруға мүмкіндік береді. Бұл негізгі конденсаттың жоғары температурасына ие болатын жылу турбиналары үшін өте маңызды, сонымен бірге бұл қарапайым үш сатылы эжектордың жұмысына теріс әсер етеді.

Шавдинова М.Д., Шарипов Р.Ж., Меццьякова Т.Ю.

СОВЕРШЕНСТВОВАНИЕ ПАРОСТРУЙНОГО ЭЖЕКТОРА КОНДЕНСАТОРА ПАРОВЫХ ТУРБИН

На Алматинской электростанции ТЭЦ-2 на теплофикационных турбинах установлен трехступенчатый пароструйный эжектор ЭПО-3-200, с расходом рабочего пара 850 т/ч. В данной работе предложена и обоснована замена действующего трехступенчатого пароструйного эжектора на двухступенчатый пароструйный эжектор. В результате замены получили экономию теплоты (пара) собственных нужд на производство электрической энергии. Установлено, что при давлении в конденсаторе турбины существенно ниже 100 кПа целесообразна установка нового двухступенчатого эжектора ЭПО-2-80 вместо ЭПО-3-200. Используя существующие методики расчета, получены геометрические характеристики нового эжектора. Расход рабочего пара нового двухступенчатого эжектора составляет 579 т/ч. Кроме того, применение двух ступеней позволяет упростить конструкцию и сделать ее более надежной, также позволяет повысить давление в охладителе 1 ступени эжектора. Это важно именно для теплофикационных турбин, у которых может быть высокая температура основного конденсата, что неблагоприятно сказывается на работоспособности обычного трехступенчатого эжектора.

Танашева Н.К., Тілеубергенова А.Ж., Шаймерденова К.М., Миньков Л.Л., Узбергенова С.Ж.

ЖЕЛДІҢ ТӨМЕН ЖЫЛДАМДЫҒЫ КЕЗІНДЕ ЖЕЛ ТУРБИНАСЫНЫҢ ҮШБҰРЫШТЫ ҚАЛАҚШАСЫНЫҢ АЭРОДИНАМИКАЛЫҚ КҮШТЕРІН ЗЕРТТЕУ

Мақала желдің төмен жылдамдығы үшін жел турбинасының үшбұрышты желкенді қалақшасының аэродинамикалық сипаттамаларын зерттеуге, сондай-ақ сыни шабуыл бұрышын анықтауға арналған. Бұл мақсатта әр түрлі параметрлерге ие үшбұрышты желкенді қалақша жасалып әзірленді. Тәжірибелік үлгі металл каркасты өзекшелерден жасалған, үшбұрышты желкенді қалақшаның материалы жеңіл және берік (жібек), оның бір ұшы каркастың жоғарғы жағына берік жіппен бекітілген; сонымен бірге ішкі диаметрі 8 мм тірек өзекшелерден және подшипниктерден құрылады. Желкенді қалақшаның басқа қалақшалардан ерекшеленеді, себебі желкендер жылжымалы жіптің көмегімен шабуыл бұрышын өзгерту мүмкіндігі бар. Шабуылдың сыни бұрышын анықтау үшін желкенді қалақшаның аэродинамикалық күштері шабуылдың әр түрлі 0° ; 15° ; 30° ; 45° ; 60° ; 75° ; 90° бұрыштарында зерттелген. Мәліметтерді талдаудан шабуылдың сыни бұрышы 15° екендігі анықталды, онда көтеру күшінің мәні максималды болады. Шабуылдың сыни бұрышында көтеру күші мен мандайлық кедергі күшінің мәні 4-тен 12 м/с-ка дейін өзгертін ауа ағынының жылдамдығына тәуелділігі анықталды.

Танашева Н.К., Тлеубергенова А.Ж., Шаймерденова К.М., Миньков Л.Л., Узбергенова С.Ж.

ИССЛЕДОВАНИЕ АЭРОДИНАМИЧЕСКИХ СИЛ ТРЕУГОЛЬНОЙ ЛОПАСТИ ВЕТРОТУРБИНЫ ПРИ НИЗКИХ СКОРОСТЯХ ВЕТРА

Данная статья посвящена изучению аэродинамических характеристик, а также нахождению критического угла атаки треугольной парусной лопасти ветротурбины для малых скоростей ветра. Для этой цели была разработана треугольная парусная лопасть различных параметров. Опытный образец выполнен из металлических каркасных стержней, материал треугольной парусной лопасти состоит из легкого и прочного материала (шелк), один конец которого закреплен к вершине каркаса прочной нитью; опорных стержней и подшипника с внутренним диаметром 8 мм. Парусная лопасть отличается от других лопастей тем, что паруса выполнены с возможностью изменения угла атаки с помощью подвижной нити. Для определения критического угла атаки, аэродинамические силы парусной лопасти были исследованы под разными углами атаки 0° ; 15° ; 30° ; 45° ; 60° ; 75° ; 90° . Из анализа данных было установлено, что критическим углом атаки является 15° , при котором значение подъемной силы максимальна. При критическом угле атаки установлены зависимости подъемной силы и силы лобового сопротивления от скорости воздушного потока, значение которой варьировалась от 4 до 12 м/с.

Нижегородов А.И., Гаврилин А.Н., Мойзес Б.Б., Исмаилов Г.М.

ТЕХНИКАЛЫҚ БҰЙЫМДАРДЫ СЫНАУҒА АРНАЛҒАН ПЕРИОДТЫ ЕМЕС ҚЫСЫМ ИМПУЛЬСТАРЫНЫҢ ГИДРОКӨТЕРГІШ ГЕНЕРАТОРЫ

Жұмыста дірілге төзімділік пен дірілге тұрақтылықты механикалық сынау саласында, сондай-ақ сыртқы және ішкі қысыммен сынау кезінде әр түрлі сынақ стендтерінің конструкцияларының құрамында сызықты емес күш элементтері (серпімді қабықшалары) бар гидрокөтергіш тербеліс генераторларын пайдалану мүмкіндігі көрсетілген. Техникалық өнімдерді сынау үшін гидрокөлемді периодты емес импульстік қысым генераторы-бұл сынақ машиналары саласындағы жаңа патенттелген техникалық шешім. Жұмыста жұмыс сұйықтығының амплитудасы кездейсоқ өзгертін импульстармен периодтық емес функция түрінде сынақ стендінің атқарушы механизміне қозғалысын қамтамасыз ететін біліктердің бұрыштық жылдамдықтарының ара-қатынасы алынады, бұл қысым импульстарының үздіксіз және қайталанбайтын тізбегін жасайды және нақты жағдайдағы объектілердің жұмысына сәйкес келеді. Амплитудалық тапсырманың кездейсоқ сипаты басқарылатын таратқыштар арқылы электр генераторларынан басқарылатын дабылдармен қамтамасыз етіледі. Серпімді қабық түрінде қуат элементіне ие гидрокөлемді генератордың дамуы сәйкес кинематикалық және динамикалық тәуелділіктері бар периодты емес қысым импульстарының генераторының гидромеханикалық сұлбасы ұсынылған. Бұдан басқа, механикалық кездейсоқ дірілге, сондай-ақ осындай жағдайларда жұмыс істейтін объектілердің сыртқы және ішкі қысымымен техникалық объектілерге сынақ жүргізу үшін жаңа гидрокөлемді генераторды қолдана отырып, үш гидромеханикалық жүйе әзірленді. Орындалған жұмыстың нәтижесі әр түрлі техникалық объектілерге кездейсоқ периодты емес күш әсерінен сынақ процестерін жүзеге асыру жүйелері мен әдістерінің спектрін кеңейту болып табылады.

Нижегородов А.И., Гаврилин А.Н., Мойзес Б.Б., Исмаилов Г.М.

ГИДРООБЪЕМНЫЙ ГЕНЕРАТОР НЕПЕРИОДИЧЕСКИХ ИМПУЛЬСОВ ДАВЛЕНИЯ ДЛЯ ИСПЫТАНИЙ ТЕХНИЧЕСКИХ ИЗДЕЛИЙ

В работе показана возможность использования гидрообъемных генераторов колебаний с нелинейными силовыми элементами (упругими оболочками) в составе конструкций различных испытательных стендов в сфере механических испытаний на вибропрочность и виброустойчивость, а также при испытаниях внешним и внутренним давлением. Гидрообъемный генератор непериодических импульсов давления для испытаний технических изделий – это новое запатентованное техническое решение в области испытательных машин. В работе получены соотношения угловых скоростей валов, обеспечивающие движение рабочей жидкости в исполнительный механизм испытательного стенда в виде не периодической функции с изменяющимися по амплитуде случайным образом импульсами, что создает непрерывную и неповторяющуюся череду импульсов давления и соответствует работе испытуемых объектов в реальных условиях. Случайный характер задания амплитуд обеспечивается управляемыми от электрических генераторов сигналами через управляемые гидрораспределители. Разработка гидрообъемного генератора с силовым элементом в виде упругой оболочки представлена гидромеханической схемой генератора непериодических импульсов давления с соответствующими кинематическими и динамическими зависимостями. Кроме этого, разработаны три гидромеханические системы с применением нового гидрообъемного генератора для проведения испытаний технических объектов как на механическую случайную вибрацию, так и на испытания внешним и внутренним давлением тех объектов, которые работают в таких условиях. Результатом выполненной работы является расширение спектра систем и методов реализации испытательных процессов при случайных непериодических силовых воздействиях на различные технические объекты.

Келисбеков А.К., Данияров Н.А., Ахметбекова А.М., Оразбаев К.Н.

ҚАТПАРЛЫ КОНВЕЙЕРДІҢ КӨП ҚОЗҒАЛТҚЫШТЫ ЭЛЕКТР ЖЕТЕГІН ІСКЕ ҚОСУ РЕЖИМІН БАСҚАРУ

Тау-кен кәсіпорындарында қатпарлы конвейерді пайдалану тәжірибесі олардың құрастырылу ерекшеліктеріне байланысты оларды әр түрлі салаларда жүктердің кең спектрін тасымалдау үшін сәтті қолдануға болатындығын көрсетті. Үлкен ұзындықтағы көп қозғалтқышты тізбекті конвейерді іске қосу өте қиын есеп, себебі бұл процесс тартқыш органның шамадан тыс босануымен бірге жүруі мүмкін. Кенептің босану телімдері болғандықтан қатпарлы конвейерді іске қосу шарттары әсіресе қолайсыз болып табылады, нәтижесінде жұмыс органының қаттылығы, яғни оның кернеуі мен жүктеме функциясы салыстырмалы түрде аз болады. Осыған байланысты, күрделі тау-кен және геологиялық жағдайларда жұмыс істейтін көп қозғалтқышты тізбекті конвейердің бірқалыпты іске қосылуын қамтамасыз ету маңызды тәжірибелік есеп болып табылады және қатпарлы конвейердің негізгі құрылысының жұмысқа қабілетті динамикалық күйін басқару және қамтамасыз ету үшін маңызды. Қатпарлы конвейердің көп қозғалтқышты электр жетегінің іске қосу режимінде оның бірқалыпты іске қосылуын қамтамасыз ету және динамикалық жүктемелерді азайту мақсатында, тарту төсемінің қызмет ету мерзімін арттыру және техникалық қызмет көрсету шығындарын азайту үшін басқару әдісі әзірленді.

Келисбеков А.К., Данияров Н.А., Ахметбекова А.М., Оразбаев К.Н.

УПРАВЛЕНИЕ ПУСКОВЫМ РЕЖИМОМ РАБОТЫ МНОГОДВИГАТЕЛЬНОГО ЭЛЕКТРОПРИВОДА ПЛАСТИНЧАТОГО КОНВЕЙЕРА

Практика эксплуатации пластинчатого конвейера на горнодобывающих предприятиях показала, что благодаря своим конструктивным особенностям они могут успешно применяться в различных отраслях промышленности для транспортировки широкого спектра грузов. Запуск многоприводного цепного конвейера большой длины является довольно сложной задачей, так как этот процесс может сопровождаться чрезмерным расслаблением тягового органа. Особенно неблагоприятными являются условия для запуска пластинчатого конвейера, полотно которого имеет провисающие участки, в результате чего жесткость рабочего органа, являющаяся функцией его натяжения и нагрузки на него, относительно невелика. В связи с этим обеспечение плавного пуска многодвигательного цепного конвейера является важной практической задачей и, несомненно, имеет значение для управления и поддержания работоспособного динамического состояния основной конструкции пластинчатого конвейера, эксплуатируемого в сложных горно-геологических условиях. Разработан способ управления пусковым режимом работы многодвигательного электропривода пластинчатого конвейера для обеспечения его плавного пуска и снижения динамических нагрузок, увеличения срока службы тягового полотна и снижения затрат на техническое обслуживание.

Yadav K., Dhobi S.H., Maharajan S., Gupta S.P., Karki B., Nakarmi J.J.

КУЛОН ПОТЕНЦИАЛЫНДАҒЫ ЛАЗЕРДІҢ КӨМЕГІМЕН СЕРПІМДІ ЭЛЕКТРОНДАРДЫҢ СУТЕГІ АТОМДАРЫМЕН ЭЛЛИПТИКАЛЫҚ ПОЛЯРЛАНҒАН СОҚТЫҒЫСУЫ

Лазерлік технологиялардың дамуы оптика саласындағы зерттеулердің белсенді болуына және технологияны дамыту арқылы толығырақ ақпарат алу мүмкіндігіне әкелді. Бұл жұмыстың негізгі мақсаты - кулон потенциалы мен бір фотонды жұтылуымен эллиптикалық полярланған сәуленің қатысуымен математикалық модельді қолдана отырып, дифференциалды қиманы есептеу. Әзірленген модель дифференциалды қиманың толқын ұзындығының артуымен және эллиптикалық полярланған сәулесіне ие электрондардың энергиясының жоғарылауымен кемуімен көрсетеді. Дифференциалдық қима 1,56 радиан поляризацияланған бұрышы кезінде максималды және - 1,56 радиан поляризацияланған бұрышы кезінде минималды болады. Бақылау 1,5 эВ лазер фотонның энергиясына, 1,5 eV Вт·см⁻² лазер өрісінің кернеуіне, 1,56 радианның поляризация бұрышына және 0-ден 600 эВ-ға дейінгі электрон энергиясына негізделген. Алғашқы жуықтау мен Волковтың толқындық функциясын қолдана отырып, дамытылған теңдеу алынды. Бұл жұмыста алынған дифференциалды қима шамамен 110⁻¹⁹ м² -ден 10⁻²⁰ м² -ге дейін құрайды, бұл Флегель алған дифференциалды қимадан аз және 2013 жылы т.б. шамамен 10⁻¹⁷ м² құрайды.

Yadav K., Dhobi S.H., Maharajan S., Gupta S.P., Karki B., Nakarmi J.J.

ЭЛЛИПТИЧЕСКИ ПОЛЯРИЗОВАННЫЕ СТОЛКНОВЕНИЯ УПРУГИХ ЭЛЕКТРОНОВ С АТОМАМИ ВОДОРОДА С ПОМОЩЬЮ ЛАЗЕРА В КУЛОНОВСКОМ ПОТЕНЦИАЛЕ

Развитие лазерных технологий приводит к тому, что область исследований в оптике становится более активной, и с помощью развития технологий можно получить более подробную информацию. Основная цель данной работы - рассчитать дифференциальное сечение с использованием математической модели в присутствии кулоновского потенциала и эллиптически поляризованного пучка с однофотонным поглощением. Разработанная модель показывает, что дифференциальное сечение увеличивается с увеличением длины волны и уменьшается с увеличением энергии электронов с эллиптически поляризованным пучком. Дифференциальное сечение становится максимальным при поляризованном угле 1.56 радиана и минимальным при поляризованном угле -1.56 радиана. Наблюдение основано на энергии лазерного фотона 1.5 эВ, напряженности лазерного поля 1.5eV Вт·см⁻², угле поляризации 1.56 радиан и энергии электронов от 0 до 600 эВ. С использованием первого приближения и волновой функции Волкова получено развитое уравнение. Численно полученное дифференциальное сечение в этой работе составляет примерно от 10⁻¹⁹ м² до 10⁻²⁰ м², что меньше, чем дифференциальное сечение, полученное Флегелем и др. в 2013 году, что составляет примерно 10⁻¹⁷ м².

Жумаев М.Р.

РЕЛЯТИВИСТИК - ИНВАРИАНТТЫ ИДЕАЛ ГАЗ ТЕОРИЯСЫ

Берілген зерттеудің мақсаты релятивистік идеалды газдың түпнұсқа теориясын жасау және массасыз шекте релятивистік идеалды газ бөлшектерінің ерекше (яғни, орташа арифметикалық, орташа квадраттық) жылдамдықтары үшін арнайы салыстырмалылық теориясының постулатының әділеттілігін дәлелдеу болып табылады. Бұл жұмыста релятивистік идеал газ теориясында алғаш рет келесі әдістер қолданылады: релятивистік идеал газ бөлшектерінің жылдамдықтарын таралу функциясын алу үшін сызықты емес түрлендіру әдісі; релятивистік идеал газдың күй теңдеуі алғаш рет өзара әрекеттеспейтін бөлшектер жүйесінің энергиясы - импульстік тензорының релятивистік - инвариантты компоненттерін, яғни жылдамдықты бөлу функциясы бойынша идеалды газды орташалау арқылы алынды. Жылдамдықты таралу функцияларының белгілі релятивистік инварианттылығы негізінде релятивистік идеалды газ бөлшектерінің жылдамдығын таралу функциясының бірегейлігі мен сенімділігін дәлелдеді. Релятивистік идеал газ бөлшектерінің орташа арифметикалық және орташа квадраттық жылдамдығы үшін өрнектер алғаш рет алынды. Алғаш рет ерекше жылдамдықтар үшін арнайы салыстырмалылық постулаттарының дәлелділігі туралы іргелі қорытынды жасалды. Релятивистік идеал газдың қысымын, орташа энергия тығыздығы мен температурасын байланыстыратын күйі теңдеуі алынды.

Жумаев М.Р.

РЕЛЯТИВИСТСКИ - ИНВАРИАНТНАЯ ТЕОРИЯ ИДЕАЛЬНОГО ГАЗА

Целью настоящего исследования является разработка оригинальной теории релятивистского идеального газа и доказательство справедливости постулата специальной теории относительности для характерных (то есть средне арифметическое, средне квадратиное) скоростей частиц релятивистского идеального газа даже в безмассовом пределе. В этой работе впервые в теории релятивистского идеального газа используются следующие методы: метод нелинейного преобразования для получения функции распределения скоростей частиц релятивистского идеального газа; уравнение состояния релятивистского идеального газа было впервые получено путем усреднения релятивистски - инвариантных компонентов тензора энергии - импульса системы не взаимодействующих частиц, т.е. идеальный газ по функции распределения скоростей. На основе хорошо известной релятивистской инвариантности функции распределения скоростей доказаны единственность и определенность функции распределения скоростей частиц релятивистского идеального газа. Впервые были получены выражения для средне арифметического и средне квадратичного скоростей частиц релятивистского идеального газа. Впервые сделан фундаментальный вывод о справедливости постулатов специальной теории относительности для характерных скоростей. Получено уравнение состояния релятивистского идеального газа, которое связывает его давление, среднюю плотность энергии и температуру.

**INFORMATION
ABOUT AUTHORS**
**АВТОРЛАР ТУРАЛЫ
МӘЛІМЕТТЕР****СВЕДЕНИЯ
ОБ АВТОРАХ**

- Akhmetbekova, A.M.** - Candidate of techn.sciences, Head of the Electric Power Engineering and Labor Protection department, O. Baikonurov Zhezkazgan University.
- Daniyarov, N.A.** - Doctor of techn. sciences, Professor, Head of the Corporate University, LLP “Corporation Kazakhmys”, Karaganda, Kazakhstan.
- Dhobi, S.H.** - Master (Sc.), Senior, Researcher, Robotics Academy of Nepal and Innovative Ghar Nepal, Nepal.
- Durgadsimi, S.U.** – PhD, Associate Professor, Department of Physics, Basaveshwar Engineering College, Bagalkot, Karnataka, India.
- Gavrilin, A.N.** – Candidate of tech. sciences, Associate Professor, National Research Tomsk Polytechnic University, Tomsk, Russia.
- Gupta, S.P.** - PhD, Dr., Associate Prof., Department of Physics, Patan Multiple Campus, Tribhuvan University, Nepal.
- Ismailov, G.M.** – Candidate of tech. sciences, Associate Professor, Head of the Department of professional training, technology and design, Tomsk State Pedagogical University, Tomsk, Russia.
- Karki, B.** - PhD, Dr., Associate Prof., Department of Physics, Trichandar Multiple Campus, Tribhuvan University, Nepal.
- Kasimov, A.T.** - Candidate of tech. sciences, Docent, Karaganda Technical University, Karaganda, Kazakhstan.
- Kattimani, V.R.** – PhD, Associate Professor, Department of Chemistry, Basaveshwar Engineering College, Bagalkot, Karnataka, India.
- Kelisbekov, A.K.** - PhD, Associate Professor, Electric Power Engineering and Labor Protection department, O.A. Baikonurov Zhezkazgan University.
- Khaidolda, O.** - PhD, Associate Professor, Buketov Karaganda University, Karaganda, Kazakhstan.
- Kozlovskiy, A.L.** - PhD, Associate Professor, Head of the Laboratory of Solid State Physics, Astana branch of the Institute of Nuclear Physics of the Ministry of Energy of the Republic of Kazakhstan, Nur-Sultan, Kazakhstan.
- Kulkarni, A.B.** – PhD, Assistant Professor, Department of Physics, SKE Society’s Govindram Seksaria Science College, Belagavi, Karnataka, India.
- Maharajan, S.** - Master (Sc.), Assistant Professor, Department of Physics, Patan Multiple Campus, Tribhuvan University, Nepal.
- Makhanov, K.M.** - Candidate of phys.-math.sciences, Associate Professor, E.A. Buketov Karaganda University, Karaganda, Kazakhstan.
- Maruti, N.S.** – Master (Sc.), Assistant Professor, Department of Physics, K.R.C.E.S G.G.D Arts B.M.P Commerce and S.V.S Science college, Bailhongal, Karnataka, India.
- Mathad, S.N.** - PhD, Professor, Head of the Department of Engineering Physics, K.L.E Institute of Technology, Hubballi, Karnataka State, India.
- Meshherjakova, T.Y.** - Candidate of techn. sciences, Associate Professor, Faculty of Engineering & Information Technology, Kazakh-German University in Almaty, Almaty, Kazakhstan.
- Minkov, L.L.** - Doctor of Physical and Mathematical Sciences, Professor, National Research Tomsk State University, Tomsk, Russia.
- Moyzes, B.B.** – Candidate of tech. sciences, Associate Professor, National Research Tomsk Polytechnic University, Tomsk, Russia.
- Nakarmi, J.J.** - PhD, Dr., Professor, Department of Physics, Patan Multiple Campus, Tribhuvan University, Nepal.
- Nizhegorodov, A.I.** – Doctor of tech. sciences, Professor, Irkutsk National Research Technical University, Irkutsk, Russian Federation.
- Omarova, A.** – PhD student, L.N. Gumilyov Eurasian National University, Nur-Sultan, Kazakhstan.
- Orazbayev, K.N.** - Postgraduate student, Renewable Energy Sources department, Faculty of Energy, I. Razzakov Kyrgyz State Technical University, Bishkek, Kyrgyz Republic.
- Potapov, A.A.** – Doctor phys.-math. Sciences, Professor, Chief researcher, V.A. Kotel’nikov Institute of Radio Engineering and Electronics, Russian Academy of Sciences, Moscow, Russia; IREE joint laboratory of fractal method & signal processing, Jinan University, Guangzhou, China.
- Razzhivin, I.A.** – Candidate of techn. sciences, Associate professor, School of Energy and Power Engineering, National Research Tomsk Polytechnic University, Tomsk, Russia.

Ruban, N.Yu. – Candidate of techn. sciences, Docent, Associate professor, School of Energy and Power Engineering, National Research Tomsk Polytechnic University, Tomsk, Russia.

Rudnik, V.E. – Research engineer, School of Energy and Power Engineering, National Research Tomsk Polytechnic University, Tomsk, Russia

Shaimerdenova, K.M. – Candidate of techn. sciences, Professor, Buketov Karaganda University, Karaganda, Kazakhstan.

Sharipov, R.Zh. - Candidate of techn. sciences, Associate Professor, Faculty of Engineering & Information Technology, Kazakh-German University in Almaty, Almaty, Kazakhstan.

Shavdinova, M.D. – PhD student, Senior Lecturer, Faculty of Engineering & Information Technology, Kazakh-German University in Almaty, Almaty, Kazakhstan.

Shishulin, A.V. – Junior Researcher, G.A. Razuvaev Institute of Organometallic Chemistry, Russian Academy of Sciences, Nizhny Novgorod, Russia.

Shishulina, A.V. – PhD, Associate Professor, R.E. Alekseev Nizhny Novgorod State technical University; N.I. Lobachevsky Nizhny Novgorod State University, Nizhny Novgorod, Russia.

Shlimas, D. – PhD, Research Lecturer, L.N. Gumilyov Eurasian National University, Nur-Sultan, Kazakhstan.

Tanasheva, N.K. - PhD, Associate Professor, Buketov Karaganda University, Karaganda, Kazakhstan.

Tleubergenova, A.Zh. - PhD student, Buketov Karaganda University, Karaganda, Kazakhstan.

Uzbergenova, S.Zh. - Master of Logistics and Supply Chain Management, Senior Lecturer of the Department of Engineering Technologies and Transport of Kokshetau University named after Sh. Ualikhanov.

Yadav, K. - PhD, Dr., Associate Professor, Department of Physics, Patan Multiple Campus, Tribhuvan University, , Nepal.

Yessenbayeva, G.A. - Candidate of phys.-math. sciences, Associate Professor, Buketov Karaganda University, Karaganda, Kazakhstan.

Yurov, V.M. - Candidate of phys.-math.sciences, Associate Professor, Director of the Scientific Research Center, E.A. Buketov Karaganda University, Karaganda, Kazakhstan.

Zdorovets, M.V. - PhD, Associate Professor, Director of the Astana branch of the Institute of Nuclear Physics of the Ministry of Energy of the Republic of Kazakhstan, Nur-Sultan, Kazakhstan.

Zholmagambetov, S.R. - Candidate of tech. sciences, Docent, Karaganda Technical University, Karaganda, Kazakhstan.

Zhumaev, M.R. – Doctor of phys.-math. sciences, Associate professor, Bukhara Engineering Technological Institute, Uzbekistan, Bukhara.

About «Eurasian Physical Technical Journal»

ISSN 1811-1165 (Print); ISSN 2413-2179 (Online)

Abbreviated key title: Eurasian phys. tech. j.

Eurasian Physical Technical Journal (Eurasian phys. tech. j.) is a peer-reviewed open access international scientific journal publishing original research results on actual problems of technical physics and other related fields. Since 2004 «Eurasian phys. tech. j.» is published in English. The international editorial board consists of leading physicists from 9 countries.

Since May 2019 «Eurasian phys. tech.j.» has been indexed in the Scopus database on four scientific areas: Energy, Engineering, Materials Science, Physics and Astronomy.

Re-registration Certificate No.KZ50VPY00027647 of the «Eurasian phys. tech. j.» issued October 6, 2020 by Information Committee of the Ministry of Information and Public Development of the Republic of Kazakhstan. Now Eurasian phys. tech. j. will be published quarterly.

In January 28, 2021, the “Eurasian Physical Technical Journal” is included in the updated list of journals recommended by the Committee in the following areas: Physics, Energy, Materials Science.

Publication Ethics and Malpractice Statement

Submission of an article to the Eurasian phys. tech. j. implies that the paper described has not been published previously, that it is not under consideration for publication elsewhere, that its publication is approved by all authors and tacitly or explicitly by the responsible authorities where the paper was carried out, and that, if accepted, it will not be published elsewhere in the same form, in English or in any other language, including electronically without the written consent of the copyright holder. In particular, translations into English of papers already published in another language are not accepted.

For information on Ethics in publishing and Ethical guidelines for journal publication see <http://www.elsevier.com/publishingethics> and <http://www.elsevier.com/journal-authors/ethics>.

The Eurasian phys. tech. j. follows the Code of Conduct of the Committee on Publication Ethics (COPE), and follows the COPE Flowcharts for Resolving Cases of Suspected Misconduct (http://publicationethics.org/files/u2/New_Code.pdf).

To verify originality, your article may be checked by the originality detection service Cross Check <http://www.elsevier.com/editors/plagdetect>.

Authors are responsible for the content of their publications. No other forms of scientific misconduct are allowed, such as plagiarism, falsification, fraudulent data, incorrect interpretation of other works, incorrect citations, etc. Authors are obliged to participate in peer review process and be ready to provide corrections, clarifications, retractions and apologies when needed. All authors of a paper should have significantly contributed to the research.

Reviewers should provide objective judgments and should point out relevant published works which are not yet cited. Reviewed articles should be treated confidentially. The reviewers will be chosen in such a way that there is no conflict of interests with respect to the research, the authors and/or the research funders.

Editors have complete responsibility and authority to reject or accept a paper, and they will only accept a paper when reasonably certain. They will preserve anonymity of reviewers and promote publication of corrections, clarifications, retractions and apologies when needed.

The acceptance of a paper automatically implies the copyright transfer to the Eurasian phys. tech. j.

All submitted papers will be sent for reviewing to leading experts in the given area.

The Editorial Board of the Eurasian phys. tech. j. will monitor and safeguard publishing ethics.

The editors reserve the right to accept or reject manuscripts.

GUIDELINES FOR AUTHORS

Research articles are accepted for exclusive publication in the «**Eurasian phys. tech. j.**» in English. The manuscripts must contain original results of investigation in the 4 scientific areas:

ENERGY; ENGINEERING; MATERIALS SCIENCE; PHYSICS AND ASTRONOMY.

The publications of manuscripts should be recommended by official a Cover letter of the organization (University) in which the work was performed.

The author who submitted an article for publication will be considered as a corresponding author.

A scientific article should contain the results of original scientific research previously unpublished and not intended for publication in other publications. Scientific articles submitted for publication in scientific journals should comprise at least 70% of the original text.

The structure of the article includes the following sections:

Title: includes a separate line on the left the **UDC** index, information about the authors (surname and initials, name of institution, city, country, e-mail of a corresponding author, title of the article.

Abstract should consist of at least 5-6 sentences, not exceeding 200 words without formula, references, abbreviations. An abstract is a short and powerful summary that describes the focus of a research paper. It could contain the information about why the research study was done, background, what the methodology was and something about the findings of the author(s).

Keywords: at least 3-10 basic terms or short phrases used in the article.

The text should be divided on structural parts: **Introduction, Theoretical part, Methods and materials or Experimental technique, Results and Discussion, Conclusions.**

Conclusions: formulating main results; a comparison of the results with the existing data on this topic; assessment of scientific novelty and practical value of the results.

Acknowledgments may be shown at the end of the article text, before References.

References: a bibliographic list is compiled according to the requirements:

- Books, abstracts, patents: Surname and initials of the authors (it is enough to indicate the first three or one surnames, et al), *Title of the book* in italics, publish house or city, year and total number of pages.

- Journals, collections of papers, conference proceedings - Surname and initials of the authors (the first three are enough), the title of the article, the *Title of the journal* in italics (you can use the abbreviated title), city and / or country, year, volume, issue number, pages of the "begining and end" (pp. ... - ...).

- Internet links also must to indicated the authors, the title and URL

Title, Abstract and Keywords are given in English, Qazaq, and Russian.

The volume of the article, including bibliography, should not exceed 6-10 pages including tables, figures (no more than 6-8) and references (no more than 30-35) of text typed on a computer (Microsoft Word editor. A review paper must not be more than 15-20 pages (including no more than 10 figures).

Fields of the manuscript should be: left, upper, lower - 30 mm, right - 15 mm; font - Times New Roman, size - 11 pt; line spacing - single; alignment - in width; indent - 0.8 cm.

All abbreviations and acronyms, with the exception of obviously well-known, should be deciphered at first use in the text.

All references must be numbered in the text (for example, [1], [2-4]) and listed in numerical order.

Equations in your paper have to be written using the Microsoft Equation Editor or the MathType.

Tables must be inserted into the text.

Figures should be prepared in a digital form suitable for direct reproduction. Figures shall be submitted on the separate sheets or can be included into the text.

The following files must be submitted via e-mail:

- Article text (*.doc);

